Jet mixing in DI diesel engine combustion chamber model under quiescent and swirling conditions

Petersen, Ulf

Award date:
1991

Awarding institution:
University of Bath

Jet Mixing in DI Diesel Engine Combustion Chamber Model Under Quiescent And Swirling Conditions

submitted by Ulf Petersen

for the degree of Ph.D

of the University of Bath

1991

ProQuest LLC
789 East Eisenhower Parkway
P.O. Box 1346
Ann Arbor, MI 48106-1346

SUMMARY

A computational and experimental study on steady state and impulsive injections in a three dimensional direct injection Diesel engine combustion chamber model is described. Consideration is given to quiescent and swirling conditions.

The governing equations are solved by the use of a three dimensional finite volume computer code. Sensitivity studies are performed on the effect of grid density and method of generation, inlet and outflow boundary conditions, and turbulence model constants. By solving for a passive scalar quantity to simulate a number of air - fuel ratio boundaries typically found in Diesel engines, it is shown that undeflected injections are not well suited for applications in a direct injection Diesel engine. At the end of injection large areas of the combustion chamber remain with very weak air - fuel mixtures.

The benefit afforded by injections into a swirling flow field is illustrated by examining three different swirl rates generated prior to injection. A non - dimensional parameter expressing the relative effect of swirl to penetration is introduced to show that a variable injection pressure leads to a more favourable mixture distribution in the combustion chamber model. The implications for engine performance are discussed.

In order to provide the basis for direct validation of numerical results, an experimental study using hot film anemometry is described. The experimental programme is designed to measure mean and fluctuating velocities in the flow configurations considered computationally. The comparison between experimental and numerical results shows fair to good agreement, indicating that the gross features associated with the mixing process are well predicted. Weaknesses of the numerical model are identified with respect to the predicted location and size of recirculation zones.

ACKNOWLEDGEMENTS

The author wishes to thank Professor Frank Wallace for his encouragement and stimulating supervision in the initial stages of the work, and his continuing interest in its progress.

The author is also particularly indebted to Dr. Stuart MacGregor for his valuable advice and support during his supervision towards the completion of this work.

Thanks are also due to Dr. Michael Wilson for his guidance and assistance with the modelling programme.

The help of Eric Brain and George Bonwick in many technical matters is gratefully acknowledged.

NOMENCLATURE

A_i	cell face area i
A_1, A_2 A_3, A_4	coefficients in velocity - voltage relationship (eqn. 6.8)
a_i	coefficient in discretization equation
a_{nb}	neighbour coefficient
b	source term in pressure correction equation
C	concentration, empirical coefficient in eqn. 4.10
C_1, C_2	constants in ε equation
C_{R1}, C_{R2}	constants in Reynolds stress model (eqns. 4.26 and 4.27)
Cs	constant in Reynolds stress model (eqn. 4.28)
C_ε	constant in Reynolds stress model (eqn. 4.25)
C_μ	constant in eddy viscosity relationship
C_m	mass flow coefficient
C_ϕ	coefficient for variable ϕ
C'_μ	coefficient in one equation turbulence model (eqn. 4.12)
Co	Courant number
D	side length of square nozzle hole
D_i	Diffusion coefficient for cell face i
d_i	coefficient in velocity correction equation
D_N	equivalent nozzle diameter
D_T	tank diameter
D_ψ	diffusion term for property ψ
D/Dt	substantial time derivative
E	voltage, wall roughness parameter

f	correction parameter for axisymmetric jet
frac	fraction of tank volume injected
h	height of analogue model
k	turbulent kinetic energy
K_P	nondimensional parameter for penetration
K_S	nondimesional parameter for swirl
K_R	K_S/K_P
L	turbulence length scale
l_m	Prandtl mixing length scale
$\dot{m}$	mass flow rate
N	swirl speed [rpm]
n	number of data points
P	mean pressure
p	fluctuating pressure, injection pressure
P'	instantaneous pressure
Pe	Peclet number
P_k	production rate of k
P_ε	production rate of ε
R	outer radius
r	radial distance, radial coordinate in cylindrical polar coordinate system
Re_t	turbulent Reynolds number ($Re_t = k^2 / \nu\varepsilon$)
S_ϕ	source term for variable ϕ
s_φ	friction factor
T	temperature
TI	turbulence intensity
T_f	false time step

t_i	injection period
U_i	mean velocity component in x_i direction
u_i	fluctuating velocity component in x_i direction
$\overline{u_i u_j}$	stress in tensor notation
U'_i	instantaneous velocity component in x_i direction
U_τ	friction velocity (eqn. 3.14)
ΔU_m	maximum velocity difference across the jet
u, v, w	mean velocity components in cylindrical polar coordinates
V	injection velocity
V_m	value of mass flow
V_P	cell volume surrounding grid node P
V_ϕ	value of variable ϕ
Vol	injected volume
x_i	coordinate in tensor notation
y^+	nondimensional wall distance (eqn. 3.16)
z	axial coordinate in cylindrical polar coordinate system
Z	length scale parameter (eqn. 4.15)

Superscripts

*	intermediate value
'	instantaneous value, correction value

Subscripts

b	bridge
cl	centreline
e, h, l, n, s, w	east, high, low, north, south, west cell face

E, H, L, N, S, W	grid node of cell adjacent east, high, low, north, south, west of control volume
in	injection
P	grid node of control volume
r	radial
ref	reference
t	tangential
s	sensor
W	wall
z	axial coordinate
ϕ	general variable
θ	circumferential coordinate

Greek symbols

α_l	linear under - relaxation factor
α_t	time step under - relaxation factor
α_1, α_2	angle between velocity vector and perpendicular axis to hot films 1 and 2
β	angle between velocity vector and reference axis
δ	jet width (distance from centreline to 1 % centreline velocity at outer edge)
$\delta_{1/2}$	jet half width
δ_{ij}	Kronecker delta
ε	dissipation rate
ϕ	general variable
ϕ'	instantaneous value of general variable
φ	fluctuating value of general varible
γ	cone angle
Γ	diffusion coefficient

κ	van Karman constant
λ	molecular diffusion coefficient
ν	laminar kinematic viscosity
ν_t	turbulent viscosity
ν_{eff}	effective viscosity ($\nu_{eff} = \nu + \nu_t$)
θ	circumferential coordinate in cylindrical polar coordinate system
ρ	density
σ_k, σ_ε	constants in k - ε model
σ_t	turbulent Schmidt number
τ	shear stress
ω	angular velocity
Ω	vorticity
ψ	fluid property
ξ	coordinate along jet axis
ζ	coordinate perpendicular to jet axis

S.I. units unless stated otherwise

CONTENTS

CHAPTER 1

1. INTRODUCTION TO FLOW PROCESSES IN DIRECT INJECTION DIESEL ENGINES

This introduction to flow processes in direct injection, henceforth DI, Diesel engines focuses on fuel - air mixing in the combustion chamber. It does not attempt to give a broad overview of fluid motion in engine cylinders, from the intake through to the exhaust processes, but concentrates on aspects relevant to the present study: injection methods, fuel spray formation and combustion. A literature review and discussion of these cases in section 1.1 is followed by an outline of the objectives and structure of this thesis in section 1.2.

1.1 Direct Injection Processes in Light Duty Vehicles

Passenger car Diesel engines have until recently almost exclusively been built as prechamber engines rather than direct injection engines. Important design considerations in the prechamber concept are the limitation of both combustion noise and exhaust pollutant emission. However, compared to DI Diesel engines, prechamber versions show an up to 10 % poorer fuel economy. This is illustrated in figure 1.1 which depicts the engine efficiency of a range of turbocharged and naturally aspirated Diesel engines of both the DI and prechamber type. The engines compared are Audi passenger car Diesel engines ranging in size from 1.6 l to 3.0 l. Due to the obvious advantage of the DI version research into its suitability as a drive system for light duty vehicles is continuing.

Abthoff [1] reports that proper control of fuel - air mixing in the combustion chamber

can help to overcome the problems of noise and pollutant emission. Based on a variant of the Daimler - Benz OM 600 engine he compares two different DI techniques as illustrated in figure 1.2: the wall - wetting method and the air - mixing combustion system. While in the former method fuel is injected under a steep angle into a deep piston bowl, with surface evaporation and the wall jet formed after impingement contributing to the mixing process, in the latter technique injection takes place at a much shallower angle through a multihole nozzle. Mixing with the surrounding air occurs immediately after injection. Impingement at the piston bowl occurs, however, the formation of a wall jet at the piston liner is undesirable as it affects lubrication.

In both cases swirl in the combustion chamber was generated by specially designed swirl inlet ports of which an example is reproduced in figure 1.3. The ports where designed so as to give a high swirl rate for the wall - wetting combustion system and a lower swirl rate for the air - mixing arrangement. A one hole and a four hole nozzle were used respectively, the injection pressure was 600 bar at n = 2000/min.

The criteria used for comparing the two techniques were effective mean pressure, specific fuel consumption, smoke number, maximum pressure gradient and the exhaust NO_x and HC concentrations. Figure 1.4 indicates that for both effective mean pressure and smoke number the air - mixing scheme is superior to the wall - wetting method, particularly at low rpm values. Data for specific fuel consumption, pressure gradient and exhaust pollutant concentrations are presented in figure 1.5 for n = 2000/min. Here opposing trends become apparent. While the air - mixing arrangement gives 4 to 6 % better specific fuel consumption and lower hydrocarbon concentration, its performance is poorer when comparing maximum pressure gradient and NO_x concentration. The pressure gradient is an indicator of combustion noise and therefore an important consideration in passenger car Diesel engine design. Current and future legislation must be taken into account when addressing the problem of NO_x emissions.

One method of reducing pressure gradients , split injection, is described by Mayer [2]. This technique reduces the amount of fuel injected during the ignition delay period (see figure 1.10) and thus reduces the initial rate of cylinder pressure rise. Applied to the air - mixing scheme it led to a reduction of the maximum pressure gradient to values below 4 bar/°CA, similar to that achieved by the wall - wetting technique. With regard to NO_x emissions measures like exhaust gas recirculation, nozzle design modifications, high pressure injection and improved spray mixing hold considerable promise. Split injection was also found to reduce exhaust emissions over the entire engine speed and load range [2].

Abthoff [1] concludes that of the two direct injection techniques air - mixing has the larger potential of becoming an alternative to prechamber engines. Accordingly a thorough understanding of in - cylinder air motion, fuel spray formation and combustion processes in this application is essential to further reduce pressure gradients and exhaust pollutant emissions.

Significant progress has been achieved in fluid mechanics of DI Diesel engines over the last few years. The following sections (1.1.1 - 1.1.3) give an account of the techniques employed and the quality of agreement reached between experimental results and numerical predictions. Based on recent work reported in the literature limitations of computer simulations are also outlined. The emphasis lies on spray behaviour, however, a brief discussion of in - cylinder flows and combustion is also given to place the spray formation work in its context.

1.1.1 In - Cylinder Flows

Flow fields in reciprocating engines show complex time - varying three - dimensional structures. Only in rare cases where the combustion chamber is axisymmetric and the induction process is also symmetric, is a two - dimensional modelling approach suitable. In order to maintain a high degree of generality, computer codes must

therefore adopt multi - dimensional methods which perform time - dependent, three - dimensional calculations.

The modelling technique employed for in - cylinder engine flows in recent years has almost exclusively been the finite - difference method. It is based on solving the ensemble averaged differential conservation equations for mass, momentum and scalar quantities such as energy and density. However, these equations do not form a closed set as they contain averaged products of turbulent fluctuations, known as second moments. Second moments have to be modelled and only when this is accurately possible can the equations for velocity, pressure, temperature, etc. be solved. The subject of turbulence modelling is very complex and will be dealt with in more detail in chapter 4.

In the context of in - cylinder flow modelling, two - equation turbulence models have been widely used [3, 4, 5] and more recently the Reynolds - stress models [6].

Gosman's reciprocating piston motion, henceforth RPM code [5, 7, 8] solves the discretized conservation equations for axisymmetric cylinder flows over computational meshes similar to that shown in figure 1.6. The part of the grid lying within the piston bowl translates with it, while the remaining grid between the top of the bowl and the cylinder head expands and contracts with the piston motion [9]. Turbulence is accounted for by the two - equation k - ε model. Comparisons with measurements during the induction stroke of a model engine [10] show the flow field to be well predicted and suggest reasonably good agreement of turbulence levels at TDC. Three different versions of the k - ε turbulence model for the prediction of in - cylinder flows have been assessed by Ahmadi - Befrui et al [11] in conjunction with the RPM code. The study evaluates the performance of k - ε model variants through simulation of the complete engine cycle. The model differences reside in the form of the transport equation for the turbulence dissipation rate ε, where different additional terms were introduced to account for compressibility. It is concluded that the model is not very sensitive to compressibility effects, however, comparison with experimental

data shows that the mean flows predicted during compression are in poor agreement due to the longer persistence of the predicted flow generated during intake, which is a feature of the computational code. As mentioned earlier [10], turbulence intensities near TDC are in good agreement with experimental data. The axisymmetric RPM version has been developed into a multi - dimensional code allowing for off - centre inlet/exhaust arrangements [12]. Further comparisons of experiments and multi - dimensional predictions of mean and turbulent velocities are reported by Ahmadi - Befrui et al [13].

Another model with similar characteristics as the extended RPM version is described by Ikegami et al [3]. The algorithm is fully three dimensional and hence allows for asymmetry such as offset valves and piston bowls. Comparisons with experimental data are not given.

Fischer et al [4] report their findings of in - cylinder calculations again employing the k - ε turbulence model. The mesh comprising 12600 cells is reproduced in figure 1.7. Experimental results are of a global nature comparing pressure variation with crank angle. The agreement is generally good with the largest discrepancy observed in the heat release diagram where the predicted peak is approximately 10 % lower than the corresponding experimental value. No spatially resolved data is presented.

The most significant work in the field of Reynolds - stress models applied to IC engines was carried out by Watkins et al [6] at UMIST. Reference 6 also cites a number of other studies in this area. Three dimensional body fitted orthogonal curvilinear grids are used for modelling cylinder and piston bowl (figure 1.8), whereas non - orthogonal curvilinear grids are employed for the calculation of steady flows in manifolds. The mesh compresses and expands with the piston motion.

Experimentally, studies using photographic techniques, hot wires and LDA have been conducted. Brandl et al [14] investigated in - cylinder flows under motoring conditions using hot wire anemometry, focusing on the effect of different intake port

designs. By locating probes on the piston a two - dimensional flow field including turbulence parameters could be established throughout the whole cycle. Many other experimental studies are cited [14].

Summarizing a sentiment expressed by all workers, multi - dimensional models can be regarded as powerful tools in producing an overall flow structure. Care is necessary when defining the computational mesh and the inlet boundary conditions. Errors are likely to occur in regions where gradients in mean and turbulent quantities are large. The computational effort required particularly in the case of three - dimensional calculations poses another limitation.

1.1.2 Fuel - Spray Formation

Modelling of fuel - air mixing in DI Diesel engines has not progressed as quickly as the study of in - cylinder air motion. Since it is the principal theme of this thesis, a background to different modelling approaches followed by a review of experimental data will be given in this section. A review of phenomenological models for undeflected and deflected jets will be presented in chapter 2.

Modelling Techniques

Combustion efficiency, engine output and exhaust pollutant emission all depend critically on the air - fuel mixing process in the combustion chamber. In particular, jet penetration, mixing of fuel and air due to entrainment processes, and the recirculating motion resulting from the impingement of the fuel - air mixture on cylinder and piston walls determine these characteristics.

Two considerations have given the main impetus for developing spray - mixing computer models, namely the very high costs and practical difficulties associated with experimental studies on engines and secondly, the ability to analyse and optimize the air - fuel mixing process at any phase in the design of an engine. The different

approaches towards modelling fuel sprays are outlined in the following paragraphs.

A simplified model for spray simulation is based on the supposition that a fuel spray emerging from the nozzle atomizes and vaporizes extremely rapidly [15]. Newman and Brzustowski [16] and Chiu et al [17] report that a liquid jet near the thermodynamic critical condition behaves as a gaseous jet. Any droplets shatter as the surface tension approaches zero near the critical point. These observations allow the liquid fuel spray to be treated as a single phase gaseous jet with little loss of realism. The analysis is considerably simplified and the classical single phase jet theory of Abramovich [18] can be applied. Provided compressibility effects are negligible the simplification can be taken even further by substituting the gaseous jet with a water jet. Numerous studies into the mixing process of submerged water jets both under quiescent and swirling conditions have been carried out, several of these at Bath University using a specially designed hydraulic analogue rig [19, 20, 21, 22, 23]. Modelling of single phase jets has in recent years employed multi - dimensional finite difference codes as reported for example by Patankar [24], Kuo and Bracco [25, 26], Jones and McGuirk [27] and Hoholis [28]. Particular attention to tuning two equation turbulence models for jets was given by Rodi [29], Malin [30] and Pope [31]. The incorporation of an ensemble averaged Reynolds - stress transport closure is described by Lin and Leschziner [32].

Work on single phase jets in isolation without the influence of combustion can help highlight the aerodynamic features associated with the injection process. It therefore provides extremely useful information which can then be incorporated in multi - zone combustion models. The multi - zone model is described in section 1.1.3.

An alternative route towards multi - zone combustion models lies in what are known as integral and phenomenological models. In this approach fuel spray mixing is treated on a continuum mechanics basis so that the classical differential equations of continuity, momentum and energy may be applied. An early model by Adler and Lyn [33] has been gradually developed to include crossflow and effects of temperature

and composition variation [34]. A more detailed description of this model type is given in chapter 2, it is here however worth noting that phenomenological models only yield predictions of global characteristics without the detailed spatial and temporal property distribution provided by the finite difference schemes.

In a different approach to spray modelling the RPM model [7] refered to in section 1.1.1 has been extended by Gosman and his co - workers to incorporate a spray model based on a statistical sample of discrete, different sized droplets. A typical droplet size distribution is shown in figure 1.9. After injection the droplet history is tracked by solving the equations of motion for their position and velocity vectors. Heat transfer is accounted for by solving the conservation equations for mass and temperature, coefficients for heat transfer, evaporation rate and droplet drag must be provided.

Other more recent two - phase studies using a discrete droplet model have been detailed by Khaleghi and Watkins [35] and Brandstätter and Killmann [36]. Both modelled the liquid phase as a spray of discrete droplets represented by a number of different sized droplet parcels. The conservation equations of mass, momentum and energy, together with trajectory equations, were solved for each droplet parcel to cover evaporation history and motion of the individual droplet parcels. For the gas phase, again conservation equations of mass, momentum and energy were solved together with the k - ε turbulence model equations. The effect of liquid phase was accounted for by an additional equation for fuel vapour mass fraction.

This brief review of modelling work on sprays, which is by no means complete, does highlight the alternative approaches towards a better understanding of air - fuel mixing processes in DI combustion chambers. Comprehensive lists of references dealing with spray modelling are supplied in references [8, 37, 38, 39].

Experimental Techniques

Experimental techniques may be devided into two categories according to the kind of data they provide: flow visualization and local methods. The former yields flow field information of global nature and employs mainly photographic and dye techniques. The latter provides considerably more detailed quantitative data at discrete locations. It makes use of either hot wire/ hot film anemometry or laser anemometry.

In the former category photographic records of spray development have been obtained by Tindal et al [40] using a single shot high speed camera in a cylindrical chamber filled with nitrogen into which fuel was injected radially. The study was concerned with the variation of fuel concentration and the effect of swirl on the fuel - air mixing. Regions of different characteristics within the spray were identified.

Extensive work using a high swirl combustion bomb has been carried out at Bath University [41, 42, 43]. This bomb can reproduce conditions typical of those at the end of compression in medium or small DI engines. Swirl rate, pre - combustion pressure and temperature, as well as injection quantity and rate can be independently controlled. A variety of heads are available for the bomb so that photographic records with a high speed camera can be obtained and heat release tests providing the pressure history inside the combustion chamber performed. A series of 'cold' tests were conducted, where fuel was injected into nitrogen in order to observe jet growth and trajectory. Cold nitrogen is a very suitable medium as it keeps evaporation rates small thereby affording good visibility of the jet. Parametric studies included variation of chamber pressure (45 and 55 bar), swirl speed (between 4,500 and 7,900 rev/min), injection duration (between 1.84 and 2.40 ms) and injection pressure (between 200 and 300 bar). The records indicate that the jet reaches the chamber wall at a radius of 50 mm after approximately 1.7 ms. From the comparison of observed jet tip penetration with predictions from different models it becomes evident that the best agreement is obtained with the model by Chiu et al [17].

The bomb has proved a very valuable research tool, particularly because the effects of swirl, pressure and temperature can be studied independently. There is still scope for more detailed velocity surveys using either hot wire anemometry or employing laser systems by taking advantage of the excellent optical access. Further tests involving combustion will be refered to in section 1.1 3.

Another widely used flow visualization technique is based on the single phase gas - into - gas jet extended to a water - into - water jet provided that compressibility effects are negligible. The underlying assumption of course is that the spray evaporates extremely rapidly and can therefore be treated as a single phase air or water jet [16]. Particularly in Diesel engines this is quite realistic where injection is performed near or beyond critical conditions. Similarity between the mixing processes in an engine and a water model is based on geometric similarity and the Strouhal and Reynolds number [41], although Way [22] found that an exact agreement of Reynolds number between engine and water model is not essential. The use of Strouhal similarity increases both the length and the time scale thereby simplifying the experimental procedure significantly. Mixing in the jet is made visible by the addition of the indicator dye phenolphthalein to the water in the tank. This is kept in its colourless (acid) state before injection. Weak alkali is injected so that the mixing region is coloured red by the change in the indicator. By controlling the relative concentrations of acid and alkali, the mixture ratio between injected water and tank water at the boundaries where the colour change occurs, can be adjusted [22]. The mixture ratio can then be related to the fuel - air ratio in an engine.

Results of dye experiments in a specially designed hydraulic analogue rig are reported by Horner [20], Idoum et al [21] and Way [22]. The rig consists of a cylindrical perspex drum of 600 mm diameter which permits observation of the mixing process both from the side and the top. Swirl is generated by rotating the tank which is stopped shortly before injection to reproduce stationary combustion chamber walls. Swirl continues for some time at an almost constant rate. The complete experimental

arrangement including the microprocessor controlled data acquisition system is described in chapter 7. Subject to overriding limitations with respect to variations in density, temperature and composition, the photographic records from the analogue rig provide quantitative information of jet growth, deflection and entrainment. This information can then be used to improve the semi - empirical jet propagation expression in the mixing formulation of integral type models. Integral models for undeflected and deflected jets employing a propagation equation have been described by Abramovich [18], Adler and Lyn [33] and Adler and Baron [44] and have been implemented at Bath University by Packer [45] and Wilson [34].

Another experimental technique refered to earlier in this section, the local method, yields detailed quantitative data resolved with respect to space and time. Flow measurements of jets in a cross flow, but not in an engine configuration, have been published by Kamotani and Greber [46] and Witze [47]. In the former study velocity and turbulence intensity were measured for three different ratios of jet velocity to crossflow velocity using hot - wire probes. Results are given in the form of jet centreline trajectories and velocity contours at various jet cross sections. It was found that the entrainment rate is independently controlled by the cross flow components normal and parallel to the jet trajectory. Witze [47] considered both the steady state and the impulsively started turbulent air jet. Using a hot - film system he achieved a maximum data rate of 36 kHz which povides very detailed temporally resolved data of the suddenly started jet. His measurements show that the quasi steady state assumption used in integral models is reasonable since the impulsively started jet reaches its steady state value very quickly. Furthermore, he demonstrates that the jet tip penetration varies with the square - root of time.

Most research reported in the literature describes *either* numerical analysis *or* experimental work. There appears to be a lack of comprehensive studies allowing a detailed quantitative comparison of the two which is clearly particularly important when evaluating the accuracy of numerical predictions. One step in this direction with

an emphasis on experimental work has recently been taken by Gan [23] who conducted a detailed survey of velocity and turbulence intensity under quiescent and swirling conditions in the hydraulic analogue rig at Bath University using hot - film anemometry. Further studies in this area with a different nozzle configuration and more attention to the computational aspects is the subject of this thesis.

1.1.3 Combustion

When considering combustion in Diesel engines it is instructive to examine the heat release diagram shown in figure 1.10. Following this diagram, the combustion process may be divided into four stages which are now briefly described:

- During the ignition delay period air is entrained into the spray. The quality of mixing depends on injection characteristics such as injection rate and quantity, nozzle design, number of nozzle holes, and on operating conditions, particularly temperature, pressure, turbulence level and the presence of swirl. Immmediately after beginning of injection the temperature is usually so low that the burning rate is small. Heat is being transfered to the incoming fuel.

- The second stage is the 'premixed burning' region where the combustion is largely controlled by chemical - kinetics. As the temperature rises, the burning rate increases thereby again accelerating the temperature rise. The rate of heat release increases until it reaches its peak when all prepared fuel is used up. Depending on the time available for mixture preparation the first peak will be more or less pronounced. High speeds and loads tend to reduce the amount of premixed fuel available for rapid burning, thus leading to a relatively low peak, whereas longer ignition delays usually cause higher first peaks.

- As the accumulated mixture is being used up, the rate of burning decreases. In the third combustion stage, known as the 'mixing controlled' region, no sudden changes in heat release occur. A smaller second peak may appear as more fuel is injected and more air is entrained. The burning process is largely governed by temperature, turbulence and rate of entrainment. Since turbulence is one of the main controlling factors its correct representation by spray - mixing models is extremely important.

- Towards the end of the combustion process temperature falls due to expansion. The nature of combustion is not fully understood at this last stage, Grigg and Syed [48] suggest that the rate of burning is primarily controlled by chemical kinetics.

From the preceeding outline of the combustion process it is apparent that the complex nature of the four different stages does not lend itself easily towards modelling. The approaches that have been made fall again into the two categories, phenomenological modelling and multi - dimensional modelling, and will briefly be described in the following paragraphs.

In phenomenological models the complete process is divided into spray mixing and multi - zone combustion models. The importance of the correct representation of spray mixing for the premixed and diffusion burning processes has already been emphasised. The transient nature of the spray is represented by empirical correlations derived from experiments. Combustion is accounted for in multi - zone 'burning' submodels, in which the mass and energy conservation equations are applied to small individual zones within a fuel spray area as illustrated in figure 1.11. These burning zones provide the basis for a step - by - step calculation of the time dependent zone variables. In most models the fuel mass burning rate is determined by applying the

Arrhenius equation to all zones from the rich to the lean limit. The Arrhenius law used is based on mean values of temperature and mass fraction and does therefore not include the influence of small scale fluctuations due to turbulence. Examples of phenomenological models are described by Chiu et al [17] and Meguerdichian [49].

In multi - dimensional models it is sought to formulate expressions for the rate of heat release which can be cast into the same form as the partial differential equations for momentum, energy, etc. [50]. These expressions take account of the different burning rate control mechanisms, i.e. chemical - kinetics in the premixed burning phase and turbulent mixing in the mixing controlled stage (see figure 1.10). The major difficulty concerns the rate of reaction of fuel [51], which needs to be modelled, thereby introducing a number of empirical coefficients.

Different models have been proposed, some of which assume chemical reactions to be very fast with respect to the other phenomena, implying that the mean reaction rate is controlled by turbulent mixing. An example is the 'Eddy Break Up' model proposed by Spalding [52] which employs an integral turbulence time τ_t (readily determined from the turbulence length- and velocity scale) and an empirical constant C_{EBU}. Another example is the reaction rate expression proposed by Magnussen and Hjertager [53] which again assumes fast kinetics.

The supposition of fast kinetics is not unreasonable for hydrocarbon fuels at engine conditions. It is however likely to be inaccurate in the premixed burning stage and in regions where the temperature is low or where the mixtures are very rich or lean. Gosman and Harvey [5] found that the coefficients in Magnussen's expression are not true constants but require adjustment depending on the application. To provide for both turbulent and chemical controlled burning, they propose a combination of the Magnussen expression with an Arrhenius type formulation respectively. Depending on whether the ratio of reaction time scale to turbulent mixing time scale is less or greater than unity, either the latter or the former expression is used. Predicted heat release diagrams indicate good qualitative agreement with experimental data

exhibiting an initial sharp peak corresponding to the premixed burning phase followed by the gradual transition to the mixing controlled burning stage.

In a different approach to devise a general combustion model the 'Eddy Break Up' model mentioned earlier has been extended by Argueyrolles et al [54] to allow for situations where chemical reactions are not infinitely fast. They are again represented by an Arrhenius law based on instantaneous values. The model requires empirical input in the form of constants and a probability density function for the fuel mass fraction. This method has been implemented in two different computer codes and some results of predictions are presented in [54], however, no comparisons with experimental data are made.

Experimentally, combustion bombs as mentioned in section 1.1.2 have been designed to study the effects of pressure, temperature and swirl on the combustion process independently. Extensive tests using high - speed photography (4000 fps) were carried out at Bath University [43] under swirling and non swirling conditions. The film records provide details both of ignition delay as measured by the beginning of illumination and of the initial location of combustion nuclei. From a series of heat release tests, rate of burning diagrams were obtained for a range of pressures, temperatures and swirl rates. The influence of these independently controllable parameters on ignition delay and premixed peak burning rate is demonstrated. The data obtained from some 80 tests represent a comprehensive basis against which numerical predictions may be compared.

1.2 The Present Contribution: Objectives and Outline

Jet penetration and the mixing of fuel and air due to entrainment processes are the most influential hydrodynamic features in a DI Diesel engine, affecting both combustion efficiency and exhaust pollutant emissions. Modelling the flow, even excluding piston motion and combustion, presents an enormous task since the flow

involves complex structures of turbulent shear layers, boundary layers and recirculation regions in an unsteady three - dimensional domain. Advanced simulation codes to model the injection event have been employed by a number of workers, e.g. [23, 25, 26, 28, 32], with the emphasis on hydrodynamic and numerical aspects. Numerical studies have focused on approximation schemes for convective transport terms [28] and turbulence closure models [32]. Experimental data for validation purposes is difficult to obtain, the measurement of shear stress components to assess turbulence predictions requires elaborate experimental equipment.

The present thesis is concerned with the formulation and validation of a numerical model to simulate the three - dimensional motion resulting from steady state and impulsive injections under quiescent and swirling conditions. Attention is restricted to single phase water into water injections. The 'combustion chamber' model of the hydraulic analogue has a constant volume, combustion is not considered. The primary aim is to obtain flow field predictions for the four cases with a high spatial and, for impulsive injections, temporal resolution. Moreover, it is intended to explore the numerical capabilities of a commercially available computer code and to identify its limitations in the present application. An experimental study designed to measure both mean and fluctuating velocity components in all four flow configurations serves to validate predictions. Results obtained from the comprehensive experimental programme are valuable in their own right, for they provide insight into the physical processes occurring during the injection event.

The following main objectives are pursued in the thesis:

- examining the capabilities of a numerical solver which cannot be manipulated by the user ('black box') in a given flow configuration

- investigating means of influencing the solution procedure

- developing a model capable of accurately predicting the undeflected steady state and transient jet

- extending the model to accommodate swirling flow generated prior to injection

- exploring the influence of different swirl rates on the mixing rate and rate of spread

- demonstrating the use of dimensionless parameters to express the relative effect of swirl to penetration during injection

The material presented in the thesis is organized as follows:

To provide the background for the present study integral spray mixing models are reviewed in chapter two. Chapters three to five give a detailed account of the numerical model. In chapter three the equations for the conservation of mass, momentum and scalar quantities are presented together with auxiliary relations for boundary conditions. Chapter four is concerned with the turbulence closure problem. It contains a brief account of turbulence mechanisms followed by a description of modelling approaches and the associated problems. Modifications to the $k-\varepsilon$ turbulence model for axisymmetric jets are outlined. The numerical procedure employed to solve the governing equations presented earlier is described in chapter five. It details the discretization procedure and the solution algorithm used to solve the discretized equations. The experimental study is the subject of chapter six. It contains remarks on the hydraulic analogy and a description of the test facility, including the measurement and data analysis technique. Results are presented and discussed for four flow configurations: (i) undeflected steady state jet, (ii) undeflected impulsive jet, (iii) deflected steady state jet, and (iv) deflected impulsive jet. The computational study, comprising chapters seven and eight, is concerned with the same four flow configurations. In chapter seven, results for the steady and transient undeflected jet are presented. The discussion includes a sensitivity study concerning the effect of co-ordinate system orientation and different inflow and outflow

boundary conditions. Chapter eight details results for steady state and impulsive injections into swirling flow. The relative effect of injection and crossflow momenta on the mixture formation is discussed. Finally, the main conclusions of the study are given in chapter nine: the results of the present study are summarized and some suggestions are made for future work.

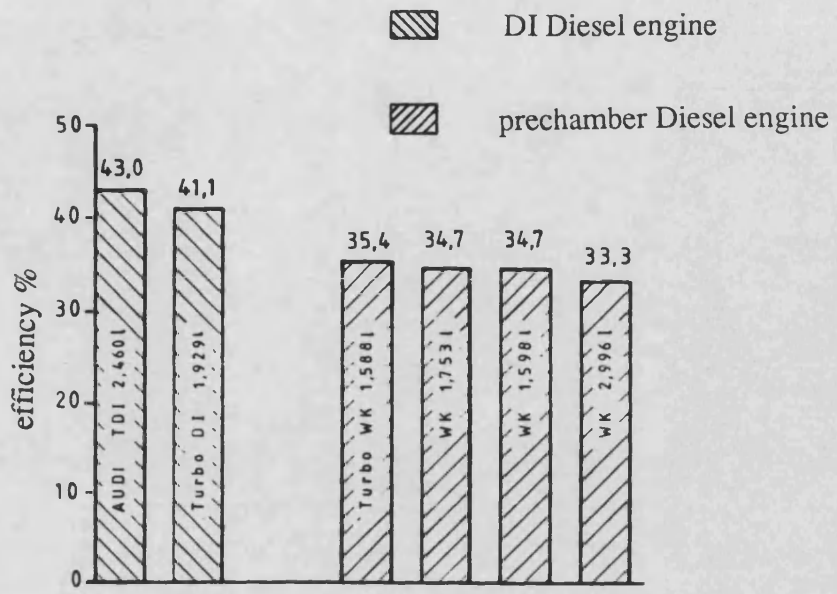

Fig. 1.1: Engine efficiency at optimum operating point [van Basshuysen et al]

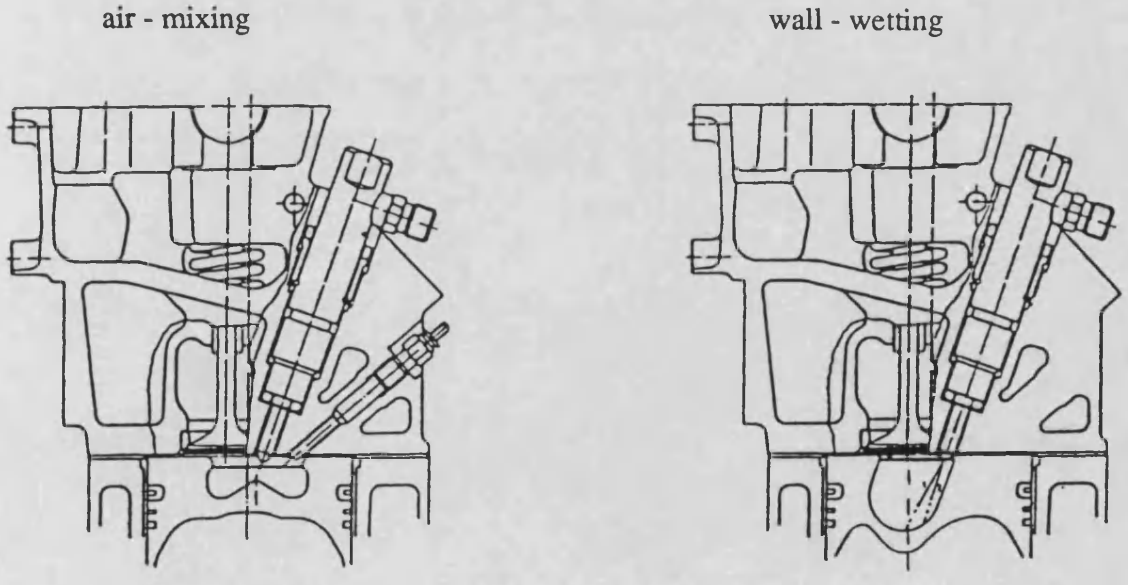

Fig. 1.2: Air - mixing and wall - wetting direct injection combustion system

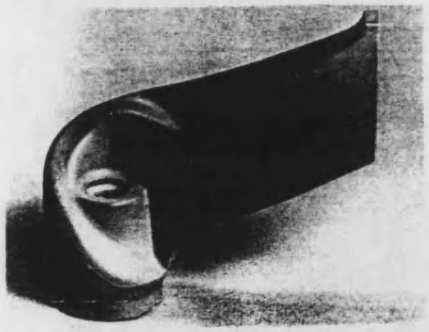

Fig. 1.3: Example of intake swirl port
[van Basshuysen et al]

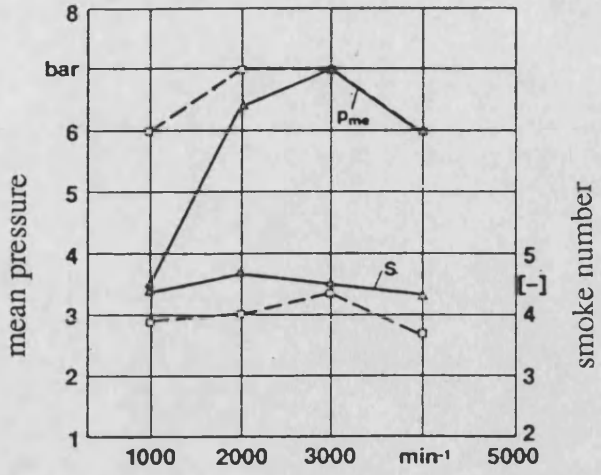

Fig. 1.4: Comparison between wall - wetting (△——△) and air - mixing (□– –□) direct injection combustion system at full load

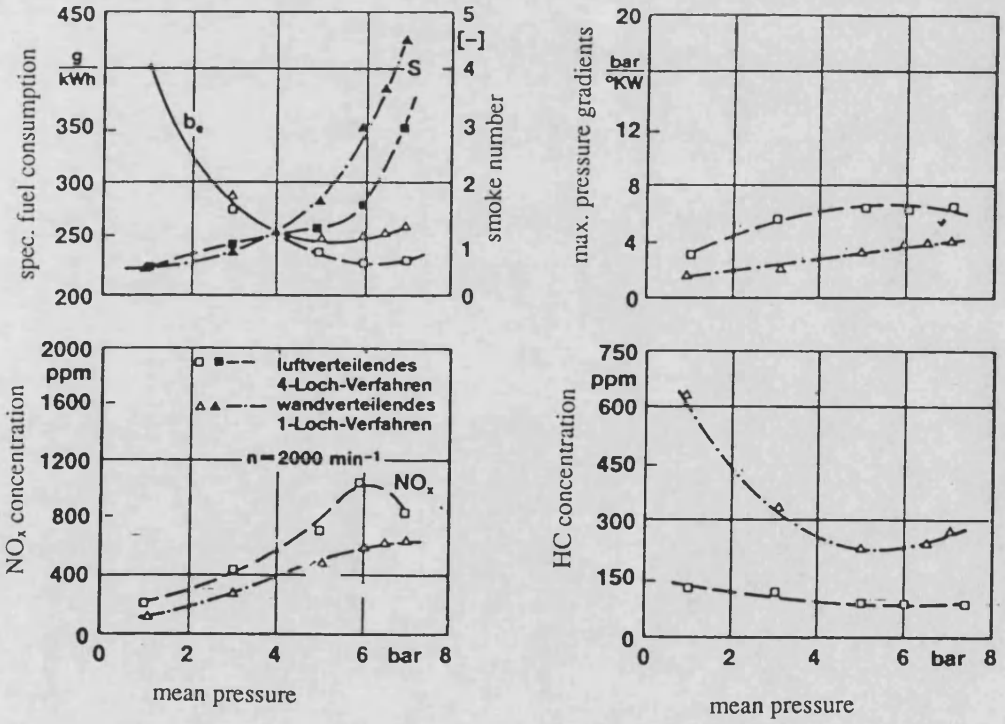

Fig. 1.5: Comparison between wall - wetting (△–·–△) and air - mixing (□– –□) direct injection combustion system at part load, n = 2000 min-1

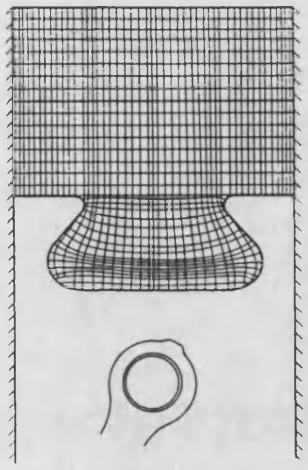

Fig. 1.6: Typical grid structure used by RPM multi - dimensional method

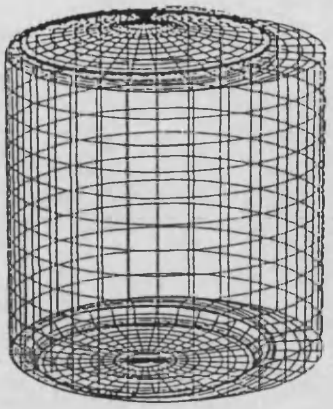

Fig. 1.7: Surface mesh

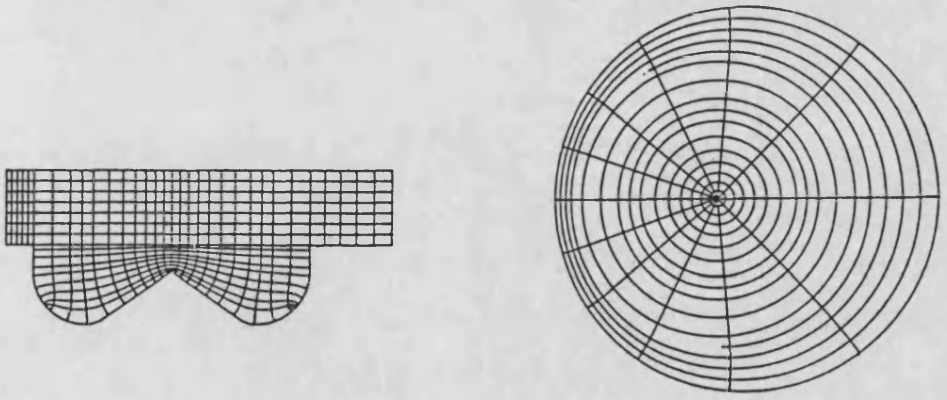

Fig. 1.8: Body fitted orthogonal grid for cylinder and piston bowl [Watkins et al]

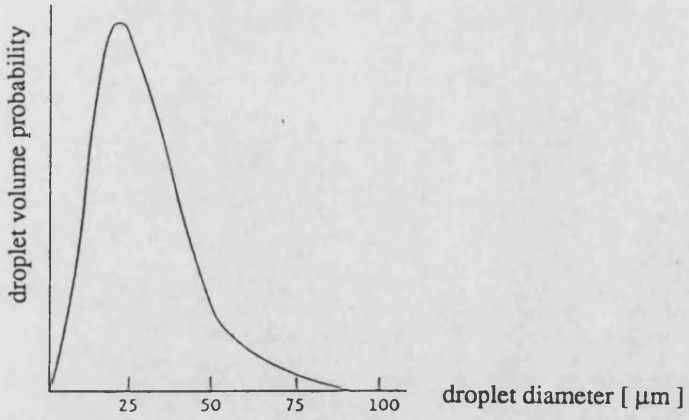

Fig. 1.9: Initial droplet size distribution

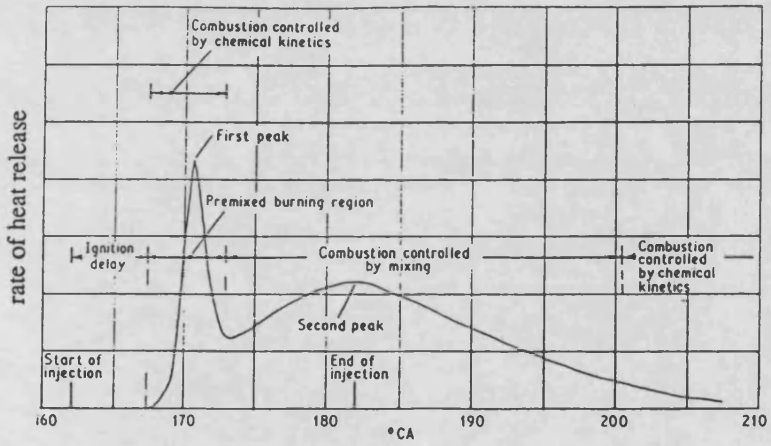

Fig. 1.10: Typical heat release diagram

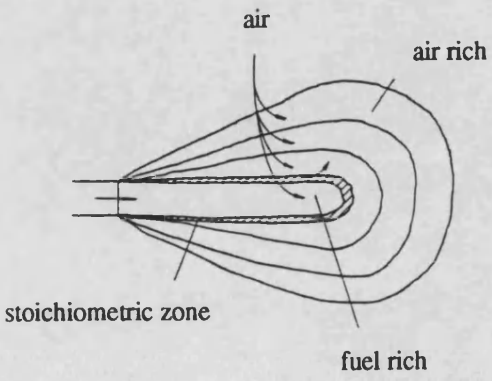

Fig. 1.11: Simple zone boundaries for axisymmetric jet

CHAPTER 2

2. REVIEW OF INTEGRAL SPRAY - MIXING MODELS

When considering mathematical modelling of mixing in DI Diesel engines two main approaches are available, either a full field (or multi - dimensional) technique or an integral method. Both techniques are well known and widely applied with the emphasis in recent years shifting towards multi - dimensional models. These models have a sound physical basis in solving the partial differential conservation equations governing the spatial and temporal variations of velocity, pressure, temperature, etc.. They include mathematical models of sub - processes like turbulent motion and employ computer based numerical procedures for solving the relevant equations for the flow under consideration. Owing to the rapid improvements of computers in recent years, both in terms of speed and memory, multi - dimensional spray mixing models are becoming technically and economically feasible (chapter 1). A less fundamental approach towards spray modelling is represented by the so called integral or phenomenological technique. This type of model has been developed over many years [33, 42, 44] and has been implemented and modified at Bath University by Packer et al [41], Idoum [21] and Wilson [34]. In its final form [34] the model allows the quantitative prediction of round axisymmetric and deflected jets and sprays. The present study should be viewed against this background. In order to provide the context for the multi - dimensional approach adopted in the thesis, this chapter gives an outline of the phenomenological technique applied to sprays. Starting with a basic model, the potential and the limitations of this approach are described. Extensions to the basic model are presented together with remarks on the accuracy and generality of the solution.

2.1 Basic Integral Model for an Isothermal, Isodense, Axisymmetric Spray

The simple case of a steady state isothermal, isodense, axisymmetric spray is the natural starting point for any mixing model (figure 2.1). Experimental data for validation purposes is readily available [55], allowing a careful matching of empirical input data to observed mixing patterns. In order to apply the classical jet theory based on continuum mechanics due to Abramovich [18], two assumptions are made:

- the transient spray is treated on a steady state basis
- the relative velocity of droplets in the spray to the entrained air is very small

The analysis transforms the governing partial differential equations into ordinary differential equations and eliminates shear stress terms which would require turbulence model closure. The local rate of entrainment is calculated using a width growth law deduced from similarity profiles or an entrainment model.

A turbulent flow is described by the three - dimensional, time - dependent conservation equations for momentum, mass and scalar quantities such as energy or concentration. For a practical solution these equations must be simplified by time - averaging to give the Reynolds equations with time - averaged rather than instantaneous properties. For axisymmetric jets the Reynolds equations are further simplified using the following assumptions:

- the flow is two - dimensional, i.e. there is no flow in circumferential direction
- the flow is steady with respect to time
- radial gradients dominate over gradients in axial direction
- turbulent shear stresses dominate over viscous stresses
- the flow is sourceless

Implementing these assumptions leads to the boundary layer form of the equation of motion. The equation contains correlations of fluctuating components for which a turbulence closure scheme is needed. A widely used method proposes to relate the time

averaged products of fluctuating components to mean property gradients [56]. However, for the axisymmetric jet, radial property gradients at the outer jet boundary are assumed to be negligible small; upon integration from the jet axis to the outer boundary the fluctuating component correlations therefore disappear. Integrating the remainder of the conservation equation from the centreline to the jet boundary and applying mathematical transformation rules, further reduces the complexity of the mathematical system. Mass continuity is expressed in integral form from a mass flux balance over a control volume (figure 2.2). The mass flux across face A_2 is increased from that across face A_1 by the amount of fluid entrained into the jet from the surroundings through the surface A_3. The entrainment rate must be determined from experiments. Including the entrainment rate into the model via an expansion rate equation or an entrainment model renders the system of equations mathematically closed.

2.2 Extensions to Basic Integral Model

Adler and Lyn [33] (1971) described a model for a spray evaporating in swirling air. Their approach adopts the classical turbulent jet theory [18] to two - phase sprays, solving integral equations for continuity, momentum and energy. In addition, the formulation includes an evaporation function based on a mean droplet diameter which is assumed to be representative of all droplets in the spray. The trajectory is calculated from equilibrium considerations of a spray segment. The formulation is based on important simplifying approximations:

- jet cross sections are rectangular and throughout the spray geometrically similar (constant depth/width ratio)
- two - dimensional similarity profiles are used to describe the distributions of velocity, temperature and concentration across the jet

- a single equivalent velocity represents the undisturbed flow field prior to injection
- an equivalent temperature describes the external flow field
- the gas forces acting on the spray are accounted for by a deflection coefficient. The magnitude of this coefficient must be determined to agree with experimental observations
- spray growth is accounted for by a growth coefficient for the mixing region

The implementation of the Adler and Lyn model identified a fundamental weakness [41], in that increasing swirl was seen to reduce the rates of air entrainment. This deficiency is attributed to the width growth expression which includes no facility to represent enhanced mixing, and hence entrainment, due to a crossflow [34].

An analysis of crossflow enhanced mixing in single - phase jets has been reported by Adler and Baron [44] (figure 2.3). The model was implemented at Bath University by Packer [57] with uniform crossflow replaced by swirl. It comprises two momentum equations in integral form in tangential direction and normal to the centreline. The expansion rate of the jet cross section area is calculated from the growth of an undeflected jet plus the growth of a vortex pair. In addition, the cross section distortion is determined by evenly seeding a finite number of vortex elements on the instantaneous boundary of the jet and calculating their displacement over a small period of time due to their induced velocity. The vortex strength and hence its induced velocity is expressed in terms of the crossflow velocity. To complete the formulation, property profiles are provided by the solution of a second order partial differential equation over the distorted jet cross section [44]. The unrealistic use of similarity profiles is thus avoided.

Packer et al [42] incorporated a gas property sub - model for a simple hydrocarbon fuel and an additional conservation equation for energy into the computer program. Solutions showed physically correct trends, in that the effect of temperature variations was correctly predicted. Higher jet temperatures (and hence lower densities) resulted in a faster mixing and dissipation of the jet.

A re - examination of the fundamental mathematical analysis underlying integral models by Wilson [34] lead to a spray mixing model capable of quantitative predictions of the trajectory and inner structure of the spray in a prescribed crossflow. The model divides the spray into three regions which are examined separately (figure 2.3):

1. The initial region with enhanced mixing due to lateral shear induced by the crossflow. The enhanced mixing results in a shorter potential core compared with the axisymmetric jet.
2. In the region of maximum deflection two entrainment mechanisms are considered: (i) fluid drawn into the low pressure region at the jet downstream surface and (ii) turbulent entrainment due to the discontinuity in velocities.
3. In the far region the jet approaches asymptotically the main stream, leaving a pair of counter - rotating vortices moving at approximately the speed of the crossflow. With increasing downstream distance from the point of injection the velocity difference at the jet boundary decreases. Consequently, the angular velocity of the vorticies diminishes, so that the entrainment rate and the jet spreading rate decreases.

The model includes the effects of temperature and composition variation. An empirical 'enhanced entrainment coefficient', which takes into account the effect of the crossflow velocity component normal to the local jet trajectory, is derived to give good agreement with experimental observations reported by Kamotani and Greber [46] and others.

Integral spray mixing models have proved valuable for predicting the spray structure under varying injection and crossflow conditions. They are sensitive to initial and external conditions and can form the basis for multi - zone combustion models (section 1.1.3). Attention is however limited to the influence of the air motion on the spray behaviour, no details of the reverse effect can be obtained from integral models. Gosman and Johns [7] describe the strong influence the spray exerts on both the mean and turbulent motions outside the spray envelope, depending on the relative momentum of the spray and the prevailing flow field prior to injection. Moreover, due to the

underlying assumption of integral models (quasi - steady state) the transient nature of the injection event cannot be properly accounted for. These limitations have motivated the application of a more fundamental modelling technique which allows a detailed spatial and temporal resolution of the flow, i.e. the finite difference method (section 1.1.2). Without the same reliance on empirical input for spray propagation and deflection, the finite difference technique employs numerical procedures to solve the time averaged governing partial differential equations. It is potentially the more universal method requiring less a priori knowledge of the flow under consideration, however, significant problems still exist, mainly in relation to turbulence closure and numerical approximations for convective transport terms.

In the present thesis a finite difference model is used to predict the flow field resulting from steady state and transient injections under quiescent and swirling conditions. In chapters three to five the governing partial differential equations are presented together with the numerical solution procedure and an account of turbulence closure schemes.

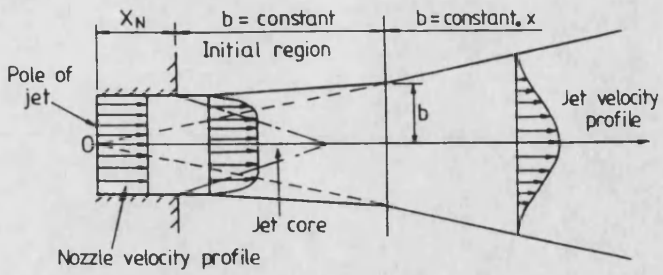

Fig. 2.1: Free jet

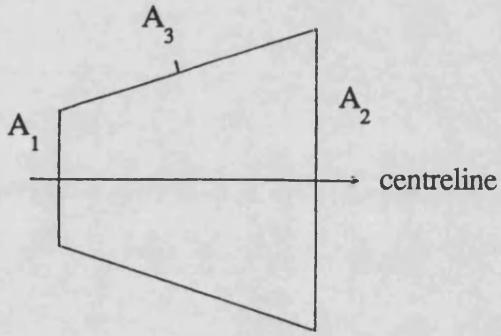

Fig. 2.2: Control volume for continuity

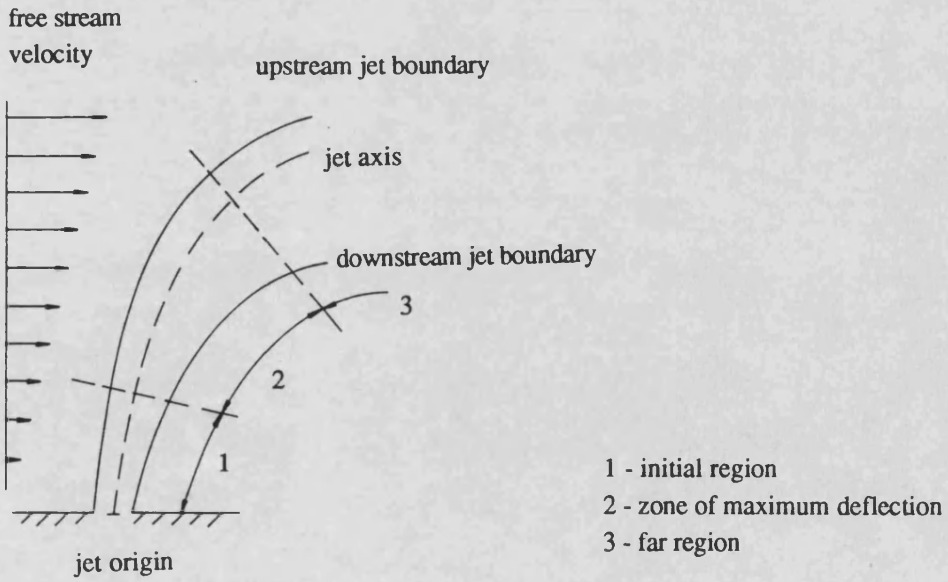

Fig. 2.3: Deflected jet in a crossflow

CHAPTER 3

3. THEORETICAL FORMULATION

This chapter provides the theoretical basis for the flow problem under investigation. A brief introduction is followed by the presentation of the governing equations in cylindrical polar coordinates for both the instantaneous and the time averaged flow properties. An outline of the treatment of boundary conditions and near wall regions concludes the chapter.

3.1 Introduction

Fluid flow problems can mathematically be described by a set of partial differential equations derived from control volume analysis known as the Navier - Stokes equations, (see e.g. Bird, Stewart, Lightfoot [58]). They represent the conservation of momentum and, together with the continuity equation and the conservation equation for scalar quantities, govern turbulent flows. Applying the appropriate boundary conditions over the flow domain and specifying initial conditions completes the problem description. Before the conservation equations can be presented, the coordinate system needs to be defined. Figure 3.1 depicts a portion of the hydraulic analogue rig used in the present investigation and shows the cylindrical polar coordinate system employed. The z - axis is aligned with the axis of symmetry of the cylindrical drum, r is the radial and θ the circumferential coordinates. The problem of solving the exact conservation equations is one of resolution of scale. A solution must represent all scales of the flow motion, from the large scales corresponding to the largest flow dimension to the smallest scales where the eddies are destroyed by viscous dissipation. The extremely fine numerical grid and small time intervals required to resolve all turbulence details are beyond current computing capacities. A statistical approach is therefore widely used, whereby the conservation equations are averaged over a time long compared with the

turbulent time scale. The instantaneous conservation equations are presented in the following section.

3.2 Instantaneous Conservation Equations

In the absence of external forces the conservation equations for mass, momentum and scalar quantities for an incompressible, time - dependent, three dimensional flow take the following form:

conservation of mass:

$$\frac{\partial}{\partial r} U_r' + \frac{U_r'}{r} + \frac{1}{r} \frac{\partial}{\partial \theta} U_\theta' + \frac{\partial}{\partial z} U_z' = 0 \qquad (3.1)$$

conservation of momentum:

r - direction:

$$\frac{D U_r'}{Dt} - \frac{U_\theta'^2}{r} = \frac{1}{\rho} \frac{\partial P'}{\partial r} + \nu \left(\nabla^2 U_r' - \frac{U_r'}{r^2} - \frac{2}{r^2} \frac{\partial U_\theta}{\partial \theta} \right) \qquad (3.2)$$

θ - direction:

$$\frac{D U_\theta'}{Dt} + \frac{U_r' U_\theta'}{r} = - \frac{1}{r\rho} \frac{\partial P'}{\partial \theta} + \nu \left(\nabla^2 U_\theta' - \frac{U_\theta'}{r^2} + \frac{2}{r^2} \frac{\partial U_r'}{\partial \theta} \right) \qquad (3.3)$$

z - direction:

$$\frac{D U_z'}{Dt} = - \frac{1}{\rho} \frac{\partial P'}{\partial z} + \nu \nabla^2 U_z' \qquad (3.4)$$

conservation of scalar quantities:

$$\frac{D \phi'}{Dt} = \Gamma_\phi \nabla^2 \phi' + S_\phi' \qquad (3.5)$$

r, θ and z are the radial, circumferential and axial coordinates respectively, while U_r', U_θ' and U_z' represent the corresponding instantaneous velocity components (the superscript (') denotes an instantaneous value). ρ is the density, ν the kinematic viscosity, Γ_ϕ the diffusion coefficient for property φ and S_ϕ' a source term for φ'. The operators D/Dt and ∇^2 read in full:

$$\frac{D}{Dt} = \frac{\partial}{\partial t} + U_r' \frac{\partial}{\partial r} + \frac{U_\theta'}{r} \frac{\partial}{\partial \theta} + U_z' \frac{\partial}{\partial z} \qquad (3.6)$$

and

$$\nabla^2 = \frac{\partial^2}{\partial r^2} + \frac{1}{r} \frac{\partial}{\partial r} + \frac{1}{r^2} \frac{\partial^2}{\partial \theta^2} + \frac{\partial^2}{\partial z^2} \qquad (3.7)$$

Expressions (3.1) to (3.5) form an exact set of equations which describe every detail of the turbulent motion. However, as indicated in the introduction, they cannot be solved for practical purposes with current computer resources. The route most commonly used to overcome this problem is to average the equations over a period of time (i.e. time averaging) or sampling at the same point while repeating the experiment (i.e. ensemble averaging). It is also necessary to introduce approximations into the model for the new unknown correlations that appear in the mean - flow equations.

3.3 Mean - Flow Equations

To obtain the mean - flow equations, the instantaneous values for the pressure P', the velocity U_i' and the scalar property φ' are decomposed into their mean and fluctuating components:

$$P' = P + p \qquad U_i' = U_i + u_i \qquad \phi' = \phi + \varphi$$

Substituting these expressions into the conservation equations for mass, momentum and scalar quantities (3.1 to 3.5) and averaging according to

$$\phi = \frac{1}{t_2 - t_1} \int_{t_1}^{t_2} \phi' \, dt$$

where $(t_2 - t_1)$ is long compared with the turbulent time scale leads to the following mean - flow equations for incompressible flow in cylindrical polar coordinates [59]:

continuity equation:

$$\frac{\partial}{\partial r} U_r + \frac{U_r}{r} + \frac{1}{r} \frac{\partial}{\partial \theta} U_\theta + \frac{\partial}{\partial z} U_z = 0 \qquad (3.8)$$

momentum equation:

r - direction:

$$\frac{D\, U_r}{Dt} - \frac{U_\theta^2}{r} = - \frac{1}{\rho} \frac{\partial P}{\partial r} + \nu \left(\nabla^2 U_r - \frac{U_r}{r^2} - \frac{2}{r^2} \frac{\partial U_\theta}{\partial \theta} \right) - \frac{1}{r} \frac{\partial}{\partial r} \left(r \overline{u_r^2} \right)$$

$$- \frac{1}{r} \frac{\partial}{\partial \theta} \left(\overline{u_r u_\theta} \right) - \frac{\partial}{\partial z} \left(\overline{u_r u_z} \right) + \frac{1}{r} \overline{u_\theta^2} \qquad (3.9)$$

θ - direction:

$$\frac{D\, U_\theta}{Dt} + \frac{U_r U_\theta}{r} = - \frac{1}{r\rho} \frac{\partial P}{\partial \theta} + \nu \left(\nabla^2 U_\theta - \frac{U_\theta}{r^2} + \frac{2}{r^2} \frac{\partial U_r}{\partial \theta} \right) - \frac{1}{r} \frac{\partial}{\partial \theta} \overline{u_\theta^2}$$

$$- \frac{\partial}{\partial r} \left(\overline{u_\theta u_r} \right) - \frac{\partial}{\partial z} \left(\overline{u_\theta u_z} \right) - 2 \frac{\overline{u_\theta u_r}}{r} \qquad (3.10)$$

z - direction:

$$\frac{D\, U_z}{Dt} = - \frac{1}{\rho} \frac{\partial P}{\partial z} + \nu \nabla^2 U_z - \frac{\partial}{\partial z} \overline{u_z^2} - \frac{1}{r} \frac{\partial}{\partial r} \left(r \overline{u_r u_z} \right)$$

$$- \frac{1}{r} \frac{\partial}{\partial \theta} \left(\overline{u_\theta u_z} \right) \qquad (3.11)$$

scalar conservation equation:

$$\frac{D\phi}{Dt} = \Gamma_\phi \nabla^2 \phi - \frac{\partial}{\partial z} \left(\overline{u_z \varphi} \right) - \frac{1}{r} \frac{\partial}{\partial r} \left(r \overline{u_r \varphi} \right) - \frac{1}{r} \frac{\partial}{\partial \theta} \left(\overline{u_\theta \varphi} \right) + S_\theta \qquad (3.12)$$

The operators D/Dt and ∇^2 were given in expressions (3.6) and (3.7). Capital symbols denote mean values while lower case letters represent the corresponding fluctuating quantities. An analogy with the instantaneous conservation equations is evident when the instantaneous values are replaced by mean quantities, however the averaging process has introduced new correlations between fluctuating velocity components $\overline{u_i u_j}$ and between velocity and scalar fluctuations $\overline{u_i \varphi}$ which need to be evaluated either from known or from computable quantities. Multiplied by the density ρ, the term $-\rho\overline{u_i u_j}$ acts as a stress on the fluid and is termed Reynolds stress. Similarly, the expression $-\rho\overline{u_i \varphi}$ is known as turbulent heat or concentration flux, depending on the scalar quantity solved for. In most flow regions the turbulent stresses and fluxes are much larger than their laminar counterparts. The latter are therefore often negligible. Equations (3.9) to (3.12) cannot be solved, because of the correlations of fluctuating components, without the aid of further equations for $\overline{u_i u_j}$ and $\overline{u_i \varphi}$. Exact transport equations for these correlations can be derived (see equation 4.23), however, they contain triple correlations, for which equations are needed. This problem continues at all higher levels where correlations of the next higher order appear in the exact equations and is referred to as the closure problem. Approximations making use of either mean flow quantities or lower order turbulence correlations are required to close the set of equations formed by (3.8) to (3.12). These approximations are termed turbulence models and will be discussed in chapter 4.

3.4 Boundary Conditions

In the previous sections a set of partial differential equations was introduced which can only be solved for a particular problem, when appropriate boundary conditions are specified. The relevant boundary types in the present study are solid walls, prescribed pressure boundaries, inlets, and symmetry planes. These will in turn be described in the following paragraphs.

Wall boundaries

Of all boundaries, solid walls require the most elaborate treatment. The turbulence model adopted in the present work applies to fully turbulent flows at high Reynolds numbers. Both the mean and the fluctuating velocities are zero at the wall. As a consequence, there are regions where the local Reynolds number of turbulence ($Re_t = k^2 / \nu \varepsilon$) [60] is small and viscous effects predominate. These regions, termed the viscous sublayer, are distinguished from other boundaries by steep gradients and require a different treatment from the general flow domain. Two modelling techniques describe viscous sublayers: (i) the low Reynolds number modelling method and (ii) the wall - function method.

(i) Extensions to high Reynolds number turbulence models have been proposed by a number of workers (e.g. Launder and Spalding [60]) to include approximations for laminar flow in the existing set of equations. These are however computationally expensive (both in terms of time and storage requirements) because of the many grid points needed in the proximity of the wall to resolve the steep gradients. It is mainly for this reason that wall - functions are more widely used to connect the wall conditions to the flow just outside the viscous sublayer.

(ii) Figure 3.2 illustrates part of a finite difference grid near a wall where the distance between points P and W is large enough to ensure that turbulence effects dominate over viscous effects, i.e. P lies just outside the viscous sublayer. The wall - function method incorporates a logarithmic expression to relate the velocity U_p to the wall conditions [61]:

$$\frac{U_P}{U_\tau} = \frac{1}{\kappa} \ln (Ey^+) \qquad (3.13)$$

U_τ is the friction velocity as defined below, κ is the von Kármán constant ($\kappa = 0.435$), E is a roughness parameter taken as 9.0 [60] and y^+ is the dimensionless distance from the wall.

$$U_\tau = \left(\frac{\tau_w}{\rho} \right)^{1/2} \tag{3.14}$$

and τ_w is the wall shear stress:

$$\tau_w = \frac{\rho C_\mu^{1/4} k_P^{1/2} U_P \kappa}{\ln (E y^+)} \tag{3.15}$$

where k_p is the kinetic energy at P.

The dimensionless wall distance can be written as

$$y^+ = \frac{y_P}{\nu} U_\tau = \frac{y_P}{\nu} C_\mu^{1/4} k_P^{1/2} \tag{3.16}$$

where ν is the laminar kinematic viscosity. It should be noted that the 'wall law' was developed for one dimensional flows and that its extrapolation to three dimensional recirculating flows is physically not well founded. In the absence of alternatives its use has however become accepted practice with the tangential velocity taken to be the resultant of the two velocity components parallel to the wall under consideration.

Rodi [61] suggests that the logarithmic law should be applied to a point where

$$30 < y^+ < 100$$

At $y^+ = 11.6$ the two curves for the viscous sublayer and the 'wall law' velocity distribution intersect as indicated in figure 3.3. If, during the calculation process, the value for y^+ should drop below 11.6, then the wall shear stress is approximated by:

$$\tau_w = - \nu \rho \frac{U_P}{y_P} \tag{3.17}$$

Expressions used as boundary conditions for the kinetic energy, k, and the dissipation rate, ε, which will be introduced in chapter 4.4, are based on the assumption of a local equilibrium in the y^+ region. In this case convection and diffusion are negligible and it follows [61]:

$$k_P = \frac{U_\tau^2}{C_\mu^{1/2}} \tag{3.18}$$

and

$$\varepsilon = \frac{U_\tau^3}{\kappa y_P} = \frac{C_\mu^{3/4} k_P^{3/2}}{\kappa y_P} \tag{3.19}$$

Expressions (3.18) and (3.19) are applied to a point within the y^+ range specified above.

Prescribed pressure boundaries

Prescribed pressure boundaries are located well outside the jet shear layer allowing ambient fluid to be entrained across the boundary. Velocities for flow leaving or entering the domain are calculated from a local mass balance applied to the cells of the last plane closest to the free boundary. The ambient medium is assumed to be free of turbulence.

Inlet boundaries

At the fluid entry all conditions have to be defined. Both a uniform inlet velocity and a parabolic velocity profile are considered. The pressure gradient is fixed in each cell. The turbulence quantities are estimated based on inlet size and velocity as length and velocity scales respectively. Guidance was obtained from reference [62], and a parametric study of the effect of different inlet boundary conditions was undertaken.

Planes of symmetry

In contrast to the other boundary types, planes of symmetry are not physical boundaries but take advantage of symmetrical flow patterns to reduce the computational effort. At symmetry planes, such as the axis of an undeflected jet, the gradients of all the properties are zero. This zero - flux condition is implemented by setting the appropriate coefficients in the source terms of the discretized equations equal to zero. The equations are presented in section 5.3.

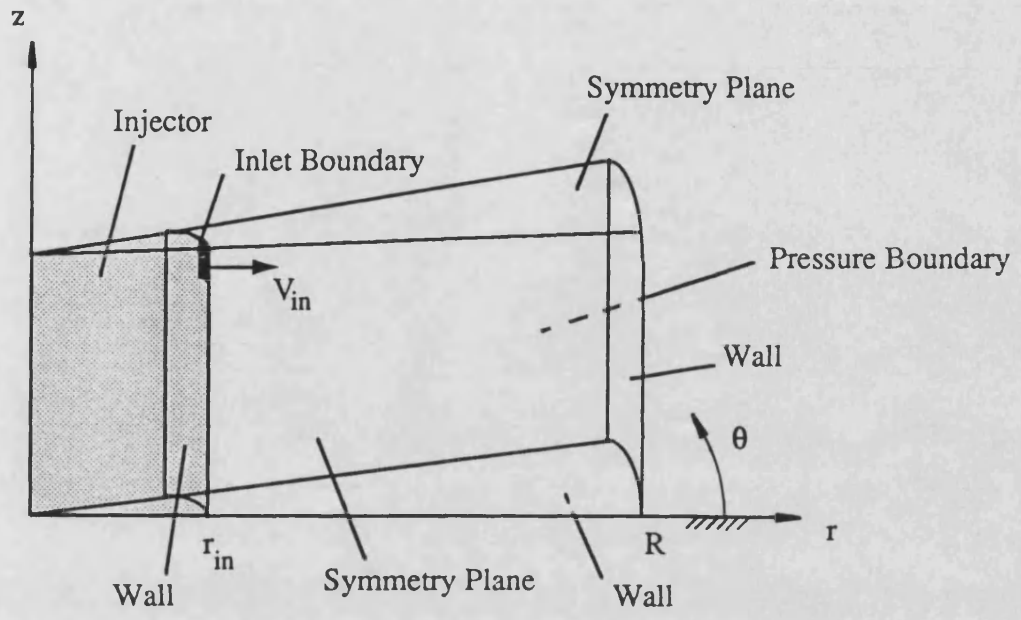

Fig. 3.1: Computational domain

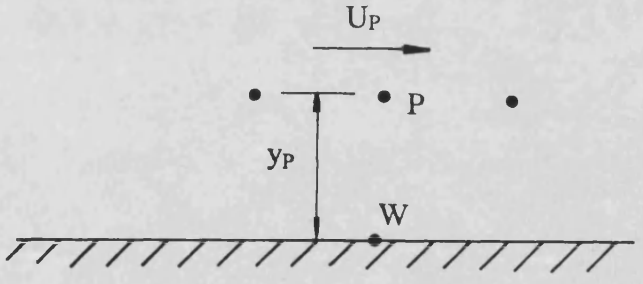

Fig. 3.2: Near wall region

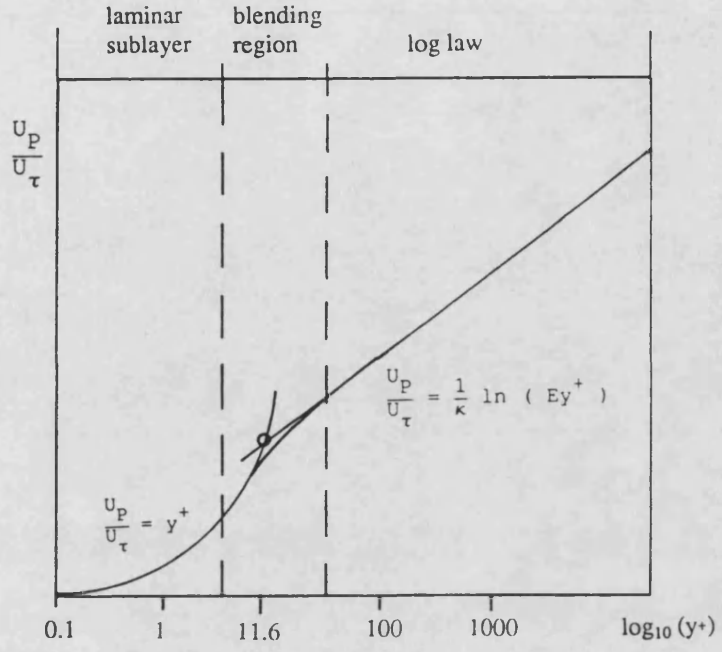

Fig. 3.3: Mean velocity distribution near wall in turbulent flow

CHAPTER 4

4. TURBULENCE MODELLING

The prediction problem of turbulent flows is of both mathematical and physical nature. The mathematical aspect, which consists of solving the discretized conservation equations, will be discussed in chapter 5. The physical problem lies in the construction of an accurate turbulence model. In this chapter a brief account of turbulence mechanisms is followed by a description of modelling approaches and the associated problems.

4.1 Introduction to Turbulence Mechanisms

At high Reynolds numbers turbulence is an eddying motion comprising a wide range of eddy sizes. Eddies are considered to be an assembly of interacting vortex lines or sheets, interacting with other eddies (Bradshaw [63]). Low frequency fluctuations associated with large eddies are mainly determined by boundary conditions, whereas high frequency fluctuations, corresponding to small eddies, depend primarily on viscous forces. Since large eddies and the mean flow are of a similar scale, it is here that interaction occurs and kinetic energy is passed from the mean flow into the turbulent motion. The large eddies are then broken up by vortex stretching, thereby transferring energy to the small scales of motion. Through repeated vortex interactions energy is passed on to smaller and smaller scales until eventually kinetic energy is destroyed by viscous dissipation. This process is termed energy cascade. It is assumed that the smallest scale motion destroys energy as quickly as it is received, the large scale fluctuations determine therefore the rate at which mean flow energy is transferred into the turbulent motion.

In engineering applications the mean flow may often have a preferred direction and hence be strongly anisotropic. The three dimensional, undeflected, turbulent jet under investigation is an example for this type of flow. Through interactions between meanflow and large scale turbulent motion the anisotropic behaviour is imposed on large scale eddy interactions. During the cascade process described above the direction sensitivity is progressively diminished until in the smallest eddies, where viscous dissipation occurs, the turbulence energy may have no preferred direction. This concept where the small scale motion is isotropic while the large scale motion is not, is called local isotropy.

Turbulent motions are strongly damped in the proximity of walls where viscous effects predominate. This complicates near wall modelling since molecular effects can be of the same order as turbulence influences. The use of a very fine grid in the near wall region to represent the viscous sublayer is computationally expensive and therefore in most cases impractical. Separate wall solutions are usually employed to link the wall with the flow region of interest. A detailed treatment of turbulence mechanisms can for example be found in references [63] and [64].

4.2 Model Classification

The basic conservation laws for mass, momentum and scalar quantities were presented in chapter 3. They contain energy fluctuations corresponding to a wide frequency range which implies the need for a very fine finite - difference grid in the three orthogonal directions and in time. Even for relatively low Reynolds numbers with a moderate frequency spectrum the storage requirements are beyond present - day computing resources. In addition, the number of arithmetic operations required for such a fine mesh would increase computing time prohibitively [63]. Once this restriction is

recognized it becomes necessary to identify means by which the numerical task can be simplified: turbulence models are introduced.

Turbulence models may be divided into two categories: (i) the pragmatic Large - Eddy Simulation (LES) approach and (ii) statistical models. These two alternatives will in turn be considered in the following sections. Since a model of the second class is used in the present study it is discussed in some detail. This includes an overview of different alternatives within this category to provide the context for the two equation k - ε turbulence model chosen for this investigation.

4.3 Large - Eddy Simulation

As discussed in section 4.1, kinetic energy is transferred to the turbulent motion through the interaction of large scale eddies with the mean flow. The philosophy of large - eddy simulation is outlined by W.C. Reynolds in reference [65]. The method employs numerical grids which properly resolve the problem dependent large scale motion and use sub - grid scale models to represent small scale turbulence that cannot be resolved by the chosen grid. The models employed for approximating small scale motion are of the statistical type which will be discussed in the following section. They are particularly suited for modelling microscale turbulence since the implicit condition of isotropy is believed to be met (local isotropy). Furthermore, the accuracy of sub - grid scale models does not appear to be of great consequence for the prediction of general flow characteristics because the main contributor to turbulent motion, large scale eddies, is properly resolved by the relatively fine grid. Computationally, large - eddy simulation is expensive due to the three dimensional nature of the large scale motion and the need for fine meshes to represent the spectrum of large eddies, the latter very much depending on the problem under consideration. Difficulties arise in representing the interaction between modelled and accurately calculated solution component. Gosman

[66] also points to the problem of defining realistic inflow boundary conditions for both the mean and the stochastically varying turbulent components.

4.4 Statistical Models

Statistical turbulence models are well documented in the literature, e.g. Tennekes and Lumley [64], Rodi [29, 61], Spalding [67], Gibson et al [68]. This section does therefore not attempt to reproduce the development of this model class but rather to summarize its most important features and its variants. Accordingly, these are arranged under the following headings:

- eddy - viscosity / - diffusivity concept
- overview of statistical models
- two equation models applied to undeflected and deflected jets

4.4.1 Eddy - Viscosity/ -Diffusivity Concept

The closure problem described when introducing the mean - flow equations (see chapter 3.3) makes it necessary to identify ways of approximating the correlations of fluctuating quantities. The eddy - viscosity concept relates them to the mean velocity gradients. It is based on an analogy between Reynolds stresses and viscous stresses. The expressions proposed by Boussinesq to determine the turbulent stresses and fluxes can be written in tensor notation:

$$- \overline{u_i u_j} = \nu_t \left(\frac{\partial U_i}{\partial x_j} + \frac{\partial U_j}{\partial x_i} \right) - \frac{2}{3} k \, \delta_{ij} \qquad (4.1)$$

$$- \overline{u_i \varphi} = \frac{\nu_t}{\sigma_t} \frac{\partial \phi}{\partial x_i} \qquad (4.2)$$

where ν_t is the turbulent (or eddy) viscosity, σ_t is the turbulent Schmidt number (for mass flux), k is the kinetic energy, and δ_{ij} is the Kronecker delta ($\delta_{ij} = 1$ for $i = j$ and $\delta_{ij} = 0$ for $i \neq j$). For a three dimensional, incompressible flow the individual Reynolds stresses take the following form in cylindrical polar co-ordinates:

Shear stresses

$$-\overline{u_r u_z} = \nu_{rz} \left(\frac{\partial U_z}{\partial r} + \frac{\partial U_r}{\partial z} \right) \tag{4.3}$$

$$-\overline{u_r u_\theta} = \nu_{r\theta} \left(\frac{\partial U_\theta}{\partial r} + \frac{1}{r} \frac{\partial U_r}{\partial \theta} - \frac{U_\theta}{r} \right) \tag{4.4}$$

$$-\overline{u_z u_\theta} = \nu_{z\theta} \left(\frac{\partial U_\theta}{\partial z} + \frac{1}{r} \frac{\partial U_z}{\partial \theta} \right) \tag{4.5}$$

Normal stresses

$$-\overline{u_r^2} = 2\nu_{rr} \frac{\partial U_r}{\partial r} - \frac{2}{3} k \tag{4.6}$$

$$-\overline{u_z^2} = 2\nu_{zz} \frac{\partial U_z}{\partial z} - \frac{2}{3} k \tag{4.7}$$

$$-\overline{u_\theta^2} = 2\nu_{\theta\theta} \frac{1}{r} \left(\frac{\partial U_\theta}{\partial \theta} + U_r \right) - \frac{2}{3} k \tag{4.8}$$

and

$$\overline{u_r u_z} = \overline{u_z u_r} \,, \quad \overline{u_r u_\theta} = \overline{u_\theta u_r} \,, \quad \overline{u_z u_\theta} = \overline{u_\theta u_z}$$

The indices indicate the stress component with which the turbulent viscosities are associated. For isotropic conditions all double subscript viscosities are equal to one turbulent viscosity ν_t. Assuming isotropy and substituting the stress equations (4.3) to (4.8) into the time averaged momentum equations (3.9) to (3.11) yields the final set of equations that forms the basis for the modelling techniques discussed in chapter 5. The complete set in cylindrical polar co-ordinates is given in Appendix A.

In contrast to the laminar viscosity ν, the turbulent viscosity is not a fluid property but changes with the state of turbulence. ν_t is defined as a scalar and hence isotropic quantity. This constitutes an important limitation of the eddy - viscosity concept as in

more complex flows the individual Reynolds stresses are likely to vary in different directions. Where reliable experimental data is available the model can be adjusted accordingly, at the expense of generality.

Relating the turbulent stresses and fluxes to the mean gradients via the eddy - viscosity concept shifts the closure problem from directly computing the fluctuation correlations to identifying means of prescribing the turbulent viscosity ν_t. From dimensional analysis it follows that the eddy - viscosity is proportional to a turbulence velocity scale and a turbulence length scale. Modelling differences exist in the various approaches towards determining these scales, they will be outlined in order of increasing complexity in the following paragraphs.

4.4.2 Overview of Statistical Models

Zero Equation Models

At the simplest level closure is achieved by directly relating the turbulent viscosity to a mean velocity gradient. One such model is Prandtl's [69] mixing length model involving an empirically prescribed length scale l_m:

$$\nu_t = l_m^2 \left| \frac{\partial U_1}{\partial x_2} \right| \qquad (4.9)$$

For round jets issuing into quiescent surroundings the value for l_m divided by the local jet width δ is:

$$\frac{l_m}{\delta} = 0.075$$

In a simpler model for free shear layers Prandtl [56] assumed the eddy - viscosity to be proportional to the local jet width and the maximum velocity difference across the jet:

$$\nu_t = C\,\delta \left| U_{max} - U_{min} \right| \qquad (4.10)$$

where the empirical constant C for round jets takes the value C = 0.011. Models of the above type have been fairly successfully applied to predictions of mixing layers, jets and wakes provided suitable empirical constants were used. The major disadvantage lies in the model's lack of generality which is illustrated by the fact that even for apparently similar flows like round and plane jets the constant C was found to differ by 30 % [61]. For more complex flows which may exhibit recirculation a prescription of the length scale distribution becomes very difficult. The assumption implied in the model that at each point turbulence is dissipated at the same rate as it is generated and that convection and diffusion are negligible (i.e. that turbulence is in local equilibrium) means that transport effects cannot be accounted for. As a result, turbulence production at one point does not influence turbulence at other points in the flow domain. Similarly, the time dependent nature of turbulence in unsteady flows is not reflected in zero equation models.

One Equation Models

To account for the transport of turbulence quantities and history effects, one equation models employ a transport equation for the velocity scale, usually taken as $k^{1/2}$ where k is the turbulent kinetic energy:

$$k = \frac{1}{2} \overline{u_i u_i} \qquad (4.11)$$

The turbulent kinetic energy expression contains only normal stresses, whereas the turbulent stress tensor (eqn. 4.1) represents all stress components of the three by three matrix. When this scale is used in the eddy - viscosity formulation, the so called Kolmogorov - Prandtl expression results:

$$\nu_t = C'_\mu \sqrt{k}\ L \qquad (4.12)$$

where C'_μ is an empirical constant and L the turbulence length scale. An exact k - equation can be derived [61] which is of little practical use as it contains new unknown correlations. Modelling of the diffusion and dissipation terms yields the following form:

$$\underbrace{\frac{\partial k}{\partial t}}_{\text{rate of change}} + \underbrace{\frac{\partial}{\partial r}(U_r k) + \frac{1}{r}\frac{\partial}{\partial \theta}(U_\theta k) + \frac{\partial}{\partial z}(U_z k)}_{\text{convection}} =$$

$$\underbrace{\frac{\partial}{\partial r}\left(\frac{\nu_e}{\sigma_k}\frac{\partial k}{\partial r}\right) + \frac{1}{r^2}\frac{\partial}{\partial \theta}\left(\frac{\nu_e}{\sigma_k}\frac{\partial k}{\partial \theta}\right) + \frac{\partial}{\partial z}\left(\frac{\nu_e}{\sigma_k}\frac{\partial k}{\partial z}\right)}_{\text{diffusion}} +$$

$$\underbrace{\nu_t P_k}_{\text{production}} - \underbrace{\varepsilon}_{\text{dissipation}} \qquad (4.13)$$

where

$$P_k = 2\left(\frac{\partial U_z}{\partial z}\right)^2 + 2\left(\frac{\partial U_r}{\partial r}\right)^2 + 2\left(\frac{1}{r}\frac{\partial U_\theta}{\partial \theta} + \frac{U_r}{r}\right)^2 + \left(\frac{\partial U_z}{\partial r} + \frac{\partial U_r}{\partial z}\right)^2$$

$$+ \left(\frac{\partial U_\theta}{\partial z} + \frac{1}{r}\frac{\partial U_z}{\partial \theta}\right)^2 + \left(\frac{1}{r}\frac{\partial U_r}{\partial \theta} + \frac{\partial U_\theta}{\partial r} - \frac{U_\theta}{r}\right)^2$$

with $\nu_e = \nu + \nu_t$

The diffusion flux is assumed to be proportional to the gradient of k, where σ_k is an empirical constant. Dimensional analysis suggests for the dissipation rate ε:

$$\varepsilon \propto \frac{k^{3/2}}{L} \qquad (4.14)$$

It is still necessary to define the length scale L which poses a problem similar to the prescription of the Prandtl mixing length l_m in zero - equation models. This weakness of one - equation models has led to the development of two - equation models which also determine the length scale from a transport equation.

Two Equation Models

Two equation models account for the transport of both the turbulence velocity scale and the length scale. The velocity scale $k^{1/2}$ is determined in the manner described above. In

a similar way a transport equation may be formulated for a new dependent variable related to the length scale L. This new quantity must not necessarily be L itself, but may be a combination of L and k in the form

$$Z = k^{\alpha} L^{\beta} \tag{4.15}$$

where k is known from the solution of its transport equation and α and β are constants. Many expressions for Z have been considered and are reviewed in references [61] and [64]. They include an equation for the frequency of energy containing motion $k^{1/2} / L$ and an equation for the turbulence vorticity k / L^2, however, the most widely used choice is

$$Z = \varepsilon \propto \frac{k^{3/2}}{L} \tag{4.16}$$

where ε is the dissipation rate of turbulence. The reason for choosing ε is the assumption that the rate of energy dissipation is controlled by the large scale fluctuations (see section 4.1) feeding energy to the smaller scales where it is dissipated. With L being the large - eddy turbulence length scale, the dissipation should then scale on k and L as in equation (4.16). An exact transport equation can formally be obtained from the Navier - Stokes equations [64] which like the exact k - equation contains complex correlations and is therefore of little practical relevance. Modelling of the ε - equation is based on dimensional considerations and on an analogy with the k - equation. Thus, a modelled form must contain approximations for a source, a sink and a diffusion term. A source term is required to ensure that an increase in kinetic energy leads to a greater dissipation rate. From dimensional analysis it follows that the production rate of ε is proportional to the turbulent motion time scale:

$$P_{\varepsilon} \propto P_k \frac{\varepsilon}{k} \tag{4.17}$$

with P_k from equation (4.13). A sink term is needed to allow for decaying kinetic energy, which for dimensional reasons is proportional to ε^2 / k

$$S_{\varepsilon} \propto \frac{\varepsilon^2}{k} \tag{4.18}$$

Diffusion is usually modelled with the gradient assumption:

$$D_\varepsilon \propto \frac{\nu_t}{\sigma_\varepsilon} \frac{\partial \varepsilon}{\partial x_i} \tag{4.19}$$

where σ_ε is an empirical diffusion coefficient. Introducing these three terms into a transport equation for ε, in which the rate of change is balanced by convective and diffusive transport and by production and destruction processes, yields:

$$\underbrace{\frac{\partial \varepsilon}{\partial t}}_{\text{rate of change}} + \underbrace{\frac{\partial}{\partial r}\left(U_r \varepsilon\right) + \frac{1}{r}\frac{\partial}{\partial \theta}\left(U_\theta \varepsilon\right) + \frac{\partial}{\partial z}\left(U_z \varepsilon\right)}_{\text{convection}} =$$

$$\underbrace{\frac{\partial}{\partial r}\left(\frac{\nu_e}{\sigma_\varepsilon}\frac{\partial \varepsilon}{\partial r}\right) + \frac{1}{r^2}\frac{\partial}{\partial \theta}\left(\frac{\nu_e}{\sigma_\varepsilon}\frac{\partial \varepsilon}{\partial \theta}\right) + \frac{\partial}{\partial z}\left(\frac{\nu_e}{\sigma_\varepsilon}\frac{\partial \varepsilon}{\partial z}\right) +}_{\text{diffusion}}$$

$$\underbrace{C_1 P_k \frac{\varepsilon}{k}}_{\text{source}} - \underbrace{C_2 \frac{\varepsilon^2}{k}}_{\text{sink}} \tag{4.20}$$

with P_k from equation (4.13). An expression for the eddy - viscosity ν_t is recovered by combining equation (4.16) with the Kolmogorov - Prandtl relation (4.12), hence

$$\nu_t = C_\mu \frac{k^2}{\varepsilon} \tag{4.21}$$

where C_μ, C_1, and C_2 are constants of proportionality which are determined by comparing experimental data with computer predictions for particular flows. C_2 is approximated with respect to turbulence downstream of a rectangular grid where the diffusion and production terms in the transport equations for k and ε become negligible, leaving C_2 as the only remaining constant in equations (4.13) and (4.20) which then reduce to:

$$U_i \frac{\partial k}{\partial x_i} = -\varepsilon \quad , \quad U_i \frac{\partial \varepsilon}{\partial x_i} = -C_2 \frac{\varepsilon^2}{k}$$

The variation of k behind a grid is determined as [61]:

$$k \propto x^{-n} \qquad \text{with } n = \frac{1}{C_2 - 1}$$

Experimentally found values for the exponent n vary from 1.08 [61] to 1.25 [68], giving the following range for C_2:

$$1.92 > C_2 > 1.80$$

$C_2 = 1.92$ is used in the present study, a value which has been successfully employed for free shear flows by many workers [24, 27, 30] .

C_μ is evaluated from the consideration of local equilibrium shear layers, where the rates of turbulence production and dissipation are in balance. Measurements yield [61] $C_\mu = 0.09$.

An equation for C_1 can be derived by applying near wall conditions (i.e. local equilibrium, logarithmic velocity profiles, negligible convection of ε) to the ε - equation which reduces to:

$$C_1 = C_2 - \frac{\kappa}{\sigma_\varepsilon \sqrt{C_\mu}}$$

where κ is the von Kármán constant (0.435). Thus C_1 can be determined once values for C_2 and C_μ have been chosen. The diffusion coefficients σ_ε and σ_k are assumed to be close to unity, specific values are obtained by optimization on a computer in the light of validated experimental data. An optimized set of coefficients as suggested by Launder and Spalding [60] and successfully applied to a range of flows by numerous workers is given in table 1.

C_μ	C_1	C_2	σ_ε	σ_k
0.09	1.44	1.92	1.0	1.3

Table 1: Constants in k - ε turbulence model

The model is particularly sensitive to variations in C_1 or C_2 alone, a problem that may be overcome by altering both and maintaining a constant difference between the two. As described above the k - ε model constants are determined with reference to particular flow situations, implying that they are not necessarily applicable to more complex flows. In practice it was found that they are well suited for a wide range of three dimensional turbulent flows, including some recirculating and wall flows. However, complete generality cannot be assumed, e.g. in situations where anisotropy of the flow has a significant influence, as in the case of the jet in stagnant surroundings under investigation, modifications to some of the constants may be required. These are outlined in the following section.

Modifications to k - ε Model

In most cases it is the present form of the ε - equation that is to blame for the model's lack of generality [61]. Using the coefficients given in table 1, the rate of spread of an axisymmetric jet issuing into a quiescent medium is reported to be overpredicted by about 25% to 30%. Rodi [61] suggests the introduction of a parameter, f, based on the centre line velocity decay into the functions for C_2 and C_μ:

$$f = \left| \frac{\delta}{\Delta U_m} \left(\frac{\partial U_{cl}}{\partial x} - \left| \frac{\partial U_{cl}}{\partial x} \right| \right) \right|^{0.2} \qquad (4.22)$$

thus

$$C_2 = 1.92 - 0.0667\, f \quad ; \quad C_\mu = 0.09 - 0.04\, f$$

where the velocity gradients are made dimensionless with the jet width δ and the maximum velocity difference ΔU_m across the jet.

Two other proposals to modify C_1 due to Morse [70] and McGuirk [71] take the following form:

Morse:

$$C_1 = 1.4 - 3.4 \left(\frac{k}{\varepsilon} \frac{\partial U}{\partial x} \right)^3_{cl} \qquad (4.23)$$

McGuirk:

$$C_1 = 1.14 - 5.31 \frac{\delta_{1/2}}{U_{cl}} \frac{\partial U_{cl}}{\partial x} \qquad (4.24)$$

where $\delta_{1/2}$ is the jet half width defined as the distance from the centreline, where the velocity is half the centreline velocity. The modifications produce very similar results in the fully developed part of the jet with slight variations in the initial region.

Another situation where the assumption of local equilibrium used in evaluating C_μ is not met are weak shear flows and far - field jets. The rate of turbulence production, P, can be significantly smaller than the rate of dissipation, ε, leading to unrealistic predictions. Launder et al [72] show that a functional relationship $C_\mu = f(P/\varepsilon)$, where P/ε is the average value of P/ε across the shear layer, significantly improves the k - ε model's performance.

4.4.3 Two - Equation Models Applied to Undeflected and Deflected Jets

Turbulence models for all closure levels described above have been applied to axisymmetric jets in stagnant surroundings and in crossflows. Many of the studies are reviewed by Schetz [73] and Kuo and Bracco [26] who compare solutions of different studies employing mixing length models, one - and two equation models, and algebraic stress models. The numerical solutions from these reviews provide useful data against which results obtained in the present investigation are compared in chapter seven. At this point, attention is restricted to relevant investigations which have used a two equation model applied to the types of flow under consideration.

The constants in the k - ε model given in table 1 require modifications in certain flow configurations, for example, predictions of undeflected axisymmetric jets with the standard settings inadequately reproduce the rate of spread and centreline velocity decay. This deficiency is generally attributed to the source term in the ε - equation which has therefore been the focus of most efforts to improve the models performance. Launder [72] introduced a parameter based on the centreline velocity which he applied to the coefficients C_μ and C_2. In different approaches Morse [70] and McGuirk [71] proposed variable C_1 models with the centreline velocity and the jet half width as parameters. According to Pope [31], the two latter models gave the best near field velocity predictions. Whereas these model corrections are only applicable to axisymmetric round jets, Pope [31] sought a more general expression which would perform equally well for round and for plane jets. He regards the dissipation rate, ε, as the rate of energy transfer from the large scale fluctuations to the smaller scales (cascade process) and proposes to capture the influence of vortex interactions on this scale reduction process through an additional expression in the source term of the ε - equation. Solutions obtained with this correction indicate very good agreement with experimental data for mean velocity profiles of axisymmetric jets [31], however, dissipation profiles in the self - similar region still show poor accord near the jet centreline for both the corrected and the standard ε - equation [74].

Kuo and Bracco [26] undertook a parametric study of the effect of the turbulence constant C_1 on the centreline velocity decay, the centreline kinetic energy distribution, and on the unsteady penetration - time history. They found the model to be highly sensitive towards C_1 variations; an increase of C_1 from 1.45 to 1.60 caused a 45 % decrease in the jet spreading rate.

Another application of the two equation model of interest was conducted by Malin [75] who replaced the ε - equation with an equation for the transport of the time mean square vorticity fluctuation, W. An equation for the concentration fluctuations to predict the concentration field is also included. The computed results are shown to be in

generally good agreement with experimental data, however, the W - equation does not appear to be sufficiently general to predict both round and plane jets without modifications similar to the ones suggested by Pope [31]. An additional term representing the production of mean - square turbulent vorticity due to vortex interactions is believed to improve the models universality.

It is worth noting that the much more complex Reynolds stress models do not seem to perform better than the standard k - ε model, thus apparently not justifying the significantly larger computational effort.

Jets deflected in a crossflow present a more difficult modelling task. To the author's knowledge no work on jets injected radially from the centre into swirling flow using two equation turbulence models is reported in the literature. Other workers have concentrated on jets in crossflows in cartesian co-ordinates for a range of velocity ratios. These studies are used for comparing near field predictions. Due to the jet curvature the numerical mesh contains regions with very little disturbance, hence a nonuniform grid must be employed to properly resolve the jet shear layers while economizing computer time and storage where a relatively coarse grid is adequate. It is also important to ensure that the boundaries of the flow domain are sufficiently remote so as not to influence predictions, particularly where steep pressure gradients occur.

A detailed three dimensional computation of a round turbulent jet discharging into a confined cross - flow is described by Jones and McGuirk [27]. Using the standard k - ε model they obtained jet trajectories and axial velocity and temperature contours in planes parallel and perpendicular to the cross - flow. The mesh comprised 20 x 15 x 15 nodes which was deemed insufficient to resolve all the shear regions; comparisons with flow visualization experiments indicate good agreement for the jet trajectories, however, the rate of spread appears to be overpredicted.

Also of interest in this context is an investigation by Patankar et al [24] into the three dimensional velocity field of a deflected turbulent jet, again using the standard k - ε

model. Results for the jet centreline trajectories obtained with a 10 x 15 x 15 grid are in good accord with experimental data. Predicted velocity profiles at several stations downstream of the injection point are found to deviate significantly from measured profiles; the error is partly attributed to the fairly coarse grid.

Another investigation reported by McGuirk and Rodi [76] describes two dimensional predictions of a side discharge into an open channel flow. A depth - averaged form of the k - ε model with standard coefficients was found to predict the recirculation zone downstream of the discharge well. Near field predictions were in much better agreement with experimental data than those obtained with constant eddy - viscosity models.

It is well known that 'numerical' diffusion occurs when the flow is skewed relative to the grid. The more formally correct Reynolds stress models (see section 4.5) have therefore been applied to a range of flows with varying streamline curvature [77]. However, these are computationally expensive for three dimensional calculations and it appears that computer resources are better spent on grid refinement in the context of two equation models [68].

4.5 Advanced Turbulence Models

The statistical models discussed so far are based on the eddy - viscosity / - diffusivity concept which assumes isotropy, i.e. the individual $\overline{u_i u_j}$ and $\overline{u_i \varphi}$ correlations take the same value in all directions. The models also assume the same velocity scale, $k^{1/2}$, for the various $\overline{u_i u_j}$ ' s, a supposition that may be too simple in complex recirculating flows where the individual components can develop quite differently. In order to account for the different stress terms, an exact transport equation for $\overline{u_i u_j}$ can be derived by manipulating the Navier - Stokes equations, (Hinze [59]). Models incorporating six Reynolds stress equations ($\overline{u_i u_j} = \overline{u_j u_i}$) have been developed and may be

categorized as (i) Reynolds stress models and (ii) algebraic stress models. A brief account of these two types is given in the following sections.

4.5.1 Reynolds Stress Models

The exact Reynolds stress transport equation can be derived by subtracting the time averaged momentum equation from the instantaneous Navier - Stokes equation for both the x_i and the x_j momentum. The resulting equation for the component j is multiplied with u_i and vice - versa. The equations are then summed and averaged and yield the $\overline{u_i u_j}$ - equation for high Reynolds numbers. An analogous treatment of the scalar quantity conservation equations leads to equations for the transport of $\overline{u_i \varphi}$. The modelling approximations with respect to the latter are nor outlined here, instead the form as given by Launder [78] is presented in Appendix A.

Neglecting buoyancy effects the Reynolds stress transport equation reads:

$$\underbrace{\frac{\partial \overline{u_i u_j}}{\partial t}}_{\text{rate of change}} + \underbrace{U_k \frac{\partial}{\partial x_k} \left(\overline{u_i u_j} \right)}_{\text{convection}} = \underbrace{- \overline{u_i u_k} \frac{\partial U_j}{\partial x_k} - \overline{u_j u_k} \frac{\partial U_i}{\partial x_k}}_{P_{ij}} \underbrace{- 2\nu \frac{\partial u_i}{\partial x_k} \frac{\partial u_j}{\partial x_k}}_{\varepsilon_{ij}}$$

$$+ \underbrace{\overline{\frac{p}{\rho} \left(\frac{\partial u_i}{\partial x_j} + \frac{\partial u_j}{\partial x_i} \right)}}_{\psi_{ij}} \underbrace{- \frac{\partial}{\partial x_k} \left(\overline{u_i u_j u_k} + \overline{\frac{p}{\rho} (u_j \delta_{ik} + u_i \delta_{jk})} - \nu \frac{\partial u_i u_j}{\partial x_k} \right)}_{d_{ij}} \tag{4.23}$$

The terms on the right hand side represent the following processes:

P_{ij} : stress production by mean shear
ε_{ij} : viscous dissipation
ψ_{ij} : pressure strain
d_{ij} : diffusive transport

Stress production P_{ij} can be evaluated directly, as it only contains mean velocity gradients and Reynolds stresses which are calculated as part of the solution procedure.

The other three terms (dissipation, pressure strain and diffusive transport) require model approximations which are given below. A derivation of the closure scheme is detailed by Launder et al [79].

The viscous dissipation (ε_{ij}) term is modelled following the hypothesis of local isotropy at high Reynolds numbers (section 4.1). It can be written as

$$\varepsilon_{ij} = \frac{2}{3} \delta_{ij} \varepsilon \qquad (4.24)$$

Thus, along with the Reynolds stress equations an expression for the dissipation rate ε must be supplied in the closure scheme. Relation (4.20) is usually taken with a modified diffusion term:

$$\text{diffusion}_{\varepsilon} = C_{\varepsilon} \frac{\partial}{\partial x_k} \left(\frac{k}{\varepsilon} \overline{u_k u_l} \frac{\partial \varepsilon}{\partial x_l} \right) \qquad (4.25)$$

with $C_{\varepsilon} = 0.15$ [79]. The most important approximations concern the pressure strain terms since they are the main terms to balance the shear stress production. An analysis involving a Poisson equation for the pressure field suggests two different kinds of interaction: one containing fluctuating quantities only ($\psi_{ij,1}$), and another arising from mean strain rates ($\psi_{ij,2}$). The pressure strain is the sum of the quantities $\psi_{ij,1}$ and $\psi_{ij,2}$.

An expression for $\psi_{ij,1}$ proposed by Rotta (1951) relating the fluctuating correlations to the degree of anisotropy is widely accepted:

$$\psi_{ij,1} = - C_{R1} \frac{\varepsilon}{k} \left(\overline{u_i u_j} - \frac{2}{3} \delta_{ij} k \right) \qquad (4.26)$$

with $C_{R1} = 1.5$. It should be noted that for $u_i^2 = 2/3\ k$, isotropic turbulence prevails.

For the second pressure strain part, $\psi_{ij,2}$, Launder et al [79] suggest an expression comprising a number of terms. Analysis of this expression indicates that one particular term is dominant and that the other terms can be accounted for by adjusting the empirical constant employed, thus

$$\psi_{ij,2} = - C_{R2} \left(P_{ij} - \frac{2}{3} \delta_{ij} P \right) \qquad (4.27)$$

with $C_{R2} = 0.6$. P_{ij} is the Reynolds stress production and P the production of kinetic energy. As mentioned earlier, sources such as gravity effects which would give rise to a third term, $\psi_{ij,3}$, are not considered.

Comparisons of experimental data for two cases, free shear layers and near wall flows, show that the corresponding individual stress components develop differently. In particular the streamwise stress component near the wall is significantly larger than it is in free shear layers. The model approximations underlying the pressure strain relations (i.e. small convection and diffusion of Reynolds stresses and near equilibrium of production and dissipation rates) imply that the Reynolds stresses should be of the same order in each of these flows. As a consequence of the observed discrepancy further pressure strain term modelling is needed to allow for the influence of strong mean velocity gradients near walls. Expressions that can be added to the pressure strain terms (4.26) and (4.27) have been developed and are detailed in references [78] and [79].

The third term in equation (4.23) requiring model approximations is the diffusive transport expression d_{ij} which consists of three contributions representing turbulent velocity fluctuations, pressure induced diffusion, and diffusion by molecular action. In high Reynolds number flows the influence of molecular interactions is negligible. Most workers also deem the pressure diffusion contribution to be insignificant, leaving diffusion by turbulent velocity fluctuations as the only term requiring a model representation. An exact transport equation for $\overline{u_i u_j u_k}$ can be derived (e.g. [63]) which contains quadruple correlations. At the Reynolds stress closure level simplifications are therefore necessary, the most important of which is to ignore convective transport of $\overline{u_i u_j u_k}$. This reduces the differential equation to an algebraic one which can be written in the following form:

$$- \overline{u_i u_j u_k} = C_s \frac{k}{\varepsilon} \left(\overline{u_i u_l} \frac{\partial \overline{u_j u_k}}{\partial x_l} + \overline{u_j u_l} \frac{\partial \overline{u_k u_i}}{\partial x_l} + \overline{u_k u_l} \frac{\partial \overline{u_i u_j}}{\partial x_l} \right) \qquad (4.28)$$

where C_s is an empirical constant to be evaluated by computer optimization. A value of $C_s = 0.11$ is recommended by Launder et al [79]. All necessary terms to solve the approximated equations for the Reynolds stresses $\overline{u_i u_j}$ are thus provided.

4.5.2 Algebraic Stress Models

Solving the differential equations for the individual Reynolds stresses is computationally expensive and for many engineering applications not economical. For this reason a simplified model has been developed which retains the production, dissipation and pressure strain terms but represents convection and diffusion with algebraic expressions. It consists of six algebraic equations for the components of the stress tensor and two transport equations for the kinetic energy and the dissipation rate. The gradient terms are eliminated according to a proposal due to Rodi [61] which assumes that the transport of $u_i u_j$ is proportional to the turbulence energy transport:

$$\frac{D}{Dt} \left(\overline{u_i u_j} \right) - \text{diffusion} \left(\overline{u_i u_j} \right) \propto \frac{D}{Dt} k - \text{diffusion } k$$

If the proportionality factor is taken as the ratio $\overline{u_i u_j} / k$ and the gradients are expressed through the production and dissipation terms (equation 4.13), the relation may be written as:

$$\frac{D}{Dt} \left(\overline{u_i u_j} \right) - \text{diffusion} \left(\overline{u_i u_j} \right) = \frac{\overline{u_i u_j}}{k} \left(P_k - \varepsilon \right) \qquad (4.29)$$

Introducing this expression together with the pressure strain model (equations 4.26 and 4.27) and the dissipation term (4.24) into the Reynolds stress transport equation (4.23) yields for non - buoyant shear flows:

$$- \overline{u_i u_j} = \frac{2}{3} \frac{1-C_{R2}}{C_1} \frac{C_{R1}-1+C_{R2}\frac{P}{\varepsilon}}{(C_{R1}-1+\frac{P}{\varepsilon})^2} \frac{k^2}{\varepsilon} \frac{\partial U_i}{\partial x_j} \qquad (4.30)$$

with $C_{R1} = 1.5$ and $C_{R2} = 0.6$

An analogy to the Kolmogorov - Prandtl expression (4.21) is evident, with the constant C_μ replaced by a function of P/ε .

A modelled version of the transport equation for scalar fluxes can be derived in a similar manner as outlined above (see e.g. references [61] and [78])

Algebraic stress / flux models are suitable for flows where convective and diffusive transport does not play an important role. While the Reynolds stress / flux model is the most rigourous and fundamental approach towards representing anisotropic behaviour, algebraic models provide a compromise between computational economy and the universality afforded by solving for individual stress / flux components. They can simulate many of the flow phenomena that were predicted successfully by Reynolds stress models. A potential weakness of both stress / flux models lies in their dependence on the ε - equation. In flows such as round jets and weak shear flows where the standard k - ε model may not perform well due to the ε - equation, stress models are not likely to improve predictions.

CHAPTER 5

5. NUMERICAL SOLUTION METHOD

In chapters 3 and 4 the governing equations for the flow considered in this thesis were presented. Due to their complexity iterative methods must be applied for the solution, and it is the purpose of this chapter to describe the numerical procedure employed.

In section 5.1 a brief overview of the PHOENICS code used in this study is given. This is followed by a description of the grid system together with its notation in section 5.2. The discretization of the conservation equations is outlined in section 5.3, remarks on the implementation of boundary conditions and on relaxation are made in section 5.4. The solution algorithm for solving the discretized conservation equations is detailed in section 5.5, finally, the concluding remarks in section 5.6 summarize this chapter.

5.1 The PHOENICS Fluid Dynamics Code

The PHOENICS code is a general purpose fluid dynamics program that is intended to be applicable to a wide range of different flows [80]. These include parabolic, hyperbolic and elliptic flows under steady state and transient conditions. The program also allows for two - phase flows. The numerical procedure used by PHOENICS is based on the well documented SIMPLE algorithm, [81]. Although this technique is described in detail elsewhere, it is worthwhile to outline it with particular reference to the grid used in this study in the remainder of this chapter.

PHOENICS is a modular code consisting of three main components: 'Satellite', 'Earth' and 'Photon'.

- 'Satellite' is the pre - processor for setting the input data. It is used to define the numerical mesh and to activate appropriate solution and output options. This is

effected by way of PHOENICS specific commands which are detailed in reference [82]. A description of the input file for the flow under investigation is given in section 7.1.1. The 'Satellite' does not communicate with the central equation solver, it merely writes a data file which is subsequently read by 'Earth'.

- 'Earth' is the main equation solver and is not accessible to the user. However, during the iteration process 'Earth' interacts with a number of subroutines, most notably 'Ground' and 'Grex 2', by means of which the user can influence the equations solved for. The user can also specify his own coding and output sequences in 'Ground' in cases where the options provided in 'Satellite' are not adequate. This need may arise from complex boundary conditions or property relationships not provided as standard options. Both 'Ground' and 'Grex 2' are organized in a group structure comprising 24 groups which are visited at specific times during the iteration process.

- 'Photon' is the graphics post - processor. It can present results in three dimensional vector plots and contour plots of the variables solved for. If the results are required in a different format (e.g. velocity profiles, distribution of variables along particular grid lines) it is necessary to introduce new coding in 'Ground' which creates new output files.

The PHOENICS code is written in ANSI Fortran. At Bath, version 1.4 was installed on a departmental VAX 11/750 in the School of Mechanical Engineering and, since February 1990, runs on SUN Sparc stations connected to a SUN sparc server 330.

5.2 Grid and Notation

The hydraulic analogue model and a segment of it are illustrated in figures 5.1 and 5.2. For both cases under consideration, i.e. deflected and undeflected jet, it is possible to take advantage of the symmetry within the flow field in order to reduce the computational effort, both in terms of CPU time and storage requirements. In the case of the undeflected jet the segment shown in figure 5.2 represents the flow domain with the r - θ and r - z planes through the jet centreline taken as planes of symmetry. For the deflected jet, only the r - θ plane through the centre of the jet can be treated as a plane of symmetry and the domain reduces to the bottom part of the configuration shown in figure 5.1.

For computational purposes the flow field is subdivided into control volumes which are generated in cylindrical - polar co-ordinates. The grid is nonuniform in each direction with a higher cell density near the nozzle exit and in the jets shear layer. Also, near the wall at r = R the cells become gradually smaller to capture the development of the wall jet. The ratio of any two neighbouring node spacings does not exceed 1.5. Nodes are situated at the centre of each cell as indicated in figure 5.3. In figure 5.3a, the grid nomenclature is illustrated in the r - θ plane for cells of constant thickness in z - direction. Such a layer of unit height is termed z - slab. Figure 5.3b depicts the grid in the r - z plane. The cell node of any variable of interest, ϕ, is designated P, the neighbouring nodes in x - direction are called E and W (East and West), in y - direction N and S (North and South), and in z - direction H and L (High and Low). The faces between adjacent cells are referred to in lower case letters, i.e. e, w, n, s, h and l. Since neighbouring cells may vary in size, the cell faces do not necessarily lie midway between grid nodes and any parameters prevailing at the cell faces must be interpolated accordingly. In PHOENICS, linear interpolation is used for determining exchange coefficients at cell faces.

While values for the pressure, P, kinetic energy, k, rate of dissipation, ε, and other scalar variables are calculated at the grid nodes, velocities are calculated at the cell faces. This 'staggered' grid arrangement is discussed in detail in reference [81] and illustrated for the r - θ plane in figure 5.4. The control volumes used for evaluating velocities are displaced in the direction of each velocity such that the grid nodes of the scalar variable mesh lie on the cell boundaries of the staggered grid. This practice rules out the possibility of an unrealistic pressure field as a numerically valid solution. It also ensures that the pressures between adjacent grid points become the driving force for the velocities at the cell faces. Moreover, velocities stored at cell boundaries are directly available for calculating convection fluxes across these faces without any interpolation. It is assumed that scalar variables evaluated at grid nodes prevail over the entire control volume and similarly velocities are assumed to be constant over a cell face area.

5.3 Discretization of Conservation Equations

The governing equations presented in chapter 3 are discretized by dividing the flow domain into a number of control volumes or cells. Each of these cells surrounds a grid node, P, as illustrated in figure 5.3. The essence of the discretization process is to replace the differential equations for the whole flow field with algebraic equations that can be evaluated by integration over each control volume. This effectively balances the variables at each cell. Although a staggered grid as outlined in the previous section is used, the discretization principles apply to any general variable with differences only appearing in the coefficients and source terms.

The following discussion is largely based on Patankar [81] and on lecture notes from a Computational Fluid Dynamics Course at Imperial College [83] with due account taken of the cylindrical - polar co-ordinate system used in this work. The conservation equation for any general variable ϕ may be written in the following form:

$$\underbrace{\frac{\partial}{\partial t}\left(r\rho\phi\right)}_{\text{rate of change}} + \underbrace{\frac{\partial}{\partial r}\left(r\rho U_r\phi\right) + \frac{\partial}{\partial \theta}\left(\rho U_\theta\phi\right) + \frac{\partial}{\partial z}\left(r\rho U_z\phi\right)}_{\text{convection}} =$$

$$\underbrace{\frac{\partial}{\partial r}\left(r\Gamma_\phi \frac{\partial\phi}{\partial r}\right) + \frac{\partial}{\partial \theta}\left(\Gamma_\phi \frac{\partial\phi}{r\partial\theta}\right) + \frac{\partial}{\partial z}\left(r\Gamma_\phi \frac{\partial\phi}{\partial z}\right)}_{\text{diffusion}} + \underbrace{S_\phi}_{\text{Source}} \qquad (5.1)$$

The actual grid geometry has no influence on the discretization principles presented in the following discussion as long as the mesh is orthogonal. Deviations from a cartesian grid merely affect coefficients relating to distances, areas and volumes. The terms appearing in equation (5.1) represent rate of change, convection, diffusion and sources. The discretization methods for each of these terms will be outlined in the following paragraphs.

5.3.1 Transient Term

The first term in equation (5.1), representing the rate of change of the general variable ϕ, is integrated over the control volume and over the time interval from t to t + Δt. The value of ϕ is assumed to prevail over the entire cell, the density ρ is constant.

$$r\rho \int_t^{t+\Delta t} \iiint_{V_p} \frac{\partial}{\partial t}\phi \, \partial V \, \partial t = \left(r\rho\phi V_p\right)^{t+\Delta t} - \left(r\rho\phi V_p\right)^{t}$$

$$= r\rho V_p \left(\phi^{t+\Delta t} - \phi^{t}\right) \qquad (5.2)$$

Equation (5.2) is implemented using the implicit scheme, hence the new values prevail over the entire time step. The Courant stability criterion is thus avoided which could not have been satisfied without excessively small time steps:

$$Co = U_i \frac{\Delta t}{\Delta x}$$

where u_i is the velocity and Δt and Δx are the time and space step sizes respectively. To obtain a stable solution Co must be less than unity. For cells near the nozzle exit the

time interval would therefore have to be smaller than 0.4 ms which would clearly increase computing time prohibitively.

5.3.2 Convection

The convection terms of equation (5.1) are integrated over the control volume shown in figure 5.3 and over the time interval. For reasons of clarity the latter is temporarily omitted; as it only adds the coefficient Δt, it will be reintroduced when the complete discretized equation is presented.

$$C = \iiint_{V_p} \left[\frac{\partial}{\partial r}\left(r\rho U_r\phi \right) + \frac{\partial}{\partial \theta}\left(\rho U_\theta\phi \right) + \frac{\partial}{\partial z}\left(r\rho U_z\phi \right)\right] \partial r\, \partial\theta\, \partial z =$$

$$\left[\left(r\rho U_r\phi \right)_n - \left(r\rho U_r\phi \right)_s\right] \partial\theta\, \partial z$$

$$+ \left[\left(\rho U_\theta\phi \right)_e - \left(\rho U_\theta\phi \right)_w\right] \partial r\, \partial z$$

$$+ \left[\left(r\rho U_z\phi \right)_h - \left(r\rho U_z\phi \right)_l\right] \partial r\, \partial\theta \qquad (5.3)$$

Introducing abbreviations for the finite volume areas

$$\left(r\, \partial\theta\, \partial z \right)_n = A_n \qquad (5.4.1)$$

$$\left(r\, \partial\theta\, \partial z \right)_s = A_s \qquad (5.4.2)$$

$$\left(\partial r\, \partial z \right)_e = A_e \qquad (5.4.3)$$

$$\left(\partial r\, \partial z \right)_w = A_w \qquad (5.4.4)$$

$$\left(r\, \partial r\, \partial\theta \right)_h = A_h \qquad (5.4.5)$$

$$\left(r\, \partial r\, \partial\theta \right)_l = A_l \qquad (5.4.6)$$

leads to

$$C = \left(\rho AU_r\phi \right)_n - \left(\rho AU_r\phi \right)_s + \left(\rho AU_\theta\phi \right)_e - \left(\rho AU_\theta\phi \right)_w +$$

$$\left(\rho AU_z\phi \right)_h - \left(\rho AU_z\phi \right)_l \qquad (5.5)$$

All variables except the velocities are stored at the grid nodes. A scheme is therefore needed to relate the boundary values of ϕ in equation (5.5) to nodal values of neighbouring cells. A variety of schemes have emerged over the last years, some of which are reviewed by Leschziner [84]. They employ linear or polynomial relationships involving two or more grid points. The choice of approximation scheme is very much flow and grid dependent, the Quadratic Upstream - weighted Differencing Scheme (QUICK) has recently emerged as the method favoured by the UMIST group [84], other workers employ first and second order linear schemes. In the present study the well established Hybrid scheme [81] is used. It is not within the scope of this work to study the effect of different approximation schemes on this particular flow, however, some comparisons for a similar flow configuration are reported by Hoholis [28] and will be referred to in chapter seven.

As the name suggests the Hybrid scheme combines two methods: (i) the central - difference scheme and (ii) the upwind scheme. These methods are used alternatively depending on the ratio of convection and diffusion defined by the cell Peclet number (Pe). In the limit of Pe = 0, the problem reduces to a mere diffusion situation, on the other hand, for large Peclet numbers the flow is dominated by convection, and the nodal values of ϕ are very close to the upstream values. For the flux across the west face the Peclet number can be written with reference to figure 5.3a as:

$$Pe_w = \frac{\rho U_{\theta,w} (Dist)_{W,P}}{\Gamma_w} \qquad (5.6)$$

where $(Dist)_{W,P}$ denotes the distance between the W and P cell nodes. Corresponding expressions apply to fluxes across the other cell faces.

The Hybrid scheme represents a piecewise linear approximation of the exact solution for the following Peclet number ranges:

- $Pe < -2$
- $-2 < Pe < 2$
- $Pe > 2$

Within the range -2 < Pe < 2 diffusion and convection are of a similar magnitude and the central - difference approximation is used with piecewise linear profiles between adjacent grid nodes. Outside this range the upwind scheme is used and the cell face value is assumed to be the value of the grid node on the upwind side of the face.

5.3.3 Diffusion

Attention is now turned to the diffusion terms in equation (5.1). Again, integration over the time interval is temporarily omitted. Integration over the control volume leads to:

$$D = \iiint_{V_p} \left[\frac{\partial}{\partial r}\left(r\Gamma_\phi \frac{\partial \phi}{\partial r}\right) + \frac{\partial}{\partial \theta}\left(\Gamma_\phi \frac{\partial \phi}{r\partial \theta}\right) + \frac{\partial}{\partial z}\left(r\Gamma_\phi \frac{\partial \phi}{\partial z}\right)\right] \partial r\, \partial \theta\, \partial z$$

$$= \left[\left(r\Gamma_\phi \frac{\partial \phi}{\partial r}\right)_n - \left(r\Gamma_\phi \frac{\partial \phi}{\partial r}\right)_s\right] \partial \theta\, \partial r$$

$$+ \left[\left(\Gamma_\phi \frac{\partial \phi}{r\partial \theta}\right)_e - \left(\Gamma_\phi \frac{\partial \phi}{r\partial \theta}\right)_w\right] \partial r\, \partial z$$

$$+ \left[\left(r\Gamma_\phi \frac{\partial \phi}{\partial z}\right)_h - \left(r\Gamma_\phi \frac{\partial \phi}{\partial z}\right)_l\right] \partial r\, \partial \theta \qquad (5.7)$$

The gradients of ϕ at the cell faces are approximated using a linear variation between adjacent grid nodes. With the finite volume areas from equation (5.4), equation (5.7) may be written as:

$$D = \frac{(A\Gamma_\phi)_n}{(Dist)_{N,P}}\left(\phi_N - \phi_P\right) - \frac{(A\Gamma_\phi)_s}{(Dist)_{P,S}}\left(\phi_P - \phi_S\right)$$

$$+ \frac{(A\Gamma_\phi)_e}{(Dist)_{E,P}}\left(\phi_E - \phi_P\right) - \frac{(A\Gamma_\phi)_w}{(Dist)_{P,W}}\left(\phi_P - \phi_W\right)$$

$$+ \frac{(A\Gamma_\phi)_h}{(Dist)_{H,P}}\left(\phi_H - \phi_P\right) - \frac{(A\Gamma_\phi)_l}{(Dist)_{P,L}}\left(\phi_P - \phi_L\right) \qquad (5.8)$$

or in a more compact form:

$$D = (-D_n -D_s -D_e -D_w -D_h -D_l) \phi_P + D_n\phi_N + D_s\phi_S + D_e\phi_E + D_w\phi_W + D_h\phi_H + D_l\phi_L \quad (5.9)$$

with

$$D_n = \frac{(A\Gamma_\phi)_n}{(Dist)_{N,P}} \quad (5.10)$$

etc.

The diffusion coefficients Γ_ϕ at the cell boundaries are taken as the arithmetic mean of the adjacent nodal values.

5.3.4 Source Terms

The last term in equation (5.1) represents the in - fluid source term. Assuming a uniform distribution it is integrated over the control volume. After integration the source term is linearized to yield the following form:

$$\iiint_{V_p} S_\phi \, \partial r \, \partial\theta \, \partial z = S_C + S_P\phi_P \quad (5.11)$$

To ensure numerical stability the coefficient S_p must be negative. A detailed discussion of source term linearization can be found in reference [81].

The following sources appear in the governing equations:

- pressure forces in momentum equations
- centrifugal force in U_r momentum equation
- Coriolis force in U_θ momentum equation
- turbulence production term P_k in kinetic energy and dissipation rate equation (see equation 4.13)

The discretization practice for each of these terms is briefly outlined in the following paragraphs with reference to figure 5.3.

Pressure Forces

The pressure forces added to the U_θ , U_r and U_z equations are, respectively:

$$A_e \ (P_P - P_E)$$

$$A_n \ (P_P - P_N)$$

$$A_h \ (P_P - P_H)$$

where the finite volume areas A_e , A_n and A_h are defined in equation (5.4).

Centrifugal Force

The centrifugal force in the U_r equation is accounted for by the following expression [85], ensuring that the upwind face circumferential velocity is used to calculate the force:

$$\frac{A_n}{r_n} (r_N - r_P) \ [U_{\theta,wn} \max (0 , U_{\theta,wn}) - U_{\theta,en} \max (0 , U_{\theta,en})]$$

Coriolis Force

The Coriolis force term added to the U_θ equation is written as [85]:

$$- \sin \left(\frac{\theta_{we}}{2}\right) (U_{r,n} + U_{r,s}) \max \left(0 , A_e \frac{U_{\theta,w} + U_{\theta,e}}{2}\right)$$

$$+ \sin \left(\frac{\theta_{eeE}}{2}\right) (U_{r,nE} + U_{r,sE}) \max \left(0 , - A_e \frac{U_{\theta,e} + U_{\theta,eE}}{2}\right)$$

Turbulence Production

The production term P_k (4.13) appearing in the turbulence model equations contains velocity gradients of the three velocity components in each direction. The gradients of U_θ in θ - direction, U_r in radial direction and U_z in z - direction are approximated as follows:

$$\frac{\partial U_\theta}{\partial \theta} = \frac{U_{\theta,e} - U_{\theta,w}}{(Dist)_{w,e}}$$

$$\frac{\partial U_r}{\partial r} = \frac{U_{r,n} - U_{r,s}}{(Dist)_{n,s}}$$

$$\frac{\partial U_z}{\partial z} = \frac{U_{z,h} - U_{z,l}}{(Dist)_{h,l}}$$

For the remaining six terms the average of four adjacent gradients is formed as shown in the following example:

$$\frac{\partial U_\theta}{\partial r} = \frac{1}{4}\left[\frac{U_{\theta,eN} - U_{\theta,e}}{(Dist)_{P,N}} + \frac{U_{\theta,e} - U_{\theta,eS}}{(Dist)_{S,P}} + \frac{U_{\theta,wN} - U_{\theta,w}}{(Dist)_{W,NW}} + \frac{U_{\theta,w} - U_{\theta,wS}}{(Dist)_{W,SW}}\right]$$

The terms U_θ/r and U_r/r in equation (4.13) are estimated from:

$$\frac{U_\theta}{r} = \frac{U_{\theta,e} + U_{\theta,w}}{2\, r_P}$$

$$\frac{U_r}{r} = \frac{U_{r,n} + U_{r,s}}{2\, r_P}$$

With these expressions all necessary terms are provided to assemble the complete discretized conservation equation for the general variable ϕ.

5.3.5 Complete Discretization Equation

Using the Hybrid scheme to relate cell face values to nodal values in the convection expression (5.5), the complete implicit form of the conservation equation may be written in the following form:

$$\phi_P = \frac{a_E\phi_E + a_W\phi_W + a_N\phi_N + a_S\phi_S + a_H\phi_H + a_L\phi_L + a_T\phi_T + S_C}{a_E + a_W + a_N + a_S + a_H + a_L + a_T + S_P} \tag{5.12}$$

where

$$a_E = \max\,(0\ ,\ D_e - \alpha|\rho U_{\theta,e}A_e|) + \max\,(0\ ,\ -\rho U_{\theta,e}A_e)$$

$$a_W = \max\,(0\ ,\ D_w - \alpha|\rho U_{\theta,w}A_w|) + \max\,(0\ ,\ \rho U_{\theta,w}A_w)$$

$$a_N = \max\,(0\ ,\ D_n - \alpha|\rho U_{r,n}A_n|) + \max\,(0\ ,-\rho U_{r,n}A_n)$$

$$a_S = \max\,(0\ ,\ D_s - \alpha|\rho U_{r,s}A_s|) + \max\,(0\ ,\ \rho U_{r,s}A_s)$$

$$a_H = \max\,(0\ ,\ D_h - \alpha|\rho U_{z,h}A_h|) + \max\,(0\ ,\ -\rho U_{z,h}A_h)$$

$$a_L = \max\,(0\ ,\ D_l - \alpha|\rho U_{z,l}A_l|) + \max\,(0\ ,\ \rho U_{z,l}A_l)$$

$$a_T = \frac{r\rho V_P}{\Delta t} \tag{5.13}$$

In the above expression D_i denotes the diffusion coefficient as given in equation (5.10), the areas A_i are defined in equation (5.4), and the parameter $\alpha = 0.5$ ensures that for Peclet numbers outside the range $-2 < Pe < 2$ the diffusion contribution is omitted. The source term is used to represent the sources described in section 5.3.4, and also to introduce boundary conditions and underrelaxation. It is to these two latter aspects that attention is focused in the next section.

5.4 Boundary Conditions, Under-relaxation

(a) Boundary Conditions

In section 3.4 the different boundary conditions used in this study were discussed, viz. walls, prescribed pressure boundaries, inlets and planes of symmetry. These boundary conditions are introduced into the finite difference equation (5.12) through the source term. After a brief description of the general form, the practice used for each of the four boundary types is outlined in the following paragraphs.

General Form

The general form of the boundary condition contains a convective and a diffusive contribution and can be applied to the four boundary types relevant to the present study:

$$S_\phi = \dot{m}\ (V_\phi - \phi_P) + C_\phi (V_\phi - \phi_P) \qquad (5.14)$$

convection diffusion

where $\dot{m}$ is the mass flow rate across the boundary, V_ϕ and C_ϕ the value and coefficient of variable ϕ, and ϕ_P the value of ϕ in cell P. The mass flow source itself appears in the continuity equation and is calculated from

$$\dot{m} = C_m (V_m - P_P) \qquad (5.15)$$

where C_m and V_m are the coefficient and value of the mass flow. By assigning appropriate values to C_ϕ, C_m, V_ϕ and V_m the different boundary conditions can be incorporated into the finite difference equations as outlined below.

Wall Boundary

For wall boundary conditions the convective part of equation (5.14) is set to zero ($\dot{m} = 0$). In the momentum equations V_ϕ is set to zero and C_ϕ is obtained from

$$C_\phi = \rho A_w s_\varphi U_P \tag{5.16}$$

where A_w is the wall cell face area, s_φ a friction factor and U_P the velocity parallel to the wall at adjacent grid node P. Different expressions for the friction factor s_φ are used depending on whether the flow is laminar or turbulent, thus incorporating the wall-law relationship illustrated in figure 3.3.

Special wall functions are also applied for the turbulence parameters k and ε as given in equations (3.18) and (3.19). The value in the cell next to the wall, ϕ_P, is fixed by assigning the following values in equation (5.14): $\dot{m} = 0$, $C_\phi = 10^{10}$, V_ϕ = required value. The comparatively large coefficient C_ϕ effectively fixes ϕ_P to the value of V_ϕ:

$$\phi_P = \frac{\text{small terms} + 10^{10}\, V_\phi}{\text{small terms} + 10^{10}} \approx V_\phi \tag{5.17}$$

Prescribed Pressure Boundary

When prescribing an external pressure, the diffusion part of equation (5.14) is cut out by setting C_ϕ equal to zero. As no mass flow source is required, V_m in equation (5.15) is also set to zero. The choice for C_m depends on the displaced and entrained mass flow. In the present case a value of unity was found to give a well converged solution. When fluid is entrained, V_ϕ in equation (5.14) is specified for the variables entering the domain.

Inlet Boundary

At inlet boundaries the diffusion part in equation (5.14) is omitted and the following values are assigned to the other parameters: $C_m = 10^{-10}$, $V_m = 10^{10}\ \dot{m}$, and V_ϕ is the required value. Thus, the source term in the continuity equation takes the following form:

$$P_P = \frac{\ldots\ldots + 10^{-10}\ 10^{10}\ \dot{m}}{\ldots\ldots + 10^{-10}} \tag{5.18}$$

This prescribes a net source of $\dot{m}$. For the variables convected into the domain the appropriate V_ϕ's must be set.

Planes of Symmetry

At planes of symmetry no convective or diffusive fluxes cross the boundary, i.e. $S_\phi = 0$. This condition is implemented by setting $\dot{m}$ and C_ϕ in equation (5.14) to zero.

(b) Relaxation

During the iterative solution process the values of flow variables fluctuate and situations can occur where the solution becomes unstable and does not converge. It is therefore often desirable to artificially slow the iteration process down leading to a slower variation in the values of dependent variables. This practice is termed under-relaxation. Two types of under-relaxation are employed in the present study and these are described below.

Linear Under-relaxation

The values of variable ϕ are modified according to the following expression:

$$\phi = \alpha_l \phi_{new} + (1 - \alpha_l)\ \phi_{old} \qquad (5.19)$$

Thus ϕ is obtained from both the previous (ϕ_{old}) and the current (ϕ_{new}) value and the under-relaxation factor α_l. If α_l is less than unity the iterative process is slowed down.

Time Step Under-relaxation

In this under-relaxation method the following source term is added to the finite difference equation for variable ϕ:

$$S_\phi = \alpha_t\ (\phi_{P,old} - \phi_P) \qquad (5.20)$$

where

$$\alpha_t = \frac{\rho V_P}{T_f} \tag{5.21}$$

where V_P is the cell volume and T_f a 'false' time step. With this extra source equation (5.12) for reads:

$$\phi_P = \frac{.... + \alpha_t \phi_{P,old}}{.... + \alpha_t} \tag{5.22}$$

Small false time steps and hence large coefficients α_t lead to an increasingly dominating influence of the old value of ϕ_P. Thus, the smaller the chosen time step is, the more is the variation of ϕ slowed down.

5.5 Solution Procedure

In the previous sections the general form of the discretized conservation equation and some auxiliary relationships were described. The present section outlines how these equations are solved in the PHOENICS computer code.

All conservation equations for velocities and scalar variables can be cast in the form of equation (5.12) which, although seemingly linear, is non - linear because the coefficients and sources are themselves functions of the dependent variables. Furthermore, there is no direct way of obtaining the pressure field which is needed to compute the pressure gradients in the source terms of the momentum equations. An iterative 'guess - and - correct' solution procedure is therefore adopted which, in the case of PHOENICS, is based on a variant of the SIMPLE algorithm [81]. SIMPLE stands for 'Semi - Implicit Method for Pressure - Linked Equations', an acronym not entirely appropriate in the context of this work as calculations are performed using a

fully - implicit scheme [86]. A detailed description of the algorithm can be found in the literature [81, 83], however, a brief outline is given with reference to the equations presented in sections 5.3 and 5.4.

The method is based on a guessed pressure field from which velocities are calculated that do not satisfy the continuity equation (unless the guessed pressure field was correct). The pressures are then corrected so as to satisfy continuity, and the velocities are recalculated using the pressure corrections. The process is repeated with the updated pressure fields until the solution converges, i.e. until the mass imbalance falls below a prescribed value or until a set maximum number of iterations is reached.

The pressure and the velocities are written as:

$$P = P^{*} + P' \tag{5.23}$$

$$U_{\theta} = U_{\theta}^{*} + U_{\theta}' \tag{5.24.1}$$

$$U_{r} = U_{r}^{*} + U_{r}' \tag{5.24.2}$$

$$U_{z} = U_{z}^{*} + U_{z}' \tag{5.24.3}$$

where P^{*}, U_{θ}^{*}, U_{r}^{*} and U_{z}^{*} represent the guessed or intermediate values of pressure and velocities, P' is the pressure correction and U_{θ}', U_{r}' and U_{z}' are the velocity corrections. From the actual and the intermediate momentum equations a velocity correction formula can be constructed which relates the current velocity value to the previous velocity and the pressure correction. Thus, the formulae may be written with reference to figure 5.3 as:

$$U_{\theta} = U_{\theta}^{*} + d_{e} (P_{P}' - P_{E}') \tag{5.25.1}$$

$$U_{r} = U_{r}^{*} + d_{n} (P_{P}' - P_{N}') \tag{5.25.2}$$

$$U_{z} = U_{z}^{*} + d_{h} (P_{P}' - P_{H}') \tag{5.25.3}$$

where

$$d_{e} = \left(\frac{A}{\Sigma a_{nb}} \right)_{e} \tag{5.26.1}$$

$$d_n = \left(\frac{A}{\Sigma a_{nb}} \right)_n \qquad (5.26.2)$$

$$d_h = \left(\frac{A}{\Sigma a_{nb}} \right)_h \qquad (5.26.3)$$

where the finite volume areas A_e, A_n and A_h are given in equation (5.4) and the neighbour coefficients $(a_{nb})_e$, $(a_{nb})_n$ and $(a_{nb})_h$ account for the combined convection - diffusion influence at the control volume faces in the staggered grid. To evaluate equation (5.25) an expression for the pressure correction P' is needed which can be derived by substituting equations (5.25) into the discretized form of the continuity equation. The resulting form of the pressure correction equation has a similar appearance to equation (5.12) and can hence later be solved using the same techniques:

$$P_P' = \frac{a_E P_E' + a_W P_W' + a_N P_N' + a_S P_S' + a_L P_L' + a_H P_H' + b}{a_E + a_W + a_N + a_S + a_L + a_H} \qquad (5.27)$$

where

$$a_E = \rho d_e A_e$$
$$a_W = \rho d_w A_w$$
$$a_N = \rho d_n A_n$$
$$a_S = \rho d_s A_s$$
$$a_L = \rho d_l A_l$$
$$a_H = \rho d_h A_h \qquad (5.28)$$

$$b = (\rho A U_\theta^*)_w - (\rho A U_\theta^*)_e + (\rho A U_r^*)_s - (\rho A U_r^*)_n + (\rho A U_z^*)_l - (\rho A U_z^*)_h \qquad (5.29)$$

The term b represents a mass source which reduces to zero when the intermediate velocities denoted by an asterisk satisfy the continuity equation. In this case no further pressure corrections are required and a converged solution is reached.

All relevant components for solving the discretized conservation equation are now provided and the solution sequence may be summarized as follows:

(i) guess the initial pressure field P^*

(ii) using this pressure field solve momentum equations for U_θ^*, U_r^* and U_z^*

(iii) calculate coefficients in pressure correction equation (5.27) and solve for P'

(iv) correct pressure and velocities using equations (5.23) and (5.25)

(v) solve for scalar variables k, ε and C

(vi) return to step (ii) using the new pressure field and repeat until convergence

Two different procedures are used for solving the sets of linear equations: (i) a slab - wise method which operates on successive r - θ planes for the velocities, turbulence kinetic energy, dissipation rate and concentration, and (ii) a whole - field simultaneous method for the pressure correction equation. Details of these schemes are given by Markatos [87]. The treatment of the momentum equations differs from the SIMPLE method in that the coefficients in equation (5.12) contain only diffusion contributions, the convection terms are included in the source term. This variant, known as SIMPLEST [86], enhances convergence, particularly when using fine grids.

5.6 Concluding Remarks

In this chapter the derivation of the finite volume equations from the governing partial differential equations for the flow under consideration has been outlined. The inclusion of boundary conditions and source terms into the finite volume equations has also been described. Finally, the iterative method used for solving these equations has been outlined. Computational results for the different flow configurations under investigation will be presented in chapters seven and eight.

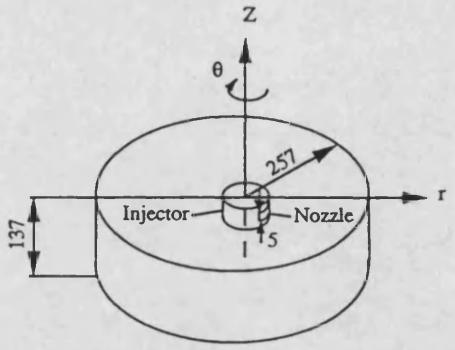

Fig. 5.1: Flow configuration

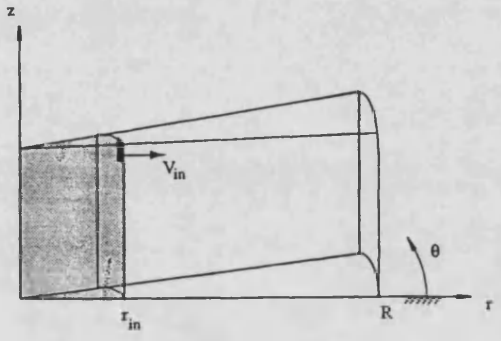

Fig. 5.2: Computational domain, undeflected jet

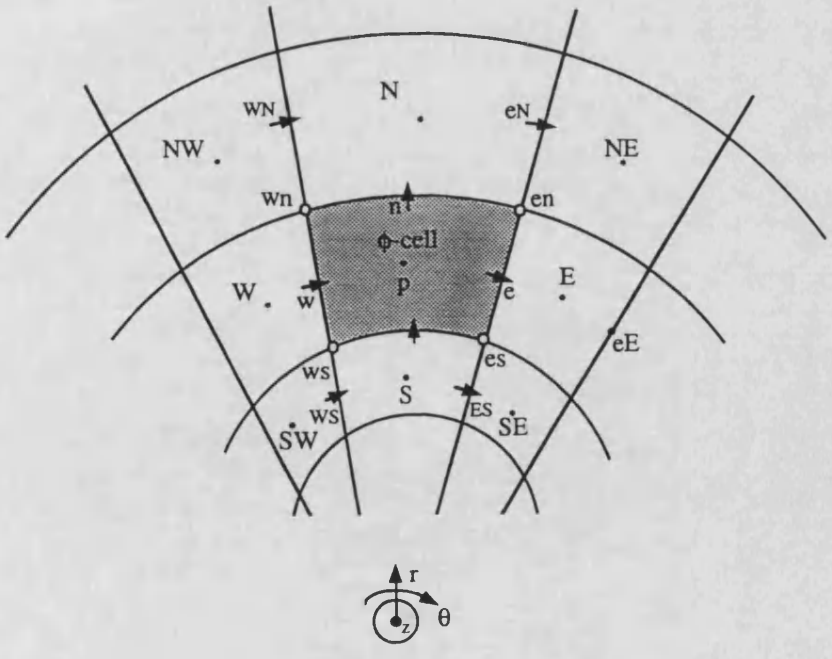

Fig. 5.3 a: Grid nomenclature in r - θ plane for variable ϕ

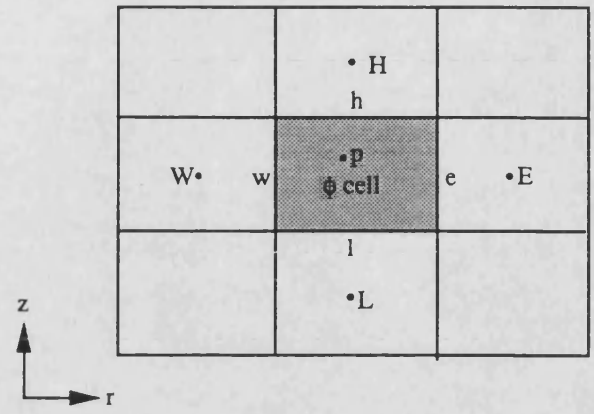

Fig. 5.3 b: Grid nomenclature in r - z plane for variable ϕ

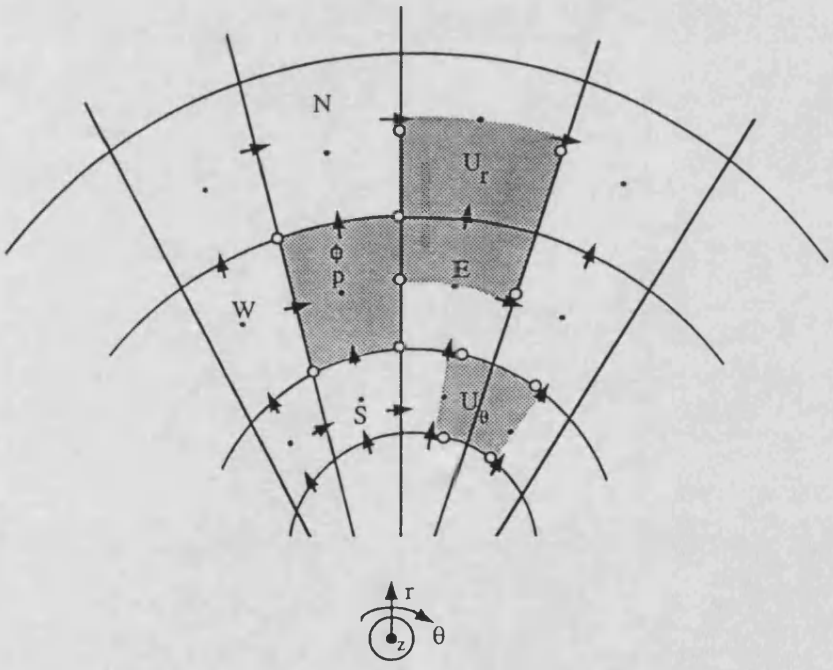

Fig. 5.4: Control volumes for ϕ, U_θ and U_r

CHAPTER 6

6. EXPERIMENTAL STUDY

An experimental study of the steady state and transient jets under quiescent and swirling conditions was undertaken to support the computational part of this thesis. Its main purpose is to provide quantitative data to validate predictions by measuring radial and tangential velocity distributions at five radial positions in the combustion chamber model. Apart from the validation aspect, the experimental results on their own provide detailed insight into the jet development and structure. The presentation of results in sections 6.5 to 6.8 is preceded by introductory remarks on the hydraulic analogy in section 6.1. This is followed by a description of the test facility in section 6.2 which includes a summary of the scale relationships between engine and analogue model. Section 6.3 describes the measurement technique. It contains a discussion of hot film anemometry in the context of hydraulic analogy, an account of the calibration method, and a description of the data analysis technique employed. The main features of the data acquisition system are related in section 6.4. The remaining sections of this chapter present results for the four different flow configurations under investigation: steady state undeflected jet (6.5), transient undeflected jet (6.6), steady state deflected jet (6.7) and transient deflected jet (6.8). Finally, the concluding remarks in section 6.9 summarize this chapter.

6.1 Hydraulic Analogy

Previous work on the penetration and mixing rate of oil sprays [14, 16, 88] has established that the penetration of a single droplet in quiescent air is negligible compared with the penetration of an oil spray. The momentum of the droplets is transferred very rapidly to the surrounding air so that some distance from the nozzle the jet behaves as an air jet with the same inlet momentum as the fuel at the point of injection. Thus, from

a fluid dynamics point of view, the fuel jet may be represented without serious error by an air jet in air or, provided compressibility effects are not important, by a water jet in water. Hence with suitable scaling the water analogy method allows the flow processes occurring in a Diesel engine to be studied on a much more leisurely time scale than would be the case in the actual engine. Apart from the assumption regarding individual fuel droplets it is also important to realize other simplifications made in the water model approach:

- piston movement is not taken into account and hence velocities generated by a moving piston, such as squish, are not included. The combustion chamber height corresponds to the top dead centre position.
- a uniform density is assumed, neglecting density variations in the jet and the surrounding air caused by combustion heat.
- swirl is generated by rotating the cylindrical drum. The level of turbulence associated with the swirling motion is lower than would be expected in an actual engine.

Despite these limitations the hydraulic analogy has proved a valuable tool in combustion studies, particularly since the phenomena occurring in a firing engine are too complex to be represented analytically. Information regarding jet penetration and rate of spread can provide input for multizone combustion models or, as in the present study, serve to validate predictions from multidimensional computer codes.

Previous work using the hydraulic analogue technique was, until recently, concerned with flow visualization experiments. All studies using this method reported in the literature [19, 20, 22, 28, 41] employ dye techniques and high speed photography to examine the progressive development of air - fuel ratio boundaries. The technique permits visual observation of jet development by injecting a weak alkali solution into a similarly weak acid solution in the tank, using phenolphtalein as a chemical indicator. It is not proposed to go into greater detail here since the method is well documented in the

literature. Results were mainly of a qualitative nature showing the jet evolution and the approximate location of different air - fuel ratio boundaries. No quantitative information about the mean velocity field and turbulence generated during injection could be obtained. In view of the importance of convective transport and turbulence for the mixing process and hence ultimately combustion efficiency, Gan [23] recently undertook a detailed velocity survey using the analogue model at the University of Bath. He examined the flow field generated by a four hole nozzle using hot film anemometry under quiescent and swirling conditions. Particularly at high swirl rates the jets were swept around and could be seen to influence one another. In the present study a different nozzle configuration is used, viz. a one hole nozzle with a 5 mm square exit allowing the jet to be studied in isolation and without interference from other jets. A square nozzle was chosen mainly for convenience as it was numerically much easier to specify a square inlet boundary when injecting radially into a cylindrical polar co-ordinate system, the angular co-ordinate being used for the cylindrical drum of the analogue model. More details of the test facility are given in section 6.2 below.

6.2 Test Facility

The combustion chamber represented by the analogue model is that of a six cylinder Perkins DI Diesel engine with a swept volume of 5.8 l. The relationship between rig parameters and equivalents has been described by Way [22]. The assumptions made are outlined in the previous section. Since his flow visualization studies the injection system has been modified and consequently the Reynolds - and Strouhal number ratios between analogue model and actual engine have changed slightly. Both now take a value of 0.95. A summary of the scale relationships is given in table 6.1 and 6.2 below.

Parameter	Engine (air)	Analogue model (water)
density, ρ (kg/m^3)	23.4	10^3
viscosity, μ (kg/ms)	$4.42\ 10^{-5}$	$9.8\ 10^{-4}$
equiv. nozzle dia., D_N (mm)	1.78	5.64
bowl dia. (mm)	73	609
nozzle velocity (m/s)	170	10
mass injected (g)	0.076	600
injection period t_i (s)	0.002	0.3
no. of nozzle holes	4	1

table 6.1: engine parameters and analogue model equivalents

Analogue / Engine Ratios	Values
density R_ρ	42.74
viscosity R_μ	22.17
length R_l	8.34
velocity R_u	0.0588
time R_t	150
Reynolds no.	0.95

table 6.2: analogue / engine ratios

The general arrangement of the hydraulic analogue test facility is depicted in figures 6.1 and 6.2 a. Schematic diagrams of the chamber model and the injection system are provided in figures 6.3 and 6.4. Reference is made to these figures in the following description.

Previous work at Bath on the hydraulic analogue rig has been concerned with flow visualization studies using a chemical indicator technique. The combustion chamber model is made of perspex to permit visual or photographic observation of mixing. Recently the cylindrical tank has been modified by Gan [23] and the author to accommodate hot film and pitot probes for velocity measurements during injection. The main components of the analogue rig are the cylindrical drum representing the combustion chamber and the injection system which permits both continuous and impulsive injection.

The cylindrical drum is supported in another cylindrical tank sealed by a perspex lid. To generate swirl the inner drum can be rotated by an electric motor via a belt drive (figures 6.1 and 6.3). The stationary lid carries mounting pads for both the hot film probe holder and a pitot tube. Hot film measurements can be taken at five radial positions, measured from the tank's axis of symmetry at r = 75 mm, r = 119 mm, r = 164 mm, r = 208 mm and r = 253 mm. The pitot tube allows measurements closer to the nozzle, i.e. up to 48 mm. By rotating the nozzle a profile of the jet and the associated entrainment region on either side can be obtained. The lid also supports the injector and incorporates the outflow for displaced water. Water is supplied from a reservoir tank and fed to the nozzle alternatively through a pump or the injector. Since hot film probe contamination presented a problem a water softener has been installed to filter and clean water before it enters the reservoir tank. This device has proved very effective and reduced levels of probe contamination significantly. In the analysis of hot film signals changes in water temperature must be taken into consideration. Consequently, temperatures in the analogue model and the hot film calibration rig are monitored during measurements using platinum resistance thermometers (PRT). The location of the thermometers is indicated in figures 6.1, 6.2 a and 6.6. They require calibration to match the output signal range to the data acquisition hardware and to convert voltages into temperatures. The calibration method for the two PRT s is outlined in the following paragraphs.

Figure 6.8 shows a block diagram of the signal processing circuit for temperature measurement. The PRT signal is passed through a signal conditioning card and an A/D converter into the PC. The signal conditioning card is adjusted to give an output of zero volts at zero degree Celsius and 10 volts at 100 degrees C . The PRT s are calibrated by applying an exact signal from a resistance box at the signal conditioning card input. Voltages are recorded at the card's output using a digital voltmeter (DVM) and at the computer. The calibration process involves two stages:

(i) adjusting the gain on the card to give zero volts DVM reading at 100 ohm and 1.001 volts at 138.5 ohm where 100 ohm and 138.5 ohm correspond to 0 degree C and 100 degree C respectively

(ii) setting the card amplification to give 0.007 volts on the DVM (0.05 °C on the PC) at 100 ohm and 10.01 volts on the DVM (99.98 °C on the PC) at 138.5 ohm.

The data obtained during calibration is recorded in table 6.3.

PRT	resistance [ohm]	signal conditioning card output [V]	PC [°C]
calibration rig	100	0.007	0.05
	138.5	10.01	99.98
analogue rig	100	0.007	0.05
	138.5	10.02	99.98

table 6.3: PRT calibration data

On reconnecting the transducers the two PRT readings on the computer are compared with each other and a mercury in glass thermometer with a 0.05 degree C resolution. At room temperature the following readings were obtained:

Mercury in glass thermometer:	14.80 deg. C
PRT 1, calibration rig:	14.38 deg. C
PRT 2, analogue rig:	14.77 deg. C

Hence the gain of PRT 1 was adjusted on the signal conditioning card to give the same value as PRT 2. After adjusting some drift on the PRT s was observed, PRT 1 read between 14.65 deg. C and 14.70 deg. C, while PRT 2 varied between 14.70 deg. C and 14.77 deg. C .

The injection system permits both steady state and impulsive injection. Although the steady state case is clearly of limited relevance to the Diesel engine application it does serve to identify regions of intense and weak hydrodynamic activity and hence areas of

strong and poor mixing. It also allows observations to be made as to what extent the steady state is reached during impulsive injection. Another important aspect in the present study lies in the validation function for numerical predictions. The steady state case was used to optimize the computational model to give good agreement with experimental data. This 'tuning' was mainly concerned with the computational mesh, the turbulence model and the inlet boundary condition, and is described in detail in chapter seven. The optimized model was then used for predictions of the impulsive jet and also of the deflected steady state and transient jet. Figure 6.4 shows a schematic diagram of the injection system with the main components labelled. The sketch in figure 6.5 illustrates the nozzle, indicating piston, spring and exit canal with square cross section. During steady state injections a pump provides a constant mass flow, while in the impulsive case the injector is driven by pressurized air. To ensure a constant nozzle exit velocity of 10 m/s throughout the entire experimental study the pressure at the injector end was monitored with a pressure transducer (figures 6.1 and 6.2 a) and displayed on the PC screen. In both cases, steady state and impulsive injection, the pressure signal can be related to the injection velocity. To establish the injection pressure - velocity relationship it is necessary to calibrate the pressure transducer and then to perform a series of injections. The results of this evaluation are detailed in the following paragraphs.

A Gould Stratham (0 - 100 psi) pressure transducer is used to measure the injection pressure. The transducer output signal is passed via a 521 amplifier signal conditioning card and an A/D converter into the computer. To calibrate the pressure transducer and check its linearity a fluid gauge 0 - 10 bar was used. The resulting calibration curve is reproduced in figure 6.9. Hence zero bar corresponds to 0.076 volts (computer reading) and 6.9 bar to 9.998 volts. Voltage readings with a DVM were also taken on the signal conditioning card and found to agree well with the values displayed by the PC. To convert the pressure transducer voltage into a velocity the following relationships are used:

$$E \propto p \qquad (6.1)$$

$$p = c\ V^2 \qquad (6.2)$$

where E is the transducer voltage, p the injection pressure, c a constant, and V the injection velocity. Using the calibration data (figure 6.9) equation (6.1) can be written as

$$E = \frac{10}{6.9}\ p \qquad (6.3)$$

To determine the constant in equation (6.2) a series of injection tests was performed during which the transducer voltage variation with time was recorded. The data is listed in table 6.4.

pressure transducer output E [V]	injection time $t_1 - t_0$ [m sec]
1.75	2200
1.65	2700
1.75	2600
1.75	2600
1.70	2600
1.80	2500
1.80	2500
1.75	2600
1.80	2500
1.90	2600

$$\bar{E} = \frac{\sum_{i=1}^{10} E_i}{10} = 1.765\ V \quad , \quad \overline{t_1 - t_0} = \frac{\sum_{i=1}^{10} (t_1 - t_0)_i}{10} = 2540\ ms$$

table 6.4: pressure transducer output - injection time relationship

The average injection velocity during this series can be determined readily from

$$\dot{m} = \rho\ A_N\ V \qquad (6.4)$$

where $\dot{m}$ is the mass flow rate, ρ the density, A_N the nozzle area, and V the injection velocity. Substituting $\dot{m}$ with the injected volume Vol, density ρ and average injection time $\overline{t_1 - t_0}$, and rearranging yields for the injection velocity:

$$V = \frac{Vol}{(\overline{t_1 - t_0})\ A_N} \qquad (6.5)$$

with

$Vol = 6.0\ 10^{-4}\ m^3$

$A_N = 2.5\ 10^{-5}\ m^2$

$(\overline{t_1 - t_0}) = 2.54\ s$

it follows that V = 9.45 m/s, corresponding to an average transducer voltage of E = 1.765 volts. Combining equations (6.2) and (6.3) gives an expression for the constant c:

$$c = \frac{6.9}{10} \frac{\overline{E}}{V^2}$$

thus, c = 0.01364 and

$$V = 7.11 \sqrt{E} \qquad (6.6)$$

Equation (6.6) is implemented in the data acquisition software so that the injection velocity can be monitored during steady state and transient tests. The value of 10 m/s used corresponds to a transducer voltage of E = 1.976 volts.

This description concludes the section outlining relevant aspects of the test facility. Further details are given by Horner [20], Way [22] and Gan [23]. The data acquisition system is described in section 6.4, following some remarks on the measurement technique itself in section 6.3. below.

6.3 Measurement Technique

Flow visualization studies reported by Way [22], Idoum [21] and others illustrate the temporal evolution of the jet and have been successfully employed under quiescent and swirling conditions. To obtain quantitative mean velocity and turbulence data however, more sophisticated techniques are called for, the most suitable being hot film anemometry and laser Doppler anemometry (LDA). Both techniques could have been

used in the present study, the perspex analogue model permitting optical access for the laser, and indeed a laser system would have been preferable in view of its high accuracy and good frequency response. Unfortunately, laser systems are very costly and no suitable system was available at the time the measurements were taken. For this reason hot film anemometry was chosen and has been used throughout the experimental study. To check mean velocities and gain confidence in hot film results, pitot tube measurements were taken along the jet centreline. The purpose of this section is to outline in general terms the application of hot film anemometry to the analogue model (section 6.3.1), to describe the hot film calibration method used and present calibration curves (section 6.3.2), and finally to outline the analysis technique for hot film signals (section 6.3.3).

6.3.1 Hot Film Anemometry applied to Analogue Model

The probes used in the experiments are TSI 1210 - 20 W cylindrical hot film probes. They are operated in the constant temperature mode with a Prosser PSI 6100 anemometer system. The principles of hot film anemometry are well documented in the literature, e.g. Perry [89]. It is therefore not proposed to discuss the heat transfer relationships on the film and examine different methods of relating change in film resistance to effective cooling velocity, instead some remarks follow on the suitability and limitations of the measurement technique in the context of the analogue model.

The probe size is significant for two reasons: (i) the sensor should be as small as possible so as not to disturb the flow and capture small scale details of the flow pattern and (ii) the film probe should be thin, as this improves the sensitivity towards velocity fluctuations. The diameter of hot film probes is typically a factor of ten larger than that of hot wires, hence the frequency response of hot film probes is considerably lower. In water flows this disadvantage is to some extent offset by the generally lower frequency

scale compared with gaseous flows. Some signal analysis techniques are based on the assumption of an infinitely long sensor (e.g. cosine law), an approximation which might be acceptable for thin wires but cannot justifiably be extended to hot films. The technique employed in the present study is not based on this assumption.

Care must be exercised in choosing the sensor operating temperature by specifying the overheat ratio on the anemometer system. On the one hand a large temperature difference between water and sensor is desirable to obtain a high frequency response and decrease the sensitivity towards water temperature variations, on the other hand a high probe temperature increases the likelihood of localised boiling on the film surface. This causes air bubbles to form which have a detrimental effect on the recorded voltage. A sensor temperature of 58 degrees C was found to be more suitable than the 66.7 degrees C recommended by the probe manufacturer.

Probe contamination through deposits on the film surface adversely affect the frequency response of the sensor and heat transfer between film and water. A reduced heat transfer rate decreases the voltage required to maintain a constant sensor temperature and hence record lower velocities than actually occur. The problem of probe contamination has been largely overcome by the installation of a water softener and regular probe cleaning by dipping it into a vessel containing a weak solution of orthophosphoric acid and placing it into an ultrasonic cleaner. The film was also frequently inspected under a microscope for visual signs of deposits or damage.

The flow field in the analogue model is three dimensional. To measure the velocity magnitude and direction it would be necessary to either use a three sensor probe or position one probe in three mutually perpendicular directions and conduct three consecutive measurements. Although the use of a three sensor probe would be desirable and probably give the most accurate velocity data, its use is beyond the scope of the present work as it requires elaborate data analysis and a three channel anemometer system. Similarly, positioning the same probe in three perpendicular co-ordinate

directions is for practical reasons not feasible. In view of the fact that the flow field in most parts of the analogue rig is expected to be largely two dimensional in the r - θ plane, the above mentioned limitations are not too serious. The only region where a strong motion in z direction is expected is in the wall jet, which is not the focus of this experimental study. It is hence assumed that the flow field can be treated as two dimensional with little loss of realism. The validity of this supposition will later be confirmed in the computational study (chapters 7 and 8) for the r - θ plane bisecting the nozzle exit. To measure velocities in a two dimensional flow field two different approaches are available. In the first alternative two velocity components are measured simultaneously while in the second option two consecutive measurements are conducted with a single film probe rotated by 90 degrees about its axis. For simultaneous measurements X - film probes or split film probes are commonly used.

In steady state conditions either technique can be used since the mean velocity is constant and turbulence is random by nature. It may indeed be preferable to take consecutive measurements at the same location since the effect of possible interference by films and supports on the cooling velocity sensed by each film is eliminated.

In transient flows matters stand differently and consecutive measurements are only permissible when the transient flow pattern is strictly repeatable. Applied to the analogue model, it is essential that injection conditions are repeatable. The solenoid valve which triggers the pressurized air supply for the injector is controlled by the data acquisition system as described in section 6.4. The data acquisition control hardware includes a variable delay which allows a constant delay time between start of data sampling by the PC and opening of the solenoid valve to be set. If the solenoid valve is viewed as a junction between data acquisition system and the actual injection system then the data acquisition side does ensure repeatable conditions. A degree of uncertainty is introduced by mechanical components, in particular the injector where friction might cause slight variations between injections, and also by the nozzle where the piston - spring assembly (figure 6.5) might not always open with the same speed and at the

same pressure. Table 6.4 illustrates that some scatter was observed during a series of injections. Despite these reservations the advantages of single film probes in terms of relative ease of calibration and cost outweighed the limitations outlined above. It was hence decided to use single film probes throughout the experimental study and to interpret transient results with some degree of caution.

6.3.2 Hot Film Calibration

The response of a hot film probe to a fluid flow is a function of both velocity magnitude and direction. The effective velocity seen by the sensor is not only a function of the perpendicular component of the flow but is also affected by the parallel flow component and interference from the supports. In order to establish the relationship between bridge output from the anemometer system and velocity components in the flow it is necessary to

(i) relate the effective cooling velocity sensed by the hot film probe to the probe velocity and direction and
(ii) relate the cooling velocity to the bridge output.

For the first correlation a number of proposals of various degrees of sophistication have been suggested. The simplest scheme, termed cosine law, assumes an infinitely long sensor and ignores the contribution of parallel velocity components and interference from supports on the cooling velocity. More accurate techniques use yaw factors to account for velocities along the sensor and pitch factors for velocity components in the third co-ordinate direction. Both factors are not constant and have to be determined by calibrating the probe at different angles.

The relationship between cooling velocity and bridge voltage is nonlinear. One expression suggested by King and detailed in reference [89] is derived from an energy balance between the heat lost from the sensor due to convection and the electric energy

required to balance this loss. A variety of schemes using different heat transfer relationships have been incorporated in this method. In an alternative approach the nonlinear velocity - voltage relationship has been accounted for in a less pragmatic way by using a polynomial expression of the form:

$$U = A_0 + A_1E + A_2E^2 + \ \ldots \ + A_nE^n \qquad (6.7)$$

This method generally permits a more accurate curve fitting than King's relationship. In the present study the following polynomial relationship is used:

$$U = A_1(E_b^2 - E_0^2) + A_2(E_b^2 - E_0^2)^2 + A_3(E_b^2 - E_0^2)^3$$
$$A_4(E_b^2 - E_0^2)^4 \qquad (6.8)$$

where E_b is the bridge voltage and E_0 a reference voltage. The coefficients A_1 to A_4 are determined by a curve fitting routine. To establish the probe's angular response it was calibrated in 10 degree intervals from 0 to 90 degrees, hence a set of ten calibration curves was obtained. These curves are reproduced in figure 6.10 and later used in the data analysis technique described in section 6.3.3. During experiments great care was taken to ensure that the calibration curves were repeatable; after probe cleaning a calibration curve for one angular position was measured and compared with the original curve. Figure 6.11 depicts a comparison between a curve obtained after cleaning and an original curve. It was also noted that the probe is not symmetric. Figure 6.12 illustrates this for two curves taken at zero degree and 180 degrees. During measurements in the analogue rig it was ensured that the probe orientation relative to the nozzle agreed with that from the calibration rig.

Concluding this section on calibration a few remarks follow on the design of the calibration rig. A cross section of the nozzle chamber is shown in figure 6.6. Water supply comes directly from the mains and passes through a water softener before entering the nozzle chamber. The volume flow is regulated by a valve. Inside the nozzle chamber a baffle plate assists in stabilizing the flow and reducing the level of turbulence

before exit. The exit mean velocity profile has been measured by Gan [23] and was found to be uniform in those parts of the cross sectional area where the sensor is positioned during calibration. The positioning of the sensor in front of the nozzle exit is depicted in figures 6.2 b and 6.7. The bars and connectors permit the hot film probe to be positioned directly in front of the nozzle. The pivot allows the whole assembly to be rotated so that the sensor may be yawed relative to the flow.

6.3.3 Data Analysis Technique

This section outlines the technique used to relate the bridge voltage recorded during measurements and stored on disk to the radial and tangential velocity components in the co-ordinate system of the analogue model. Two measurements were taken at each point, the hot film being aligned with the radial direction during the first run and then rotated by 90 degrees about the probe holder's axis for the second run. The data analysis method does not use yaw factors but rather an iterative method particularly suited for digital processing. It is called the 'double look - up' table method [90] and described in the following paragraphs with reference to figures 6.13 to 6.15. The form of this method implemented in the data analysis program assumes piecewise linear profiles between adjacent calibration curves. Figure 6.13 depicts the sensor in two positions perpendicular to each other. The general velocity vector $\vec{V}$ is decomposed into its tangential velocity U and radial velocity V components, for which the following relationships may be written:

$$U = \vec{V} \cos \beta \quad , \quad V = \vec{V} \sin \beta \qquad (6.9)$$

where β is the angle between velocity and a reference axis. The yaw angles α_1 and α_2 between the normal on each sensor and the flow velocity may be written as

$$\alpha_1 = \overline{\alpha_1} + \beta \qquad (\overline{\alpha_1} = 45^\circ) \qquad (6.10)$$

$$\alpha_2 = \overline{\alpha_2} + \beta \qquad (\overline{\alpha_2} = -45^\circ) \qquad (6.11)$$

Calibration was carried out in terms of velocity and yaw angle (figure 6.10). Figure 6.14 shows the same set of calibration curves $V = f(E)_{const\ \beta}$ as depicted in figure 6.10 with two additional lines of constant voltage representing the higher (E_h) and lower (E_l) bridge voltages obtained from measurements in the analogue rig. The flow chart in figure 6.15 illustrates the structure of the data analysis program. Initially, the maximum and minimum velocity values are identified and the average is formed (V_g) as starting point for the iteration process. The iteration criterion to be satisfied is, that the sum of the absolute values of α_1 and α_2 should be 90 degrees (figure 6.13). If this sum is larger than 90 degrees the velocity is reduced, and vice versa. When the velocity and corresponding angles α_1 and α_2 are found the two velocity components are calculated from equations (6.9) to (6.11). The higher bridge voltage E_h is then compared with the voltages obtained from the sensor when the film was orientated in radial and tangential direction in order to identify the components corresponding to the radial and tangential velocity in the analogue model.

In steady state conditions measurements were taken over a period of four seconds with a sampling rate of 1000 Hz. Although the A/D converter permits a higher sampling rate when monitoring only one channel (1499 Hz or higher when disabling system interrupts), advantage of this feature could not be taken due to computer memory limitations. Hence 4000 voltage pairs were analysed at each position. Using the method outlined above the corresponding 4000 radial and tangential velocity components were calculated and stored in an array for further data reduction. They represent instantaneous velocities from which mean velocities, kinetic energy (k), radial turbulence intensity (TI_r) and tangential turbulence intensity (TI_t) were derived using the following relationships:

$$U = \frac{\sum_{i=1}^{n} U_i'}{n} \qquad (6.12)$$

$$V = \frac{\sum_{i=1}^{n} V_i'}{n} \qquad (6.13)$$

where U and V are mean velocities and U_i' and V_i' instantaneous velocities.

$$k = \frac{1}{2} \left[\sum_{i=1}^{n} (U_i' - U)^2 + \sum_{i=1}^{n} (V_i' - V)^2 \right] \frac{1}{n} \qquad (6.14)$$

$$TI_r = \frac{\sqrt{\sum_{i=1}^{n} (U_i' - U)^2 \frac{1}{n}}}{\sqrt{U^2 + V^2}} \qquad (6.15)$$

$$TI_t = \frac{\sqrt{\sum_{i=1}^{n} (V_i' - V)^2 \frac{1}{n}}}{\sqrt{U^2 + V^2}} \qquad (6.16)$$

In transient tests the 4000 data points available for analysis are divided into a suitable number of time intervals. The smaller the time intervals, the less accurate are the calculated velocities and turbulence data since fewer points around each time step are available for analysis. A slight overlap between neighbouring time intervals is acceptable and helps smooth the temporal evolution of velocity and turbulence data. To measure the jet penetration rate two channels (hot film and pressure) were monitored simultaneously. In this case the A/D converter limited the sampling rate to 749 Hz.

Data reduction is performed with a program written in Fortran by Gan [23] and modified by the author. Pairs of data files containing bridge voltages obtained from radial and tangential measurements at a range of angular locations across the jet are read and analysed according to the method described above. Equations (6.12) to (6.16) are incorporated and results written to an output file in column format.

Concluding this section a few remarks follow on the accuracy that can be expected from the measurement technique described above. One significant problem arises from the method's inability to clearly detect the flow direction. This is not generally a problem in most parts of the jet where the main flow direction is known, however it does pose difficulties at very low velocities and in recirculation zones. At very low mean velocities a situation may arise where the fluctuating components become negative, i.e. the flow direction is reversed. This reversal is not detected by the data analysis method, and in equations (6.12) and (6.13) in effect the absolute values of the instantaneous velocities,

$|U_i'|$ and $|V_i'|$, are taken rather than U_i' and V_i'. Consequently, at low mean velocities higher values may be recorded than actually occur. This ambiguity also affects the calculation of kinetic energy and turbulence intensity as is evident from equations (6.14) to (6.16). Hence flows which are highly turbulent while having a low mean velocity may not be accurately measured. In the hydraulic analogue, regions with low mean velocities are outside the jet's boundary and near the wall at $r = R$. Where this coincides with relatively high levels of turbulence, results must be viewed with some caution.

6.4 Data Acquisition System

The data acquisition system is best described by treating hardware and software separately.

Hardware

The hardware comprises the following components:

- four sensors, viz. two platinum resistance thermometers, a pressure transducer, and a hot film probe
- an electronic circuit to trigger the solenoid valve and data sampling during transient injections
- a 12 bit IBM A/D converter
- an IBM XT PC with twin floppy disk drives

All four sensors needed to be calibrated. This has been described in sections 6.2 and 6.3.2 and no further remarks are here required.

An electronic circuit triggers both the solenoid valve between injector and pressurized air supply and the start of data sampling by the data acquisition program. In transient

tests synchronization of the two is crucial to ensure that injection does not begin before the computer starts sampling data. In initial runs a variable time delay was observed in the data acquisition program which resulted in unrepeatable jet penetration rates to be recorded. This variable delay is a feature of the part of the data acquisition program supplied with the A/D converter. The problem was overcome by two measures: (i) adding an output line from the PC to the valve and (ii) adding an adjustable delay before the valve. The sketch in figure 6.16 illustrates the new arrangement. The switch on the cycle control panel triggers the data acquisition program. After the variable time delay has passed sampling begins and simultaneously the additional output line triggers an adjustable delay. At the end of this second delay the solenoid valve opens. Hence, start of data sampling and delayed valve operation are independent from the variable first delay and results proved to be repeatable. The second delay can be continuously varied from 0 to 200 milli seconds.

The 12 bit A/D converter allows 4096 discrete voltage levels to be expressed digitally. All four sensors were calibrated to give readings between 0 and 10 volts, hence 409.6 digital steps represent one volt. The sampling rate depends on the number of channels monitored simultaneously. If only one channel is scanned the maximum sampling rate is 1499 Hz. This can be significantly increased when system interrupts are disabled. If two or more channels are monitored the maximum sampling rate is obtained by dividing 1499 Hz by the number of channels. In some transient runs the hot film and pressure transducer channels were used together, however, in all other cases only the hot film channel was scanned with a sampling rate of 1000 Hz. During tests in the analogue rig the temperature channel was scanned immediately after all hot film signals were recorded.

The data acquisition system is driven by an IBM XT PC with twin floppy disks. The software installed is described in the following paragraphs.

Software

The software supplied with the data acquisition and control adapter includes a number of subroutine functions that may be called from the application program. The functions can be used with different languages, the data acquisition program used in this study is written in interpreted BASICA. It was developed by White [91] and subsequently modified by Gan [23] who provides a complete program listing. Functions are called to perform tasks such as setting the state of a bit in the binary input port of a particular channel and specifying the range of channels to be scanned during sampling. The application program is menu driven. It permits data acquisition parameters such as sampling rate, number of samples and channels, sensor temperature and reference temperature to be specified. It is also used to access submenus pertaining to probe calibration and data sampling in the analogue rig. During calibration tests the bridge voltage is corrected for water temperature deviations from a specified reference temperature using the following relationship:

$$E_b = E_b' \left(\frac{T_s - T_{ref}}{T_s - T} \right)^{1/2} \qquad (6.17)$$

where E_b' is the bridge voltage, T_s the sensor temperature, T_{ref} a reference temperature and T the water temperature. Deviations up to two degrees C did occur, particularly at low velocities, since water supply for the calibration rig is directly from the mains. Data from tests in both the calibration rig and the analogue model may be displayed graphically on the screen or written to floppy disk.

6.5 Undeflected Steady State Jet

Experimental results are presented for a single steady state jet issuing into the quiescent combustion chamber model. Measurements were taken both with a pitot tube and a hot film probe. The main purpose of the pitot measurements was to validate mean velocities

obtained from the hot film probe at several radial positions on the jet centreline. A comparison between pitot and hot film results is shown in figure 6.17. Also shown are experimental results for a free jet reported by Wygnanski et al [92] and Witze [47]. In the present investigation the jet does not exhibit a potential core due to the small nozzle length / diameter ratio of 1.6. Wygnanski's and Witze's velocity decay data in figure 6.17 is hence shown without the core reported in their studies. The favourable agreement inspired confidence in the hot film's ability to measure mean velocities in the main part of the jet with a good degree of accuracy. Some ambiguity remained as regards the flow direction at low velocities outside the jet boundary (section 6.3). Moreover, no definite statement can be made about the accuracy of kinetic energy and turbulence intensity measurements. At relatively high mean velocities the limiting factor is the sampling rate of 1000 Hz, although this rate is considered to be sufficient in view of the low frequency scale associated with water flows. At low velocities kinetic energy and turbulence intensity may be affected by the ambiguous mean velocity data.

Measurements were taken in the horizontal plane bisecting the nozzle exit at five radial positions: r = 75 mm, 119 mm, 164 mm, 208 mm and 253 mm. The corresponding nondimensional distances from the nozzle exit are r/D = 11, 20, 29, 38 and 47, were D is the side length of the square nozzle hole. The grid in figure 6.18 shows the angular positions at which measurements were taken at each of the five radii, viz. around the jet centreline from - 5° to + 5° in 1° intervals and up until - 65° and + 90° in 5° intervals. Hence profiles were obtained of radial and tangential mean velocity, kinetic energy, and radial and tangential turbulence intensity. Experimental results are presented in profile form throughout this chapter. Different, mainly nondimensional forms of presenting experimental data are used in chapters seven and eight for comparisons with computational predictions.

Radial and tangential mean velocity profiles in figure 6.19 show a fairly symmetric characteristic with respect to the jet centreline at 0° . The five radial velocity peak values are also shown in figure 6.17, indicating good agreement for the centreline velocity

decay with data for free axisymmetric jets reported in the literature. The jet's edge cannot be easily identified; its halfwidth is therefore taken as an indication of the rate of spread. Halfwidths inferred from figure 6.19 and based on 1 % of the centreline velocity are used in chapter seven (figure 7.5) for comparisons with predicted rates of spread. The halfwidth growth is a reflection of the fuller profile shape with increasing radius in figure 6.19. The tangential velocity reaches a significant level near the jet centreline and decays radially more slowly than the radial velocity. The sign change at the centreline where fluid leaves the jet to either side is not detected by the data analysis method. A slight velocity dip at the centreline is discernible in the tangential profiles at r/D = 20 and 38. It is also recalled that measurements of low mean velocities cannot be entirely relied on. The tangential mean velocity U at the jet centreline should be zero. In the present case this may not have been recorded since |U| is calculated and small fluctuating velocities around 0 m/s yield some small positive value.

Fluctuating velocity components are shown as kinetic energy profiles and turbulence intensity profiles in figures 6.20 and 6.21 respectively. The profiles are calculated from equations (6.14) to (6.16). The kinetic energy profiles are seen to be symmetric about the jet centreline and to decay with radial distance from the nozzle. Significant kinetic energy levels are only observed inside the jet boundary, outside the jet fluctuations reduce to an insignificant level. The centreline kinetic energy decay is compared with model predictions in chapter seven (figures 7.6 and 7.32). In a different form of presenting turbulence information, fluctuating components are normalized with the local velocity (figure 6.21). Radial and tangential components are calculated separately, however, they are normalized with the same local velocity. This allows direct comparisons to be made between radial and tangential fluctuations. Within the jet envelope both exhibit a similar behaviour, viz. turbulence intensity reaches a minimum at the centreline and peaks on either side at the jet edge. The minimum at the centreline is caused by the relatively large mean velocities appearing in the denominator in equations (6.15) and (6.16). Towards the shear layer at the jet

boundary turbulence activity is high but mean velocities are decreasing rapidly, hence causing a peak in turbulence intensity. Within the jet, tangential fluctuations are consistently lower than radial fluctuations. It is also interesting to note that the overall level of turbulence intensity remains fairly constant at the five radii, indicating that fluctuating velocities and mean velocities decay at a similar rate. Outside the jet boundary turbulence intensity data must be viewed with caution since both mean and fluctuating velocities are very low (figures 6.19 and 6.20).

6.6 Undeflected Transient Jet

The temporal evolution of the undeflected transient jet was examined. Aspects of the test facility associated with impulsive injections have been described in sections 6.2 and 6.4, in the present section results are presented in the form of velocity profiles at the five radial positions. In addition, results for the jet penetration rate are given. The injection lasts 2.8 seconds while data was sampled over a period of four seconds. Using a sampling rate of 1000 Hz, one instantaneous velocity value represents one ms. A selection of discrete time steps had to be made to capture the temporal flow development. Near the nozzle exit profiles are plotted at 20 ms intervals for the first 100 ms, these intervals become larger as the jet approaches steady state conditions. With increasing radius the jet slows down and time intervals could be increased. Data samples around each time step were taken until halfway to the adjacent time step, e.g. for t = 40 ms samples from 30 ms to 50 ms were considered. This policy represents a compromise between reasonable accuracy by averaging over a sufficient number of data points on the one hand and maintaining the instantaneous nature of the individual time steps on the other hand. Clearly, in this application a higher sampling rate would have allowed more data to be taken into account and hence improved accuracy. As described in section 6.4 limitations of the A/D converter and computer memory restricted the sampling rate.

The temporal evolution of radial and tangential velocities at the five radial locations is depicted in figures 6.22 to 6.26. Figure 6.26 illustrates the development closest to the nozzle at r/D = 11. In most profiles the jet appears to be symmetric with respect to the centreline. Initially, the radial velocity at the centreline can be seen to increase fairly rapidly while the jet gradually develops a fuller and more pointed profile. In particular, the irregular structure at the jet tip diminishes with time. At t = 1.50 s the radial velocity has nearly reached its steady state profile. Further into the domain the jet tip shows a similar irregular structure (figures 6.23 to 6.26) which gradually develops into a rounder profile, however, 1.50 s does not appear to be sufficient for the profiles to reach their corresponding steady state shapes. At r/D = 29, 38 and 47 they are still distinctly uneven. No particular information can be gained from the development of tangential velocities. They follow the same tendency as radial velocities in that they are initially very irregular and become gradually smoother and more even.

Of particular interest for the Diesel engine application is the rate at which the jet penetrates its quiescent surroundings. From the irregular profile shapes it is apparent that the point where the radial velocity first reaches its steady state value is difficult to identify. For this reason Kuo and Bracco [26] suggested to define the jet tip arrival time as the time where the centreline velocity reaches 70 % of its steady state value. Even this point is not easily identified, particularly close to the nozzle, as the irregular tip structure itself is not repeatable. Thus, considerable velocity variations occur on the jet centreline in the early stages of the jet development. To still get some indication of the penetration rate, six repeats of an injection were conducted at each radius. Figure 6.27 illustrates 'raw' data of typical examples for each radius, viz. bridge voltage variations with time for two signals: pressure transducer and hot film probe output. The lower curve represents the pressure transducer signal recorded during injection. Injection starts after an adjustable delay period (here set to 100 ms) which ensures a repeatable start of injection (section 6.4). The jet is considered to leave the nozzle when the pressure signal peaks as indicated in figure 6.27 by the short vertical line. The pressure

signal can be seen to be nearly constant during injection, suggesting a constant inlet velocity. The second curve represents the hot film probe output signal. A mean velocity line and a 70 % line are also shown. The 70 % line was inferred from the zero degree calibration curve and represents 70 % of the centreline velocity corresponding to the 100 % voltage line shown. The point of intersection between the 70 % line and hot film voltage defines the arrival time. The range of penetration times obtained during the six repeats at each radius are shown in nondimensional form together with computational results and experimental data reported in the literature in figure 7.42. In figure 6.27 it is interesting to note the change of the hot film signal gradient. The noticeably shallower gradient at larger radii indicates a slowing down of the jet.

In closing this section it should be pointed out that there appear to be large areas on both sides of the jet with very little hydrodynamic activity. Outside the jet envelope mean velocities are reduced to an insignificant level and the kinetic energy approaches zero at + 20° and - 20° at all five radii (figure 6.20). Mixing due to convective and turbulence transport appears therefore to be negligible in large parts of the flow domain with obvious implications for the mixing process and combustion performance in the actual engine. To improve mixing swirl should be introduced, and this is discussed in the following sections.

6.7 Deflected Steady State Jet

This section presents results for the steady state injection into a swirling flow field. Before the results are discussed, the swirling flow field itself without injection is examined and general characteristics of a jet in a cross - flow are described.

Swirling Flow Field

The swirling flow field is generated by rotating the inner drum of the cylindrical analogue model at an angular velocity of 50 rpm. The drum bottom and the side wall are rotating while the lid remains stationary. Figure 6.28 shows the tangential velocity variation in radial direction and compares it with the curve for solid body rotation. The measured velocities are seen to be considerably smaller than values corresponding to solid body rotation. The discrepancy is attributed to the stationary lid which gives rise to a velocity gradient in vertical direction. Hence the measured velocities are both smaller in magnitude and nonlinear in their radial variation. A flow field closer to a solid body rotation could have been obtained by either rotating the lid at the same angular velocity as the bottom and the side wall or by substituting the lid with a free surface. For practical reasons these two options were not feasible. With regard to the real engine situation, neither flow field can be assumed to prevail as factors like inlet port and valve geometry are not modelled in the hydraulic analogue. The swirl field in an actual engine might therefore look quite different. Knowledge of this field prior to injection is of great importance in analyzing the mixing process and adjustments to the field may help improve engine performance.

At the start of injection the rotating drum is stopped to simulate stationary cylinder walls. The velocity decay has been measured by Gan [23] who found a fairly rapid initial decay in tangential velocity. The decay is stronger at outer radii, at r/D = 47 he measured a velocity drop of 30 % during the first five seconds.

Description of the Deflected Jet

A number of experimental and computational studies of a circular jet issuing perpendicular into a free stream are reported in the literature, e.g. [24, 27, 46, 76, 93]. A typical flow configuration is investigated in reference [27] and reproduced in figure 6.29. All studies have in common that they examine a round jet issuing into a uniform cross - flow which distinguishes them from the present investigation in two respects:

(i) the present study uses a nozzle with a square cross section and (ii) the cross - flow is nonuniform as shown in figure 6.28. These differences make comparisons with data from the literature difficult, particularly since the ratio of jet to free stream velocity is often used as a parameter when presenting jet trajectories. Despite the differences however, the general characteristics of the deflected jet in a uniform cross - flow also apply to the present case and are therefore briefly described below.

Figure 6.30 from reference [94] defines the jet boundaries, the axis of maximum velocity, the jet centreline, and three distinct zones along the jet axis. In the vicinity of the nozzle turbulent mixing in the jet boundary causes a momentum transfer from the jet to the free stream. The outer part of the jet is hence easily distorted and gradually acquires a kidney shape. Figure 6.31 from reference [18] illustrates the progressive development of kidney shaped cross sections along the jet axis. Initially there remains a central part of the cross section where little mixing occurs, however this area decreases in size and disappears at the end of the potential core. The kidney shaped cross section develops into a pair of counter - rotating vortices which continue to grow in size with increasing distance along the jet axis. In the vortex zone (figure 6.30) the angular velocity of the vortices starts to decrease.

It should be noted that the axis of maximum velocity in figure 6.30 does not coincide with the jet centreline but lies closer to the upstream boundary. Hence the velocity gradient on the outer side of the jet is steeper than towards the inner boundary.

Results for the Steady State Deflected Jet

Results for the steady state injection into the swirling flow field are discussed with reference to figures 6.32 to 6.35. The experimental mesh shown in figure 6.18 was modified to capture the deflected jet axis. Thus the sector with one degree intervals was applied between 0° and $+ 10^\circ$ at the inner two radii, between $+ 10^\circ$ and $+ 20^\circ$ at r/D = 29, between $+ 15^\circ$ and $+ 25^\circ$ at r/D = 38, and between $+ 20^\circ$ and $+ 30^\circ$ at r/D = 47. Radial and tangential mean velocity profiles at r/D = 11, 20, 29, 38 and 47

are illustrated in figure 6.32. The radial velocities can be seen to decrease in radial direction at a faster rate than the corresponding radial velocities for the steady undeflected jet shown in figure 6.19. This is particularly noticeable at the outer three radii, indicating that the jet becomes strongly deflected from r/D = 20 onwards. Two complementary effects cause the fairly strong and sudden deflection. On the one hand the jet imparts its radial momentum to the surrounding fluid and decelerates considerably, on the other hand the tangential velocity of the swirl field increases in radial direction (figure 6.28). The combined effect of this momentum transfer in radial direction (from jet to ambient fluid) and tangential direction (from ambient fluid to jet) causes the jet to be deflected. The jet axis defined as the locus of maximum radial velocity is shown in figure 6.35 as a solid line. It is evident that the jet axis becomes strongly deflected midway into the domain and does not reach the cylinder wall. At r/D = 47 the radial velocity has decayed to 0.2 m/s and the jet does not have sufficient radial momentum to penetrate further. Hence the jet trajectory approaches asymptotically a line of constant radius at approximately r/D = 47.

Also shown in figure 6.32 are profiles of the mean tangential velocity. Outside the jet envelope on the upstream side the measured velocities at the inner three radii agree well with those shown on figure 6.28 for pure swirl without injection, however, at the outer two radii the measured velocities in the presence of the jet are 0.37 and 0.54 m/s respectively, compared with 0.45 and 0.70 m/s in the case of pure swirl. This velocity difference suggests that tangential momentum is transferred to the jet, thus causing the deflection. Within the jet envelope and downstream the limitations in the data analysis method in clearly identifying the flow direction obscure the results. At the inner radii a negative tangential velocity would be expected as a result of entrainment into the jet. It is therefore suggested that at r/D = 11, 20 and 29 the mirror image with respect to the zero velocity line should be taken for the tangential velocity following the peak near the jet axis. At the outer radii the tangential velocity sign is less ambiguous and follows the expected pattern.

The radial velocity profile in figure 6.32 can be seen to widen with increasing radius, a feature that is also observed in the kinetic energy and turbulence intensity profiles. The locus of maximum kinetic energy in figure 6.33 coincides with the maximum radial velocity and is hence also represented by the solid line in figure 6.35. As pointed out in the previous paragraph the jet axis is distinctly different from the jet centreline; the latter is taken to be midway between the two jet boundaries upstream and downstream (figure 6.30). These boundaries are not easily identified from the velocity and kinetic energy profiles. Some indication as to where they are located can however be obtained from examining the turbulence intensity profiles in figure 6.34. The fluctuating components are normalized with the local mean velocity, yielding high turbulence intensities where there is turbulence activity combined with low mean velocities. This situation is found in the jet's shear layer and is indicated by a turbulence intensity peak at the upstream boundary. The upstream boundary is fairly well defined in figure 6.34 and shown by a dashed line upstream of the jet axis in figure 6.35. Matters stand differently with regard to the downstream, or inner, boundary. The turbulence intensity profiles decay gradually downstream of the jet axis in an irregular manner. In figure 6.35 an attempt was made to locate the downstream boundary at r/D = 11, 20 and 29. At the inner two radii the fairly clear peak in tangential turbulence intensity was taken to represent the boundary, while at r/D = 29 the marked drop in both radial and tangential turbulence intensity at approximately 60° was used as an indication for the inner jet boundary. It is apparent from figure 6.34 that there is no clearly defined downstream boundary, but rather an extensive wake region as a consequence of the jet obstructing the swirling flow field.

The location of the jet axis in figure 6.35 is very close to the upstream boundary, resulting in a steeper velocity gradient towards the outer boundary than is observed downstream of the jet axis. The large velocity gradient in the thin outer boundary causes a strong shear flow and thus high levels of turbulence intensity. Conversely, smaller

velocity gradients in the wake region induce less turbulence as is illustrated in figure 6.34.

6.8 Deflected Transient Jet

The impulsive injection into a swirling flow field is discussed with reference to figures 6.36 to 6.46. The angular velocity of the swirl field is 50 rpm as in the case of the steady state injection. The time steps considered are: 0.04, 0.08, 0.16, 0.22 and 0.3 seconds. Figure 6.36 shows a comparison between the deflected jet axis and boundaries of the impulsive injection after 0.3 seconds and the steady state injection. The remaining figures are considered in two groups: figures 6.37 to 6.41 illustrate the temporal development of radial and tangential mean velocities at r/D = 11, 20, 29, 38 and 47, while figures 6.42 to 6.46 show profiles of the development of radial and tangential turbulence intensities at the same radial locations.

The radial mean velocities illustrate how the jet profiles gradually approach their steady state shape shown in figure 6.32. It is evident from the irregular profiles at all radii that the jet is still in an unstable state after 0.3 seconds. Although the maximum velocities at the inner two radii are reached after 0.04 seconds the profiles remain uneven, particularly at the downstream side. From theoretical considerations it is known that the outer part of the jet is being distorted and swept around the jet by the crossflow, forming a kidney shaped cross section (figure 6.31). This action may account for the irregular velocity profiles in the early stages of the jet development. With increasing radius the arrival of the jet tip is observed, again displaying very uneven profiles at the downstream side indicating the effect of the cross flow on the jet tip. The locus of the maximum radial velocity defining the jet axis at 0.3 seconds is shown in figure 6.36 together with the steady state equivalent. It is apparent that the impulsive jet has not yet been deflected as far as the steady state jet, hence not all tangential momentum has been

imparted to the jet. Also shown in figure 6.36 is the upstream boundary after 0.3 seconds which was inferred from turbulence intensity data. The location of the downstream boundary is more ambiguous, it is however evident from a comparison between steady state (figure 6.32) and transient (figures 6.37 to 6.41) velocity profiles that the transient profiles are narrower, particularly on the downstream side. This suggests that the flow field in the wake region of the jet is still developing and the recirculation zone not yet fully established. Figure 6.36 also illustrates that the distance between jet axis and outer boundary remains nearly constant in radial direction for the steady state jet, while it increases considerably in the impulsive case. At the outer radii the jet tip is strongly deflected after 0.3 seconds with an extensive region of high turbulence activity surrounding it. This may be taken as another indication of the distorted outer part of the jet developing into a kidney shaped cross section.

Together with radial velocity profiles, figures 6.37 to 6.41 show angular distributions of the tangential velocity. Upstream of the jet between - 20° and - 60° tangential velocities are very similar to their steady state equivalents (figure 6.32) and do not appear to be affected by the injection. At the inner two radii the tangential velocity increases towards the centreline reflecting fluid being entrained into the jet. As in the steady state case the sign change at the centreline is not detected by the data analysis method. The tangential velocity in the vicinity of the nozzle on its downstream side would be expected to be negative, i.e. directed towards the centreline. A dip in tangential velocity at 0° is observed at most time steps. Further into the domain the jet arrival can also be noted from the tangential velocity profiles. In particular, at r/D = 47 the jet is seen to arrive approximately 0.16 seconds after begin of injection. The arrival is followed by a marked drop in tangential velocity immediately downstream of the jet axis, indicating a transfer of tangential momentum from ambient fluid to the jet, causing the deflection.

The temporal development of turbulence intensity profiles is illustrated in figures 6.42 to 6.46. At all five radii the profiles at t = 0.3 seconds are not as fully developed as

their steady state counterparts (figure 6.34). While a consistent rise corresponding to the outer boundary is evident in most profiles, the shape around the jet axis is very irregular, indicating strong mixing during penetration. Initially the profiles are very narrow and can be seen to widen as time progresses. The main growth occurs on the downstream side as a consequence of the outer part of the jet being distorted and swept around. This is best observed at the outer two radii which show the development from the jet tip arrival onwards. Compared with the steady state profiles (figure 6.34) it is interesting to note that downstream of the jet the turbulence intensity drops to zero at approximately + 40° at the inner four radii and at + 55° at the outer radius. No extensive wake region has as yet been formed, suggesting that no turbulence induced mixing occurs in this angular range. For smaller time steps (e.g. 0.08 seconds) the angular range with turbulence activity is significantly smaller. Using the scale relationships on which the hydraulic analogue model is based (section 6.2), 0.08 seconds corresponds to 6.4° crank angle at an engine speed of 2000 rpm. In the introduction to this thesis a typical heat release diagram (figure 1.10) was discussed. The ignition delay period between start of injection and combustion lasts approximately 10° crank angle, corresponding to an injection period of 0.125 seconds in the present application. The figures discussed in this section show that after 0.125 seconds higher turbulence intensities downstream of the jet, particularly at the inner radii, would be desirable. In a multi hole nozzle the angular distribution of turbulence intensities and radial mean velocities can provide valuable input when determining design parameters such as number of nozzle holes, direction of injection and injection pressure characteristics.

6.9 Concluding Remarks

An experimental study has been described concerning the mixing of a steady state and impulsive jet issuing into a quiescent and a swirling flow field. The background of the

hydraulic analogy has been given together with an account of the advantages and limitations of this technique. The test facility has been described in some detail. The description includes the scale relationships between engine and analogue model and an account of calibration methods used for all sensors. Particular attention was given to the calibration of the hot film probe used for velocity measurements. The data analysis technique has been detailed and its limitations at low mean velocities were outlined.

Results were presented as profiles of mean velocities, kinetic energy and turbulence intensities for the four flow configurations under investigation. The undeflected steady state jet was compared with data reported in the literature and agreement of centreline velocity decay and rate of spread was found to be good. The jet's shear layer could be identified from turbulence intensity data, outside the jet envelope turbulence activity was found to be very low. The temporal development of the undeflected jet was examined for impulsive injections. The jet tip penetration was measured for comparisons with numerical predictions (chapter 7) and data reported in the literature. For the steady state injection into a swirling flow field the deflected jet axis and boundaries were inferred from velocity and turbulence intensity profiles. The jet was seen to be deflected strongly midway into the domain and not to reach the cylinder wall. The velocity gradient in the outer boundary was found to be steep compared with a gradual velocity decay downstream of the jet axis. Analyzing the impulsive injection into a swirling flow field it was shown that the jet is not deflected as much as in the steady state case. The effect of the cross flow on the penetration of the jet tip could be seen from the velocity and turbulence intensity profiles. Indications of the developing kidney shaped jet cross section were observed.

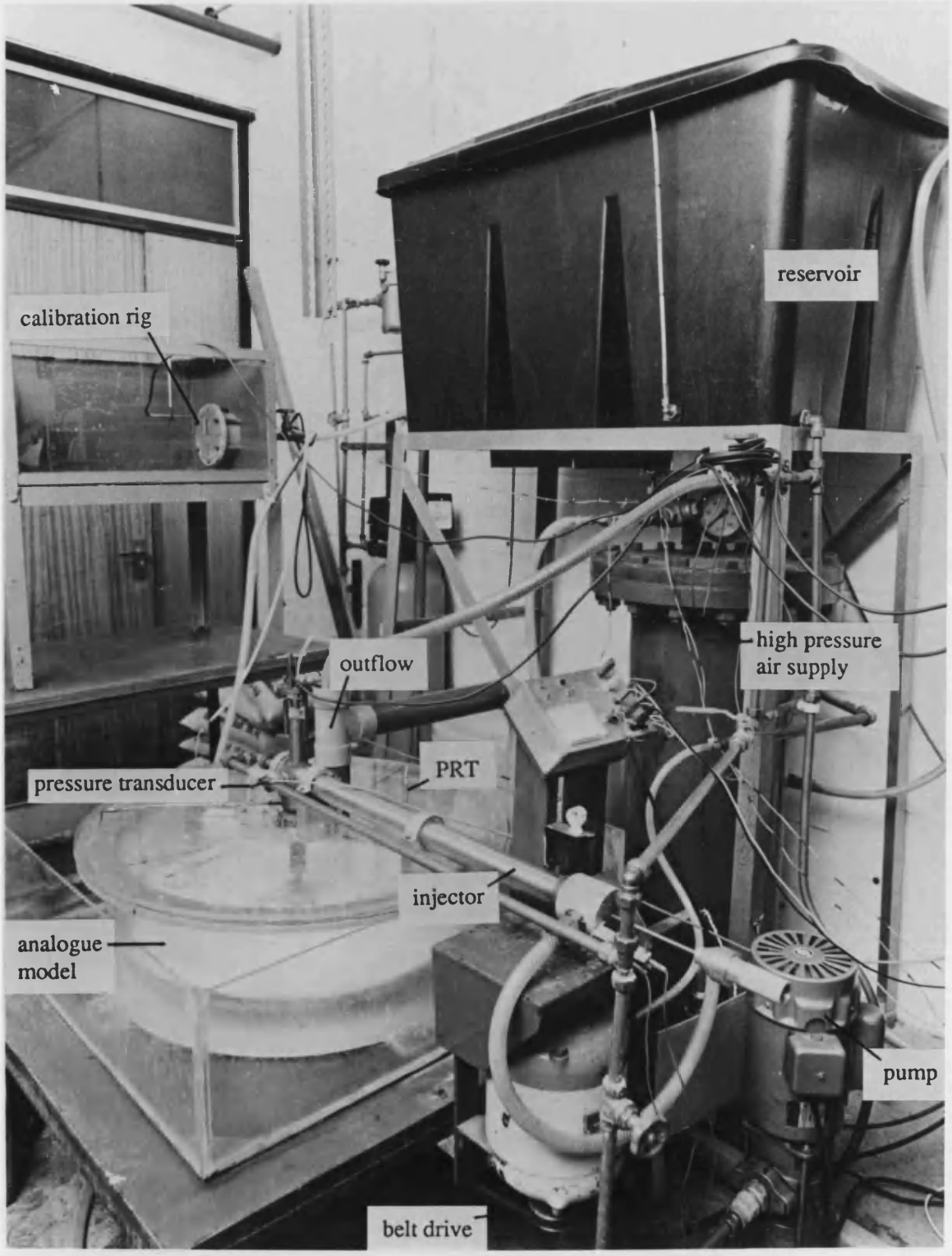

Fig. 6.1: Hydraulic analogue test facility

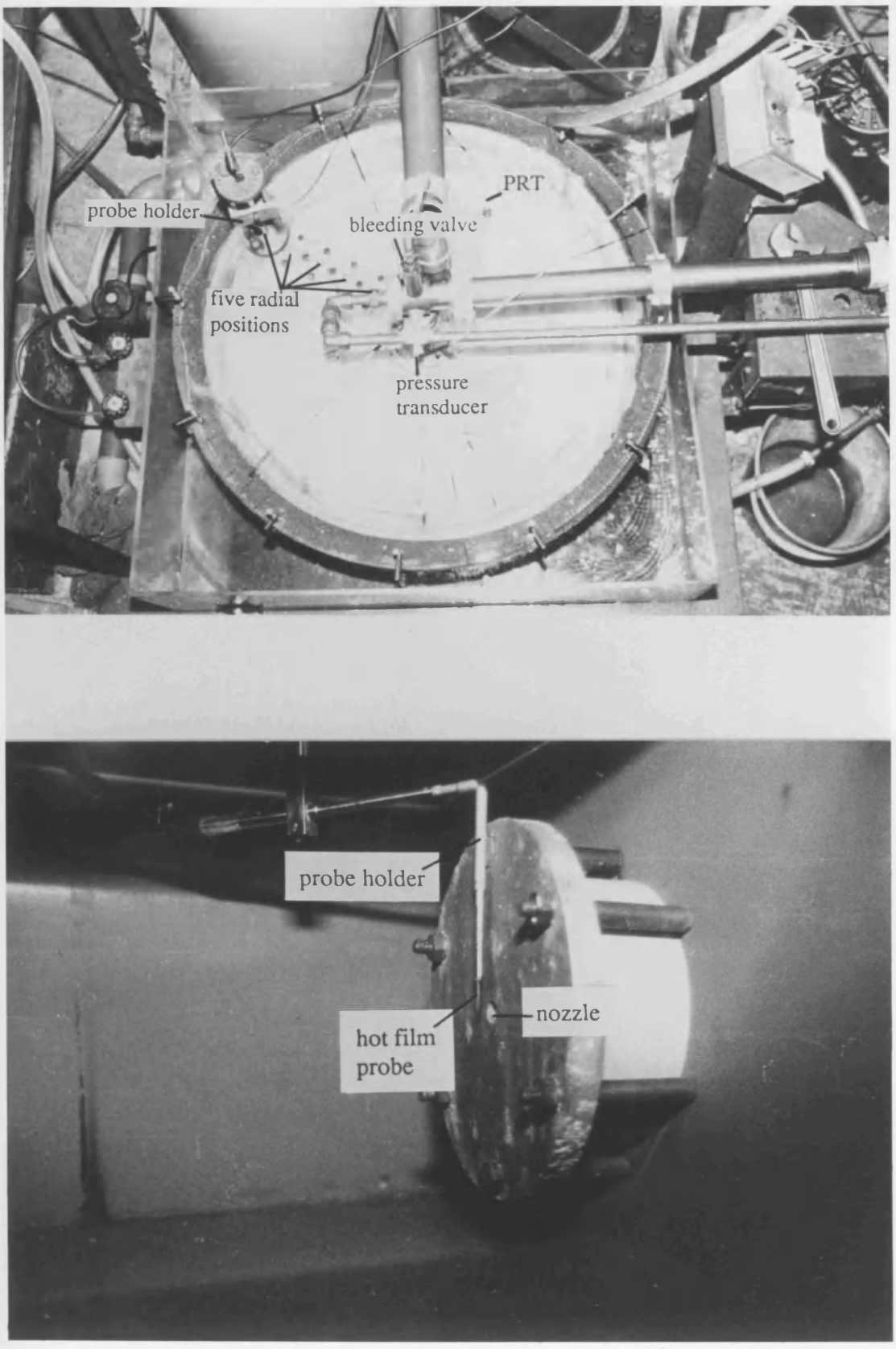

Fig. 6.2: a) top view of analogue model, b) calibration rig

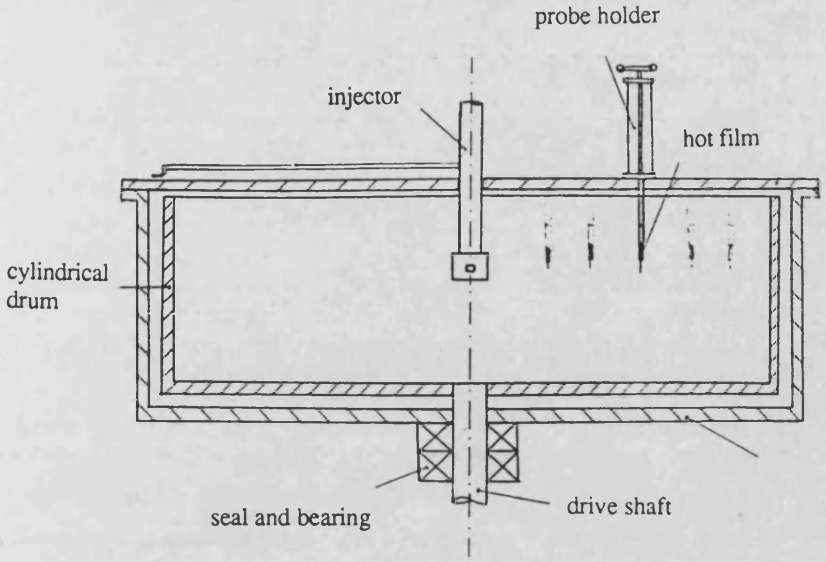

Fig. 6.3: Cross section of combustion chamber model with probe positions

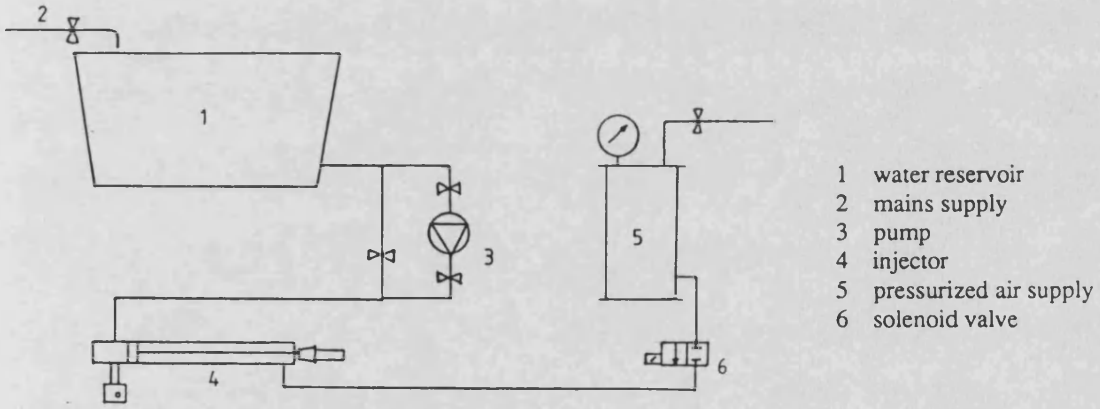

Fig. 6.4: Schematic diagram of water injection system

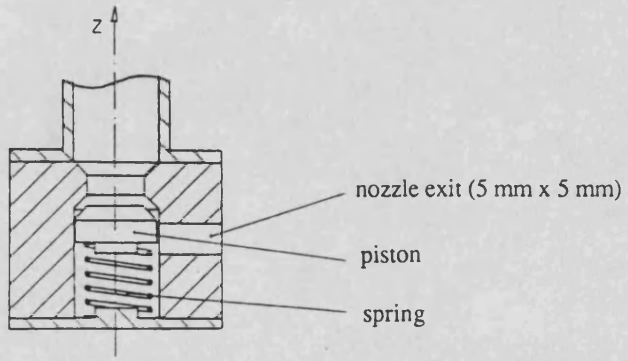

Fig. 6.5: Cross section of injection nozzle

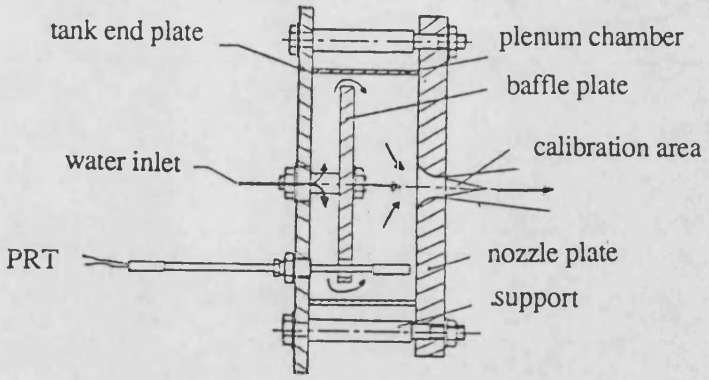

Fig. 6.6: Cross section of calibration nozzle chamber

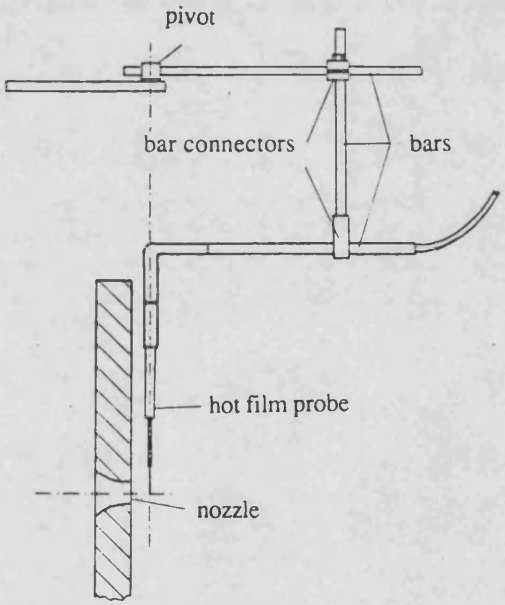

Fig. 6.7: Calibration tank probe holder in position with probe in front of nozzle exit

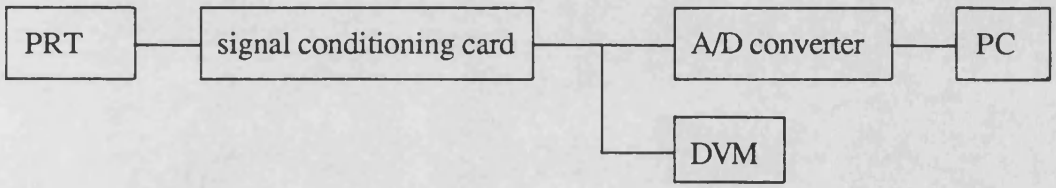

Fig. 6.8: Temperature measurement

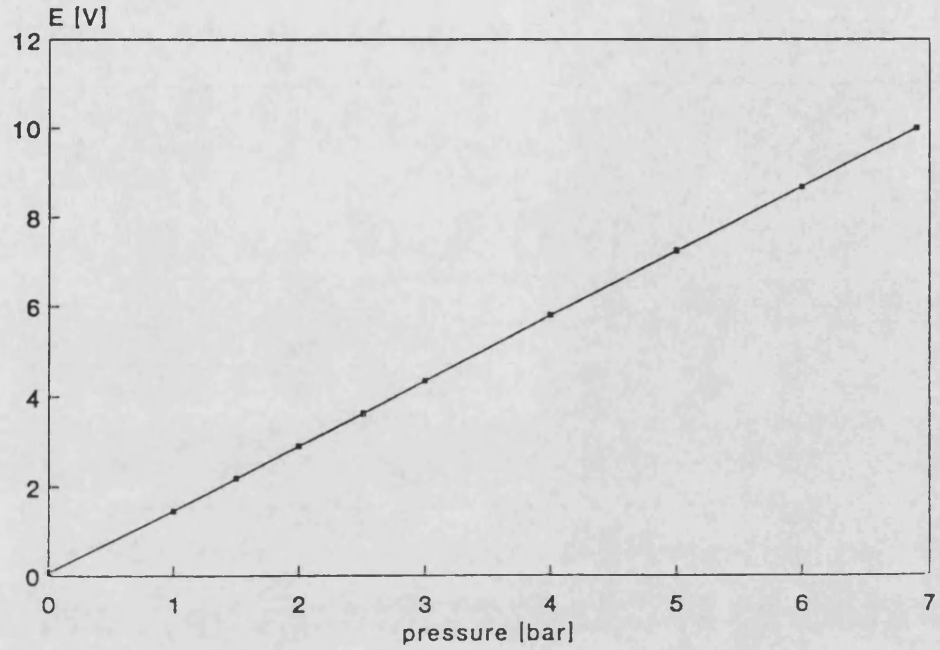

Fig. 6.9: calibration of pressure transducer

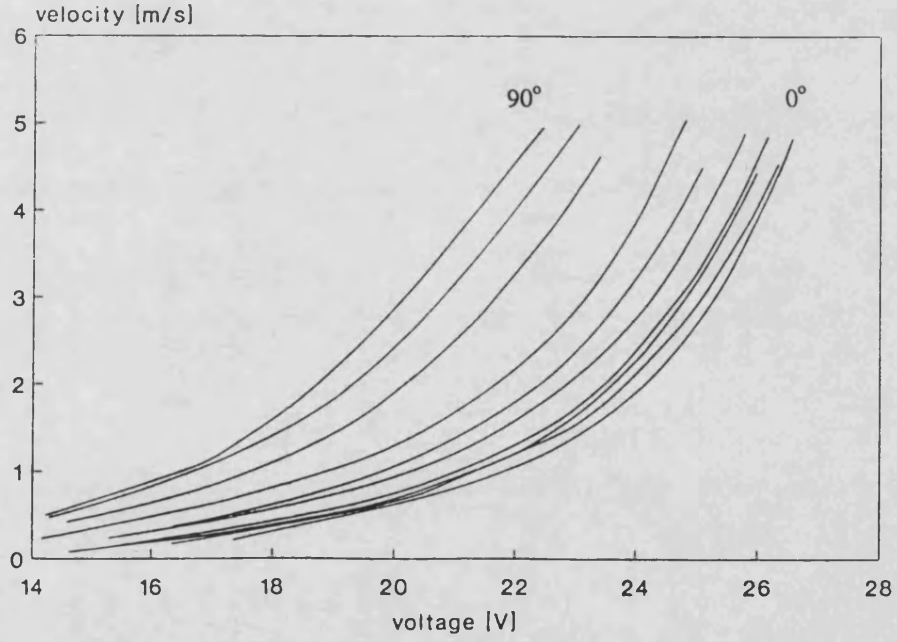

Fig. 6.10: Calibration curves for hot fim probe, $0° < \beta < 90°$

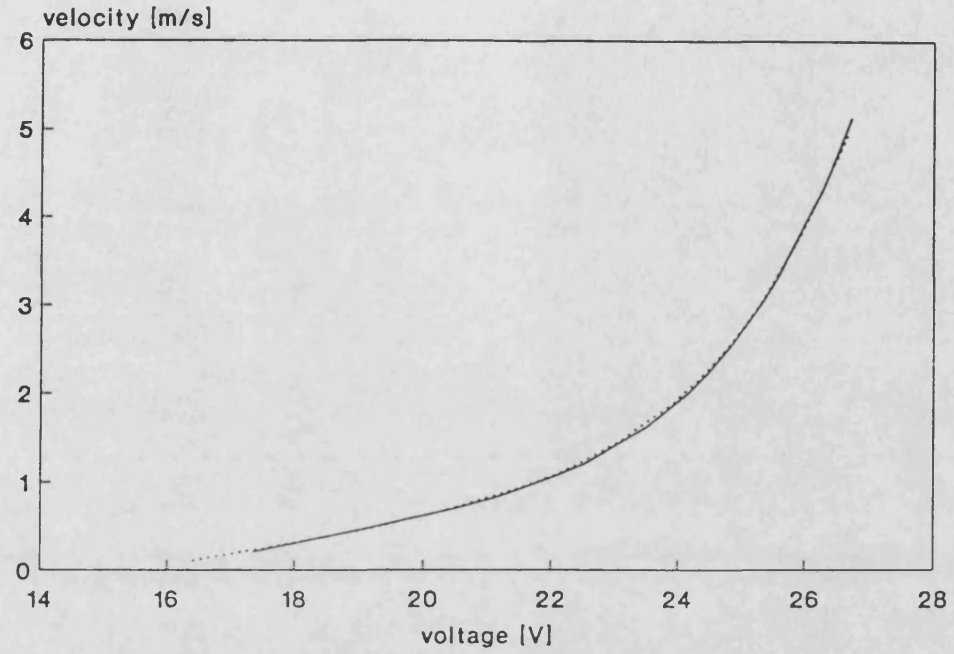

Fig. 6.11: comparison of two zero degree calibration curves

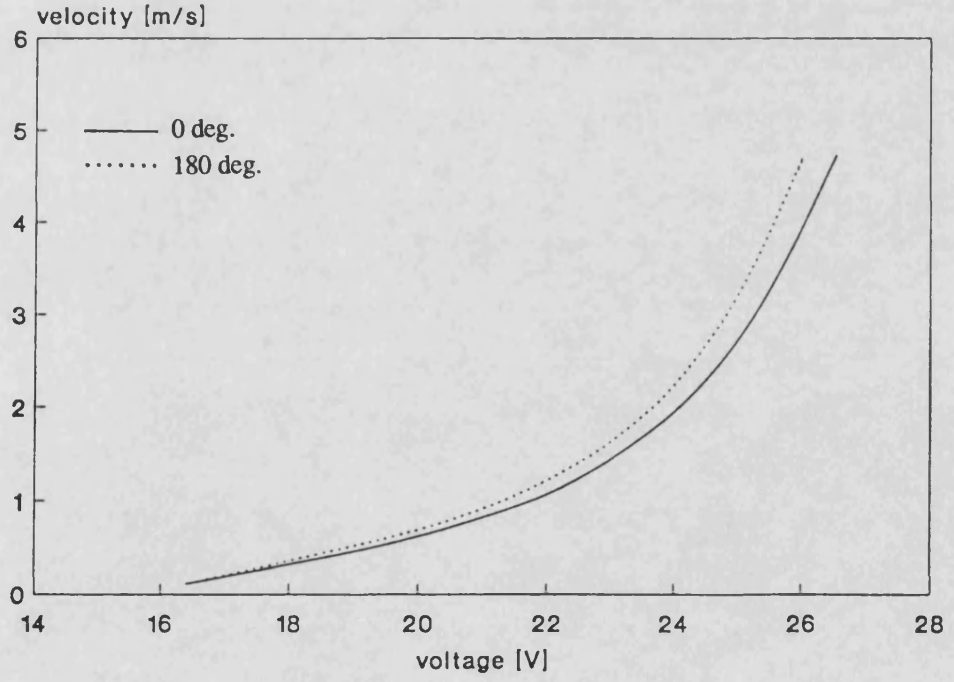

Fig. 6.12: calibration at 0 and 180 deg.

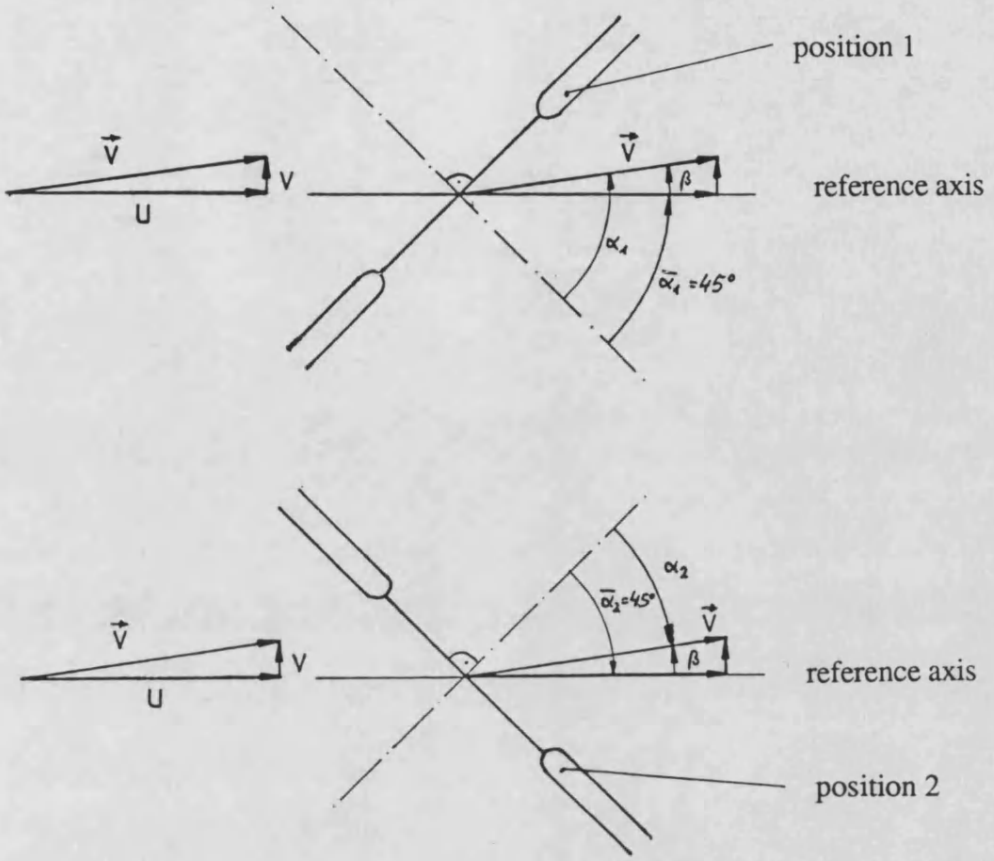

Fig. 6.13: Velocity - angle relationships for hot film probe in radial and tangential position

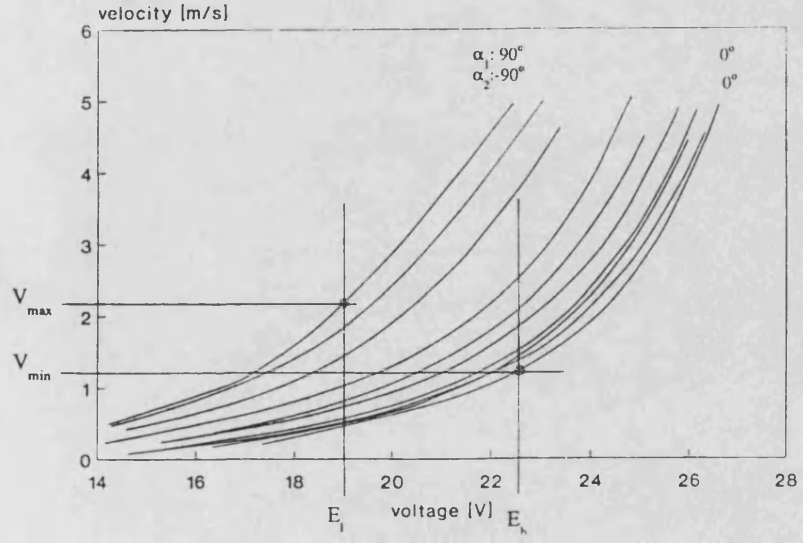

Fig. 6.14: Inference of velocity magnitude and direction from calibration curves and bridge output

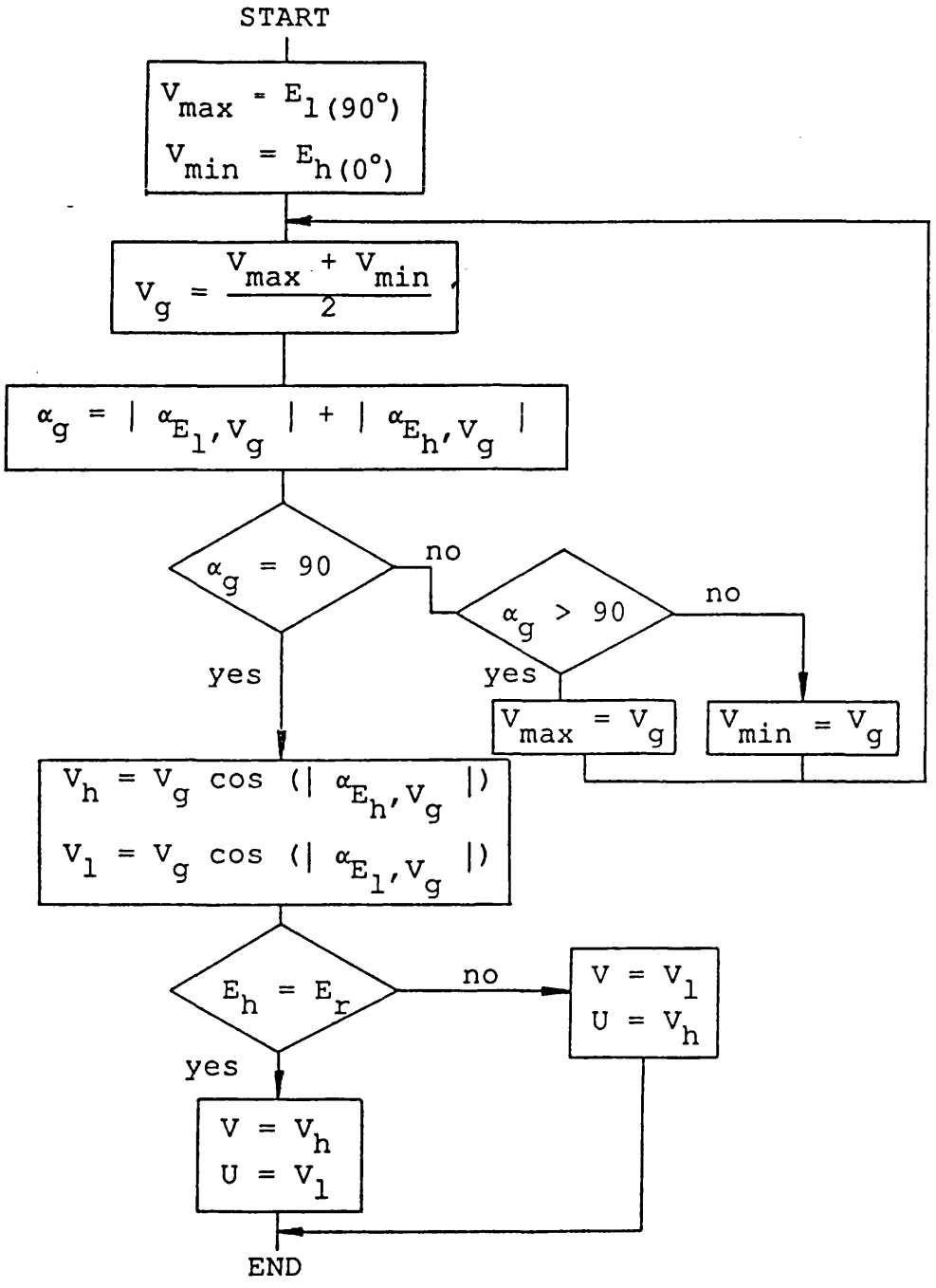

Fig. 6.15: Flow chart of data analysis program

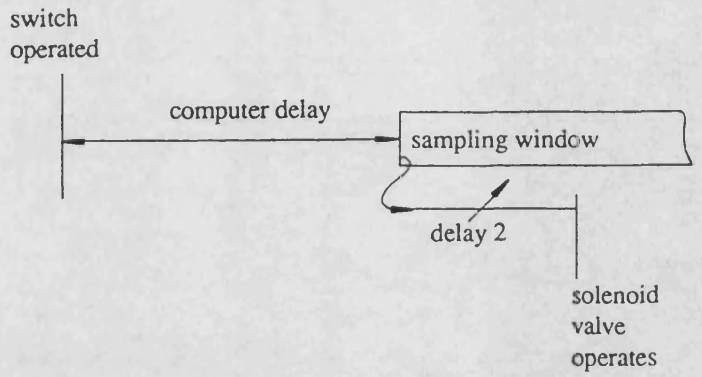

Fig. 6.16: Data acquisition layout for transient measurements

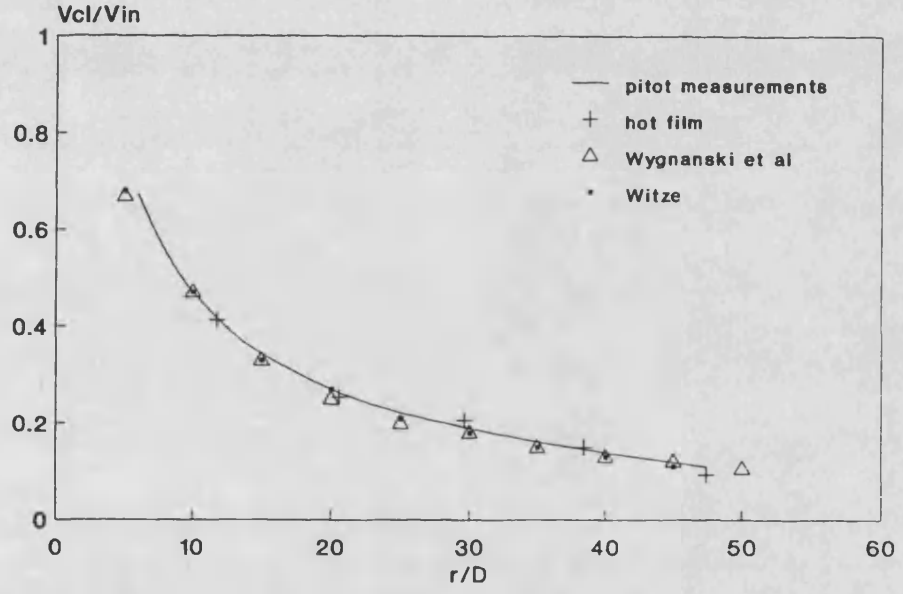

Fig. 6.17: centreline velocity decay, comparison between pitot and hot film measurements, and literature data

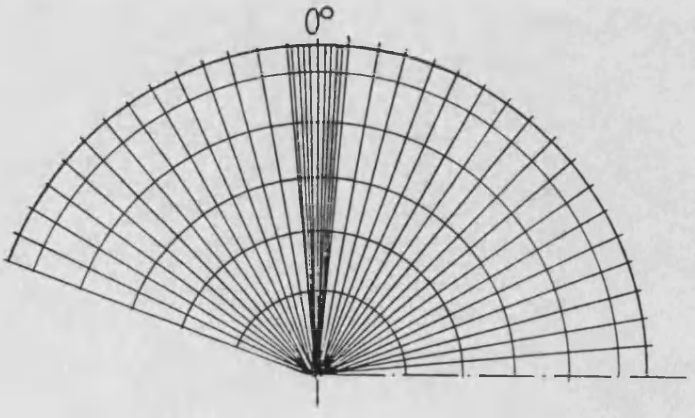

Fig. 6.18: Experimental mesh

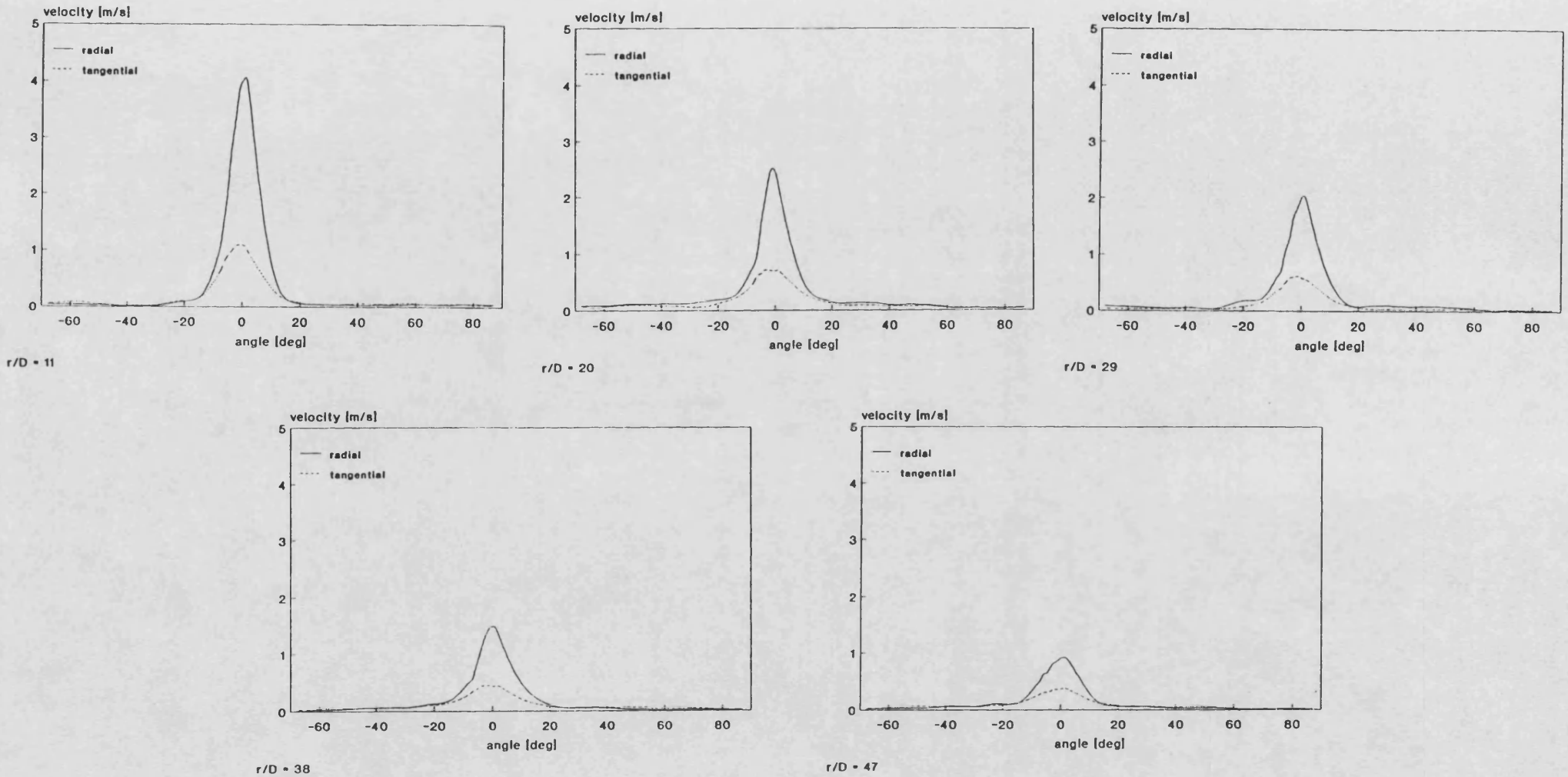

Fig. 6.19: radial and tangential mean velocity profiles at r/D = 11, 20, 29, 38 and 47

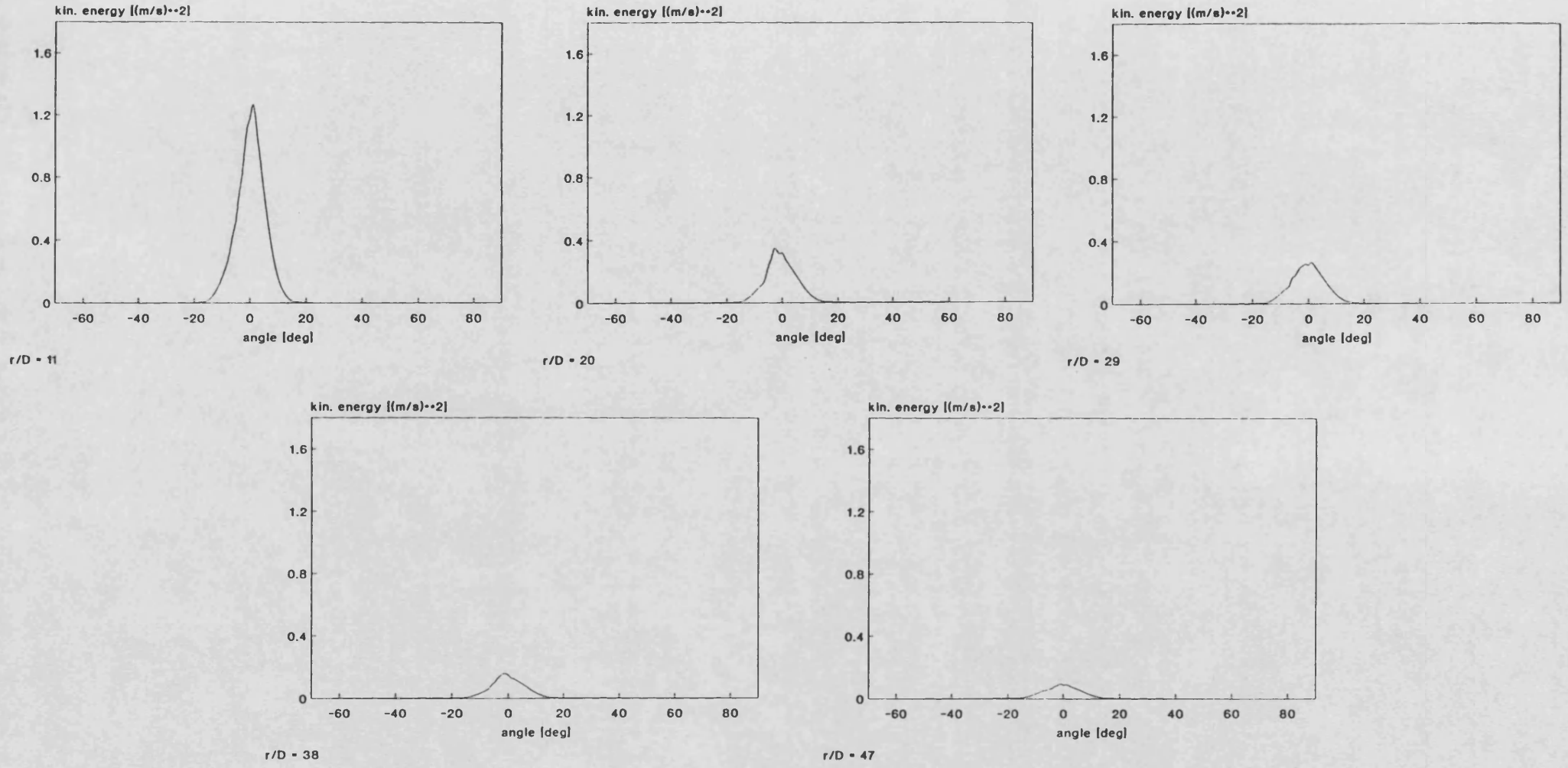

Fig. 6.20: kinetic energy profiles at r/D = 11, 20, 29, 38 and 47

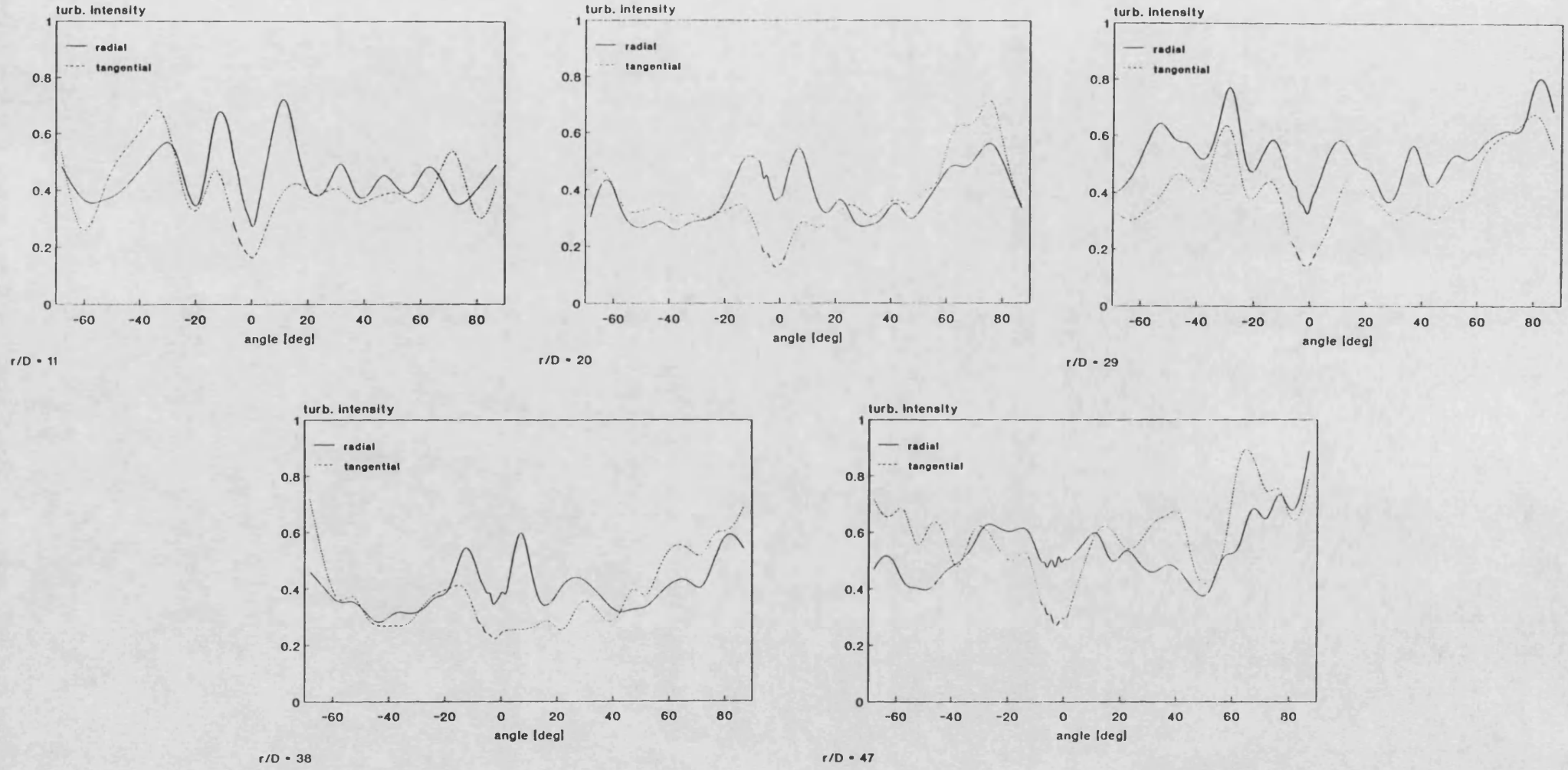

Fig. 6.21: radial and tangential turbulence intensity profiles at r/D = 11, 20, 29, 38 and 47

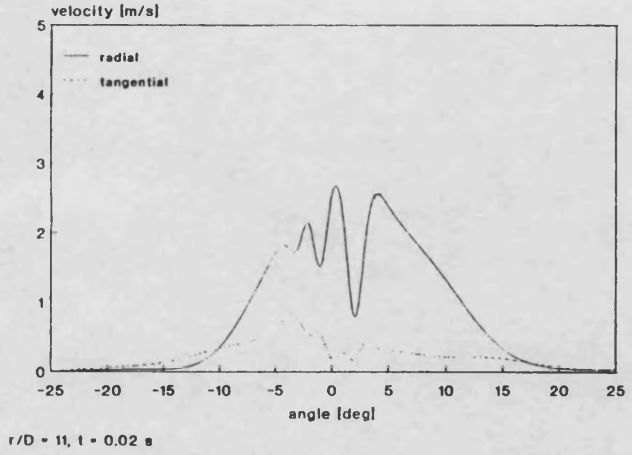

r/D = 11, t = 0.02 s

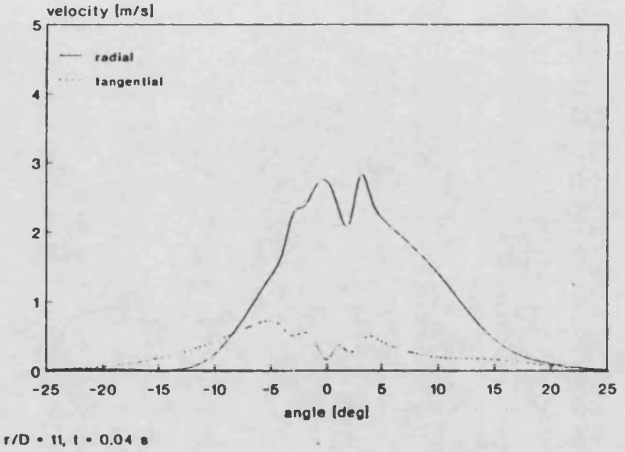

r/D = 11, t = 0.04 s

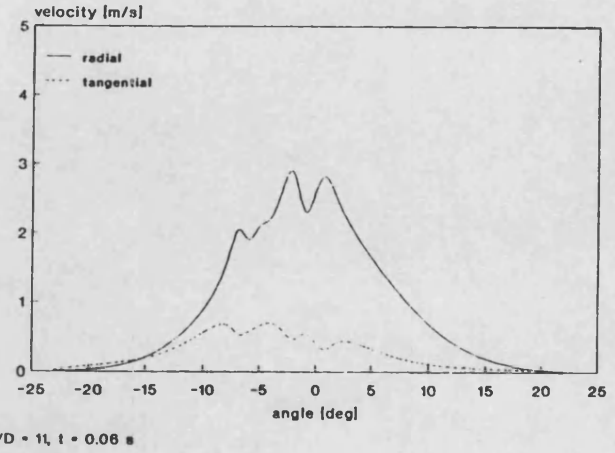

r/D = 11, t = 0.06 s

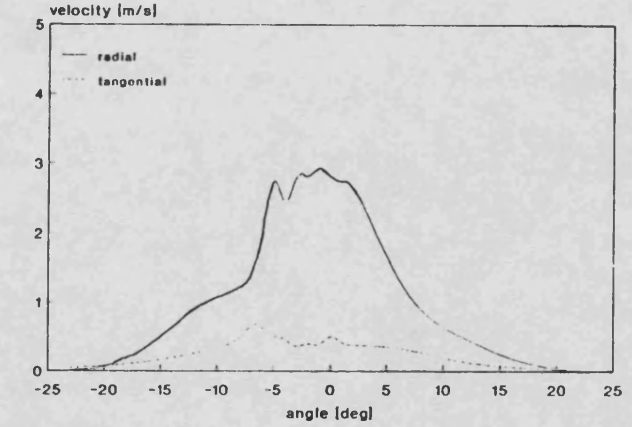

r/D = 11, t = 0.08 s

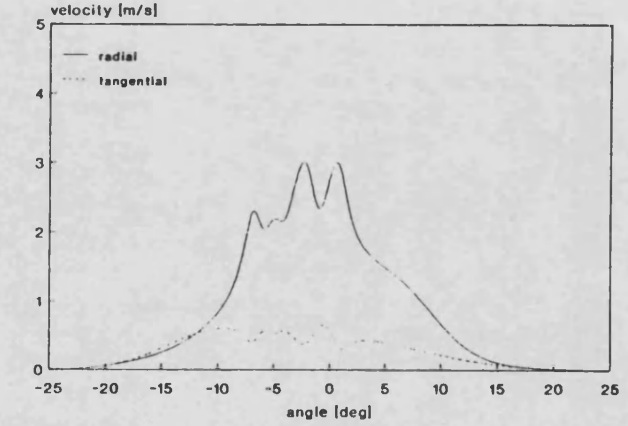

r/D = 11, t = 0.10 s

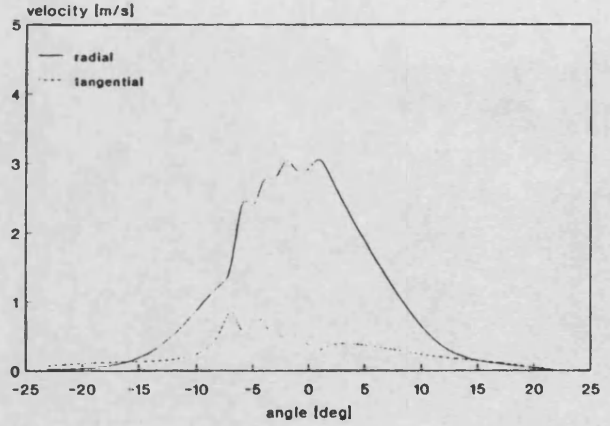

r/D = 11, t = 0.16 s

Fig. 6.22 cont.

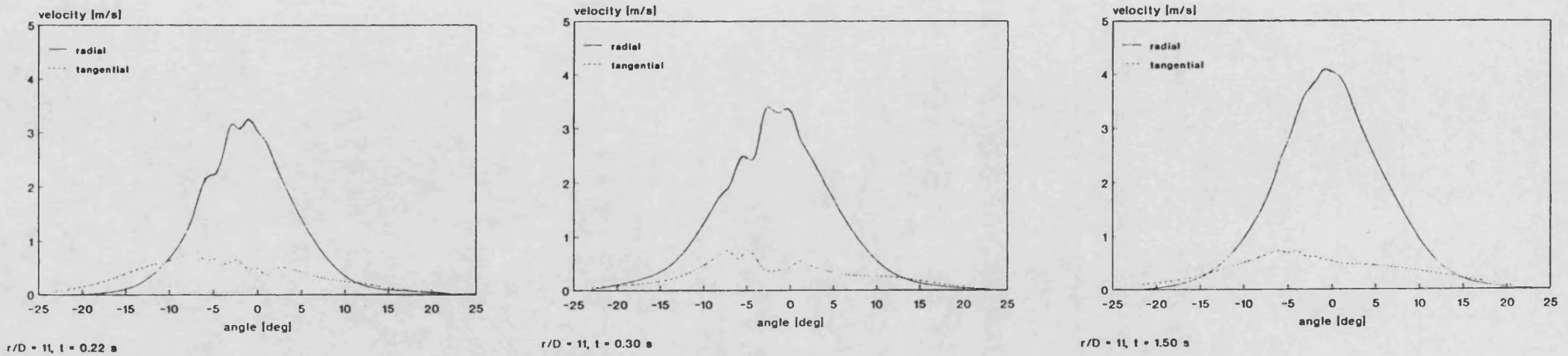

Fig. 6.22: Temporal development of radial and tangential velocity profile at r/D = 11

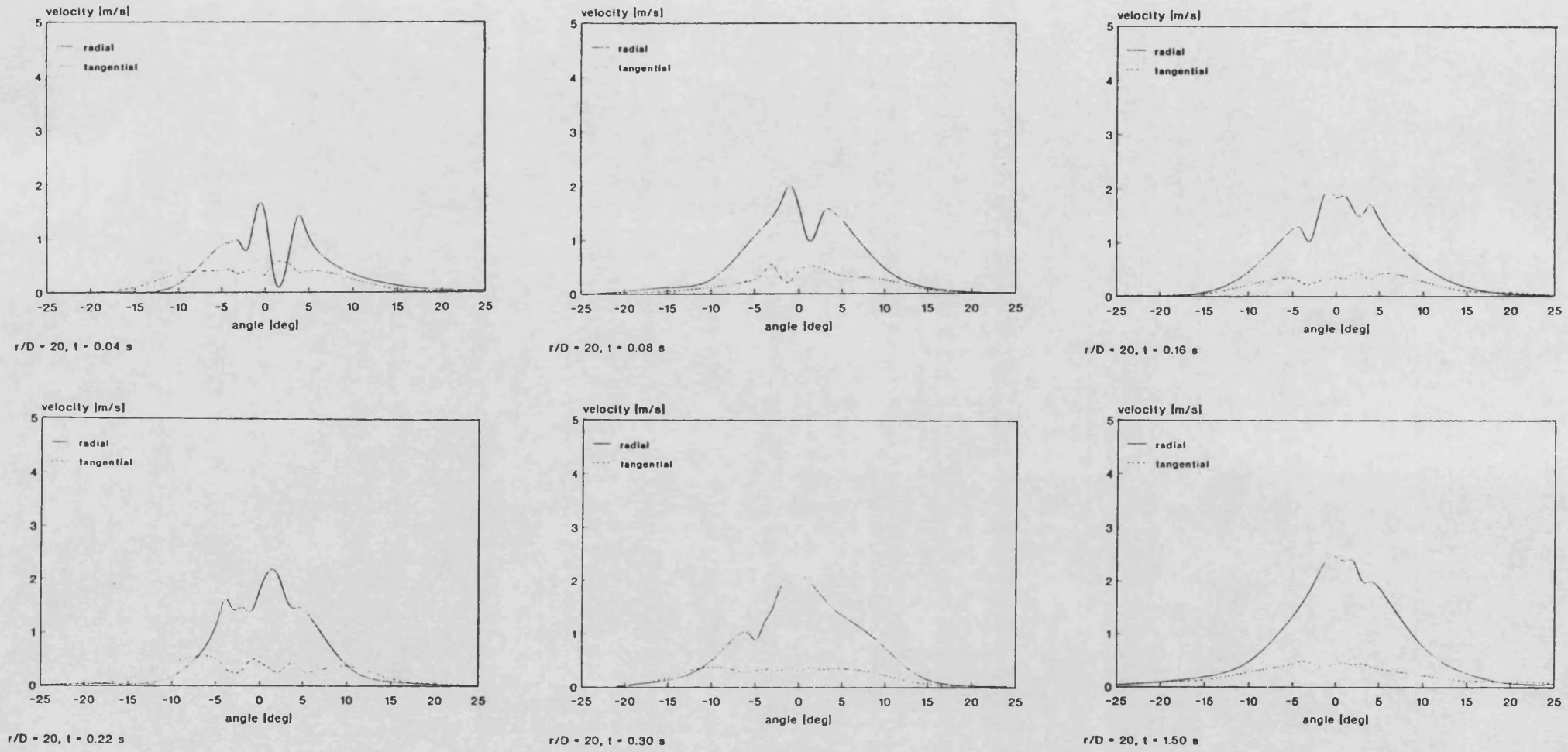

Fig. 6.23: Temporal development of radial and tangential velocity profile at r/D = 20

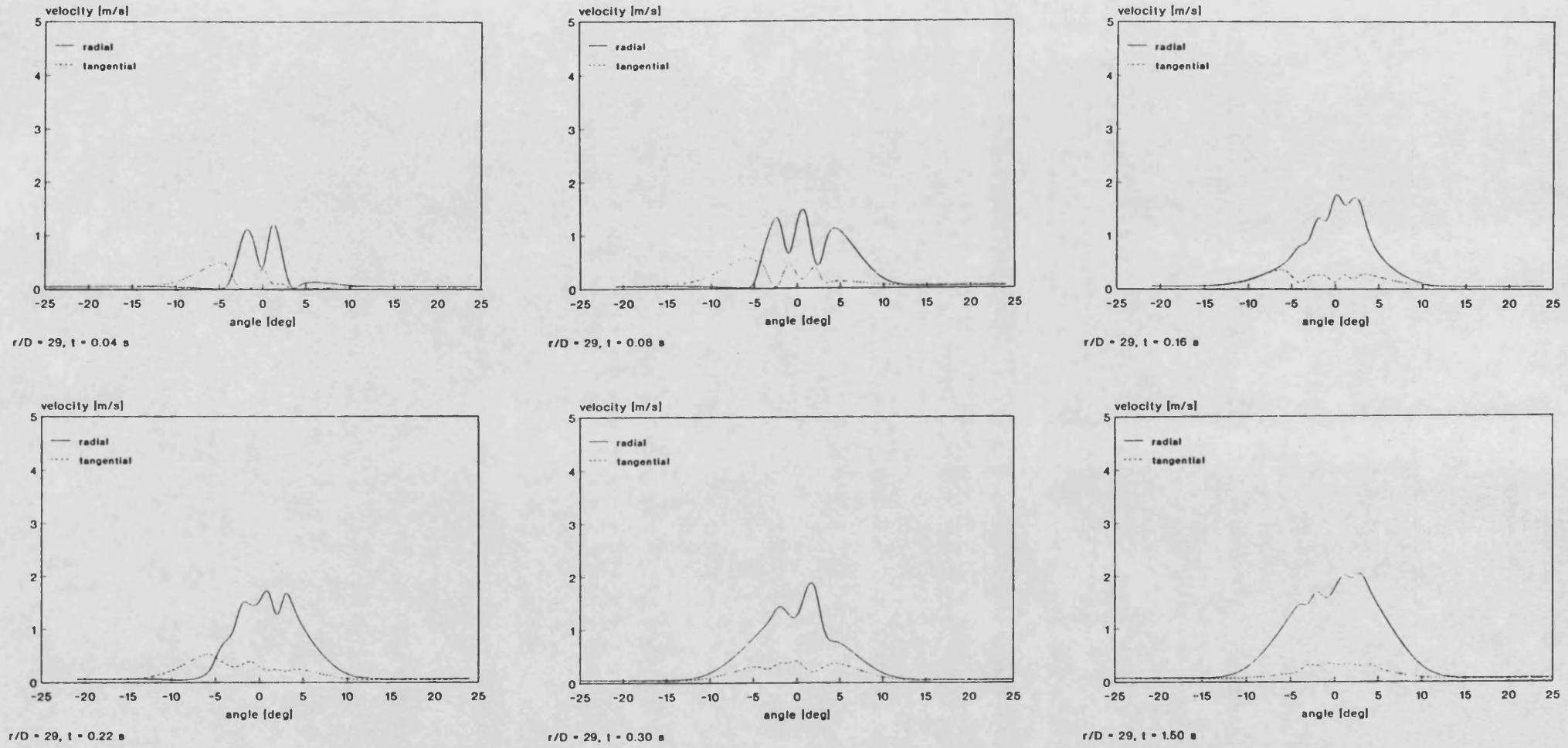

Fig. 6.24: Temporal development of radial and tangential velocity profile at r/D = 29

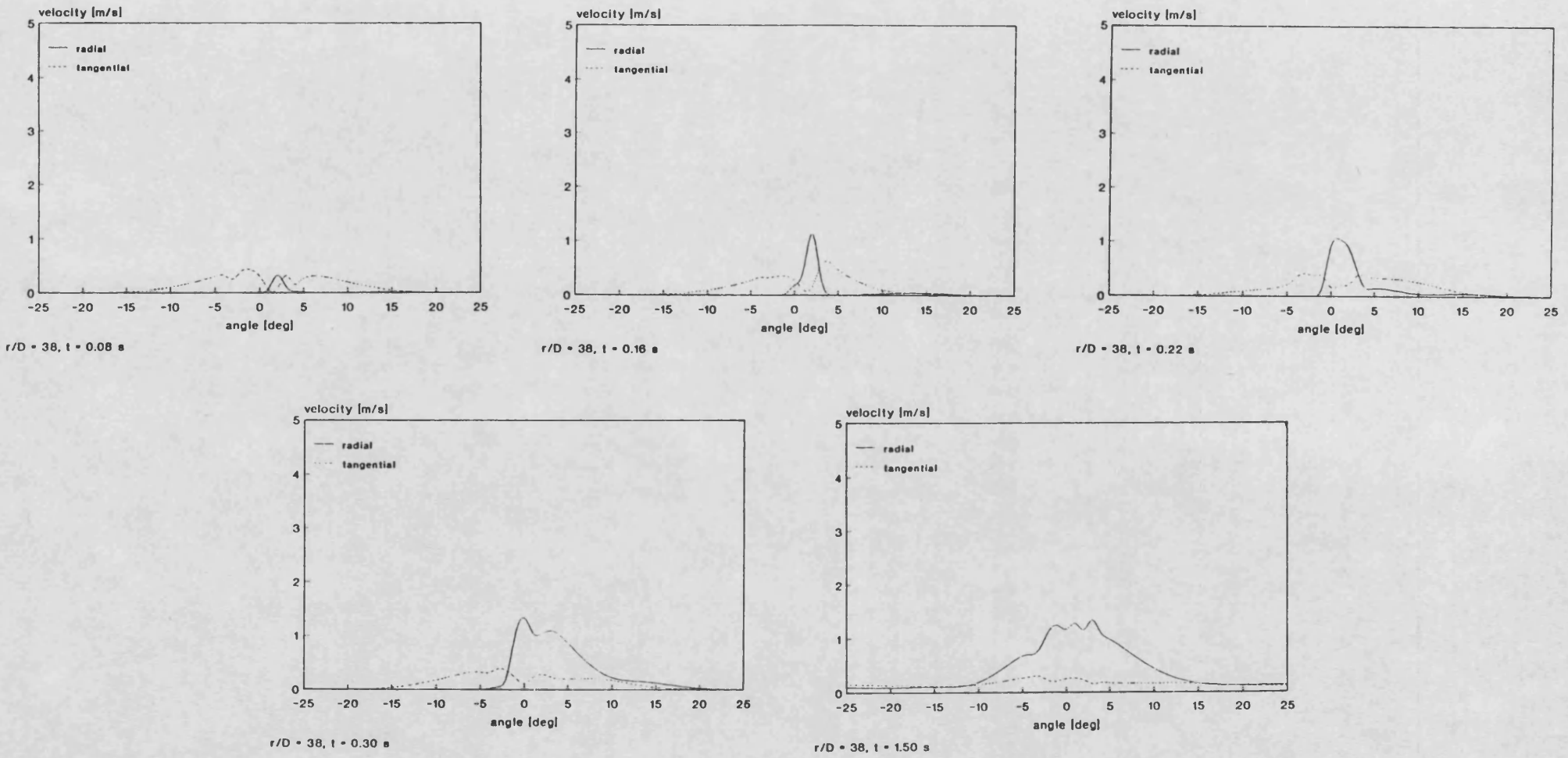

Fig. 6.25: Temporal development of radial and tangential velocity profile at r/D = 38

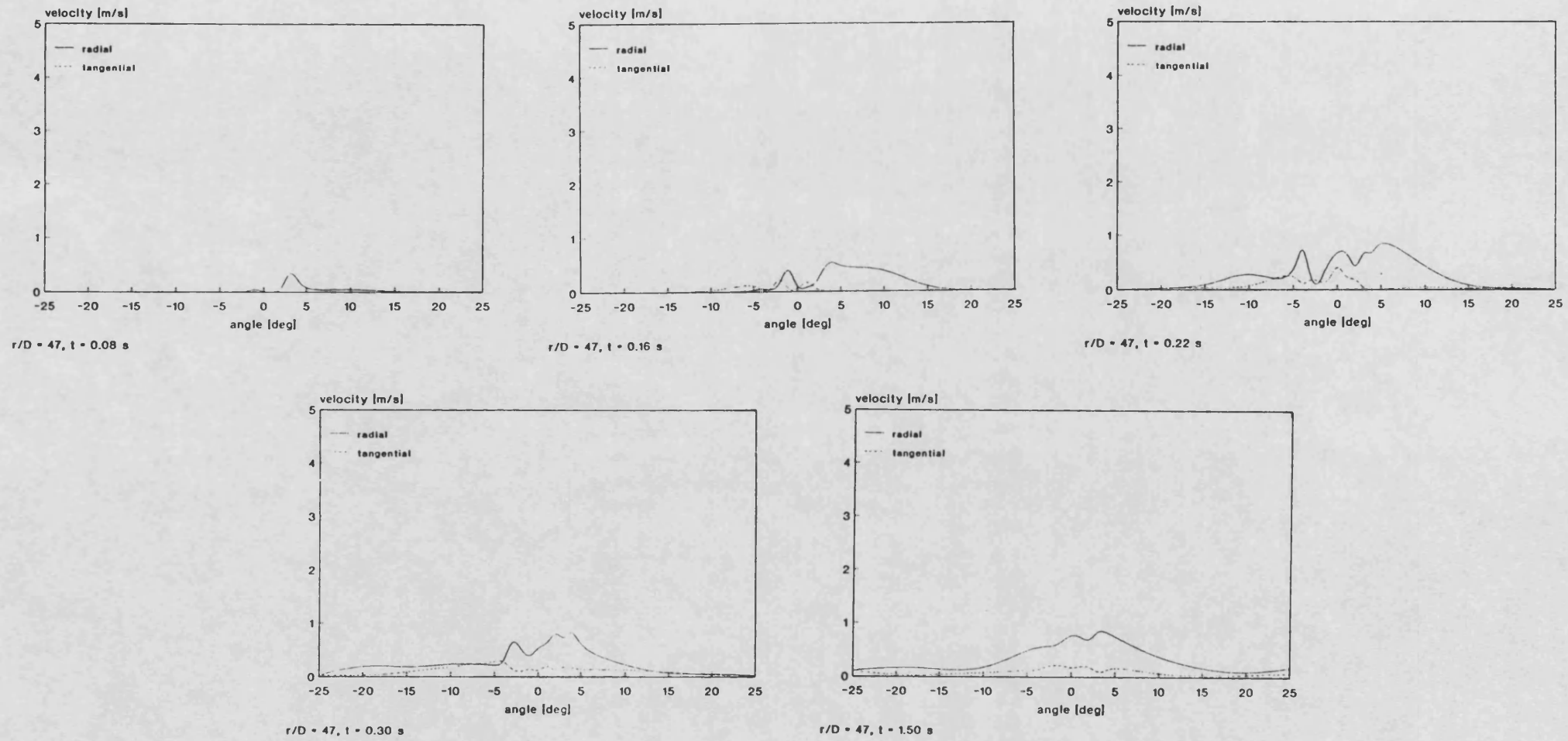

Fig. 6.26: Temporal development of radial and tangential velocity profile at r/D = 47

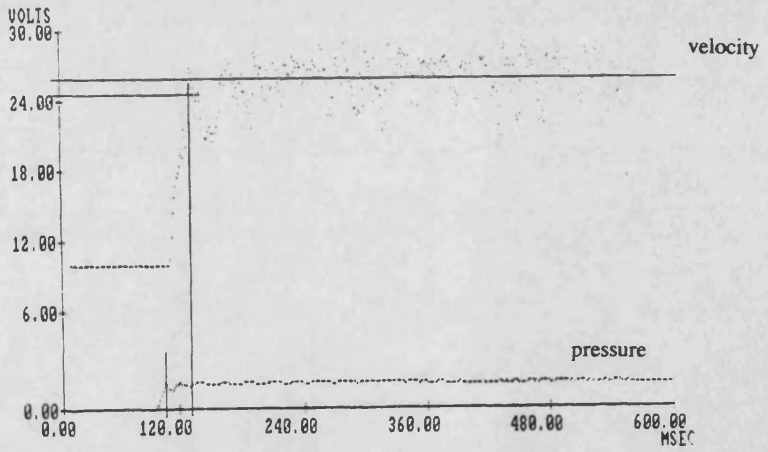

r/D = 11

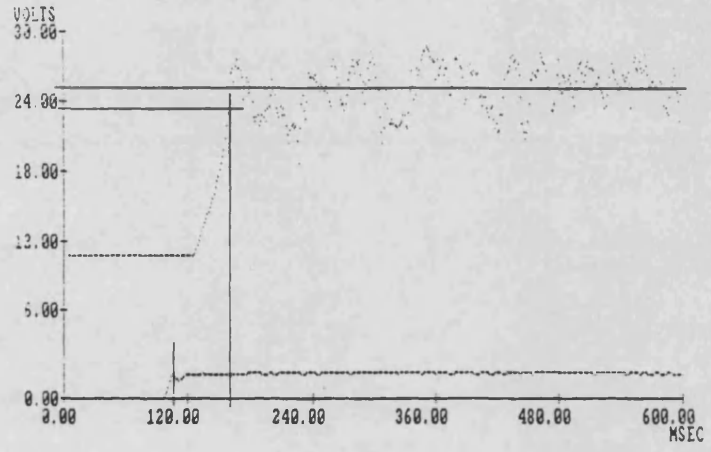

r/D = 20

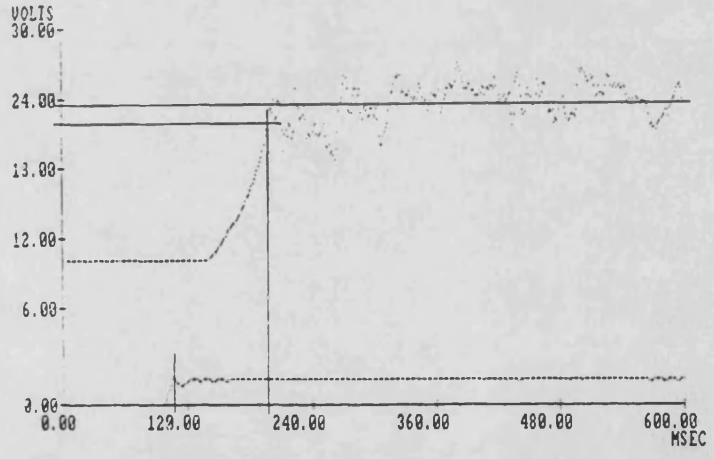

r/D = 29

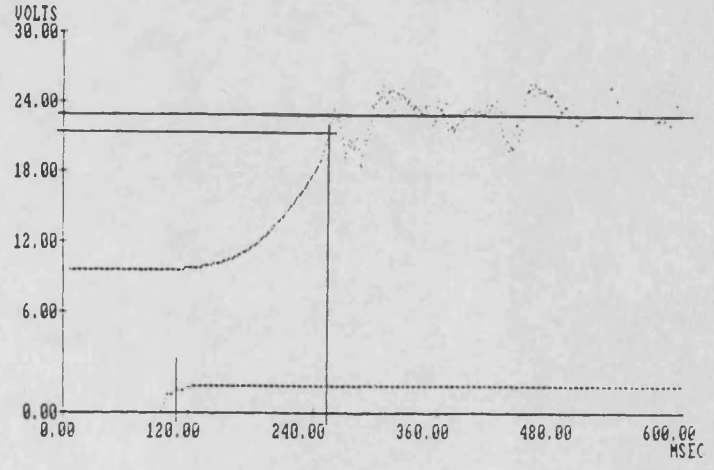

r/D = 38

Fig. 6.27 cont.

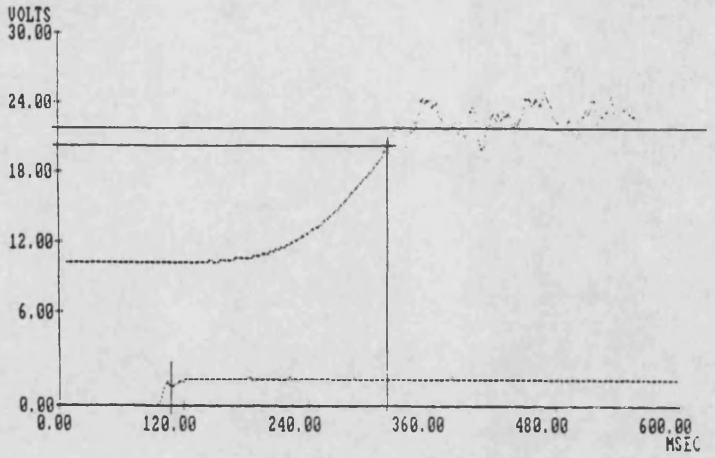

r/D = 47

Fig. 6.27: Jet penetration record at r/D = 11, 20, 29, 38 and 47

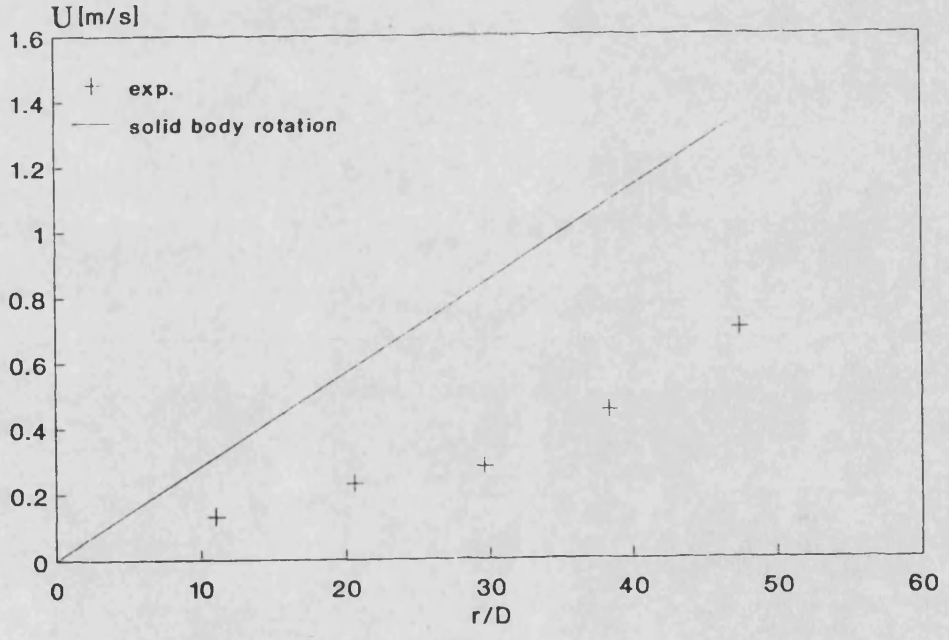

Fig. 6.28: tangential swirl velocity distribution at 50 rpm

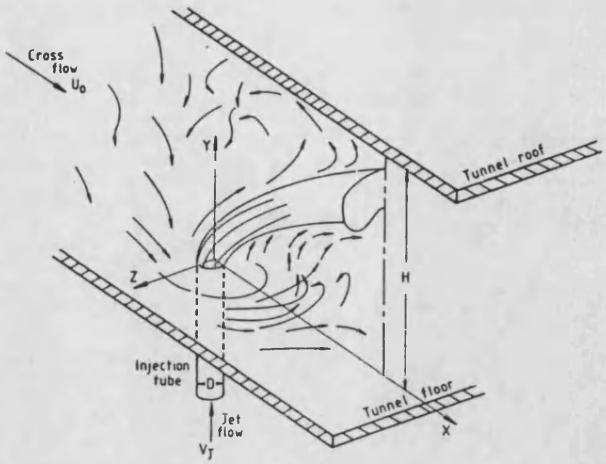

Fig. 6.29: Circular jet in a uniform cross - flow (Jones and McGuirk, 1979)

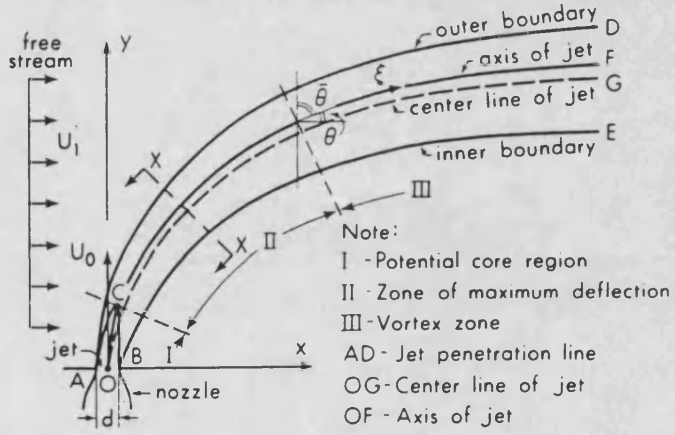

Fig. 6.30: Definition sketch of circular jet in uniform cross - flow

(Rajaratnam, 1976)

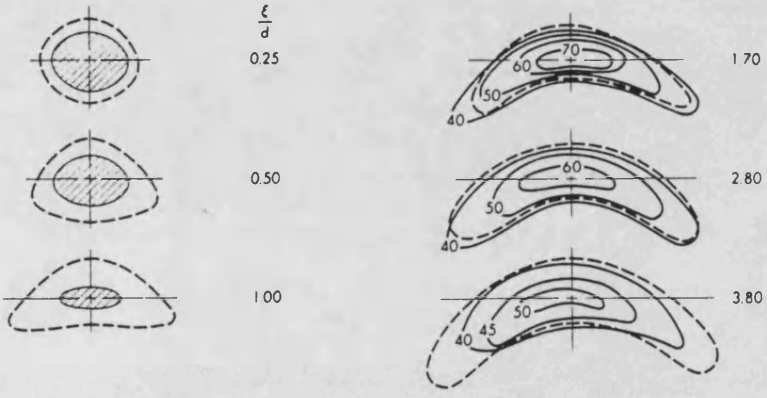

Fig. 6.31: Development of kidney shaped jet cross sections (Abramovich, 1963)

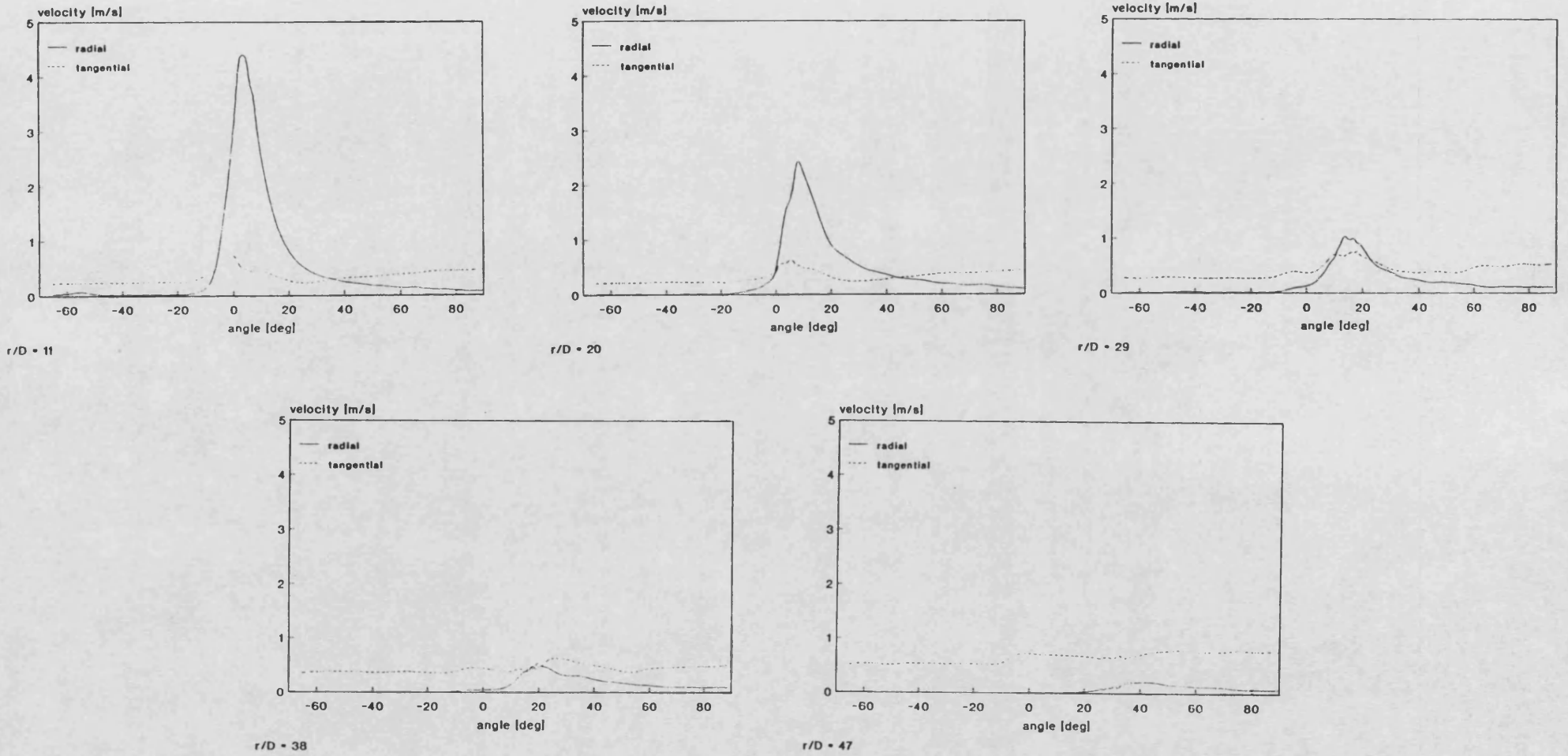

Fig. 6.32: Radial and tangential mean velocity profiles at r/D = 11, 20, 29, 38 and 47; 50 rpm

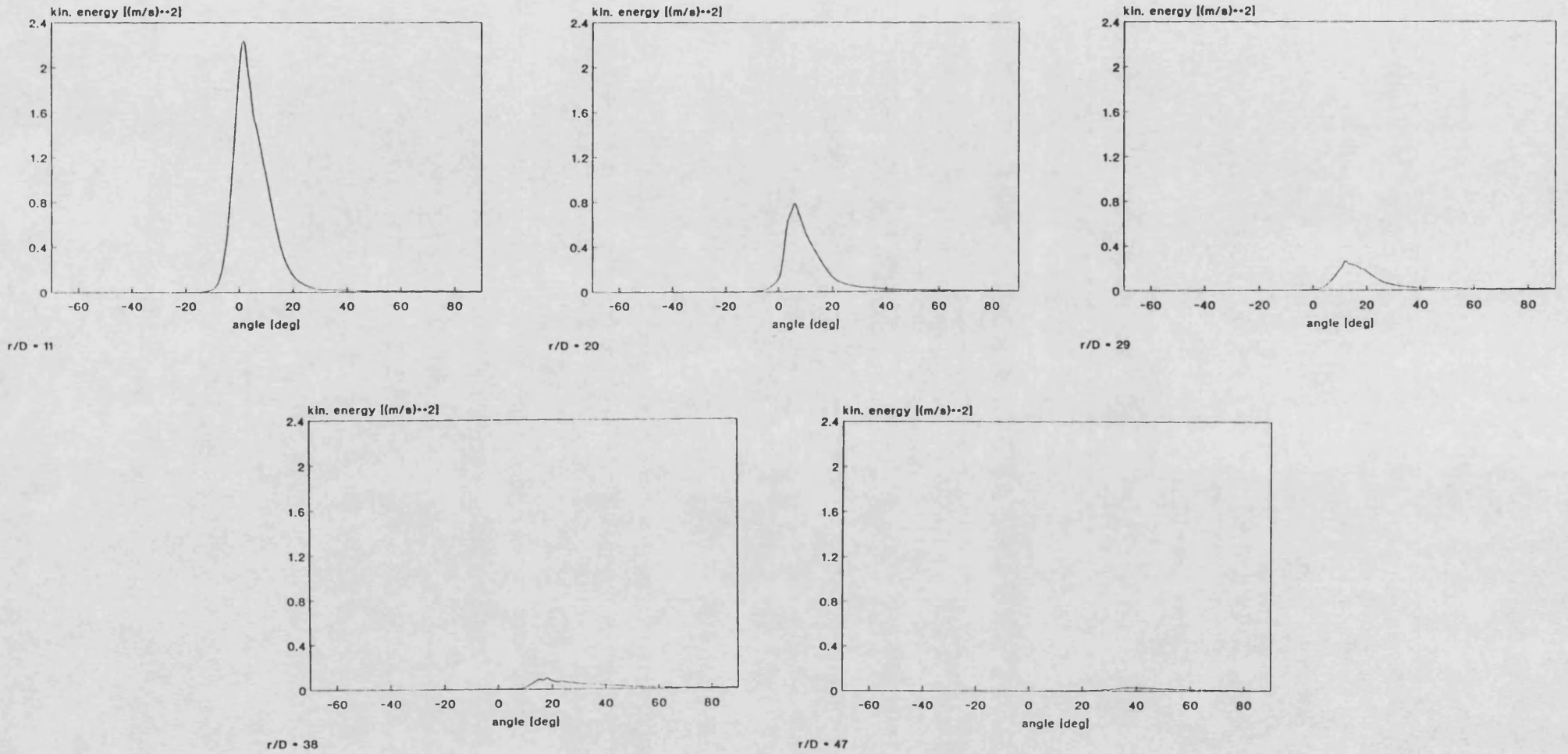

Fig. 6.33: Kinetic energy profiles at r/D = 11, 20, 29, 38 and 47; 50 rpm

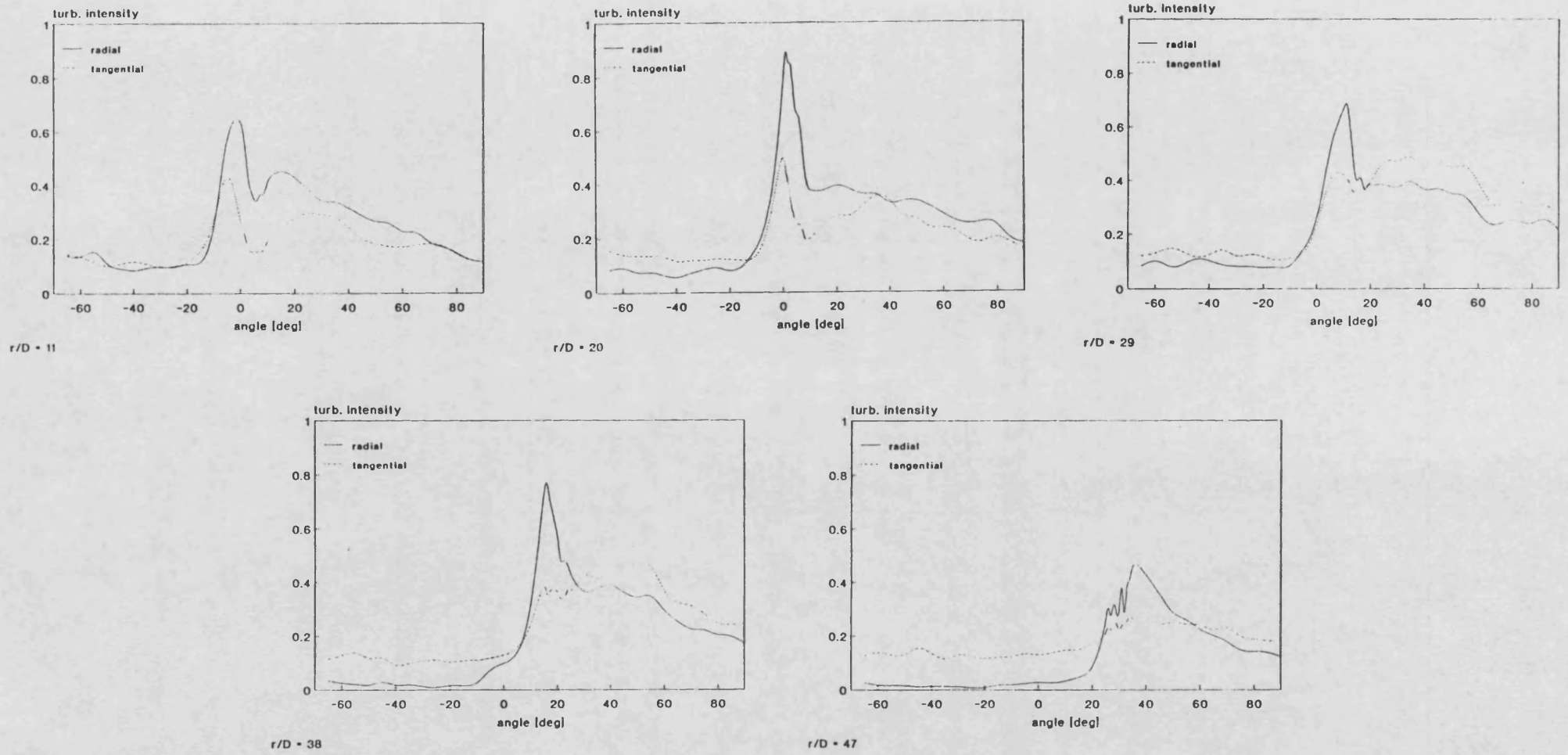

Fig. 6.34: Radial and tangential turbulence intensity profiles at r/D = 11, 20, 29, 38 and 47; 50 rpm

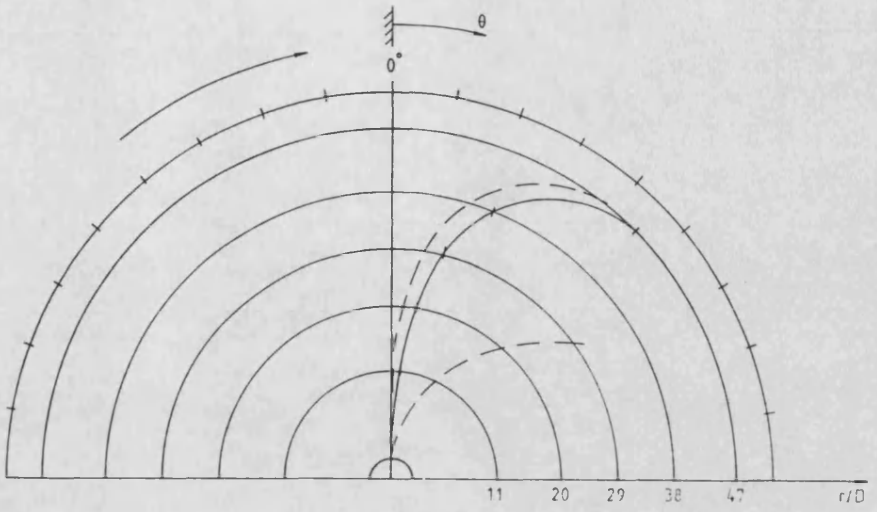

Fig. 6.35: Deflected steady state jet axis and boundaries

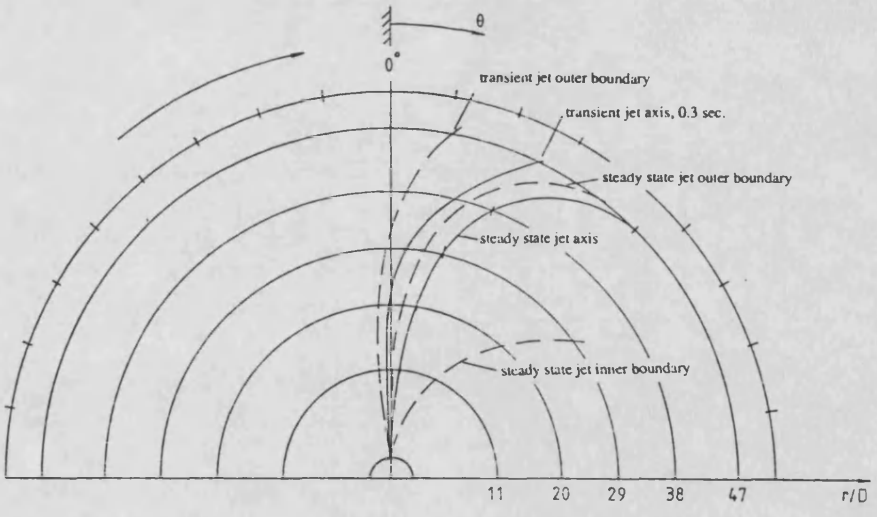

Fig. 6.36: Comparison between deflected steady state and transient jet axis and boundaries

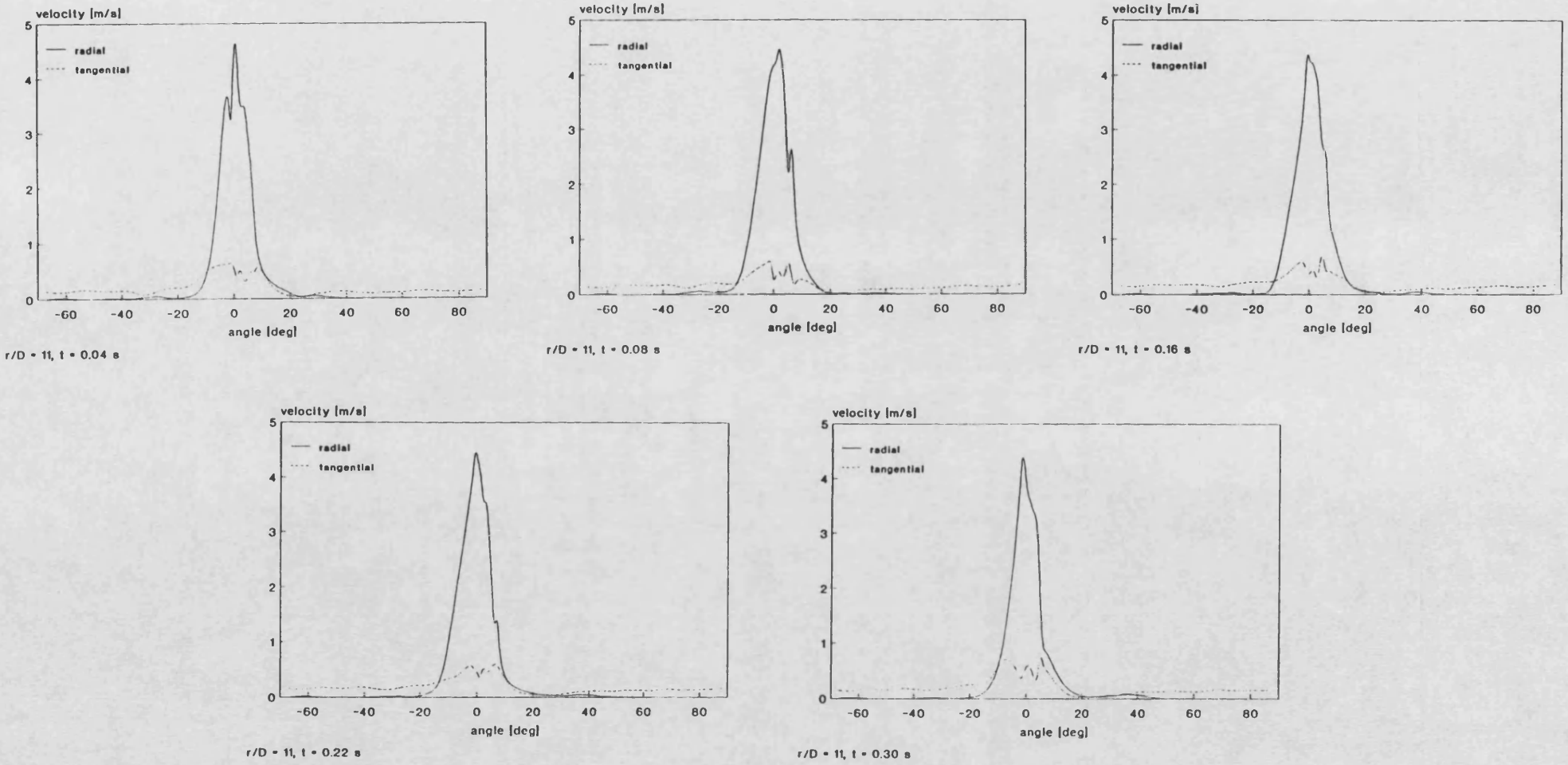

Fig. 6.37: Temporal development of radial and tangential mean velocities under swirling conditions at r/D = 11

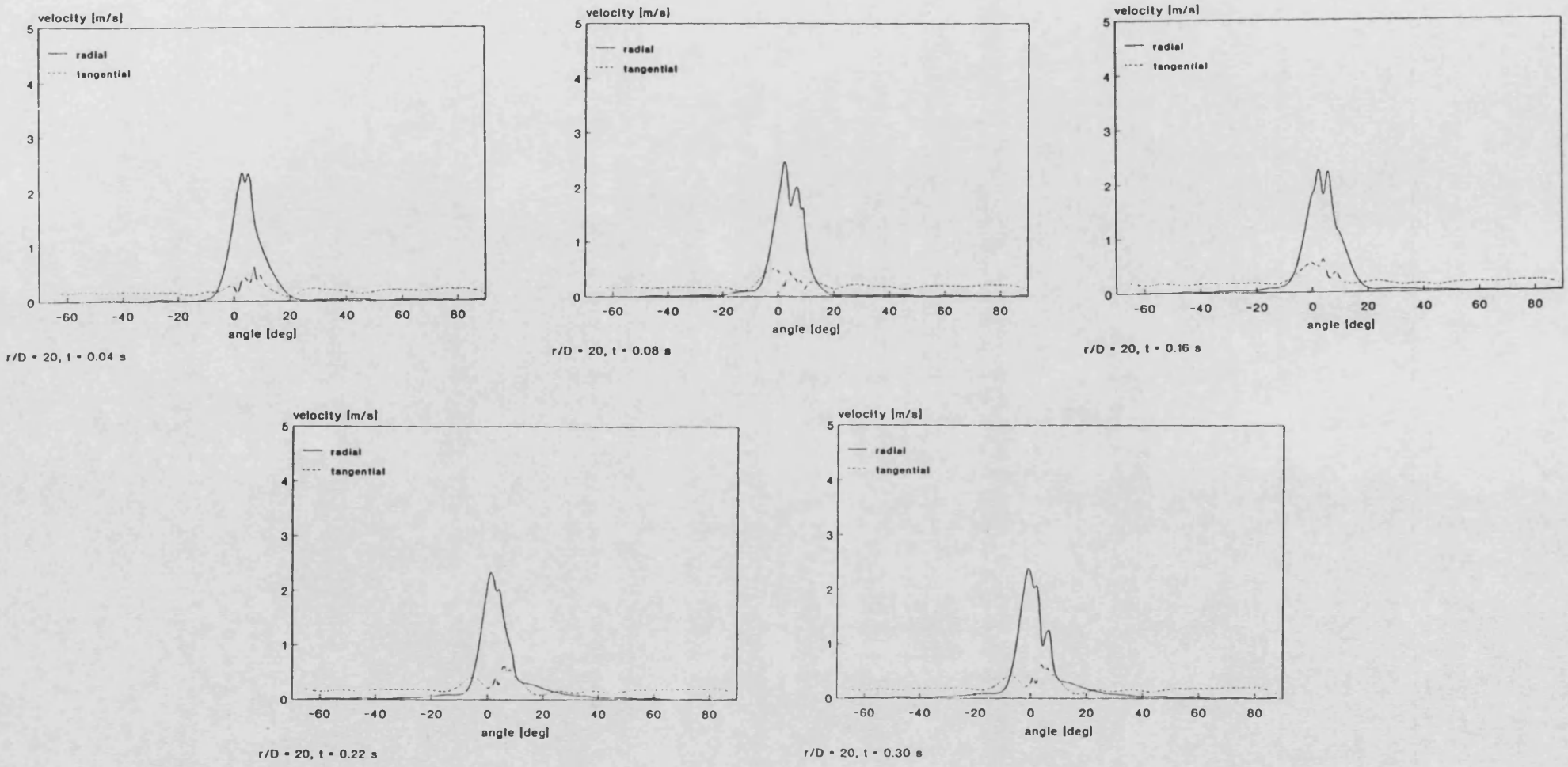

Fig. 6.38: Temporal development of radial and tangential mean velocities under swirling conditions at r/D = 20

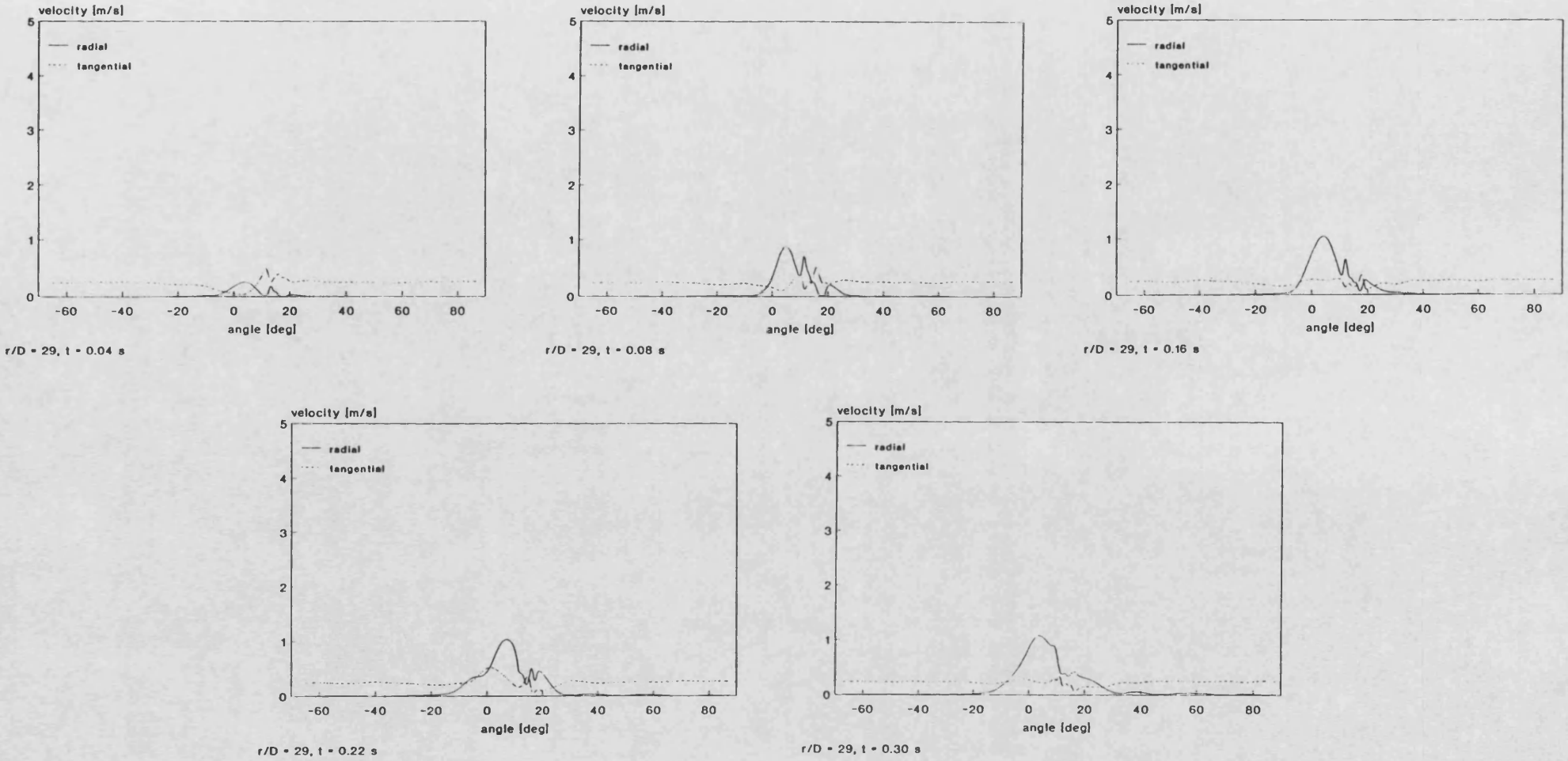

Fig. 6.39: Temporal development of radial and tangential mean velocities under swirling conditions at r/D = 29

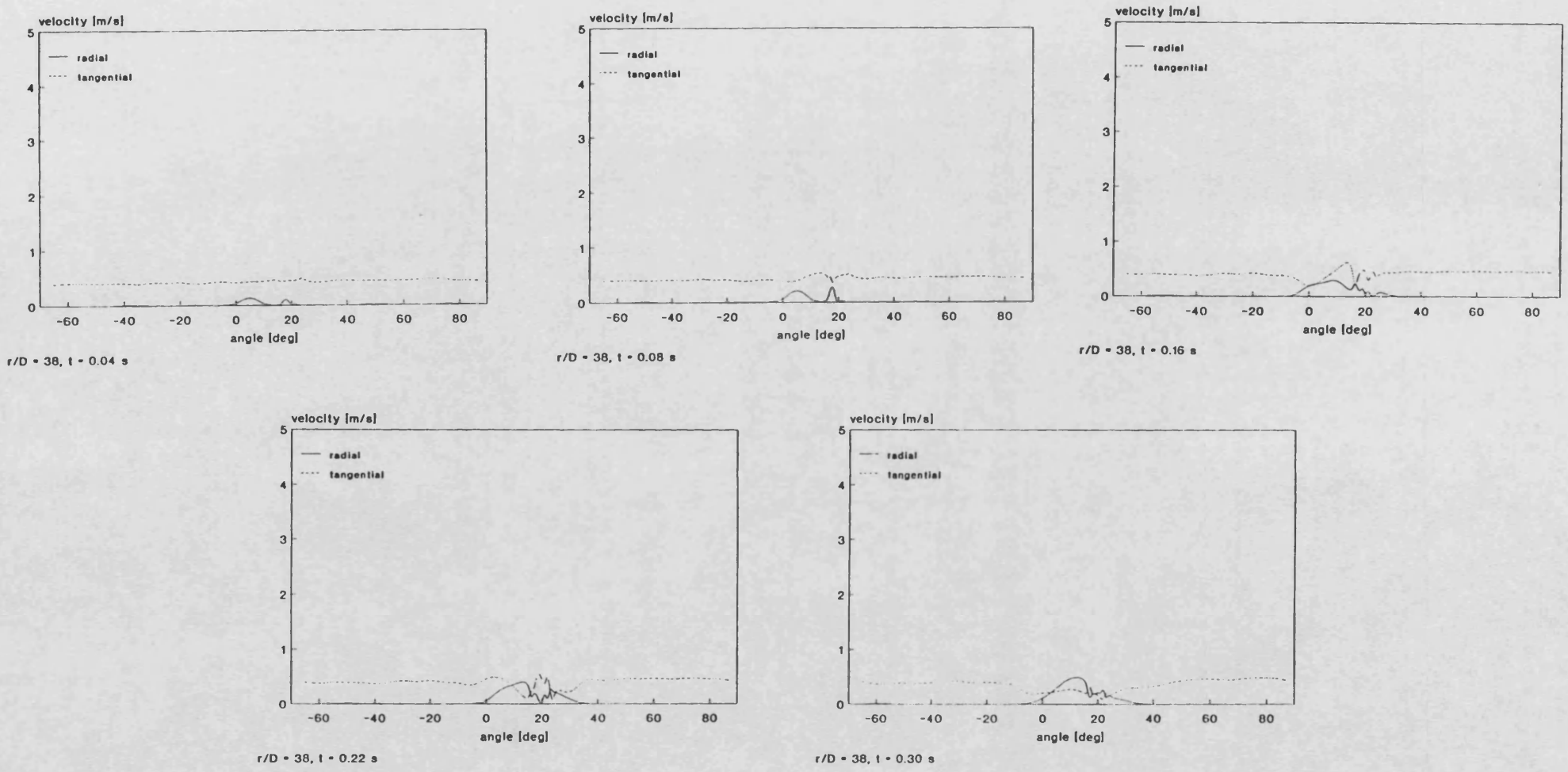

Fig. 6.40: Temporal development of radial and tangential mean velocities under swirling conditions at r/D = 38

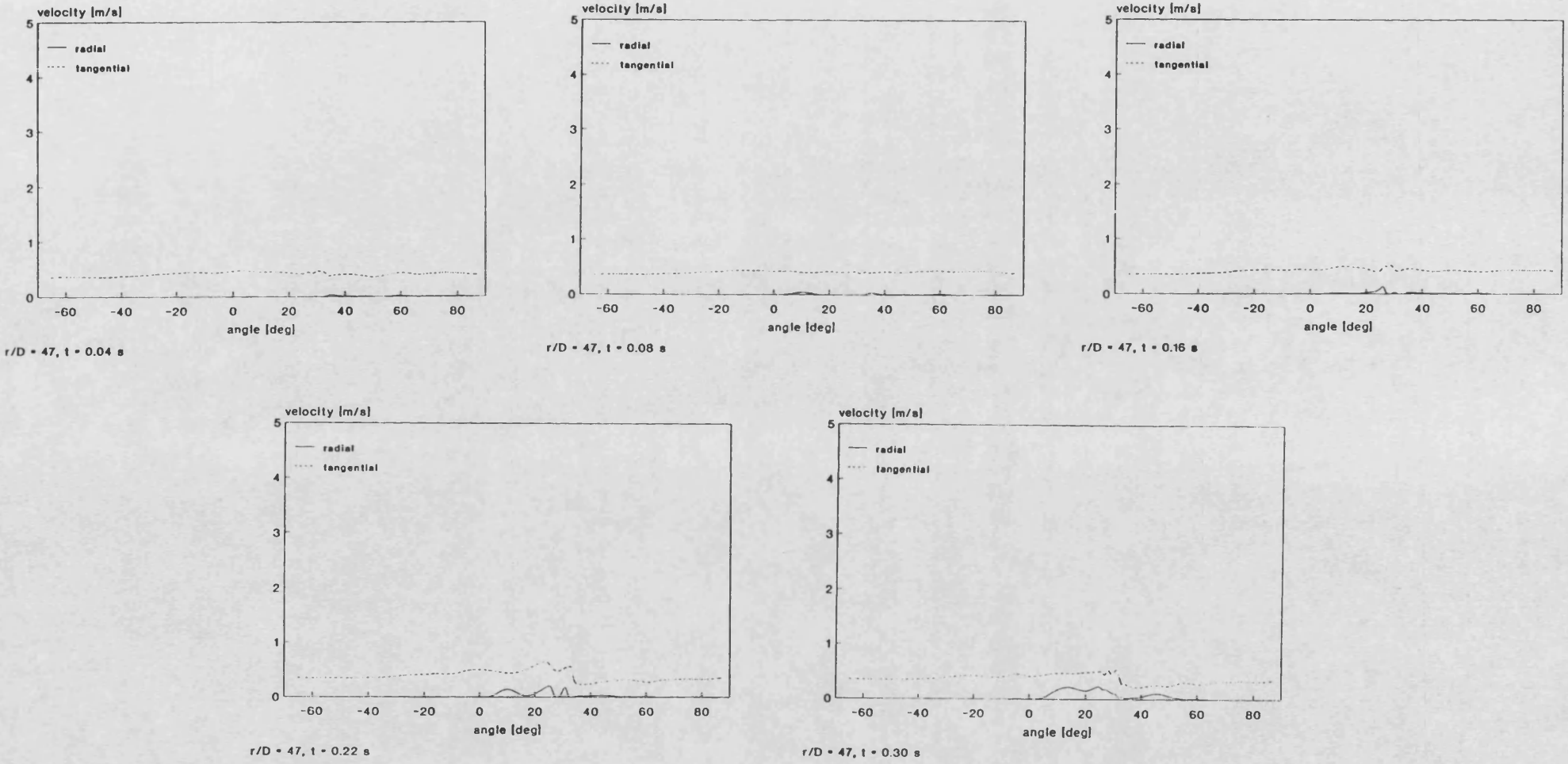

Fig. 6.41: Temporal development of radial and tangential mean velocities under swirling conditions at r/D = 47

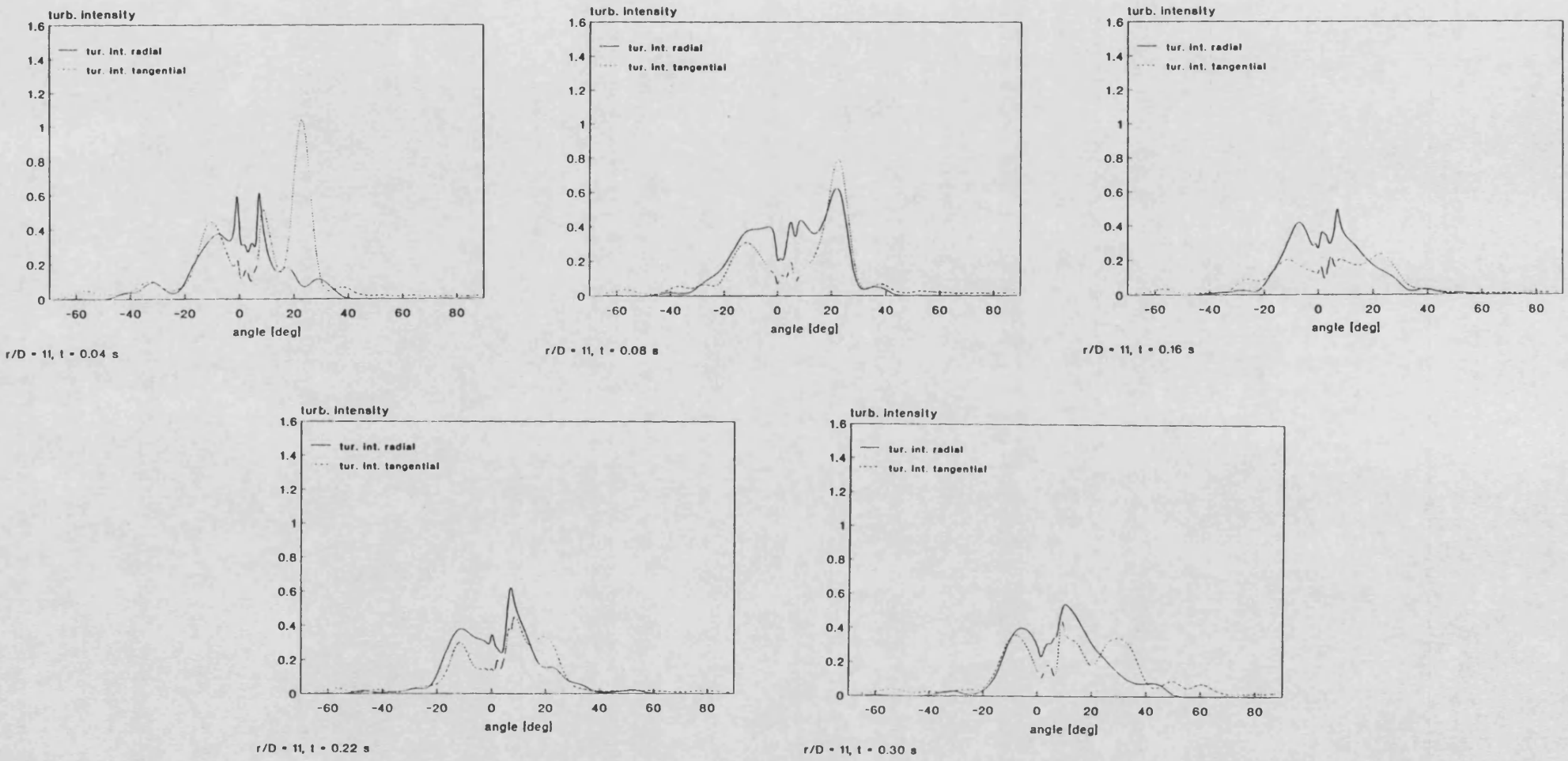

Fig. 6.42: Temporal development of radial and tangential turbulence intensity profiles under swirling conditions at r/D = 11

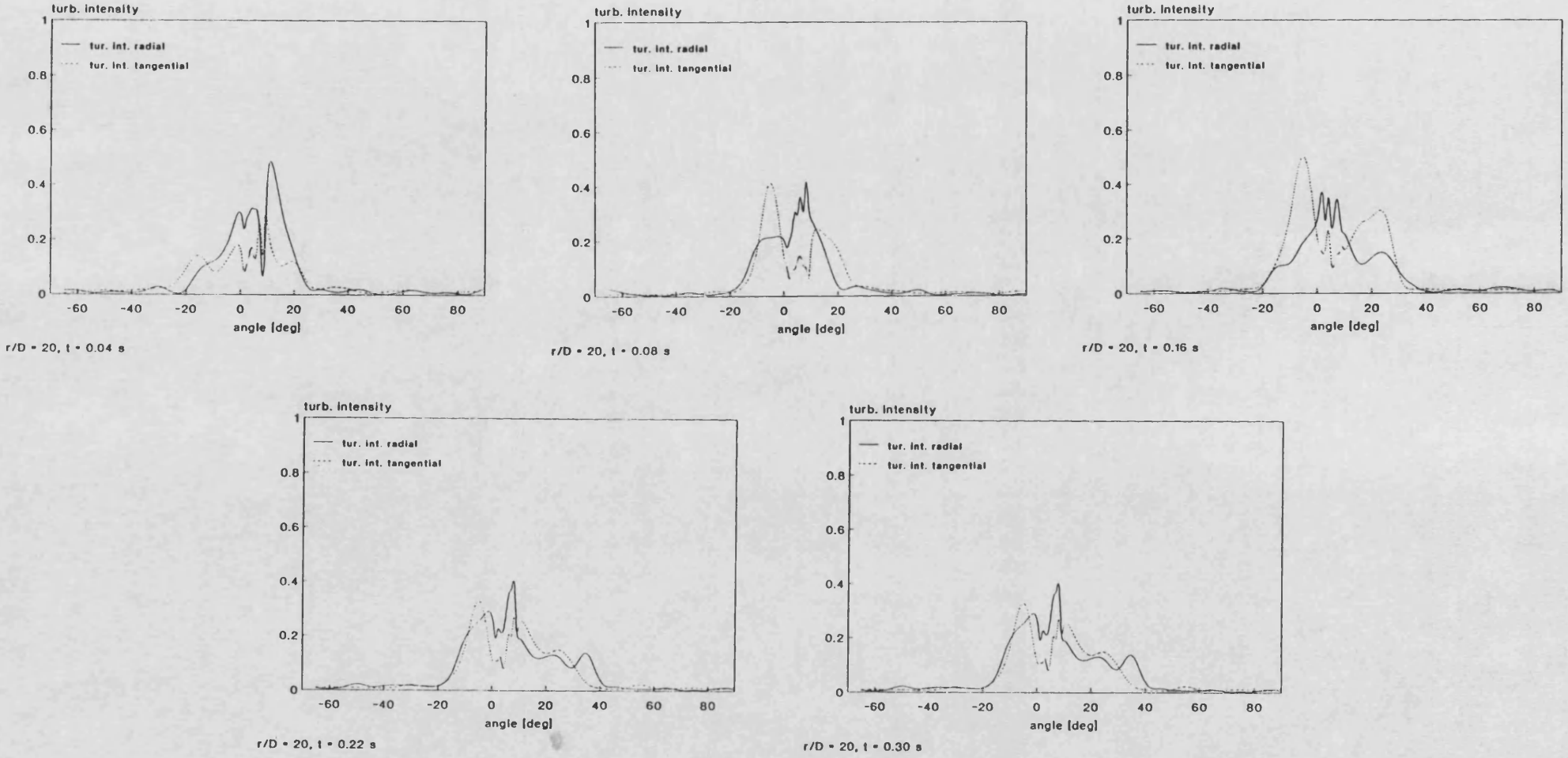

Fig. 6.43: Temporal development of radial and tangential turbulence intensity profiles under swirling conditions at r/D = 20

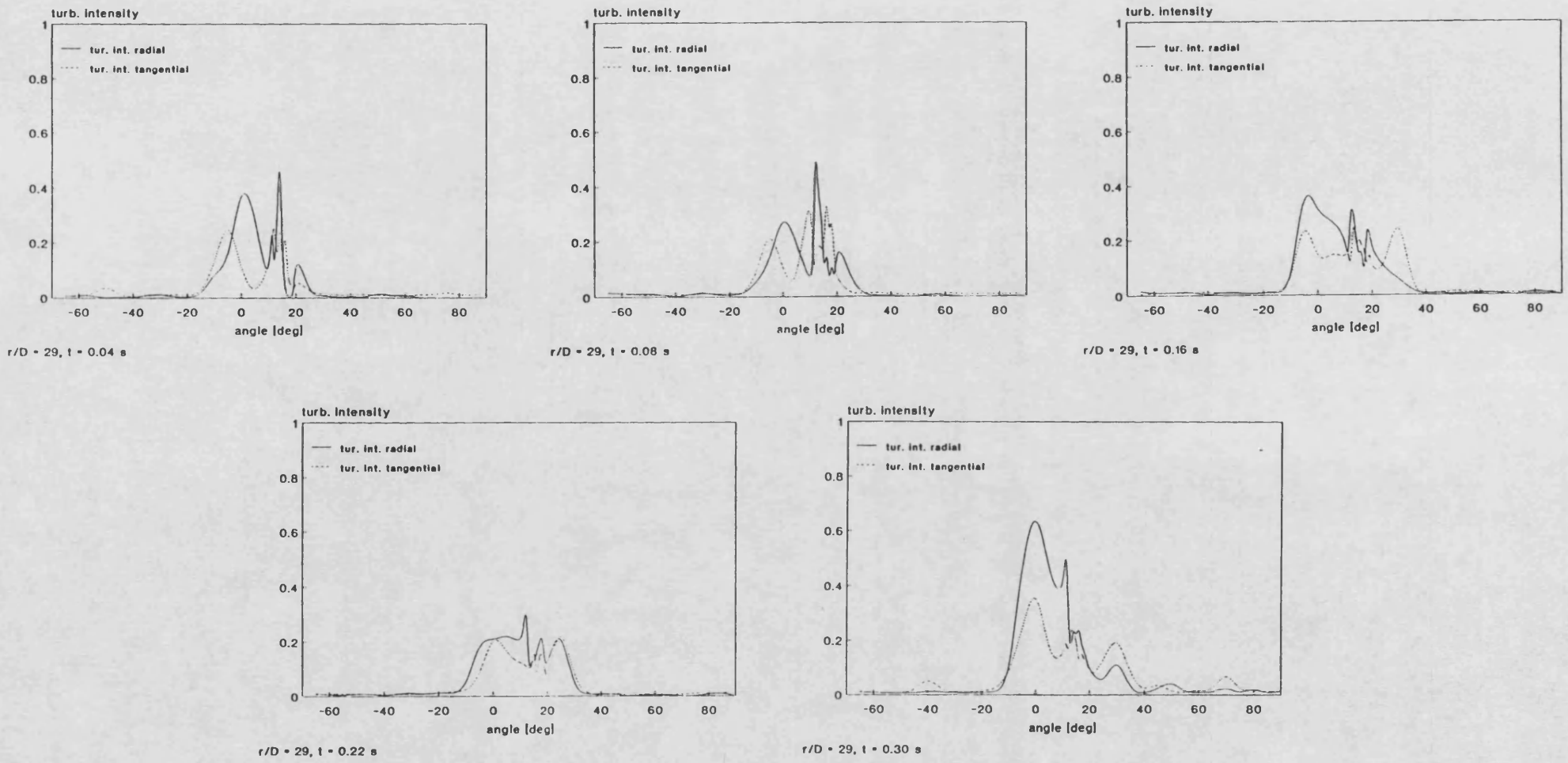

Fig. 6.44: Temporal development of radial and tangential turbulence intensity profiles under swirling conditions at r/D = 29

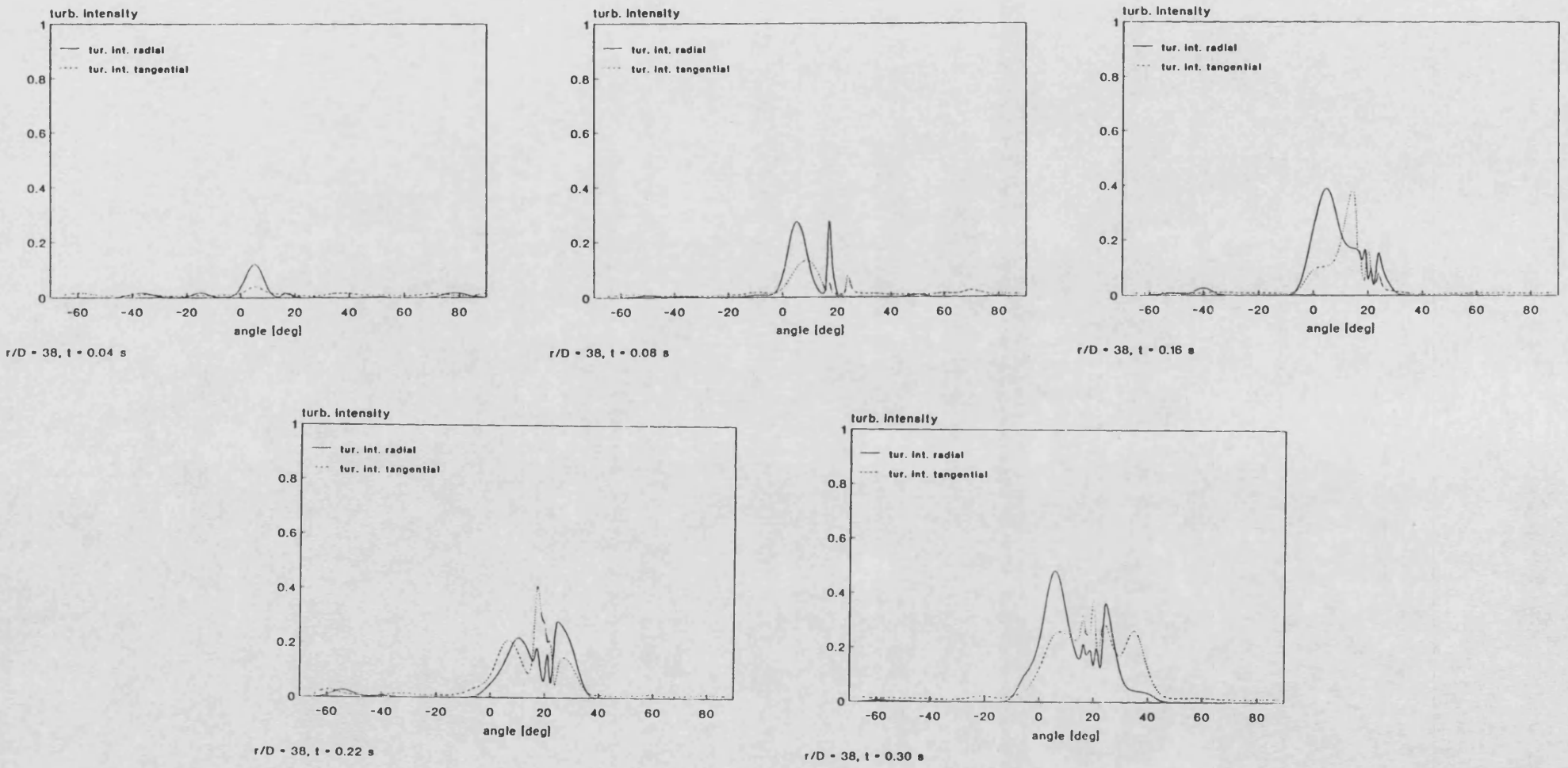

Fig. 6.45: Temporal development of radial and tangential turbulence intensity profiles under swirling conditions at r/D = 38

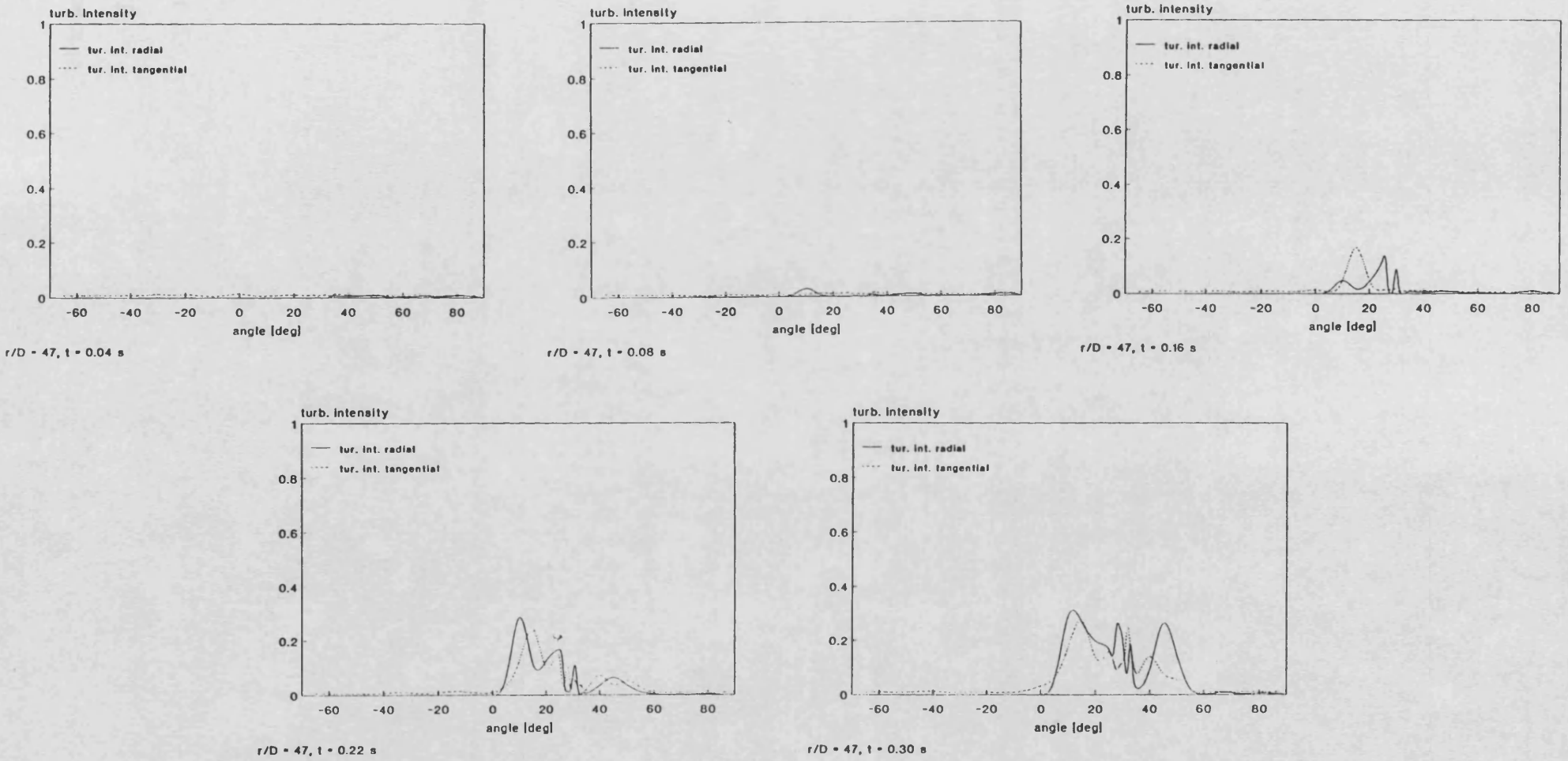

Fig. 6.46: Temporal development of radial and tangential turbulence intensity profiles under swirling conditions at r/D = 47

CHAPTER 7

7. UNDEFLECTED JET: COMPUTATIONAL STUDY

The purpose of this chapter is to present numerical results for the three - dimensional undeflected steady state and transient jet and to use the experimental results presented in chapter six to validate the predictions. Section 7.1 describes how the problem is implemented in PHOENICS with reference to the 'Satellite' file and the 'Ground' subroutines. This is followed by the presentation of results for the undeflected steady state jet in section 7.2. The material presented includes results of preliminary investigations into the effect of numerical parameters on the flow field and on convergence, and a study of inlet and outflow boundary conditions. Results are presented in the form of (i) distributions along the jet centreline, (ii) profiles at five jet cross sections, (iii) vector plots and (iv) contour plots. Experimental data obtained in the hydraulic analogue rig using hot film anemometry and a pitot tube and also experimental results reported in the literature are used to validate the predictions. In section 7.3 results for the transient undeflected jet obtained with a fully implicit scheme are presented and compared against experimental data. They illustrate the jets temporal development and the growth of the wall jet after impingement. A scalar quantity is solved for to simulate the temporal development of a range of air / fuel ratios in the combustion chamber model. Finally, the concluding remarks in section 7.4 summarize this chapter.

7.1 Problem Definition

An overview of the PHOENICS program has been given in section 5.1. The interaction of the three main components (i.e. 'Satellite', 'Earth' and 'Photon') is illustrated in figure 7.1. The 'Satellite' writes a data file ('eardat') which is read by 'Earth'. During the solution process 'Earth' does not interact with 'Satellite', however, 'Earth' does

communicate with subroutine 'Ground', allowing the user to insert his own Fortran sequences to influence the solution. Use has been made of this option in the present study and will be described in section 7.1.2. The results of the iteration process are written to a file ('phida') which can be read by the post - processor 'Photon' to display vector and contour plots on the VDU.

The basic problem is defined in the 'Q1' file which forms part of the 'Satellite', and in the following section attention is focused on the settings made here to describe the model for the undeflected jet.

7.1.1 Data Input in PHOENICS 'Satellite'

Appendix B 1 gives an annotated version of the 'Q1' file used for the transient undeflected jet. PHOENICS uses its own input language and the reader is referred to reference [82] for a complete list of commands. The intention here is to highlight settings relevant to the problem under consideration and to indicate to what extent a problem can be described in 'Satellite' and where coding in 'Ground' is required. 'Q1' is organized in a group structure comprising 24 groups. This group structure forms the framework for the following description with attention restricted to the relevant settings.

Run identifiers (group 1)

It is possible to perform consecutive runs in which the results of one run are used as initial conditions for the following run. Use of this facility has been made in the case of the deflected jet discussed in chapter eight, here only single runs were performed.

Time - dependence (group 2)

In steady state simulations no settings need to be made. If the problem is transient the number of time intervals and the time step size must be specified. In this study a

number of runs with five intervals of 3 ms each were made. Assigning an initial time value TFIRST is useful when 'restart' runs are to be performed later.

Grid specification (groups 3 to 5)

In groups three to five the choice between cartesian and cylindrical polar co-ordinates is made and the mesh itself is specified. In cylindrical polar co-ordinates x is the circumferential co-ordinate, y the radial direction and the z - axis is aligned with the axis of symmetry. The grid shown in figure 7.2 is divided into 17 x 43 x 18 cells in x, r and z direction respectively. For reasons of symmetry one half of a quadrant and the bottom part of the hydraulic analogue form the computational domain. The symmetry conditions have already been outlined in chapter five and the reader is referred to sections 5.2 and 5.4 and to figure 5.2 for further details. It should be noted that the x co-ordinate begins at the outer domain boundary and that the last x cell (IX = NX) coincides with the jet centreline. The grid is nonuniform with a higher cell density near the nozzle exit and in the jet shear layer. Large ratios between the spacings of neighbouring cells should be avoided, in the present study the ratio between any two adjacent node spacings does not exceed 1.5. Two options to generate a nonuniform grid are provided and here the so called 'method of pairs' is used since it gives the greater flexibility for grids expanding and contracting in one co-ordinate direction. The overall grid size must be specified together with the fractions into which it will be divided. The origin in radial direction is offset by the injector column radius using the RINNER command. This has implications for the inlet boundary condition and will be discussed in more detail in section 7.2.1.

Variables solved for (group 7)

In group seven the variables solved for are specified and storage is allocated. These variables are pressure, the three velocity components and the scalar quantity

concentration (for transient runs only). Commands related to the kinetic energy and rate of dissipation are introduced at a later stage. The iterative method by which the algebraic equations for each variable are solved is also specified, i.e. the whole - field simultaneous method for pressure and a slabwise procedure for the other variables. Storage may be allocated for non - standard variables calculated in 'Ground' like turbulence intensity or vorticity.

Numerical control options (group 8)

Group eight provides a number of control options pertaining to the numerical technique employed for each variable. In the present case the sources described in section 5.3.4 are activated and both, convection and diffusion, contribute to the solution. The Hybrid scheme (section 5.3.2) is activated for approximating convection.

Fluid properties and turbulence (group 9)

The properties of the medium are defined, viz. the density and the laminar viscosity, and the k - ε model of turbulence is switched on. Storage is allocated for the kinetic energy and the dissipation rate and solution is activated of the turbulence production term (equation 4.13) appearing in the source terms of the k - and ε - equation. Modifications to the standard k - ε model cannot be made in the 'Satellite' but have to be introduced in 'Ground'.

Blockages (group 11)

Parts of the computational domain inaccessible to flow can be blocked by specifying so called porosities. Porosities can either be applied to entire cells or to cell face areas, a value of zero corresponds to complete blockage while a value of unity means no blockage. In this study the first cell of the injector column in radial direction from the nozzle edge to the domain boundary at IX = 1 is blocked. Another command in group 11 has been extensively used in transient calculations, i.e. the 'restart' facility applied to

all variables to perform continuation runs in 15 ms intervals. Thus the entire flow field was available for analysis during the development of the jet.

Boundary condition (group 13)

The four different boundary types used in this study (inflow, prescribed pressure, walls and symmetry planes) have been described in section 5.4. If no settings are made in group 13 all boundaries will be treated as impenetrable to the flow of mass and momentum, thus confining the medium without any fluid entering or leaving the domain. Symmetry planes are boundaries of this kind and hence no settings have to made for the r - z plane at IX = NX and the r - θ plane at IZ = NZ (figure 5.2). To prescribe other boundary conditions the respective regions need to be defined by specifying the start and end grid cells in each co-ordinate direction. If conditions do not change during the solution process appropriate settings should be made in group 13, varying boundary conditions must be set in 'Ground'.

The 2.5 mm square inlet covers ten cells in x - direction and five cells in z - direction. The velocity profile is assumed to be parabolic in circumferential direction and the U and V velocities are defined such that the resulting inlet velocity vector in each cell is aligned with the jet centreline. Before specifying the inlet boundary conditions the mass flow rates and the levels of turbulence kinetic energy associated with the incoming flow are defined for the ten rows of cells of constant x. The kinetic energy level in each cell is based on the associated inlet velocity while the length of the nozzle side is taken as length scale for defining the rate of dissipation. Also, in order to enhance convergence, initial values of kinetic energy and dissipation rate are set for the entire domain. These are based on an average inlet velocity and the nozzle dimensions as velocity and length scale respectively. The effect of the level of incoming turbulence kinetic energy on the general flow field was examined and results are discussed in section 7.2.2. The mass flow source is prescribed through a boundary condition as given in equations (5.15) and (5.18). The following values were assigned to V_m and C_m : $C_m = 10^{-5}$ and

$V_m = 10^5 \dot{m}$. This practice differs from the settings suggested in equation (5.18) and was adopted because of the large values of $\dot{m}$ (order of 10^4). The originators of the PHOENICS program recommend a value for V_m in the order of 10^{10} as much higher values may lead to numerical inaccuracies. Variables convected into the domain are specified by assigning their respective values to V_ϕ in equation (5.14) and setting C_ϕ equal to zero.

Fluid can leave the domain across the r - z plane at IX = 1 where a value of zero pressure is prescribed. With reference to equation (5.14) the following values are assigned to the different parameters: $C_m = 1$, $V_m = 0$, $C_\phi = 0$ and V_ϕ = cell value adjacent to boundary. The latter specification ensures that fluid entrained across the boundary has the same properties as prevail in the near boundary cells within the domain. Hence no inflow source is added.

Wall boundary conditions are applied to the z - θ plane at r = R and to the r - θ plane at IZ = 1 (figure 5.2). In contrast to planes of symmetry, walls take skin friction into account by calculating the shear stress from laminar or logarithmic relationships, depending on the local Reynolds number (section 3.4). These expressions are included as source terms for the velocities parallel to the wall. It is also necessary to supply wall boundary conditions for the kinetic energy and the rate of dissipation. The former is calculated from equations (3.14) and (3.18), the latter is evaluated using equation (3.19).

Convergence control options (groups 15 to 17)

In groups 15 to 17 various parameters controlling the solution sequence are set. These include the number of sweeps of the entire domain, the number of iterations for each variable to be performed at each z - slab, and relaxation, using either the linear or the false time step method (section 5.4). The settings are very much problem dependent and some experimentation is required to optimize these control parameters. For the steady state case 250 sweeps led to a well converged solution, in transient calculations

250 sweeps were only required for the first run. For the following 'restart' runs 80 sweeps were sufficient since a realistic flow field from the previous run could be used as initial field. Some under - relaxation is necessary to avoid divergence. For the pressure, a linear under - relaxation factor in the range of 0.3 to 0.5 was found suitable, for the other variables the false time step method was used. A time step of $T_f = 0.01$ still caused the solution to oscillate and sometimes not to converge at all, $T_f = 0.001$ was therefore chosen and found to give a stable solution. The effect of under - relaxation on the convergence of radial velocity, turbulence kinetic energy and dissipation rate has been examined as part of the preliminary investigations and is discussed in section 7.2.1.

Output control (groups 20 to 24)

Print - out of field values and residuals for user specified variables aids in monitoring the solution progress. The print - out of volume flow rates across all domain boundaries provides an easy means of examining whether the continuity equation is satisfied. Care should be taken not to create unnecessarily large output files which can occupy substantial disk space, but rather to restrict the print - out to flow regions of particular interest. In the 'Q1' file of appendix B 1 only field values along the jet centreline are printed. Also, the development with time of radial velocity and concentration are monitored at five positions on the jet axis.

7.1.2 Subroutine 'Ground'

While the 'Satellite' data is supplied to 'Earth' at the beginning of the solution process, subroutine 'Ground' offers the possibility to influence the solution or to extract information during the course of the iteration. In the present work use of 'Ground' was made to calculate non - standard variables and to create output files which contain grid

geometry data and nondimensional variables for subsequent plotting of contours, jet centreline distributions and profiles at various jet cross sections.

Similarly to the 'Q1' file, 'Ground' is organized in 24 groups. One of these groups (group 19) is subdivided into a number of sections which are called from 'Earth' at distinct stages in the iteration process. It is here that Fortran sequences for the calculation of newly defined variables and output sequences are inserted. In order to identify the right location for coding in group 19 it is instructive to examine the solution sequence in the flow diagram in figure 7.3. Four nested loops can be identified pertaining to run number, time step, sweep number and slab number. 'Ground' has been used to calculate new variables in the case of the deflected jet and this will be described in chapter eight. For the undeflected jet output sequences for the centreline distribution of normalized radial velocity (V_{cl}/V_{in}), halfwidth based on 1% of the corresponding centreline velocity (0.5 X/D) and kinetic energy (KE) have been inserted in section six of group 19, i.e. at the end of iterating on a z slab. The Fortran statements are reproduced in appendix B 2. Thus, at the penultimate sweep and in this example at the end of the last z slab, the two dimensional field values of the variables concerned are accessed by the GETYX subroutine and the centreline values calculated. The variables are subsequently written to an output file 'JTPROF.RES' as illustrated in appendix B 3. The arrays were dimensioned at the beginning of 'Ground'. In addition to the variable arrays, arrays containing the grid geometry are accessed and nondimensional radial distances of the cell centres (Y/D(C)) and north faces (Y/D(N)) are written to the output file. The former distances are used for plotting the kinetic energy distribution. Since the radial velocities are stored at the north cell faces (section 5.2), Y/D(N) is used for plotting centreline velocity decay curves and jet halfwidth. In order to obtain profiles at jet cross sections output routines accessing the relevant two dimensional arrays were written. These are included in appendix B 2. An example of a file containing profile data at IY = 29 is given in appendix B 4. It contains the circumferential distribution of radial velocity (V1), kinetic energy

(KE), and normalized rate of dissipation (EP-NORM). These variables can either be plotted against normal distance from the jet centreline divided by the jet halfwidth (ETA) or against the angle (R/Y). Both ways of presenting data can be found in the literature and will be used accordingly for validation purposes.

7.2 Steady Undeflected Jet

The computational study of the three dimensional undeflected steady state jet represents the most widely documented case of the four flow configurations examined in this thesis. It was used for experimenting with the code with a view to optimize the computational mesh and numerical control parameters. Experimental data obtained by the author and reported in chapter six together with data from the literature was used for validation purposes. Experience gained from this first flow configuration fed later into the models for the transient undeflected jet and also the steady state and transient deflected jet.

The first part of this section (sections 7.2.1 to 7.2.4) describes preliminary investigations in which the model was optimized. Results of grid refinement and convergence studies are presented in section 7.2.1 together with results of test cases concerning the orientation of the co-ordinate system relative to the jet. The effect of turbulence on the flow development region is also examined. A study of inlet and outflow boundary conditions is reported in sections 7.2.2 and 7.2.3 respectively. This is followed by an examination of the effect of turbulence model constants on the flow field in section 7.2.4.

In the second part of this section results obtained with the optimized model are presented in different forms:

(i) centreline distributions in section 7.2.5

(ii) profiles at different jet cross sections in section 7.2.6

(iii) vector plots in section 7.2.7

(iv) contour plots in section 7.2.8

When variables for the entire flow field are stored, large numbers of plots can easily be generated for different parts of the computational domain. A choice must therefore be made to select meaningful representations which highlight the important characteristics of the jet under investigation. Centreline distributions and profile plots are particularly suited for nondimensional data presentation, thus allowing comparisons with results from the literature. These plots are also well suited to examine the effect of parametric studies by indicating a trend caused by parameter variations. Vector and contour plots on the other hand illustrate general flow patterns like recirculation zones and the distribution of particular variables. They also help to identify the jet's boundary and the development of the wall jet after impingement. The four forms of data presentation ((i) to (iv)) will be used in sections 7.2.5 to 7.2.8 with frequent cross references in order to establish a comprehensive picture of the characteristics of the jet.

7.2.1 Preliminary Investigations

The preliminary investigations were mainly concerned with:

1. grid refinement studies
2. convergence control
3. test cases to examine the effect of turbulence and the co-ordinate system orientation on the jet centreline velocity distribution.

These three aspects are in turn discussed below.

1. grid refinement

The computational mesh used for all predictions presented later in this chapter is depicted in figure 7.2. It comprises 17, 43 and 18 cells in x, y and z direction respectively. The grid density in y direction was considered to be the most important for correctly predicting the jet's velocity decay and rate of spread, particularly in the initial region. For this reason four different grid densities in y direction were examined. The objective was to find a grid independent solution while keeping the computational effort, both in terms of CPU time and storage requirements, to a minimum. The four grid densities considered were NY = 21, 43 and 60 uniformly spaced and NY = 43 nonuniformly spaced as shown in figure 7.2. Nondimensional centreline distributions of radial velocity, V_{cl}, jet halfradius, 0.5 r, and turbulence kinetic energy, KE were used as criteria for comparison. Experimental data for the three centreline curves was available from hot film and pitot tube measurements, and results are shown in figures 7.4 to 7.6. From figures 7.4 and 7.5 it is evident that 21 and 43 uniformly spaced radial cells are not adequate, in particular velocity and kinetic energy gradients cannot be adequately resolved by the coarse mesh in the flow development region. The sharp initial velocity drop is attributed to the relatively high level of turbulence kinetic energy associated with the incoming flow ($KE/V_{in}^2 = 0.45$). It is interesting to note in figure 7.6 how the kinetic energy oscillates near the nozzle exit, an occurrence which is more pronounced on the coarse mesh and much less evident on the NY = 60 grid. Again the coarser meshes appear not to be able to resolve steep gradients. The first experimental point in figure 7.6 must be viewed with some caution as discussed in chapter six. Along with the dip in kinetic energy at r/D = 10 goes a recovery of the mean velocity in figure 7.4 to a level much higher than measured, thus preserving the radial momentum. The halfwidth curves in figure 7.5 are based on 1 % of the centreline velocity. They are consistent with the centreline decay curves in that the rate of spread on the NY = 21 and NY = 43 uniform meshes is underpredicted by approximately the same amount that the centreline velocity is overpredicted.

From these observations it is evident that a nonuniform mesh should be employed in order to economize on computer resources. The nonuniform mesh with 43 cells eventually used is the result of three main considerations:

- a fine grid near the nozzle exit
- a reasonably fine grid at the wall at IY = NY
- the ratio of node spacings between neighbouring cells should not exceed 1.5

The nonuniform mesh can be seen to perform well and give good agreement with experimental data. Although gradually finer uniform meshes come closer to the measured points, even the NY = 60 grid does not yield the agreement obtained with the nonuniform NY = 43 mesh.

2. convergence control

In order to obtain a stable converging solution the iteration process needs to be slowed down artificially. Two different methods of achieving this have been outlined in section 5.4, viz. linear under - relaxation and false time steps. In this investigation the false time step method has been used for all variables other than pressure. Since the amount of under - relaxation needed is strongly problem dependent, some experimentation is required to find the right level. A relatively large false time step causes strong oscillations during the iteration process and is hence undesirable. Conversely time steps which are too small increase the number of iterations required, thus increasing computer time. To find an acceptable compromise the development of three variables (radial velocity, kinetic energy and dissipation rate) was monitored in one cell on the jet centreline eleven diameters downstream. The results for three different time steps, reproduced in figures 7.7 to 7.9, indicate similar trends for all three variables: Increasing under - relaxation by decreasing the time step has a dampening effect on the iteration process. While a value of 0.01 causes the solution to overshoot by more than 100 % (figure 7.9) too heavy under - relaxation would require more than 1000 sweeps of the entire flow domain to reach a converged solution. A time step of 0.001

was considered to be a reasonable compromise between the two extremes, the number of sweeps was set to 250.

3. cylindrical polar or body - fitted co-ordinates: a few test cases

Having decided on the grid density, number of sweeps and relaxation factor, a number of other parameters still needed definition. These were primarily the prescription of inflow and outflow boundary conditions, the level of turbulence associated with the incoming flow, and the constants in the two equation turbulence model. The choice for these settings is discussed in sections 7.2.2 to 7.2.4, however before attention is turned to this discussion, a few paragraphs will be devoted to the examination of an anomaly in the jet centreline velocity decay curve observed during the course of this investigation. The anomaly, which could eventually be traced back to the inflow boundary condition, is illustrated in figure 7.10. It shows the initial part of the centreline velocity curve (normalized with the inlet velocity) against radial distance (normalized with the side length of the nozzle hole, D). A sharp initial velocity drop is followed by a plateau of constant velocity at $V_{cl}/V_{in} = 0.92$ before the velocity gradually decays further. The plateau region extends approximately 4 D into the domain. This centreline velocity distribution does not agree with the classical jet velocity decay as reported in the literature (e.g. Abramovich [18]). This curve is characterized by a potential core at the inlet velocity level followed by a gradual velocity decay. For a closer examination of the velocity distribution in figure 7.10 test cases were run to study the effect on the potential core of turbulence and the co-ordinate system orientation relative to the jet. Although these test cases are of no immediate consequence for the final results presented later in this chapter, they provide insight into the flow structure of the jet development region in computational meshes generated in cylindrical polar and body fitted co-ordinates (BFC). The test cases addressed the following questions:

a) Is the pattern in figure 7.10 caused by turbulence?

b) Is the solution co-ordinate system dependent?

c) What effect does the inlet boundary condition have on the velocity decay curve?

In the following paragraphs a few remarks are made on test cases addressing each of these questions and the conclusions drawn are presented.

case a

In order to establish whether incoming turbulence kinetic energy quickly destroys the potential core and hence causes the sharp initial velocity drop, the laminar equivalent to the original case (figure 7.10) was modelled. The turbulence model was deactivated and the kinetic energy and rate of dissipation at the inlet boundary were set to zero. Since the Reynolds number based on the nozzle diameter is 42000, this is clearly an unrealistic assumption and can only serve to show the influence of turbulence on the flow development region. The initial part of the centreline velocity decay curve depicted in figure 7.11 still shows a sharp velocity drop followed by a plateau. The turbulence associated with the incoming flow does therefore not appear to have caused the pattern in figure 7.10.

case b

To examine the question whether the solution is co-ordinate system dependent three different flow configurations were considered and are briefly described below.

(i) In all jet flow examples the author has found in the literature that predicted a potential core at inlet velocity level using cylindrical polar co-ordinates, injection is along the z-axis. Unless body fitted co-ordinates are employed to model the hydraulic analogue under investigation, which will be discussed later, this is not possible in the present case as injection has to be along the radial (y) co-ordinate. To examine if the direction of injection affects the predictions, a simple model was designed (figure 7.12) in which injection takes place along the z-axis. The grid spacings of the original case along the jet and across the nozzle were maintained.

This model does not resemble the actual grid geometry but was merely meant as a test case. The result for this 1 radian segment (figure 7.13) shows a potential core at the inlet velocity level.

(ii) The two cases employing cylindrical polar co-ordinates seemed to indicate that a more realistic prediction could be obtained when the main flow direction was along the z-axis. The implication of this observation is that the radial momentum equation cannot adequately predict flows where the main flow direction is radial, an assertion which is rather suspect since no unreasonable assumptions were made in the mathematical formulation and the discretization process. Also, skewness of velocity vectors relative to the mesh, to which numerical diffusion can be attributed [84], is not present in the near nozzle region in either of the two cases. In order to examine further if the solution is co-ordinate system dependent, the two flow configurations (injection in the radial direction using the rig geometry and injection in z direction in a 1 radian segment) were modelled using body fitted co-ordinates. An option for BFC s is provided in PHOENICS, however data input in the 'Q1' file for nonuniform meshes is very elaborate. The grid generated for the body fitted equivalent of the original case is shown in figure 7.14 where the z-axis is now aligned with the jet centreline. The centreline velocity curve for the initial region is reproduced in figure 7.15 and shows a very similar characteristic to figure 7.10. The initial velocity drop is equally steep and followed by a plateau at $W_{cl}/W_{in} = 0.90$. The plateau is not as marked as the one in figure 7.10 and extends only approximately 3 D into the domain.

(iii) To complete this examination of co-ordinate system dependency the BFC equivalent to the injection into a 1 radian segment described above has been modelled. This was again meant as a test case which does not resemble the geometry of the analogue rig. The wedge shaped flow configuration is depicted in figure 7.16. The grid spacing in the flow direction and across the nozzle corresponds to the spacings used in the cylindrical polar model. The result of the

BFC simulation is reproduced in figure 7.17 which shows identical characteristics to figure 7.13 with a potential core at inlet velocity level.

Summarizing this examination of the second question raised above a few comments are called for comparing the two co-ordinate systems applied to the given flow configuration. In body fitted co-ordinates three linear momentum equations are solved with factors introduced to allow for curvature and divergence of grid lines. This approach is distinctly different from using cylindrical polar co-ordinates where the discretized equations have been derived from the momentum equations in cylindrical polar form. Modelling a cylindrical polar geometry in BFC s can therefore give some indication on whether a solution is co-ordinate system independent. Comparing figures 7.10 and 7.15 and figures 7.13 and 7.17 demonstrates very close similarity between the equivalent cases, it is therefore assumed that the co-ordinate system does not affect predictions in the near nozzle region. Since cylindrical polar co-ordinates are computationally more economical, BFC s were here abandoned and all further runs performed in cylindrical polar co-ordinates.

case c

In the preceding paragraphs it has been established that the solution is independent of the co-ordinate system, however the anomaly in the initial region in figure 7.10 has not yet been clarified. The last question therefore addresses the prescription of the inlet boundary condition. A number of different conditions have been examined and the pattern of figure 7.10 could be shown to be caused by this specification. For reasons of clarity the different options considered are described in a separate section below.

7.2.2 Inlet Boundary Condition

The inlet boundary is located at the nozzle exit some distance away from the axis of symmetry (figure 7.2). The fact that injection does not occur at the domain boundary has implications for the boundary condition specification. It can be treated in two ways:

1. making the injector column inaccessible to flow by blocking the region and injecting from the blocked cell faces
2. moving the IY = 1 boundary by the injector radius and injecting from the first y - cell

Both ways of treating the inlet boundary are feasible and produce identical results, however, since the second method requires less elaborate data input in the 'Q1' file, it has been adopted for all further runs. The two methods are discussed in the following paragraphs with reference to the source term treatment outlined in section 5.4. The discussion is followed by an explanation of the anomaly in the jet prediction, viz. the sharp initial velocity drop and the plateau at $V_{cl}/V_{in} = 0.92$ (figure 7.10). Finally, the inlet boundary condition to be used in this study is specified.

1. Injection from blocked cells

Problems may arise when specifying an inflow source at a blockage where IY > 1. The difficulties are due to the way the convective part of the radial momentum equation is treated and concern both the inlet momentum specification and momentum in cells adjacent to blockages. The problems and ways to resolve them are briefly described below. Helpful comments during the examination have been received from the originators of the program, CHAM UK Ltd. [95].

(i) inlet momentum

Apart from mass sources at the first (IY = 1) and last (IY = NY) radial cells, the convective part of the mass inlet source (equation 5.14) is distributed between the north and south staggered V - momentum cells. The one dimensional polar situation is depicted in figure 7.18. Thus [85],

$$S_{V_s} = \frac{\dot{m}}{2} (V_V - V_s) \qquad (7.1)$$

$$S_{V_n} = \frac{\dot{m}}{2} (V_V - V_n) \qquad (7.2)$$

where the mass flow source $\dot{m}$ is defined in equation (5.15), V_V is the radial velocity value and V_s and V_n are the south and north cell face velocities. Hence, applying a momentum source in front of a blockage results in only one half of the radial momentum being convected into the domain. In order to prescribe the correct inlet momentum, an additional momentum source must be inserted in the 'Q1' file.

(ii) momentum in cells adjacent to blockages

For the one dimensional case depicted in figure 7.18 the inflow of momentum across the south boundary (at P) of the staggered V_n momentum cell is given by [85]:

$$V_s \dot{m}_P = V_s \rho \frac{V_n + V_s}{2} A_n \qquad (7.3)$$

Thus the momentum across the south boundary is the mass flux at P multiplied by the radial velocity at s. In the present case the velocity at s is zero since the cell face area is zero. Hence the flow of momentum (equation 7.3) is also zero. However, the mass flow across face P still appears in the coefficient of the discretized momentum equation:

$$a_s (V_s - V_n) + S = 0 \qquad (7.4)$$

where

$$S = \dot{m}_{in} (V_{in} - V_n) \qquad (7.5)$$

hence

$$V_n = \frac{V_s a_s + \dot{m}_{in} V_{in}}{a_s + \dot{m}_{in}} \qquad (7.6)$$

With reference to figure 7.18 the correct solution of this equation is $V_n = V_{in}$. However, since $V_s = 0$ and $a_s \neq 0$, equation (7.6) reduces to

$$V_n = \frac{\dot{m}_{in} V_{in}}{a_s + \dot{m}_{in}} \qquad (7.7)$$

This is obviously not the correct solution of the momentum equation. To correct equation (7.7) velocity V_s needs to be fixed to the value of V_{in}. Equation (7.6) then reads:

$$V_n = \frac{V_{in} a_s + \dot{m}_{in} V_{in}}{a_s + \dot{m}_{in}} = V_{in} \qquad (7.8)$$

To fix V_s to the value of V_{in} this velocity must be defined for the blocked injector column at IY = 1. Prescribing a velocity in the blocked region is numerically necessary and has no physical significance. An alternative would be to cut the south convective link in equation (7.6) by setting a_s equal to zero.

2. Moving the IY = 1 boundary

The origin of the radial co-ordinate can be displaced by the injector column radius. Hence injection takes place at the south face of the first radial cell rather than some distance into the domain. The input command RINNER facilitates this offset. Its use renders the extra input statements discussed above unnecessary:

(i) The inlet momentum source is not divided between the north and south cell faces but applied entirely at the north face, thus

$$S_{V_n} = \dot{m} (V_V - V_n) \qquad (7.9)$$

No additional momentum source is required.

(ii) The south convective link is cut by setting the central coefficient equal to zero. Equation (7.6) then reads:

$$V_n = \frac{\dot{m}_{in} V_{in}}{\dot{m}_{in}} = V_{in} \qquad (7.10)$$

All results employing cylindrical polar co-ordinates presented in this study were obtained by using the RINNER command to offset the IY = 1 boundary by the injector column radius. It is important to realise one limitation of the RINNER facility, viz. it cannot be applied selectively. Hence the entire z extent of a three dimensional mesh is displaced radially.

3. Explanation of anomaly in jet centreline prediction

When examining the velocity decay curve in figure 7.10 two distinct features must be distinguished: the sharp initial velocity drop and the following plateau at $V_{clin}/V_{in} = 0.92$.

The inlet boundary condition used to predict the velocity decay in figure 7.10 applies the inlet momentum in radial direction assuming a constant inlet velocity across the nozzle. This in effect models a 'fan' jet. In the absence of entrainment the jet expands with the grid as the radial distance increases. From the viewpoint of continuity, the area through which the jet fluid is travelling increases in proportion to the radial distance, r. In order to conserve continuity the velocity will therefore have to decay proportionally to 1/r. Hence the velocity decays immediately from the nozzle exit plane and no potential core is observed. Figure 7.19 compares two velocity decay curves: initial

region with circumferential motion as in figure 7.10, and velocity decay without circumferential motion leading to a 1/r velocity distribution.

To understand the second feature, i.e. the velocity plateau following the initial drop, it is instructive to examine the pressure field near the nozzle exit shown in figure 7.20. If one considers streamlines emerging from the nozzle and applies Bernoulli then the pressure must increase with decreasing velocity. Since the pressure at the domain boundary has been fixed to zero, it has to be considerably negative at the nozzle. The pressure contours 'fan out' from the middle of the nozzle. At the centreline the velocity decays radially and hence the pressure increases rapidly. Towards the outer part of the nozzle the radial pressure gradient is less steep, this is attributed to high levels of circumferential diffusion in the jets shear layer and the circumferential pressure gradient. From the pressure contours in figure 7.20 it is evident that the gradient causes a circumferential motion towards the jet centre. The contours of circumferential velocity in figure 7.21 underline this observation, all positive circumferential velocity values point towards the centreline. What is therefore happening is that the initial outward fanning of the jet at the nozzle is being counteracted by the inward circumferential motion. The jet is gradually changing from a fanning jet to one with more classical characteristics where the velocity plateau represents a transitional region between the two.

Having thus established the reason for the velocity curve in figure 7.10, the obvious modification to the inlet boundary was to decompose the inlet velocity into a radial and circumferential component such that the resultant velocity in each inlet cell was aligned with the jet centreline. Figure 7.22 shows the effect of this modification on the velocity decay near the nozzle exit. A sharp initial drop is no longer noticeable, instead the velocity decays very gradually before decreasing more rapidly after approximately 2 D. The fact that a slight decay occurs immediately after the exit plane is attributed to diffusion caused by the k - ε turbulence model. This was also observed in figures 7.13 and 7.17.

4. Specification of inlet boundary condition

To finalize the inlet boundary specification an assumption must be made regarding the velocity profile at the nozzle exit plane. In order to observe a potential core the flow must be fully developed. In the present case this cannot be expected since the nozzle hole length / diameter ratio is 1.6 and hence too small for the flow to develop. The experimental results in chapter six confirm the absence of a potential core. Thus, to predict a velocity decay that agrees with measured data neither of the two inlet boundary conditions discussed above appeared suitable. Due to the lack of detail about the inlet velocity profile, a parabolic velocity distribution across the nozzle was assumed where there is relatively little fluid in the outer part of the jet. Entrainment therefore affects the centreline velocity very soon after injection. Furthermore, to obtain the 'classical' velocity decay curve, velocity vectors in each inlet cell were resolved into their radial and circumferential components such that the resultant velocity was aligned with the jet centreline. Thus the equivalent case to figure 7.22 was modelled with a parabolic inlet profile. Figure 7.23 compares the centreline velocity decay with experimental data. The numerical predictions were obtained with the standard k - ε turbulence model which is known to overpredict the spread of a jet and hence underpredict the centreline velocity (section 4.4) The discrepancy between prediction and experimental results was therefore not attributed to the inlet boundary condition but to the turbulence model as will be shown in section 7.2.4.

Along with the inlet momentum the turbulence parameters attributed to the incoming flow need to be specified. A literature survey yielded values for the normalized turbulence kinetic energy ($k/V_{cl,in}^2$) in the range of 0.0012 [26] to 0.03 [25]. Reference [62] uses a value of 0.0045 at the inlet for a flow over a backward facing step. In order to set the level of turbulence kinetic energy associated with the incoming flow three different values for $k/V_{cl,in}^2$ were considered: 0.45, 0.045 and 0.0045. The effect of these settings on the centreline distributions of radial velocity and kinetic

energy is illustrated in figures 7.24 and 7.25. It can be seen that the increased diffusion associated with high levels of kinetic energy leads to a more rapid velocity decay in the flow development region. Further into the domain the difference between the three curves is less pronounced, indicating that turbulence generated within the computational domain becomes more dominant. A value of $k/V_{cl,in}^{2} = 0.0045$ was chosen for all further runs as it gave, together with a modified constant in the turbulence model, very good agreement with experimental results. The dissipation rate, ε, was estimated as suggested in reference [62] from

$$\varepsilon = 1.826\ k^{3/2} / D$$

7.2.3 Outflow Boundary Condition

The objective of this thesis is to examine the flow field generated by a single jet issuing into a combustion chamber model. The restriction to a single jet eliminates possible interference from other jets in a multi - hole nozzle arrangement, however, it presents difficulties from a computational point of view, since no symmetrical conditions can be assumed. Modelling the entire 360 degree extent is computationally expensive and clearly undesirable. Earlier flow visualization work [20, 21] indicated that a jet issuing into the opposite direction of the circular outflow (located in the tank top) was not noticeably affected by the asymmetry. It was therefore decided to restrict the computational domain to a 45 degrees segment (figure 7.2) with symmetry assumed about the jet plane at $\theta = 0$ degree, the underlying assumption being that the $\theta = 45$ degrees boundary does not significantly influence the jet characteristics. This latter supposition has been examined by applying both a prescribed pressure boundary and a symmetry boundary at $\theta = 45$ degrees. In the first case fluid could leave and enter the domain and a compatible flow field established itself during the iteration process. When a symmetry condition was applied at $\theta = 45$ degrees the circumferential wall at $r = R$

was replaced with a prescribed pressure boundary to allow displaced fluid to leave the domain. Results for the two conditions are discussed in the following paragraphs. They confirm that the $\theta = 45$ degrees boundary has no discernible effect on the jet behaviour.

Figures 7.26 to 7.28 compare vector plots of the entrainment region and kinetic energy contours in the r - θ plane at three z locations: z = 27 mm, 68 mm and 72 mm (figure 3.1). The z = 68 mm plane is just below the nozzle exit whereas z = 72 mm is at the jet centreplane. Plots on the left (a)) relate to the symmetry boundary condition, the right hand set (b)) was predicted applying a fixed pressure boundary at $\theta = 45$ degrees. The two sets of plots are very similar with differences in the flow field only near the free - entrainment boundaries. In figure 7.26 both sets show a distinct recirculation zone which is more marked as a consequence of the wall jet when a free - entrainment boundary is applied at $\theta = 45$ degrees. In set a) fluid can be seen to leave the domain near the jet centreline while there is hardly any motion discernible towards the symmetry boundary. This is contrasted by the wall jet in set b) which is particularly noticeable in the lower part of the analogue model at z = 27 mm where fluid is leaving the domain across the $\theta = 45$ degrees boundary. With respect to the near nozzle region figure 7.27 illustrates clearly that the flow in the vicinity of the nozzle is not affected by the boundary conditions at $\theta = 45$ degrees. Both sets show the same entrainment pattern. The inward directed flow at z = 27 mm forms part of a large recirculation zone as can be seen in figure 7.29 which compares entrainment velocity fields in three different r - z planes (33.0 degrees, 12.0 degrees, 0.5 degrees). Again the strong effect of the wall jet is noticeable in case b), particularly at $\theta = 33$ degrees where fluid is forced back into the domain. Opening the tank wall at r = R on the other hand reduces the motion to an insignificant level at $\theta = 33$ degrees. It is interesting to note that in the absence of the wall jet a distinct recirculation zone forms near the jet's symmetry plane.

Together with vector plots, contours of constant kinetic energy were drawn and are reproduced in figures 7.28 and 7.30. The values of the contours are summarized in the table below.

contour no.	k [(m/s)**2]
1	0.5
2	0.2
3	0.1
4	0.09
5	0.08
6	0.05
7	0.03

kinetic energy contour values

The kinetic energy field highlights particularly active flow regions through the way mean velocity gradients enter into the k generation term (equation 4.13). Hence, from the jet mixing point of view, k contours help identify the jet's shear layer and thus regions critical for the mixing process. A comparison of the two sets in figures 7.28 and 7.30 confirms the observation made earlier, viz. the flow development region is hardly affected by the boundary condition applied at $\theta = 45$ degrees. In figure 7.28 no meaningful k contours could be drawn at $z = 27$ mm since the level of turbulence was very low. An increased turbulence level in the wall jet is evident from set b) in both figures.

The above - mentioned figures illustrate that only the flow near the prescribed pressure boundaries is affected and, since this motion is weak, the main flow structure associated with the jet remains largely unaffected. For this reason a free entrainment boundary was applied at $\theta = 45$ degrees to model the segment of the hydraulic analogue in all further runs presented in this chapter.

7.2.4 Specification of Turbulence Model Constants

The inability of the standard k - ε model [60] to correctly predict the centreline velocity decay and the rate of spread was discussed in section 4.4.3. This failure is generally attributed to the source term in the ε equation (4.20) which has consequently been the focus of much effort to improve the model's performance. In this study the effect of the constant C_1 on centreline variations of the radial velocity V_{cl} and the kinetic energy k has been considered and compared with hot film and pitot tube data. The runs were performed on the nonuniform NY = 43 mesh with $k/V_{cl,in}^2 = 0.0045$ and a parabolic inlet velocity profile aligned with the jet axis. A range of C_1 values was examined and the results for C_1 = 1.44, 1.47 and 1.53 are shown in figures 7.31 and 7.32. C_1 = 1.44 is used in the standard k - ε model. Figure 7.31 clearly illustrates the effect of C_1 on the predicted velocity decay and hence spread of the jet, i.e. an increase in C_1 leads to reduced rate of spread as desired. C_1 = 1.47 was found to agree favourably with experimental data. In this context it is interesting to note that Kuo and Bracco [26] have found C_1 = 1.50 gives good agreement for the centreline velocity decay. They modelled a free jet with a constant velocity profile at the inlet. The different values for C_1 found for similar flows illustrates the sensitivity of the model and shows that no universal set of turbulence model constants can applied to seemingly similar problems.

The effect of C_1 on the kinetic energy distribution is only significant in the initial region, from r/D = 11 onward the three curves agree reasonably well with the measured points and do not deviate much from one another. Since C_1 appears in the source term of the ε equation, a high value results in an increased dissipation rate which in turn leads to a depressed kinetic energy level. This trend is evident in figure 7.32 where C_1 = 1.53 results in a 40 % lower kinetic energy value than C_1 = 1.44. Along with the relatively low kinetic energy level for C_1 = 1.53 goes a slow velocity decay in figure 7.31. This was to be expected since reduced turbulence leads to a lower mixing rate. A value C_1 = 1.47 was adopted for all further runs in this thesis.

7.2.5 Analysis of Predicted Flow Field

As pointed out in the introduction, the prediction of the undeflected steady state jet was primarily intended to optimize the model with a view to obtaining agreement between predictions and experimental data, and hence gain confidence in the numerical method. The significance for a Diesel engine application is clearly rather limited, more valuable information about the mixing process can be expected from the transient simulation and the modelling of a jet issuing into a swirling flow field. Before attention is turned to these latter aspects, the remainder of this section completes the presentation of results for the undeflected steady jet and discusses their importance in the context of the DI Diesel engine combustion chamber model.

For reasons of clarity the results of the preliminary studies reported in sections 7.2.1 to 7.2.4 are summarized below:

(i) nonuniform mesh with NX = 17, NY = 43 and NZ = 18

(ii) parabolic inlet velocity profile

(iii) $k/V_{cl,in} = 0.0045$

(iv) free entrainment boundary at $\theta = 45$ degrees

(v) turbulence model constant $C_1 = 1.47$

Centreline distributions of radial velocity and kinetic energy have been used in the previous sections for validation purposes. The parameters were examined separately, thus in the analysis of turbulence model constant C_1 for example, parameters (i) to (iv) took their final form. This iterative process allowed to analyse the effect of model settings in isolation.

The centreline velocity decay and the corresponding rate of spread are illustrated by solid lines in figures 7.31 and 7.5, the kinetic energy distribution is shown in figure

7.32. Together with these figures, profiles at different jet cross sections provide an insight into the hydrodynamic processes resulting from injection.

Cross sectional distributions are presented as similarity profiles for the radial velocity and in semi - nondimensional form for kinetic energy and dissipation rate in figures 7.33 to 7.36. The profiles are calculated at the five radial positions for which experimental results were reported in chapter six, i.e. r/D = 11, 20, 29, 38 and 47. Full self similarity for a free jet can only be assumed for r/D > 70 [73]; in this study complete self similarity is therefore not expected, particularly because of the presence of the wall at r/D = 54 with the resulting wall jet and recirculation zones. Despite these features the profiles of normalized velocity against jet half width in figures 7.33 and 7.34 show that self similarity is almost reached near the jet centreline. In figure 7.33 computed values for the five radial positions are compared with the velocity similarity curve for a free jet given by Abramovich [18], in figure 7.33 the same curve is compared against experimental results. Agreement is very favourable for half width values less than 1.2, indicating that near the jet centreline the confined nature of the flow does not significantly affect the spread of the jet. Furthermore, at the centreline the wall jet does not extend far into the domain as it is not noticeable at r/D = 47, an observation confirmed by contour plots of kinetic energy and circumferential velocity (figures 7.28 b and 7.37). Further away from the centreline deviations are noticeable which may be attributed to (i) the relative closeness to the nozzle exit, particularly of profiles at r/D = 11 and 20 and (ii) the influence of the recirculation zone on the jet's shear layer. Hoholis [28] reports an inaccurate prediction of the eddy's centre in simulations of a similar flow configuration employing the Hybrid scheme. He bases his observation on comparisons with results obtained with the QUICK scheme, however, does not substantiate it with quantitative experimental data. If the predicted location of the recirculation zone must be viewed with some caution then this will have an immediate effect on the jet's spread and hence on the similarity profiles. Experimental

data in figure 7.34 suggests that the radial velocity near the jet's edge is slightly higher than predicted.

The predicted and measured turbulence kinetic energy distributions are shown in figure 7.35. For the positions closest to the nozzle exit the calculated curves are significantly higher than the measured values. This trend was also observed by Kuo and Bracco [26] in their jet studies at r/D = 8 and 12. It was reported [26] that changes in C_1, including a variable C_1 model, did not remedy the failure to accurately predict the kinetic energy distributions near the nozzle. At radial positions r/D > 29 the agreement is much improved. The fact that the discrepancy between predicted and measured data is significant in the early part of the jet where mean velocity gradients are large and differ considerably in space suggests that the concept of isotropy used in the turbulence model is too crude to model the kinetic energy distribution in the early stages of the mixing process.

Similar to figure 7.35, figure 7.36 shows profiles of the dissipation rate ε normalized with the centreline velocity at each of the five radial positions under consideration. The experimental data is taken from Taulbee et al [74] who inferred the dissipation rate from LDA measurements in a free turbulent round jet. They observed a fair degree of scatter in the data in the centreline region and considered the measurements to be somewhat inaccurate. However, in the absence of other experimental data of dissipation profiles their curve is reproduced in figure 7.36. Agreement with predicted profiles is only moderate with a fair degree of spread, particularly near the centreline. As was also observed by Taulbee et al, the calculated profiles fail to predict the measured peak at 0.05 radians.

An alternative way of obtaining insight into the hydrodynamic processes resulting from injection is to examine vector and contour plots. Velocity vectors in selected planes have been presented in figures 7.26 b, 7.27 b and 7.29 b. They give a qualitative picture of the flow field, particularly of the recirculation zone formed as a result of strong shear

induced entrainment, the entrainment region in the vicinity of the nozzle and the wall jet. More quantitative information can be gained from contour plots of kinetic energy k, circumferential velocity U and axial velocity W. The k - contours in figure 7.28 b and 7.30 b clearly indicate regions of intense activity in the jet boundary and in the wall jet, but they also highlight regions of weak fluctuating motion. Since turbulent transport is an important contributor to the mixing process this is highly significant from a practical point of view. A low mixing rate will ultimately lead to poor combustion performance. Contours of constant circumferential and axial velocity in different planes are shown in figures 7.37 and 7.38. Their values are summarized below:

contour no.	U	W
1	-0.2	-0.6
2	-0.1	-0.3
3	0.0	-0.1
4	0.01	-0.02
5	0.02	0.0
6	0.05	0.02
7	0.1	0.04
8	0.2	0.06
9		0.08
10		0.10
11		0.12
12		0.14
13		0.16
14		0.18
15		0.20

circumferential and axial velocity contours

In figure 7.37 a negative sign indicates velocities directed away from the centreline, in figure 7.38 negative velocities are directed downward. Of particular interest are the zero velocity contours which help locate the centre of the recirculation zone. Near the jet's axis of symmetry this is fairly close to the wall. The largest extent of the wall jet into the flow domain is approximately 35 mm on the jet centreline. The wall jet diminishes gradually as it spreads. It would therefore appear that the wall jet itself is, apart from its contribution to turbulence generation, not too significant in the mixing process, but rather that the large eddy is more important. Another interesting feature in figure 7.38 is

the bunching of contours in the vicinity of the nozzle indicating that the entrained fluid is being accelerated into the jet.

7.3 Transient Undeflected Jet

For the spatial discretization in transient simulations essentially the same model was used as for the steady state case. To account for time dependency the time loop in the flow diagram (figure 7.3) was activated and a fully implicit scheme was specified for temporal discretization. This scheme bases the spatial derivatives on new time level values [81]. The Courant stability criterion (section 5.3.1) was thus avoided which could not have been satisfied for reasonable time steps near the nozzle where the grid spacing is very fine and velocities are high. Using the time interval $\Delta t = 3$ ms eventually chosen in this study, a typical Courant number on the jet centreline and a few diameters into the domain is in the order of 10. Hoholis [28] observed a time step independent solution with an implicit scheme and a Courant number Co = 2.5 based on comparisons with an Alternate Direction Implicit (ADI) scheme. In the present study the effect of time step size on the steady state approach was examined for the radial velocity and results are detailed below in section 7.3.1. This is followed by the presentation and discussion of results in section 7.3.2 focusing on three distinct aspects of the jet development. The first part presents jet tip penetration predictions in nondimensional form and compares results with experimental data. The second part provides vector plots in selected planes which provide insight into the spatial and temporal development of the flow. Finally, the third part deals more directly with the Diesel engine application by illustrating simulated air / fuel ratio contours in the combustion chamber model.

7.3.1 Preliminary Investigation

Since no changes were made to the spatial discretization model the preliminary investigation was aimed at specifying a suitable time step size and ensuring that the final solution was time step independent. Figure 7.39 shows the approach to steady state of the radial velocity V on the jet centreline at r/D = 11, plotted for four different time steps ranging from 1 to 10 ms. While all four curves eventually reach the same steady state value, they differ significantly during their approach. Since this approach is of particular interest when defining the jet tip penetration, a sufficiently small time step had to be chosen. A time interval $\Delta t = 3$ ms was considered to be an acceptable compromise between accuracy and required computer time.

7.3.2 Analysis of Predicted Jet Development

Figures 7.40 to 7.42 illustrate the jet tip penetration on the centreline in dimensional and non-dimensional form. Time profiles at the five radial positions considered earlier are given in figure 7.40. The 'overshooting' particularly at the inner radii has been the focus of some attention but measures like stronger underrelaxation did not change this behaviour. Since the profile shape makes it rather difficult to define the jet tip arrival time, it was decided to follow the practice suggested by Kuo and Bracco [26] and define the arrival time as the time needed for the jet to reach 70 % of its steady state centreline value. In figure 7.41 the 70 % steady state centreline velocity is plotted against r/D. Also shown are velocity curves at a number of time steps, ranging from 9 ms to 120 ms. The jet tip arrival is then defined as the point of intersection of a transient profile with the 70 % steady state curve. In figure 7.41 it is possible to see the steady state jet centreline distribution developing, i.e. 100 % centreline velocity.

A Reynolds number dependency of the jet arrival time is reported and a scaling law suggested [26] that applies to a range $8600 < Re < 135000$. The Reynolds number in this study is 42000 and figure 7.42 indicates excellent agreement between the scaling law and computational data inferred from figure 7.41. Also shown in figure 7.42 are experimental results obtained by the author and presented in chapter six together with experimental values reported by Witze [47]. The results from chapter six are based on six repeats of an injection and show a fair degree of scatter. The extreme values at each radius are shown in figure 7.42. Moreover, there is a marked deviation between the measured penetration time and values predicted both in this study and by Kuo and Bracco [26]. The fact that a relatively low sampling rate of 749 Hz was used during the experiments might suggest that the experimental data must be viewed with some caution. It is however interesting to note that Witze [47] obtained his experimental data with a TSI hot film probe similar to the one used in this study, using a maximum sampling rate of 36 kHz. His data clearly shows a slower penetration rate than predicted and lies well within the range of experimental values obtained in this study. For this reason it is tentatively concluded that the predicted penetration rate is approximately 20 % to 30 % too high, with larger discrepancies occurring further away from the nozzle. In view of the importance of the jet penetration rate to the Diesel engine application, further measurements, possibly with LDA, would be desirable.

Figures 7.43 to 7.46 show velocity vector plots of a selection of surfaces covering the injection period ($t_i = 300$ ms). While the nondimensional form of data presentation in figures 7.41 and 7.42 focused on centreline values, vector plots help visualize the temporal evolution of the flow in the entire domain. For maximum clarity different scaling factors for the velocity vectors have been used and are indicated on the individual figures. Throughout any set of plots in a figure the scaling factor has not been altered. The flow development in the r - θ and r - z planes bisecting the jet's axis of symmetry is illustrated in figures 7.43 and 7.44. For reasons of clarity velocity vectors in the immediate vicinity of the nozzle exit are not plotted as they are of no

importance to the jet penetration and only obscure the flow field in the entrainment region. Impingement can be seen to occur approximately 120 ms after injection. As time progresses fluid is forced sideways and downwards, beginning to form the wall jet. It is interesting to note that after impingement the jet itself does not appear to change up to some distance beyond midway into the domain, indicating that the recirculation zone to its side has already established itself at the time of impingement. The wall jet has an amplifying effect on velocities in the vicinity of the wall, however, its influence does not appear to extend far into the domain. This is confirmed by figures 7.45 and 7.46 illustrating the temporal evolution of the flow field well removed from the jet axis at $\theta = 33$ degrees and $z = 27$ mm respectively. The velocity magnitudes are small as indicated by the scaling factors, however, in figure 7.45 a distinct motion towards the injector is discernible from 30 ms onwards in the region around half the domain radius. This motion forms part of the large eddy that has formed next to the jet and occupies a large part of the domain. Similarly, at $\theta = 33$ degrees fluid is drawn to the jet by the action of entrainment in the very early stages of the injection process. As time progresses the recirculating motion intensifies and the effect of the wall jet becomes evident in the r - θ plane after 120 ms. While activity near the wall increases and more fluid is being pushed sideways, the flow field in the central part of the domain and near the injector remains largely unaffected. Figure 7.46 illustrates the development of the flow field caused by shear - induced entrainment in the r - z plane at $\theta = 33$ degrees. Entrainment starts immediately after injection and the flow field appears to be largely established after 120 ms. No vertical motion near the wall is observed, suggesting that fluid leaving the domain in the r - θ plane at $\theta = 33$ degrees is merely displaced fluid and not part of the wall jet.

More insight into the jet development, particularly its spread and the formation of the wall jet, can be gained by examining contours of a scalar quantity subjected to convective and diffusive transport. In this study concentration, C, is being solved for to simulate the development of air - fuel ratios. Results are shown in figures 7.47 to 7.49.

The concentration associated with the incoming flow was set to unity while zero concentration was prescribed as an initial condition for the entire domain. In figures 7.47 and 7.48 the development of four different air - fuel ratios is illustrated: 10 : 1, 14 : 1, 25 : 1 and 100 : 1. The contour values are summarized in the following table.

contour no.	air - fuel ratio
1	10 : 1
2	14 : 1
3	25 : 1
4	100 : 1

air - fuel ratio contours

The figures illustrate very clearly the progressive development of the free and wall jets in 60 ms intervals. Wall impingement of the weakest mixture contour occurs after approximately 150 ms, i.e. about 30 ms after the jet first hit the wall. The contours follow very much the growth of the jet as shown in figures 7.43 and 7.44. In particular, the spread of contours does not appear to be significantly larger than the spread in velocity, suggesting that convective transport dominates and diffusion plays a minor part in the mixing process. From a practical point of view this is important and measures designed to enhance the mixing rate must clearly focus on convective transport.

The progressive development of contours for a slightly weaker than stoichiometric air - fuel ratio, 25 : 1, is illustrated in figure 7.49. The interval between contours in figures 7.49 a) and b) is 30 ms while in figure 7.49 c) the interval is 15 ms. Wall impingement occurs after 165 ms, corresponding to 1.2 ms or 14.5 degrees of crank angle in the engine on which the analogue model is based. A slowing down of the jet is apparent from the bunching of the contours. The spread of the wall jet in the axial z direction is much more rapid than that in the angular sense (θ direction). This is clearly

seen in figure 7.49 c) which shows the development of the wall jet viewed from the end of the jet. It is also clear that the wall jet spreads at a much slower rate than the development of the rest of the jet.

In closing this section it may be concluded that a jet issuing into a quiescent combustion chamber leaves large regions of the flow domain occupied by an uncombustable mixture. Although the simplified chamber geometry and the absence of piston motion and hence squish limit the practical importance of the simulation, it is evident that this injection configuration would lead to poor combustion performance. To improve the performance it would be necessary to introduce swirl into the chamber to enhance the mixing process.

7.4 Concluding Remarks

In this chapter the numerical procedure used to predict the flow field generated by an undeflected steady state and transient jet has been outlined and results were presented. Preliminary investigations in respect of the co-ordinate system orientation, inlet boundary condition and sensitivity towards the outflow boundary condition were used to adjust the model. Experimental results for centreline distributions of radial velocity and kinetic energy and profiles at different jet cross sections were used for validation purposes. Numerical predictions generally showed good agreement with experimental data. Some differences were observed in the velocity similarity profiles near the edge of the jet and in the kinetic energy profiles near the nozzle exit. Possible explanations were discussed such as the hybrid scheme approximation for convection and the turbulence model. The transient jet was discussed with reference to vector plots in selected planes and air - fuel ratio contours. The fuel mixture was found to be very weak in large parts of the chamber model, indicating that the injection arrangement without swirl would lead to poor combustion efficiency.

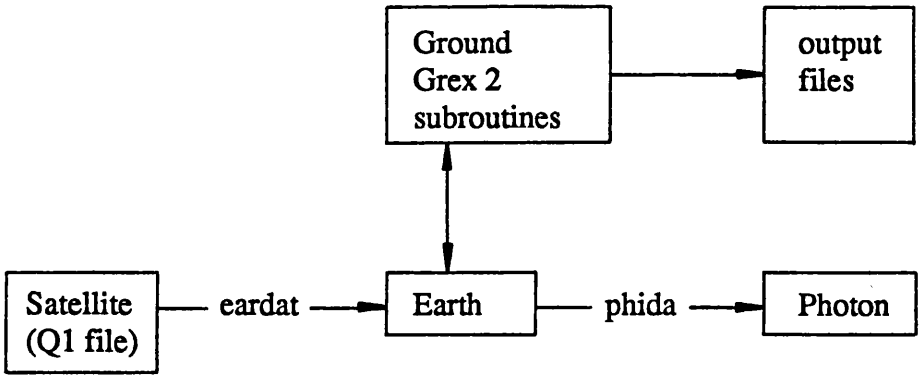

Fig. 7.1: PHOENICS program elements

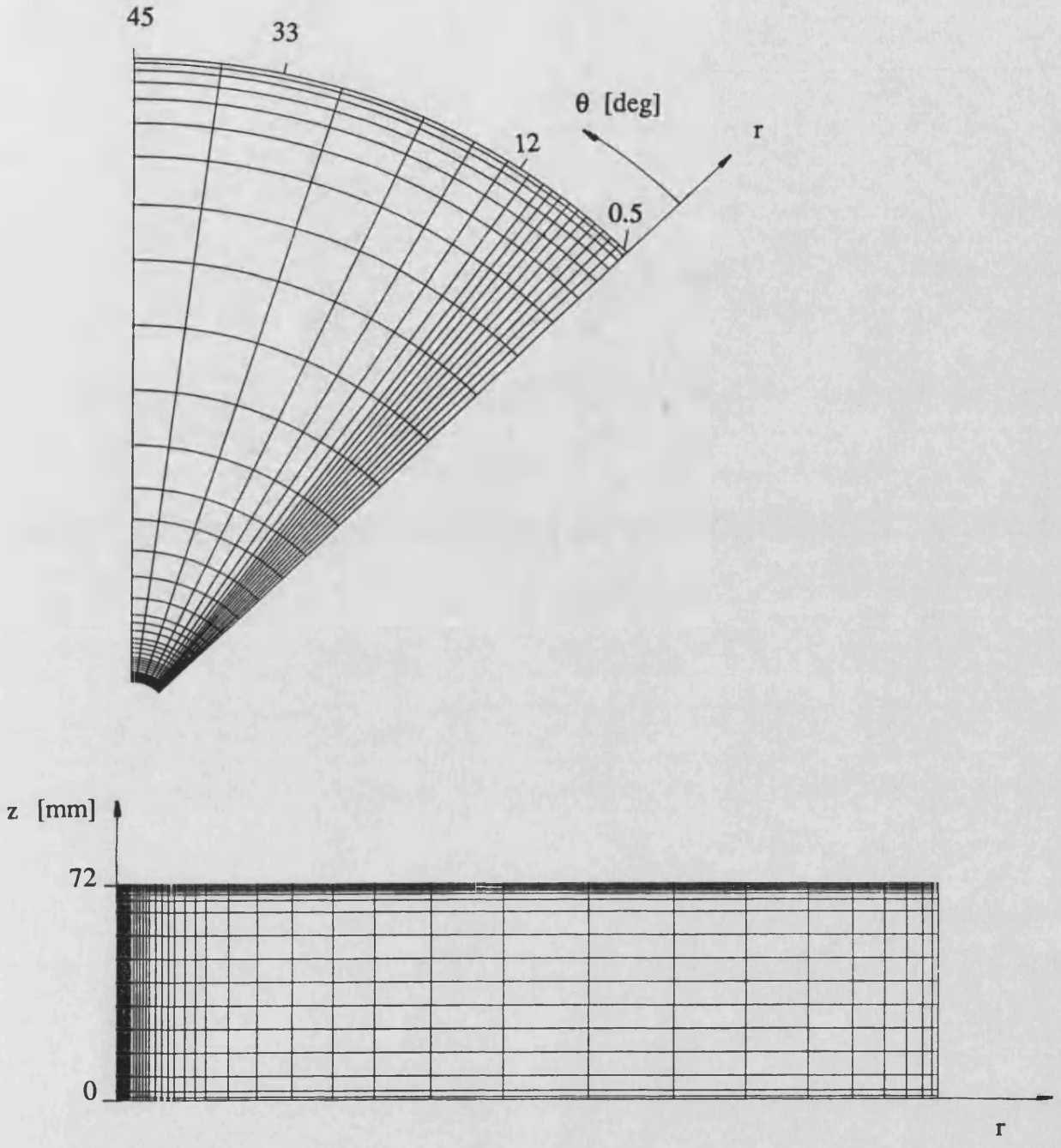

Fig. 7.2: Computational mesh for undeflected jet in cylindrical polar co-ordinates

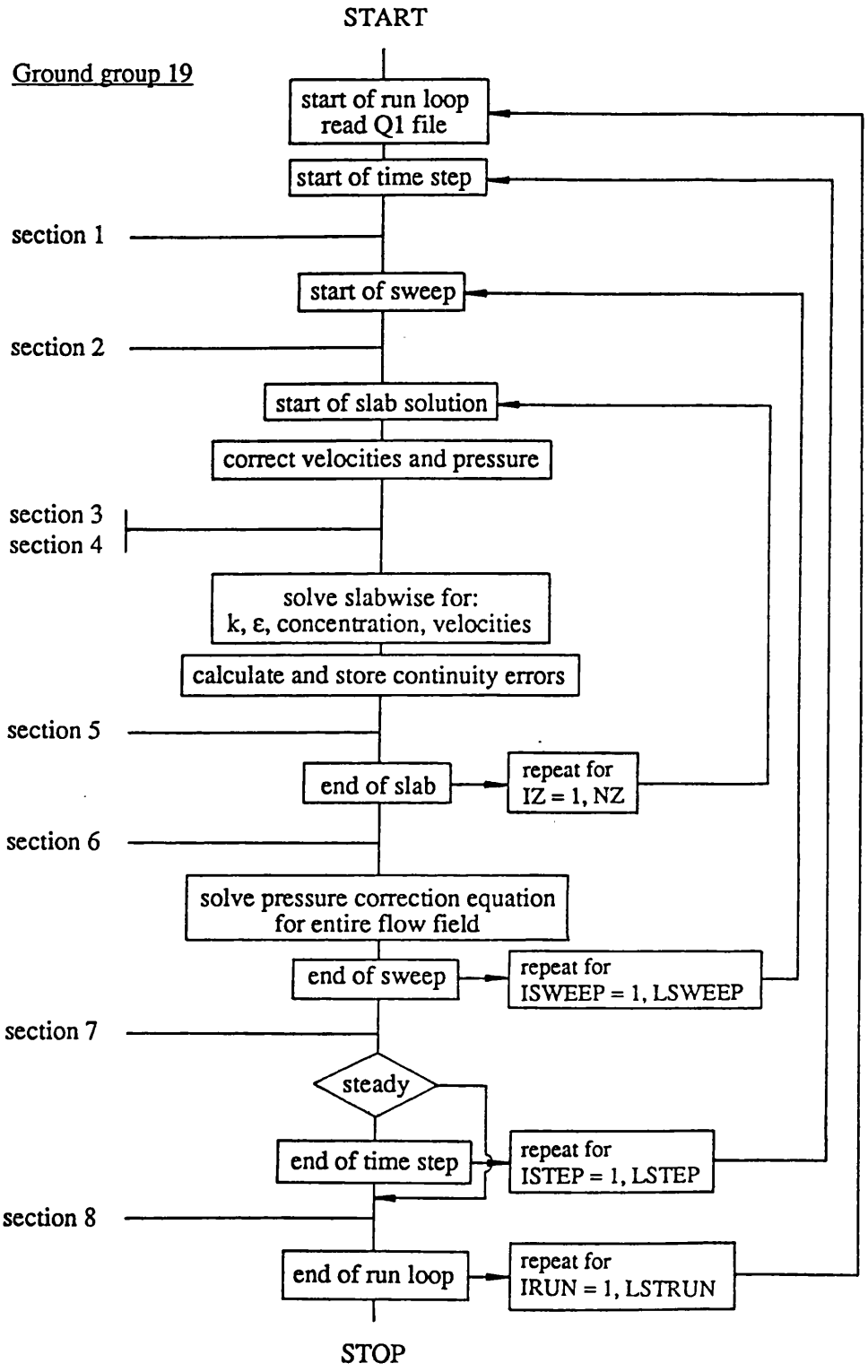

Fig. 7.3: Flow diagram of solution sequence

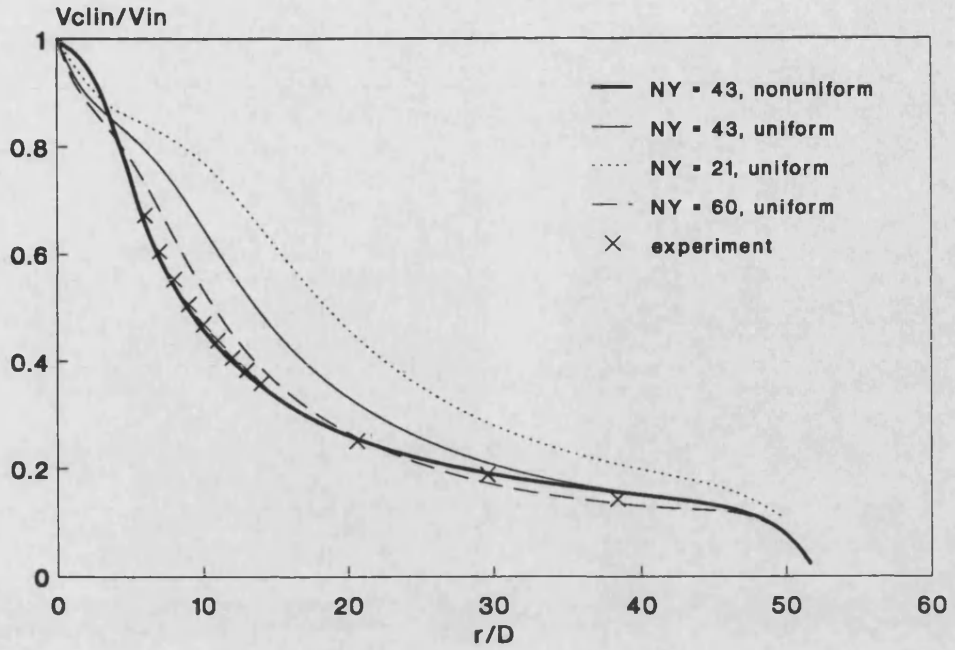

Fig. 7.4 : effect of grid density on centreline velocity decay

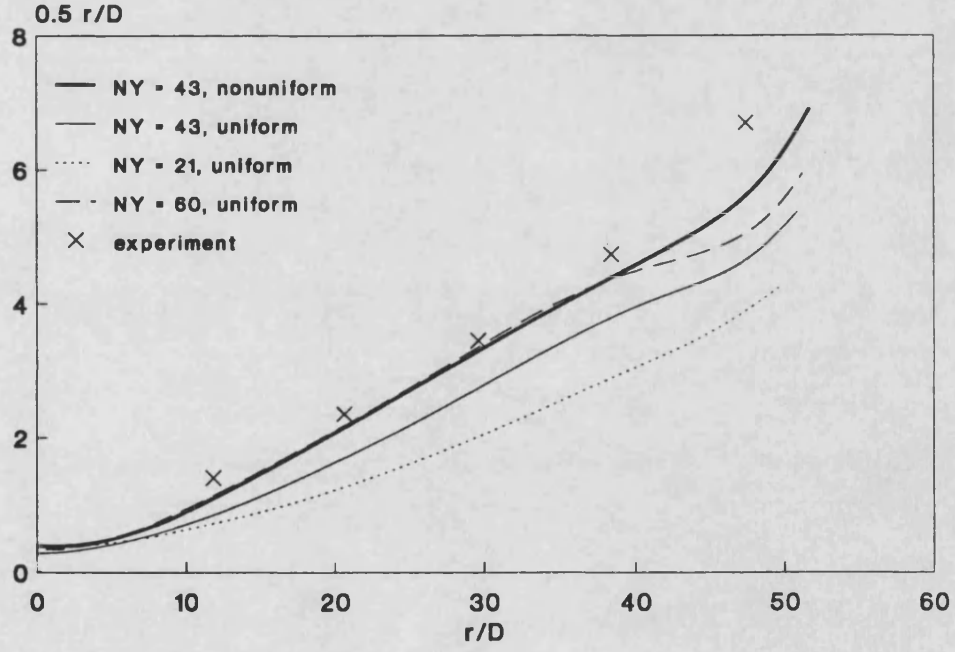

Fig. 7.5 : effect of grid density on jet halfwidth

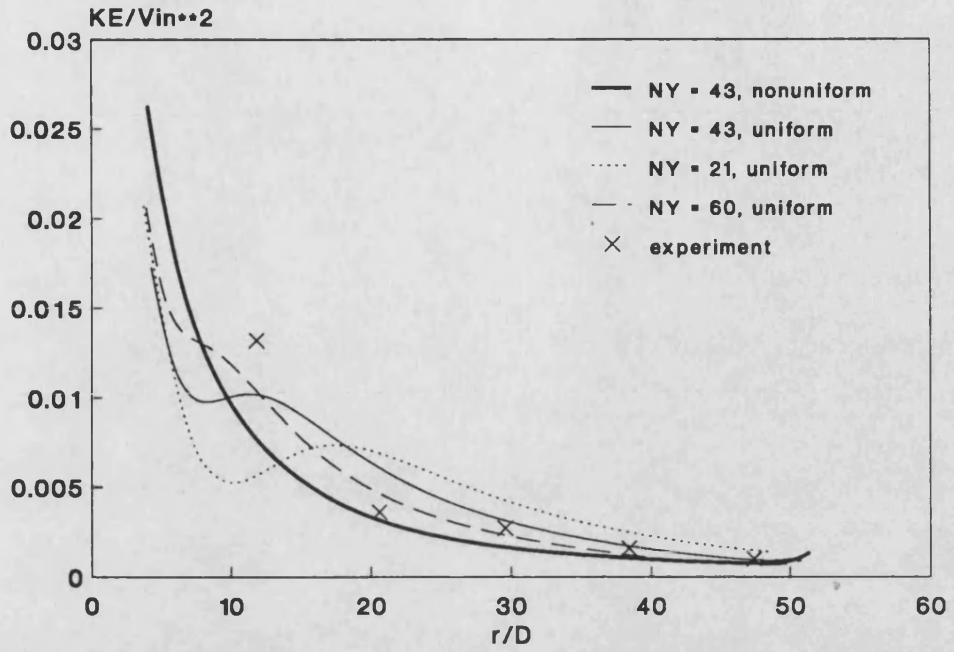

Fig. 7.6 : effect of grid density on centreline kinetic energy distribution

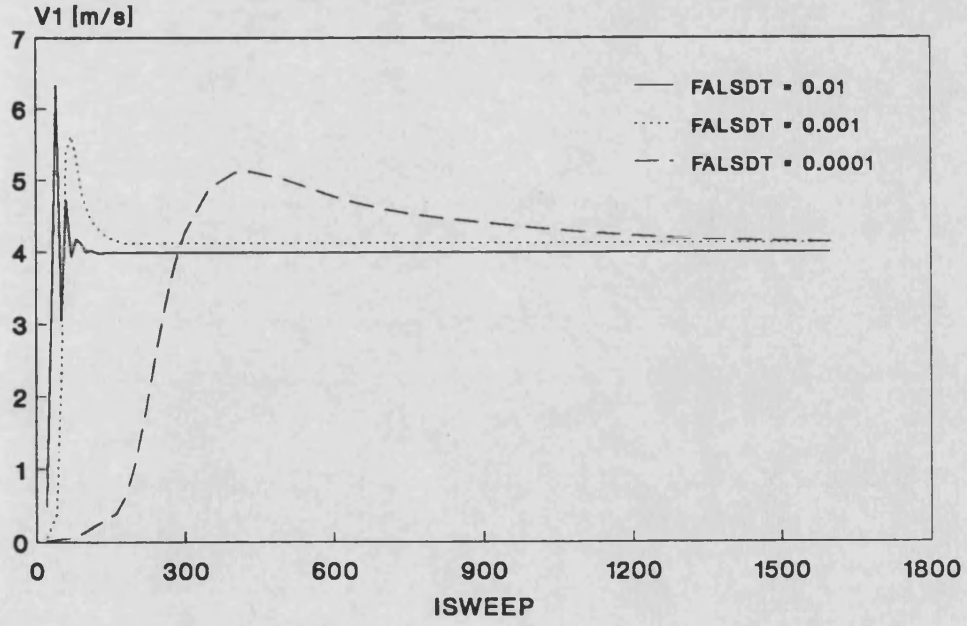

Fig. 7.7: effect of under-relaxation on velocity convergence at jet centreline and r/D = 11

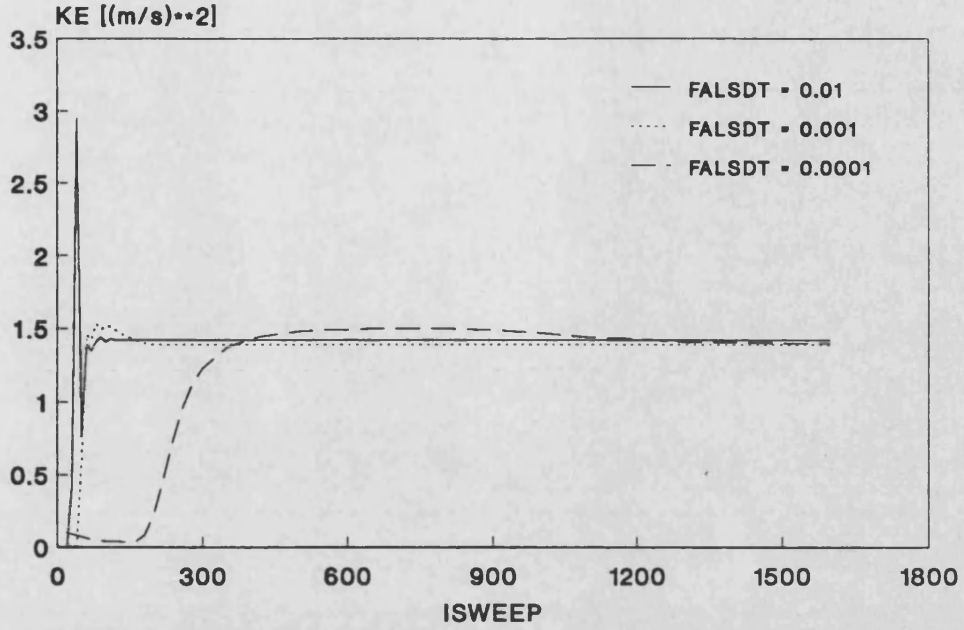

Fig. 7.8: effect of under-relaxation on kinetic energy convergence at jet centreline and r/D = 11

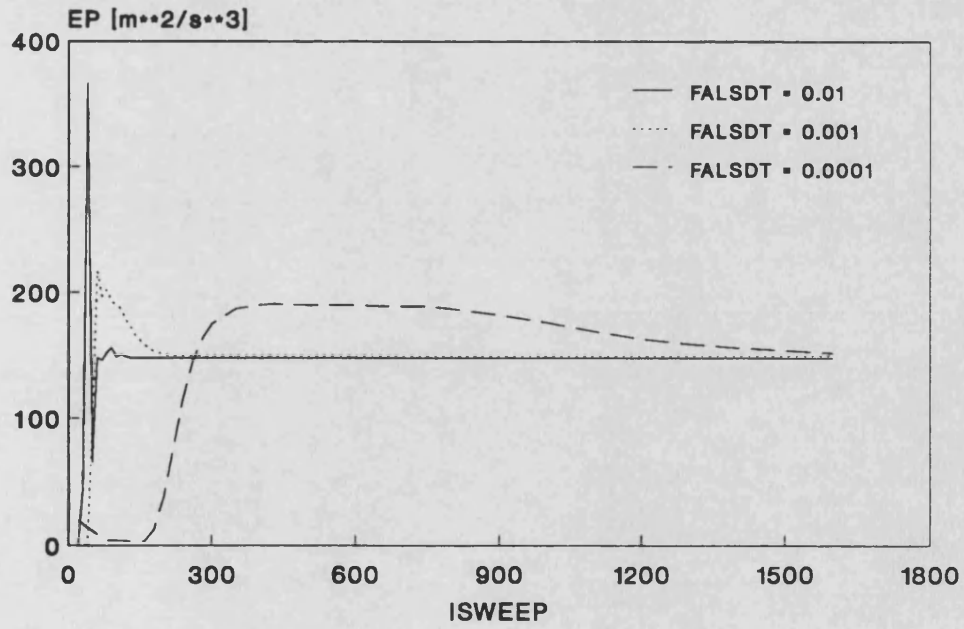

Fig. 7.9: effect of under-relaxation on dissipation rate convergence at jet centreline and r/D = 11

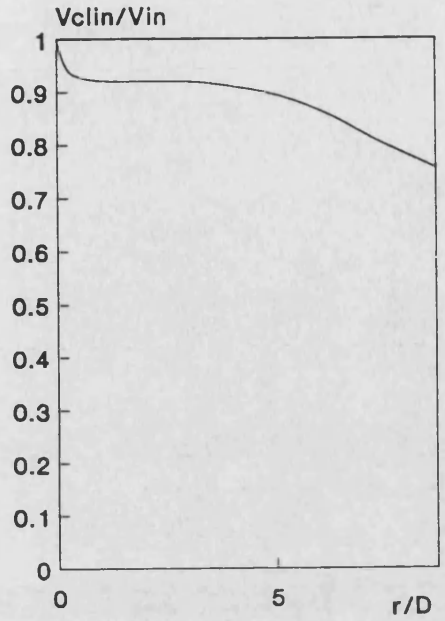

Fig. 7.10: injection along y-axis in cylindrical polar co-ordinates

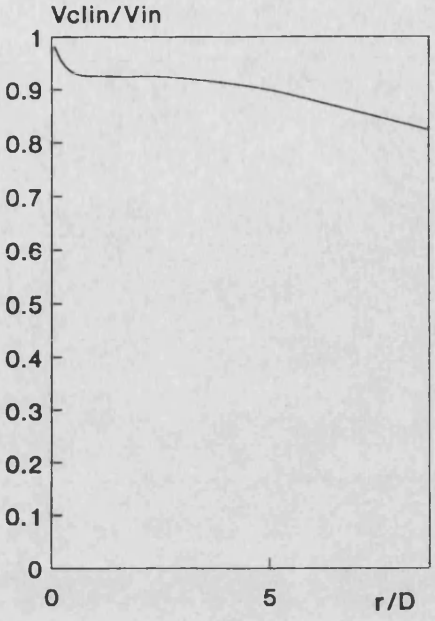

Fig. 7.11 : Injection along y-axis in cylindrical polar co-ordinates, laminar

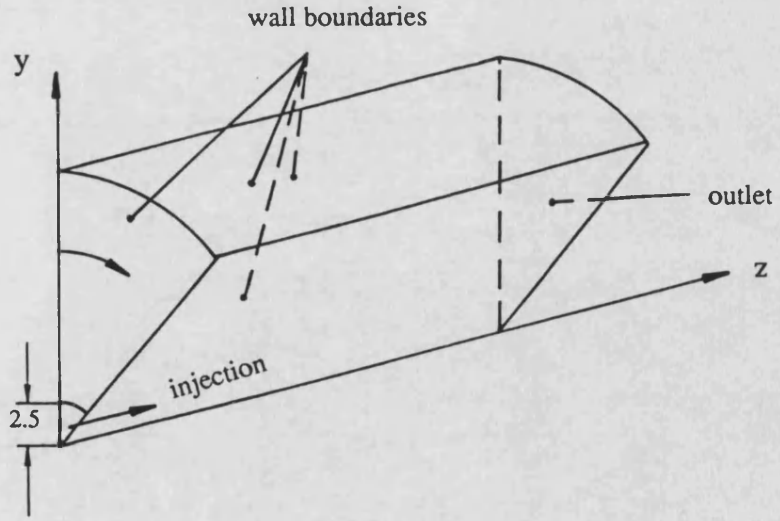

Fig. 7.12: Flow configuration for injection along z-axis in cylindrical polar co-ordinates

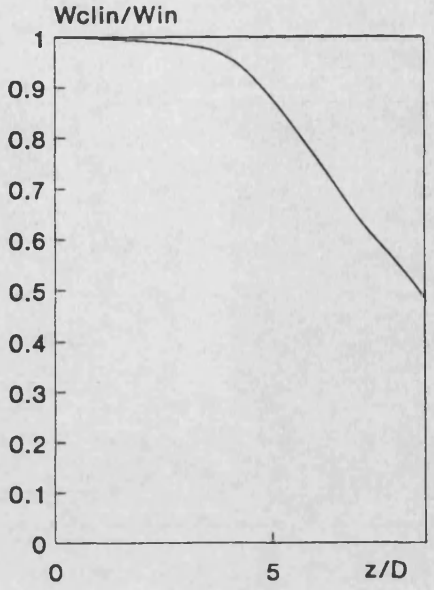

Fig. 7.13: injection along z-axis in
1 rad segment,
cylindrical polar co-ordinates

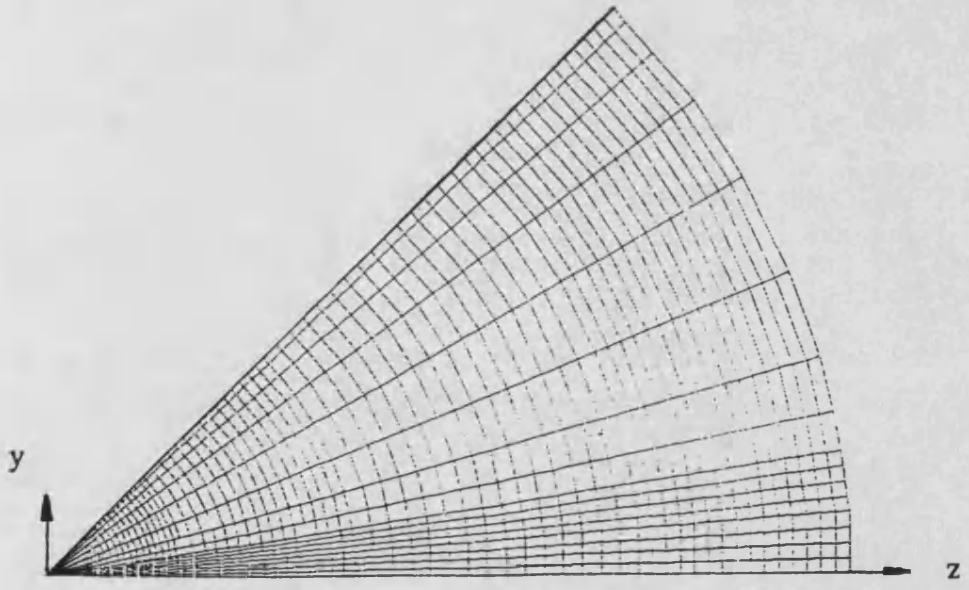

Fig. 7.14: Computational mesh for injection along z-axis in body fitted co-ordinates

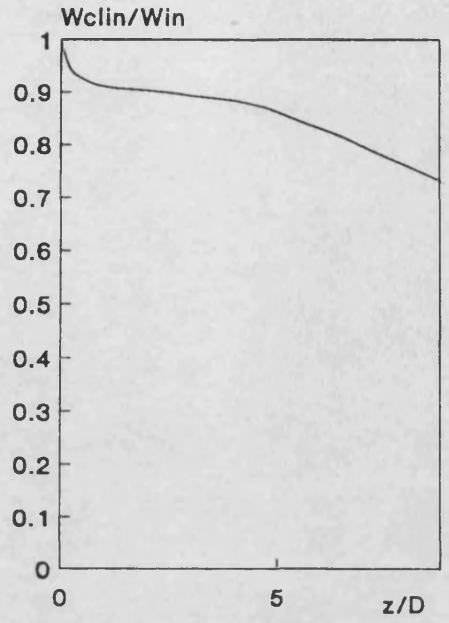

Fig. 7.15: injection along z-axis in body fitted co-ordinates

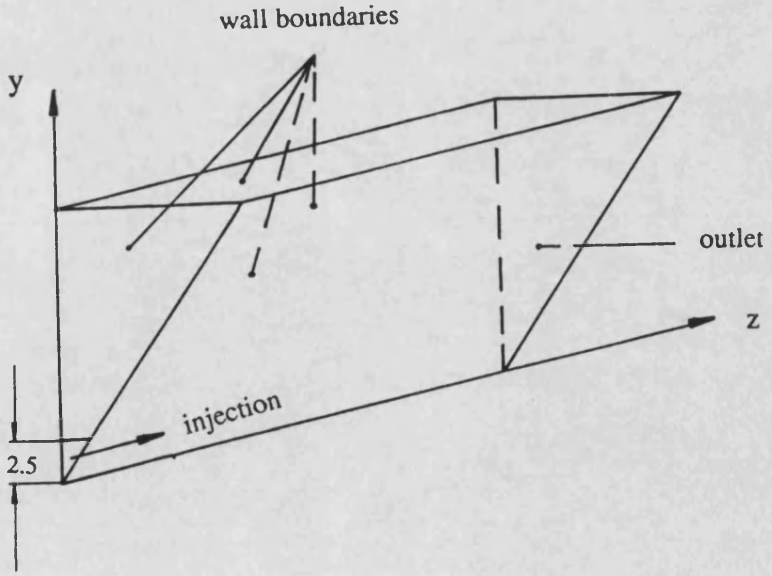

Fig. 7.16: Flow configuration for injection along z-axis in body fitted co-ordinates

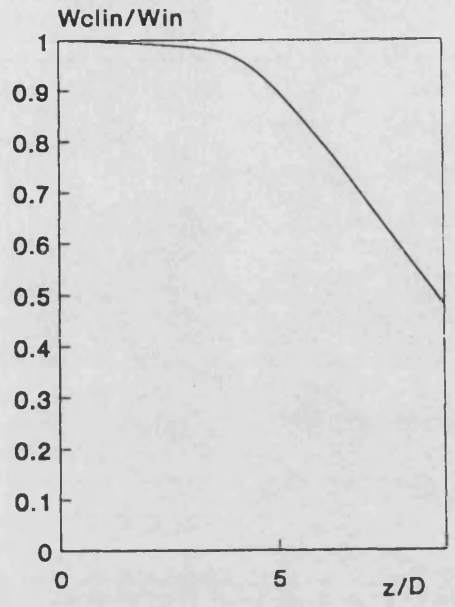

Fig. 7.17: injection along z-axis,
1 radiant segment,
body fitted co-ordinates

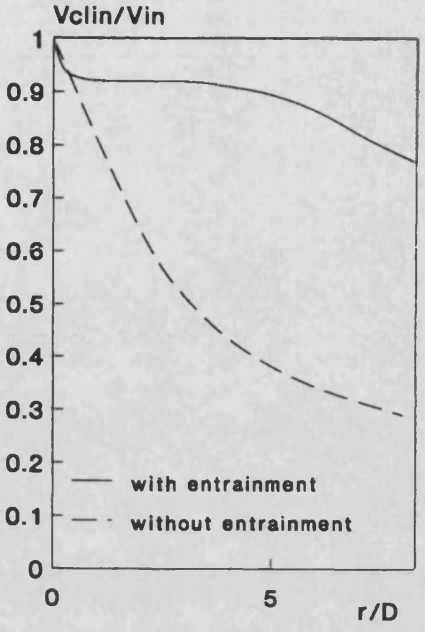

Fig. 7.19: centreline velocity decay
with and without circumferential motion

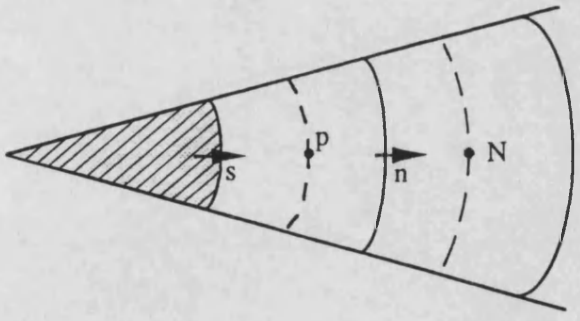

Fig. 7.18: staggered V momentum cells

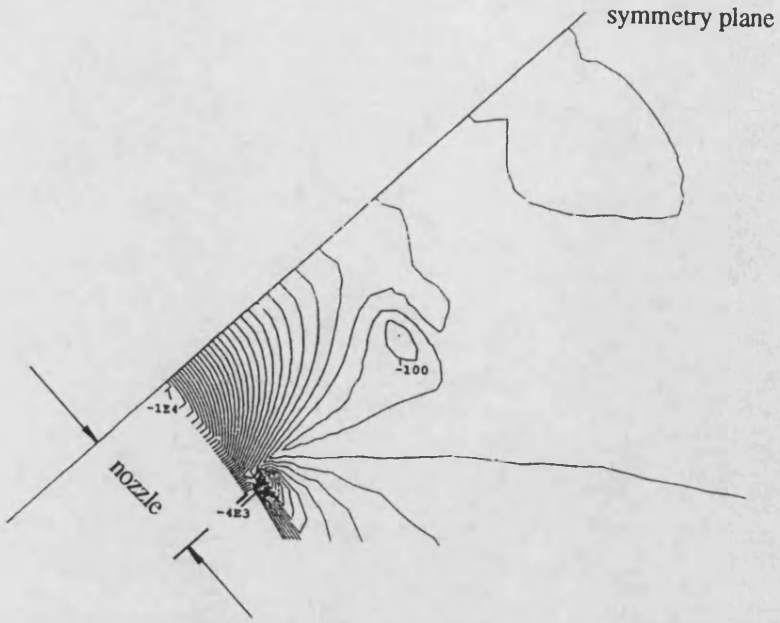

Fig. 7.20: pressure field in flow development region (in Pa)

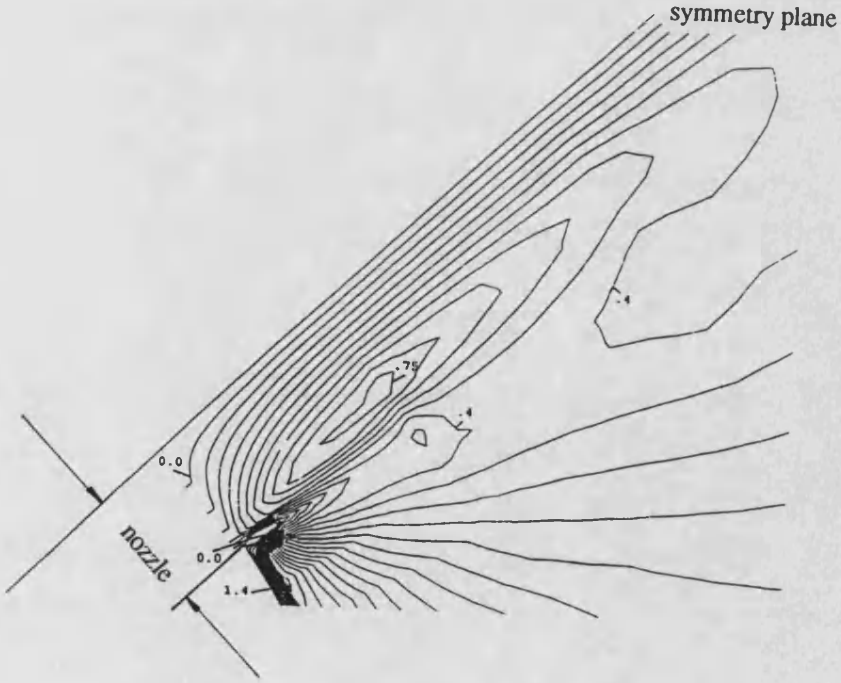

Fig. 7.21: circumferential velocity field in flow development region (in m/s)

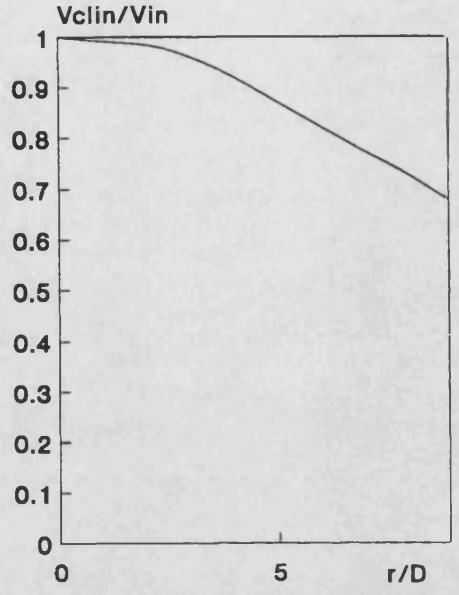

Fig. 7.22: centreline velocity decay with resolved constant velocity inlet profile

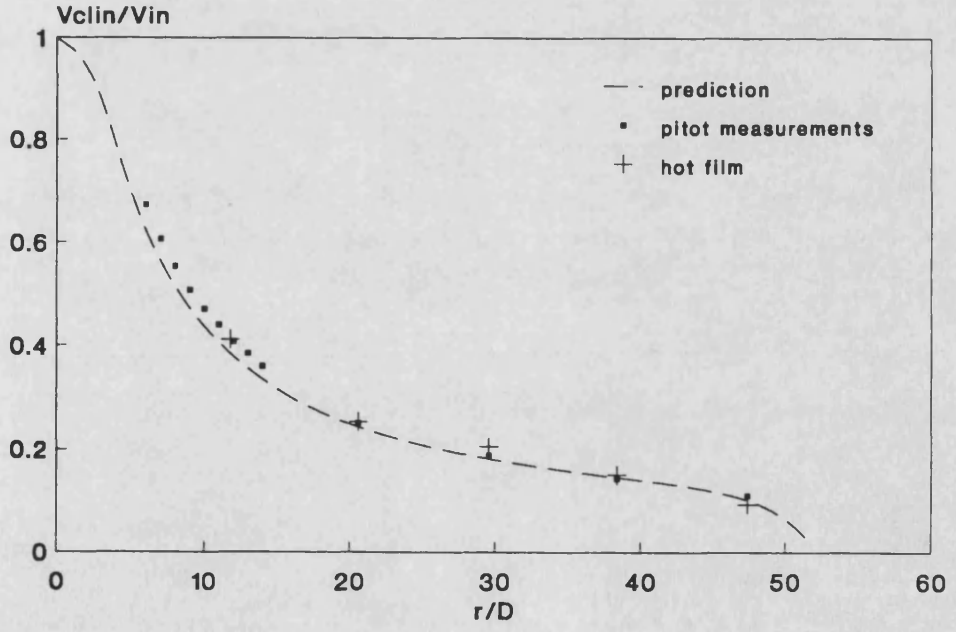

Fig. 7.23: centreline velocity decay with resolved parabolic inlet velocity profile, standard turbulence model

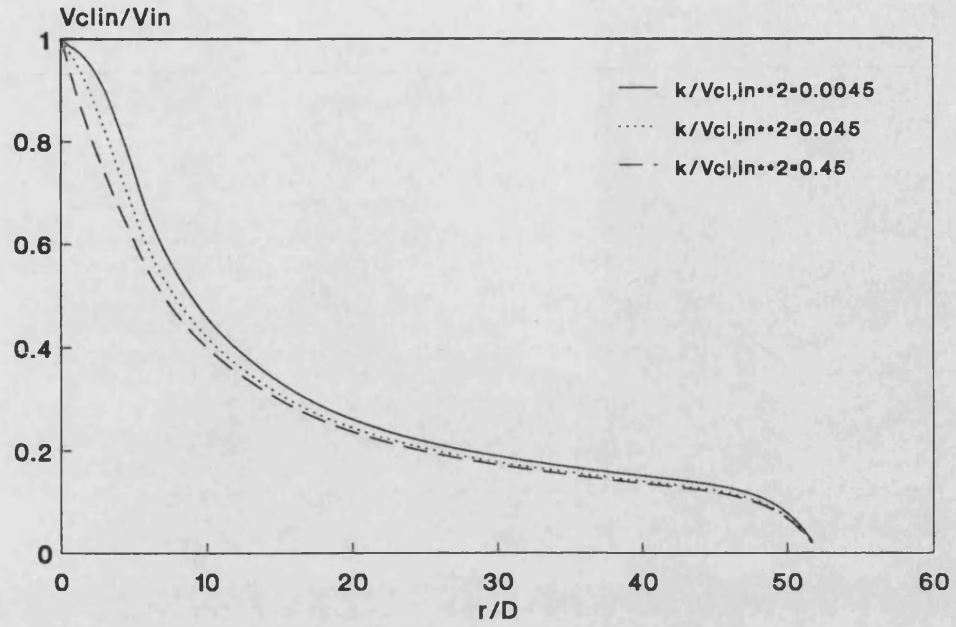

Fig. 7.24: effect of level of incoming turbulence kinetic energy on centreline velocity decay

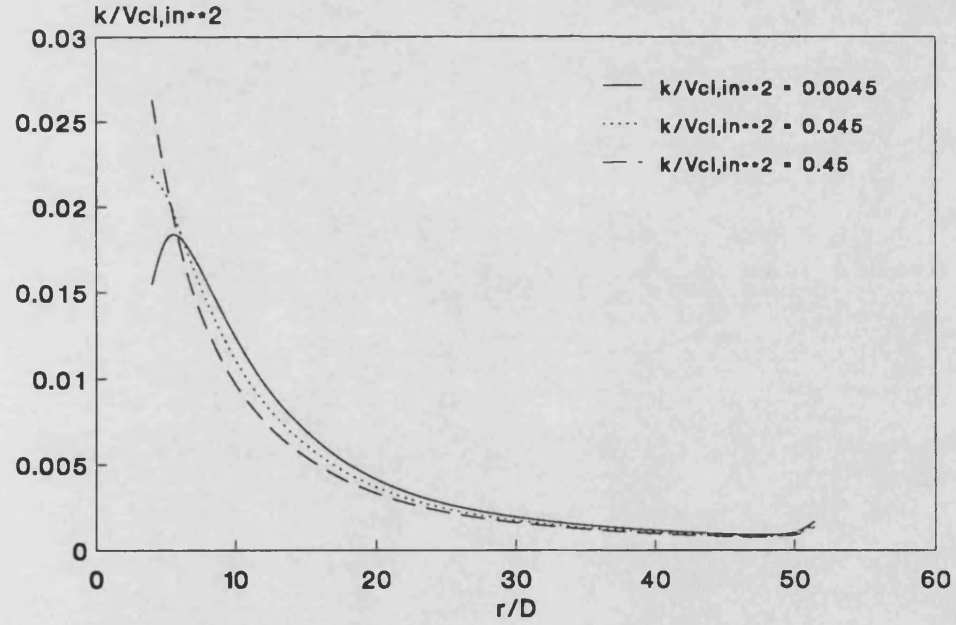

Fig. 7.25: effect of level of incoming turbulence kinetic energy on kinetic energy centreline distribution

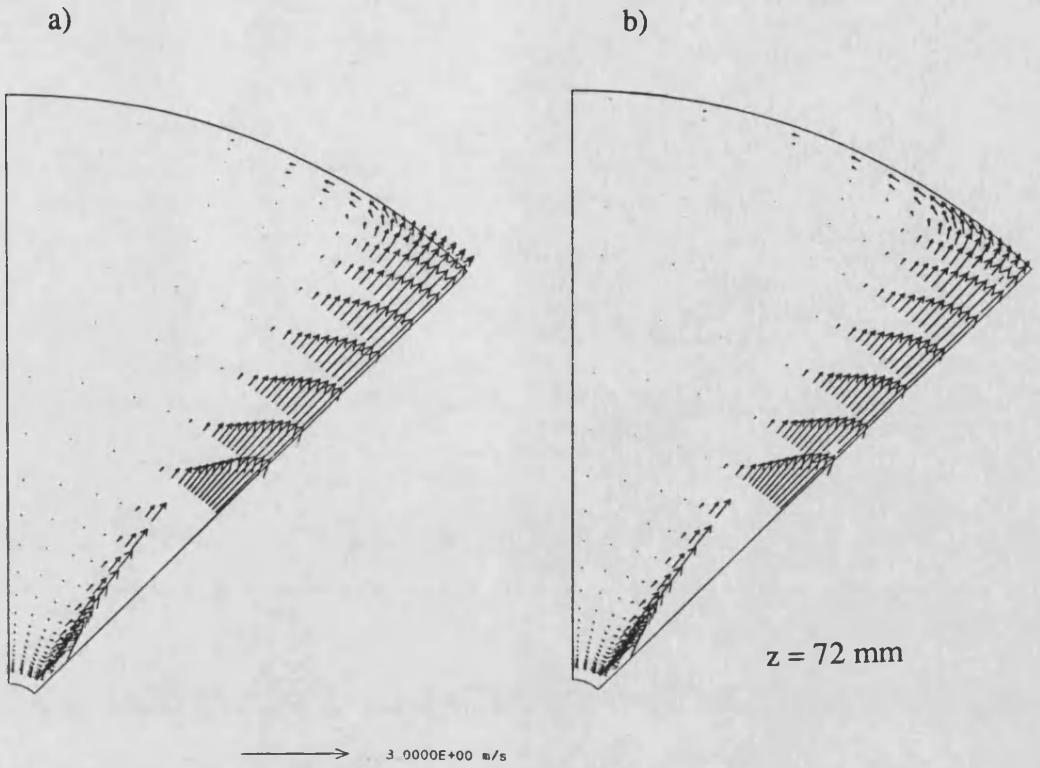

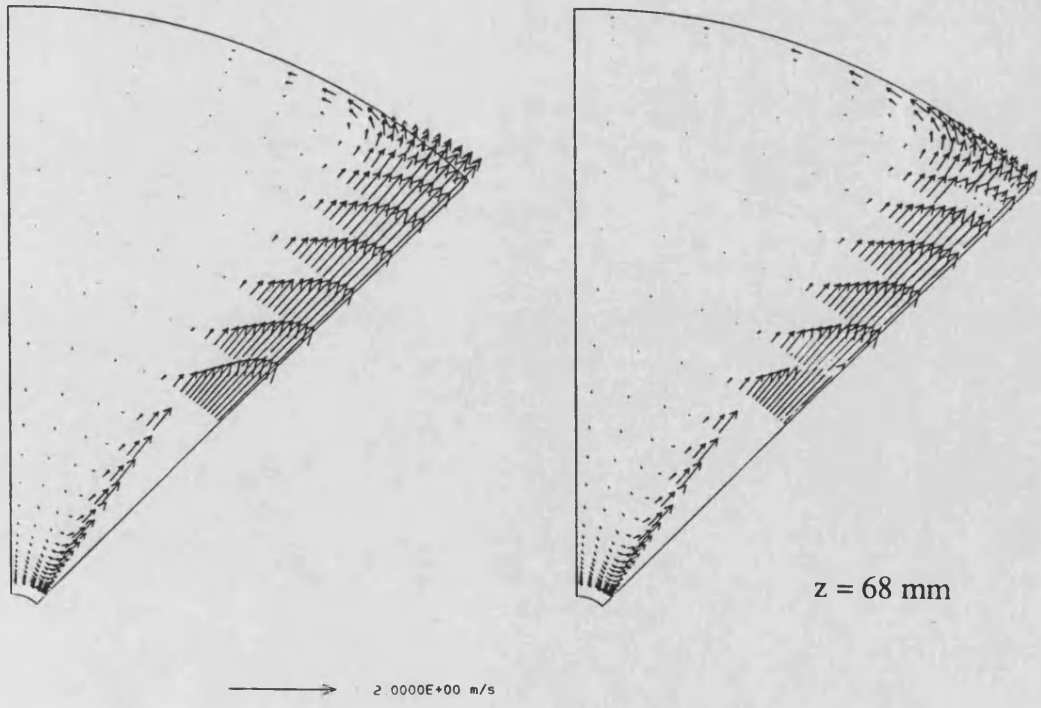

Fig. 7.26 cont.

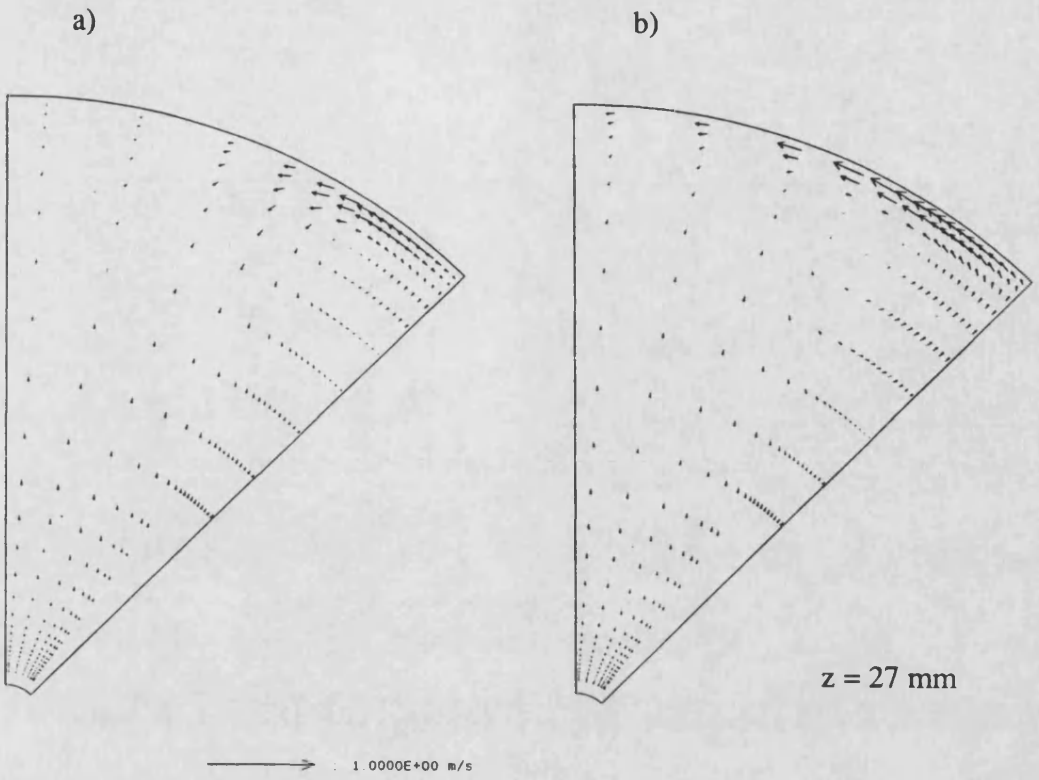

Fig. 7.26: comparison of predicted velocities in r - θ plane using a) symmetry and b) free - entrainment boundary conditions at θ = 45 degrees

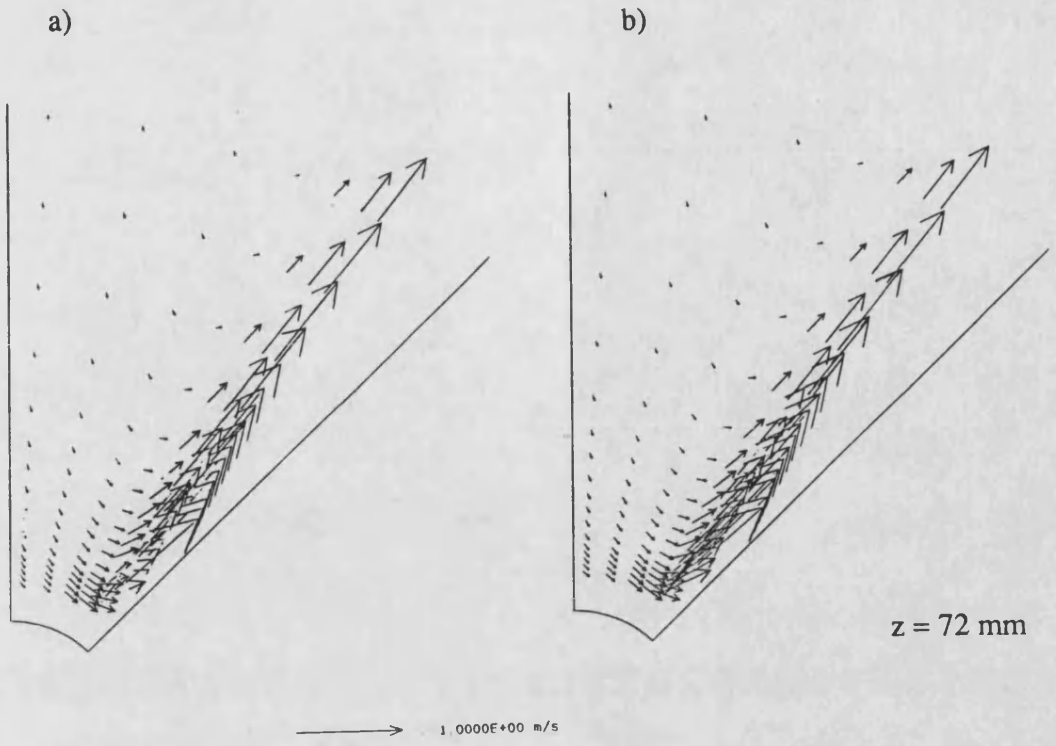

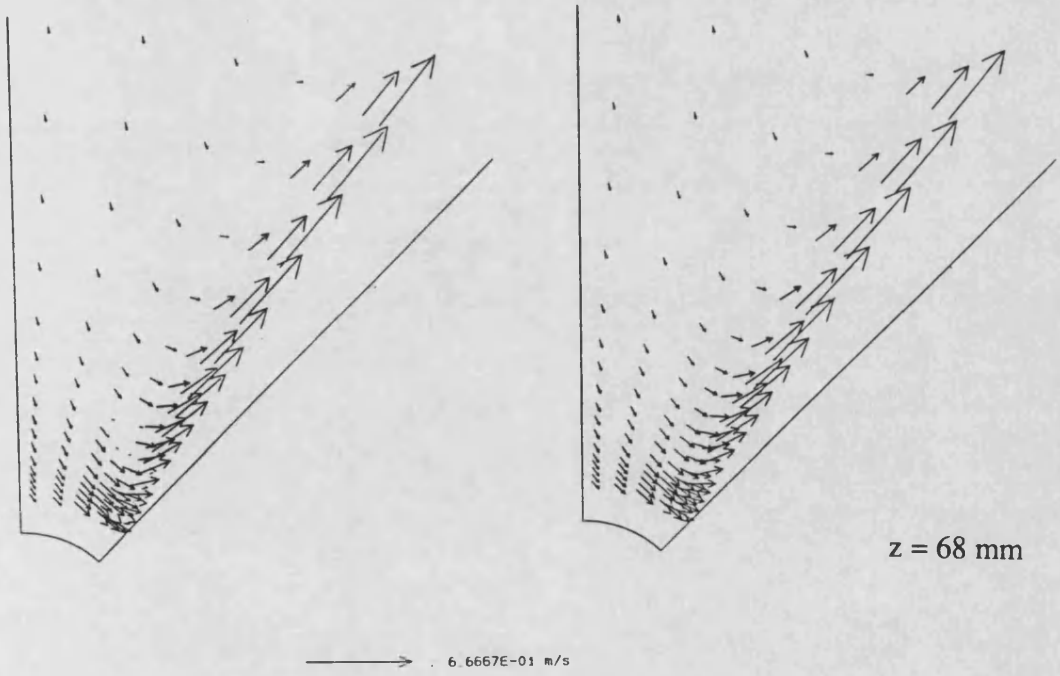

Fig. 7.27 cont.

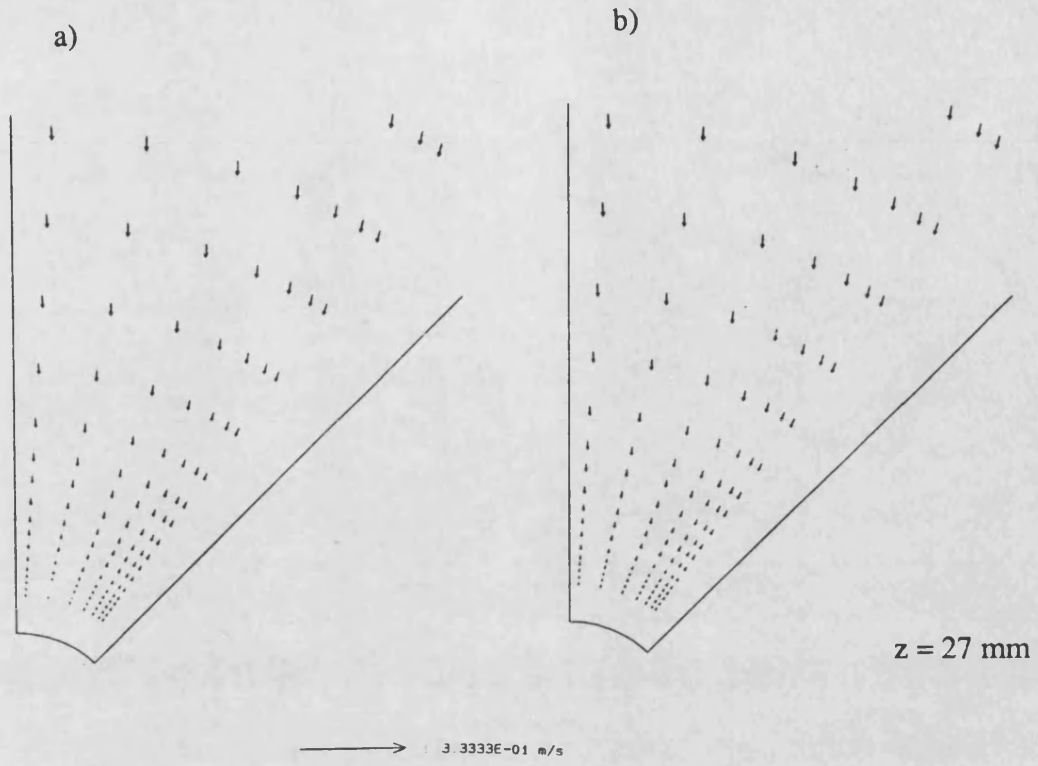

Fig. 7.27: comparison of predicted entrainment velocities in r - θ plane using a) symmetry and b) free - entrainment boundary conditions at θ = 45 degrees

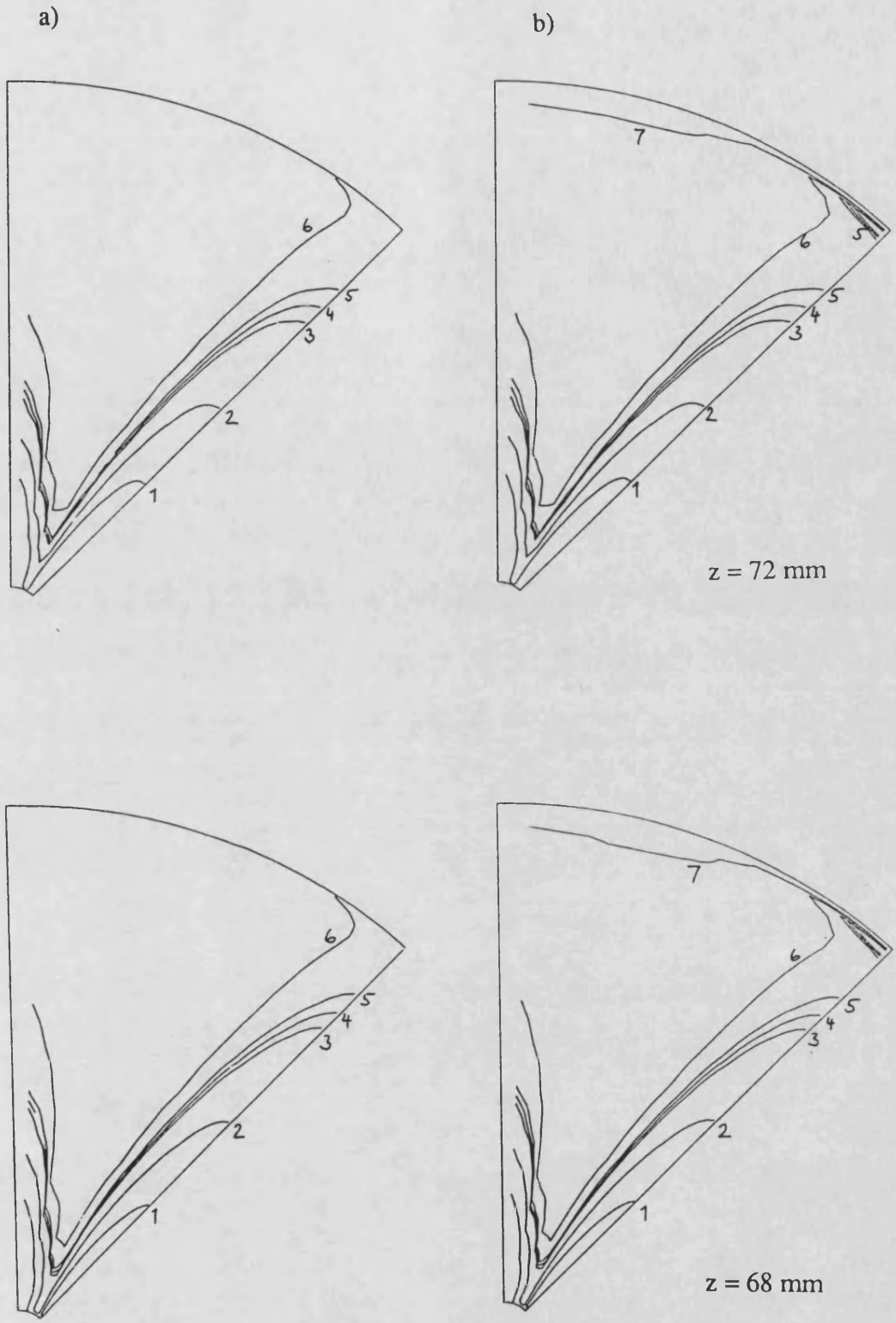

Fig. 7.28: comparison of predicted kinetic energy contours in r - θ plane using a) symmetry and b) free - entrainment boundary conditions at θ = 45 degrees

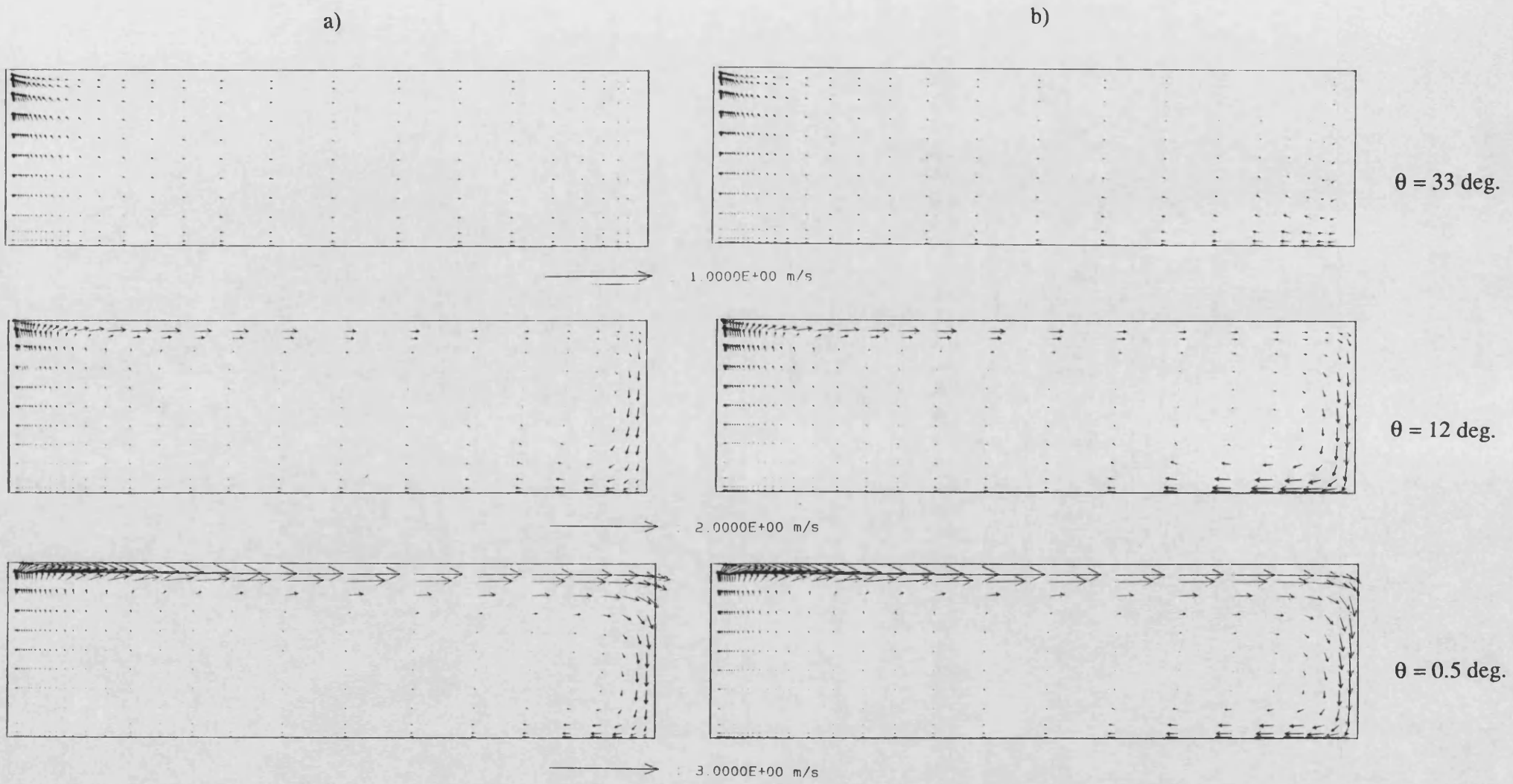

Fig. 7.29: comparison of predicted entrainment velocities in r - z plane using a) symmetry and b) free - entrainment boundary conditions at $\theta = 45$ degrees

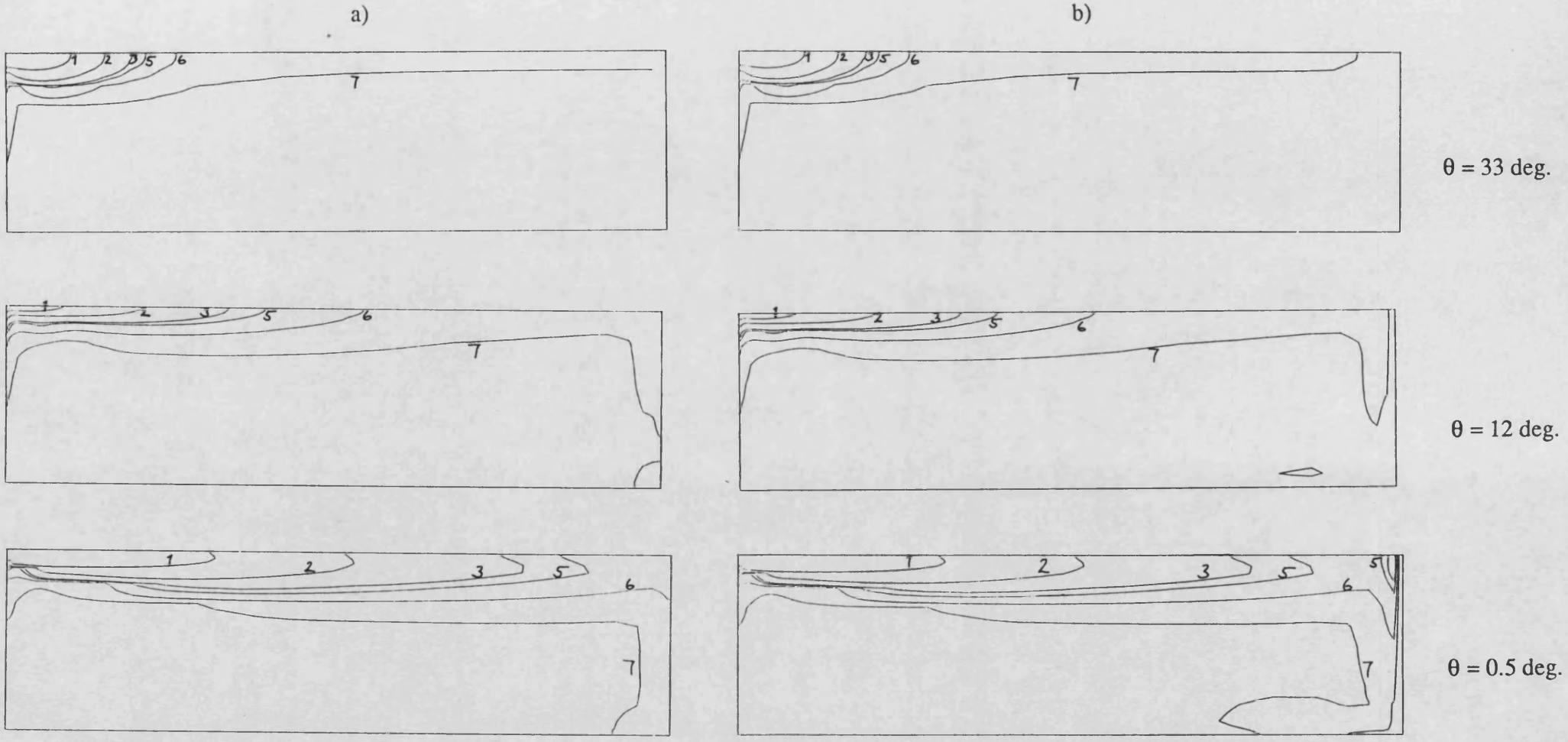

Fig. 7.30: comparison of predicted kinetic energy contours in r - z plane using a) symmetry and b) free - entrainment boundary conditions at $\theta = 45$ degrees

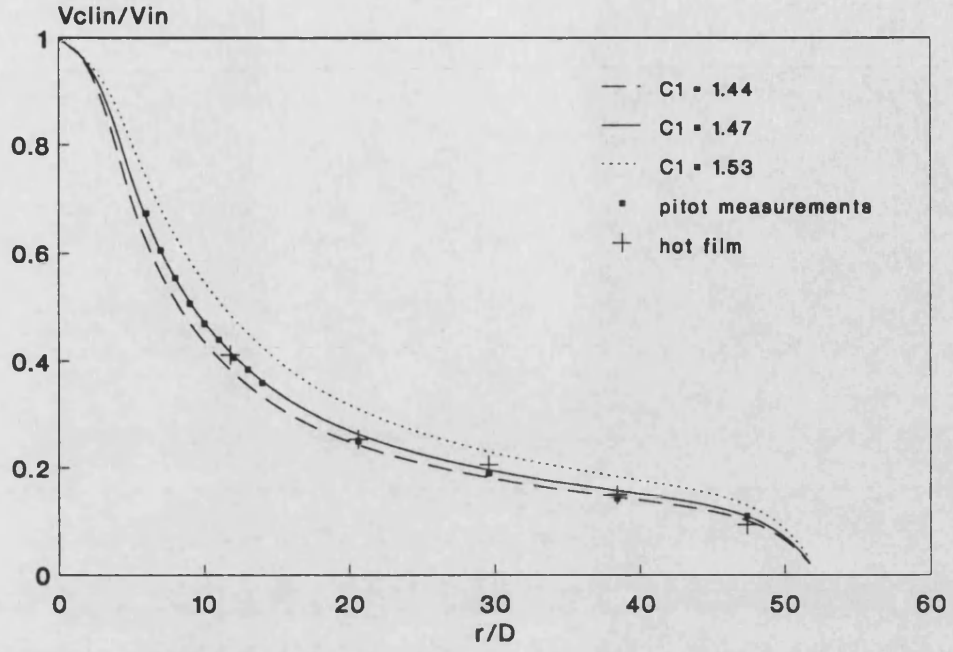

Fig. 7.31: effect of C1 on centreline velocity decay

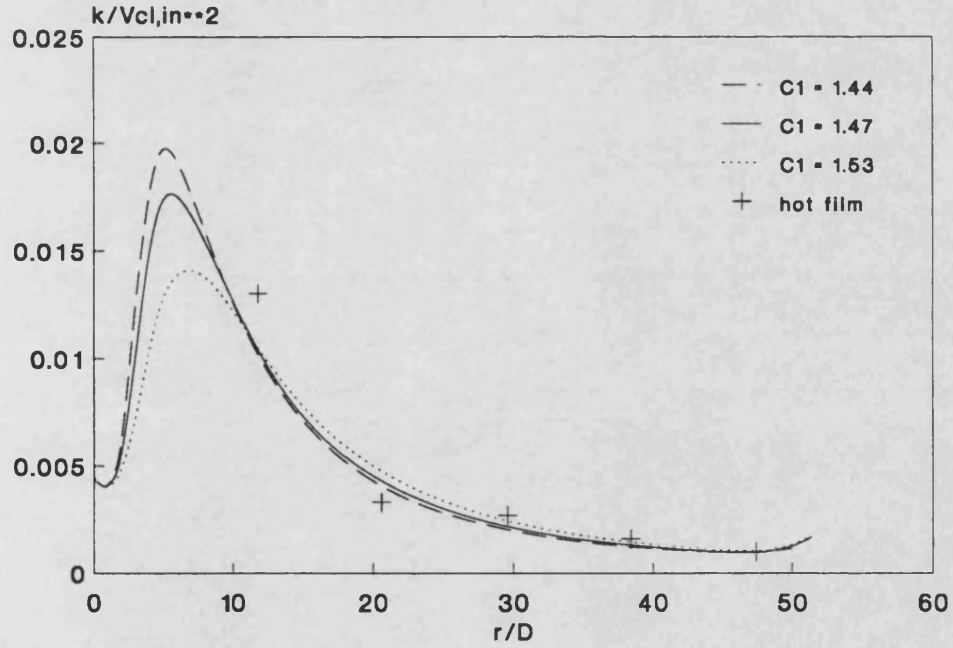

Fig. 7.32: effect of C1 on centreline kinetic energy variation

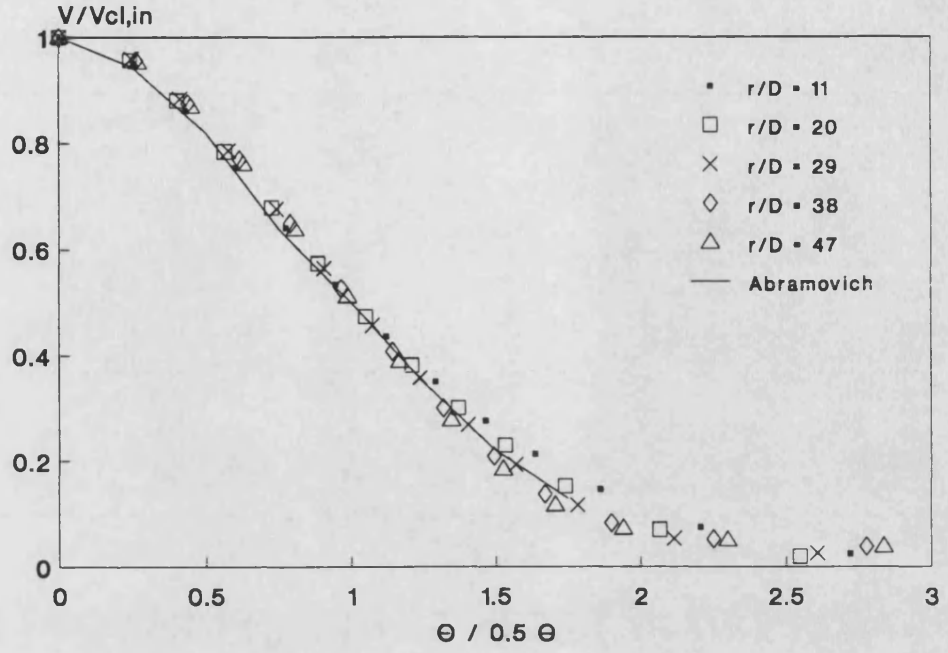

Fig. 7.33: predicted radial velocity similarity profiles

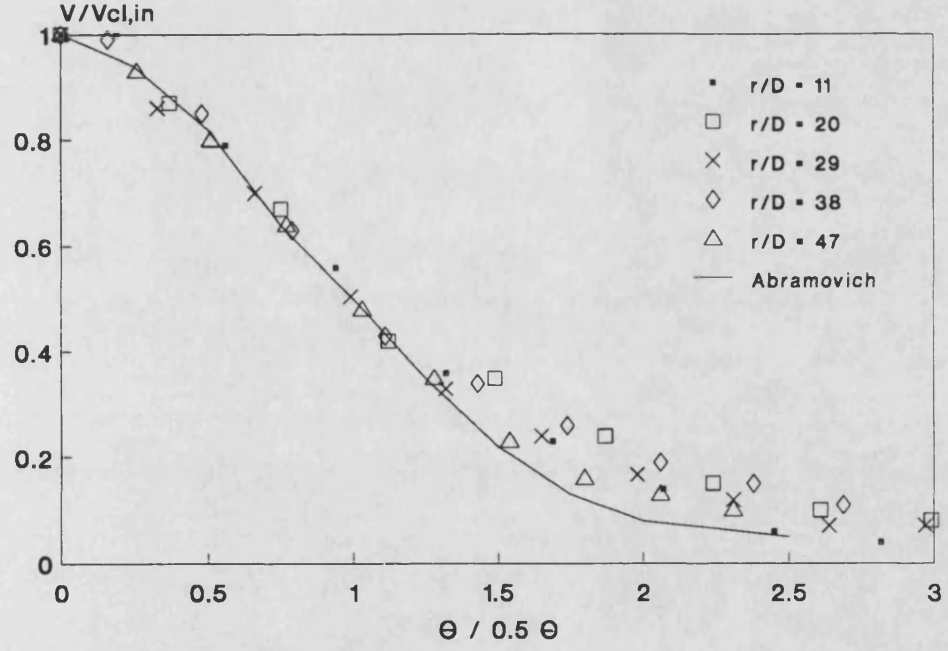

Fig. 7.34: measured radial velocity similarity profile

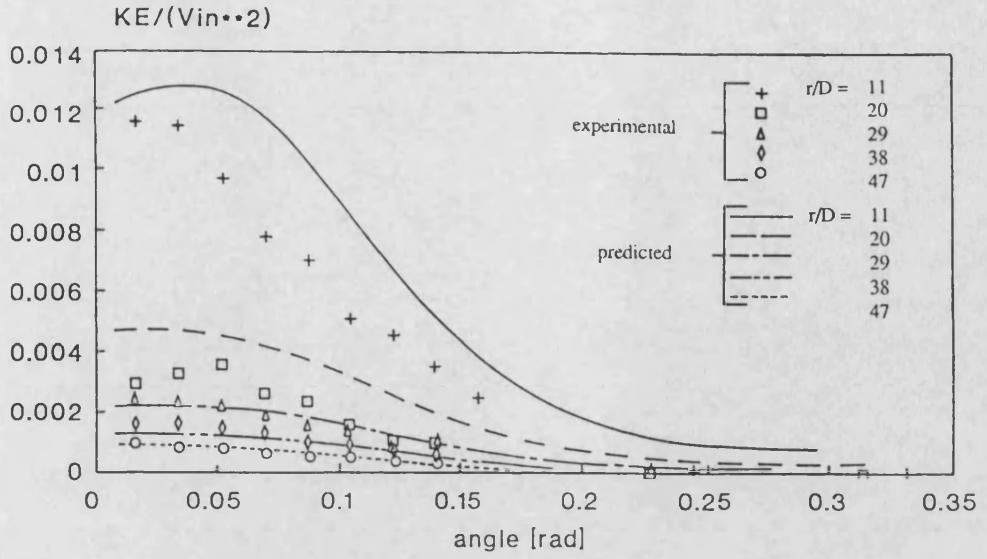

Fig. 7.35: comparison between predicted and measured kinetic energy profiles

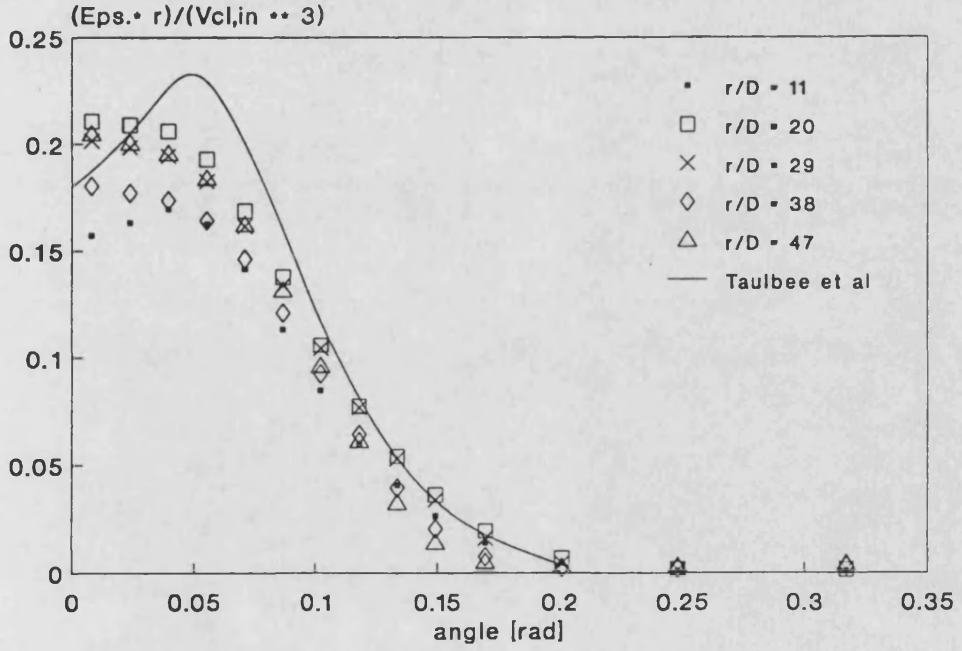

Fig. 7.36: dissipation rate similarity profiles

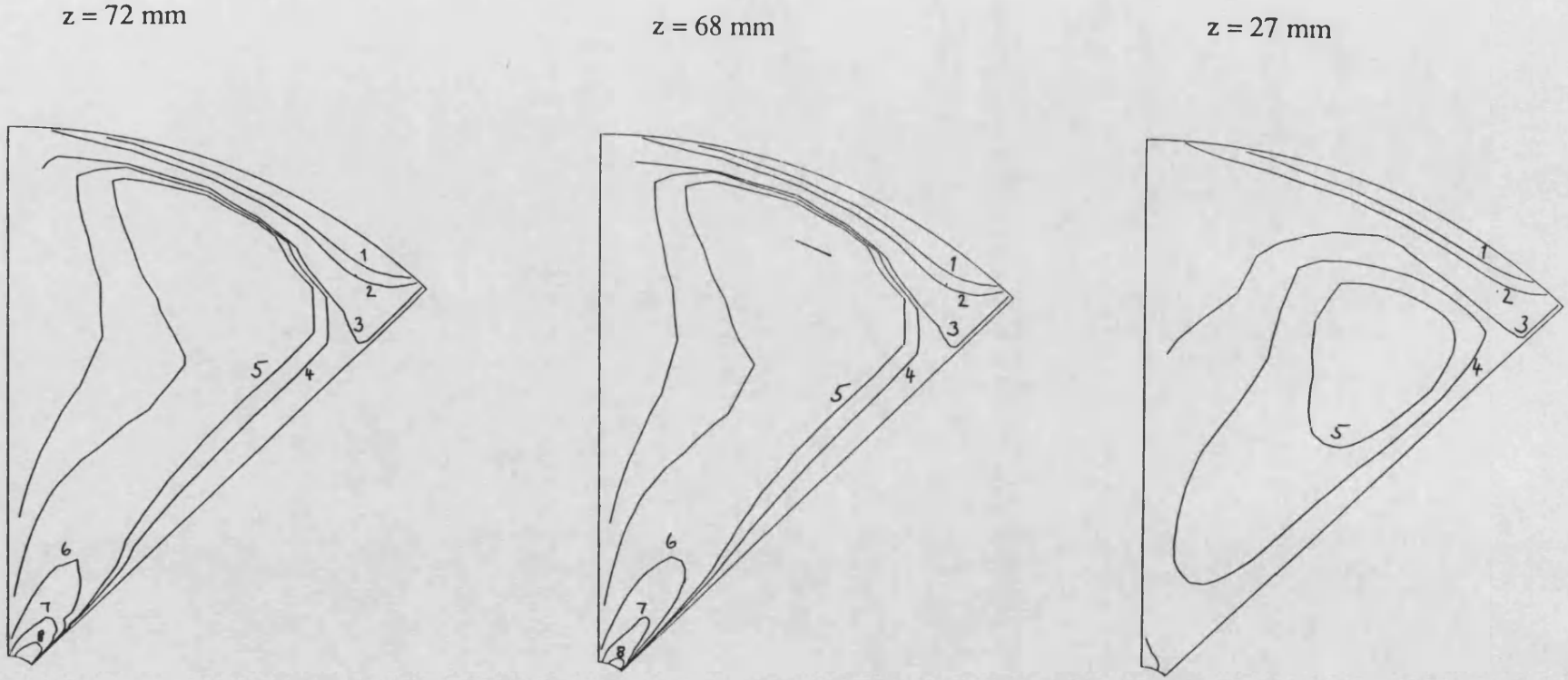

Fig. 7.37: predicted circumferential velocity contours

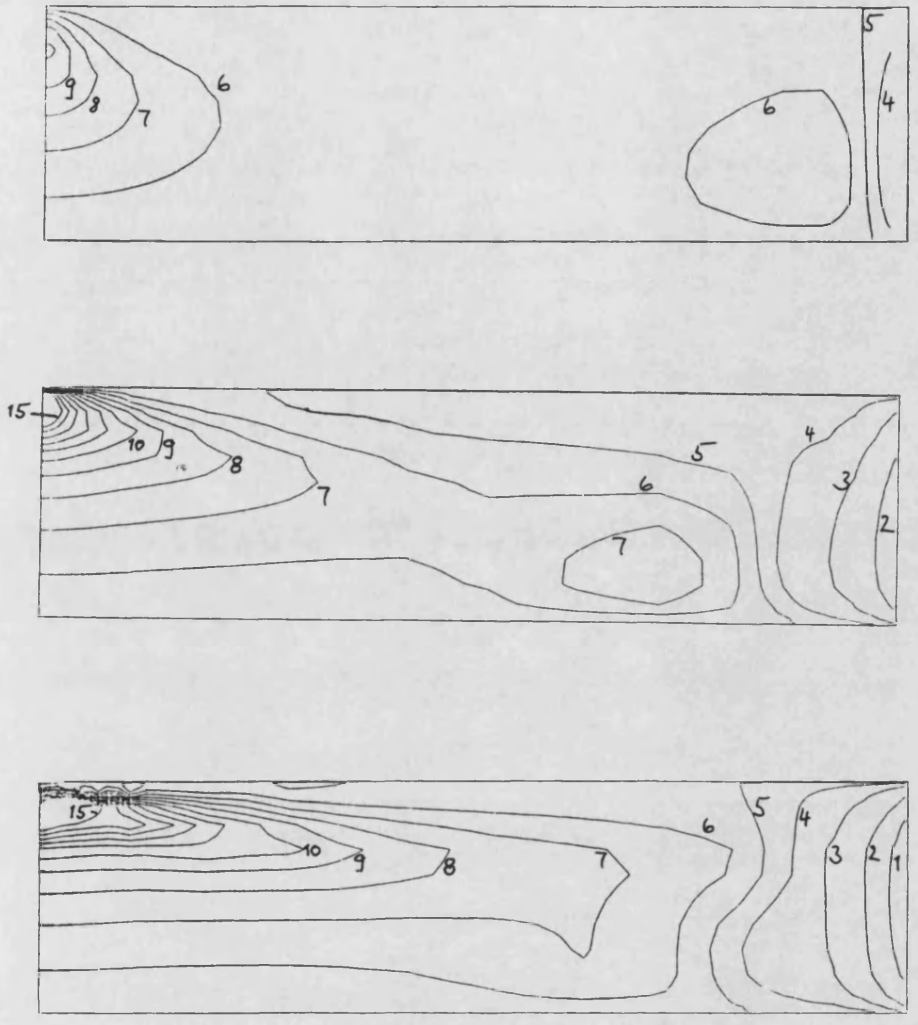

Fig. 7.38: predicted axial velocity contours

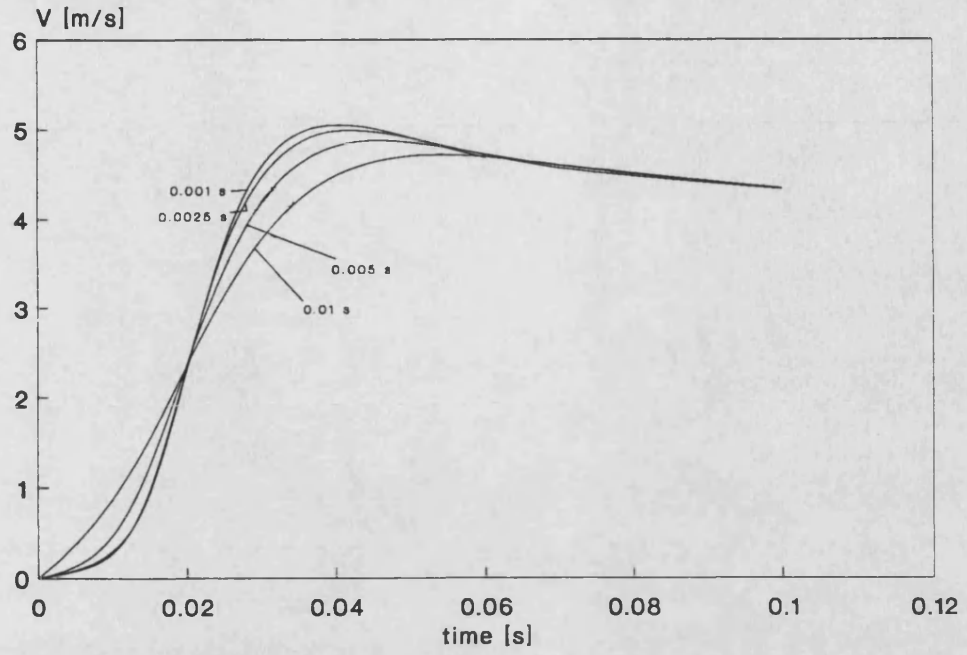

Fig. 7.39: effect of time step size on steady state approach of radial velocity

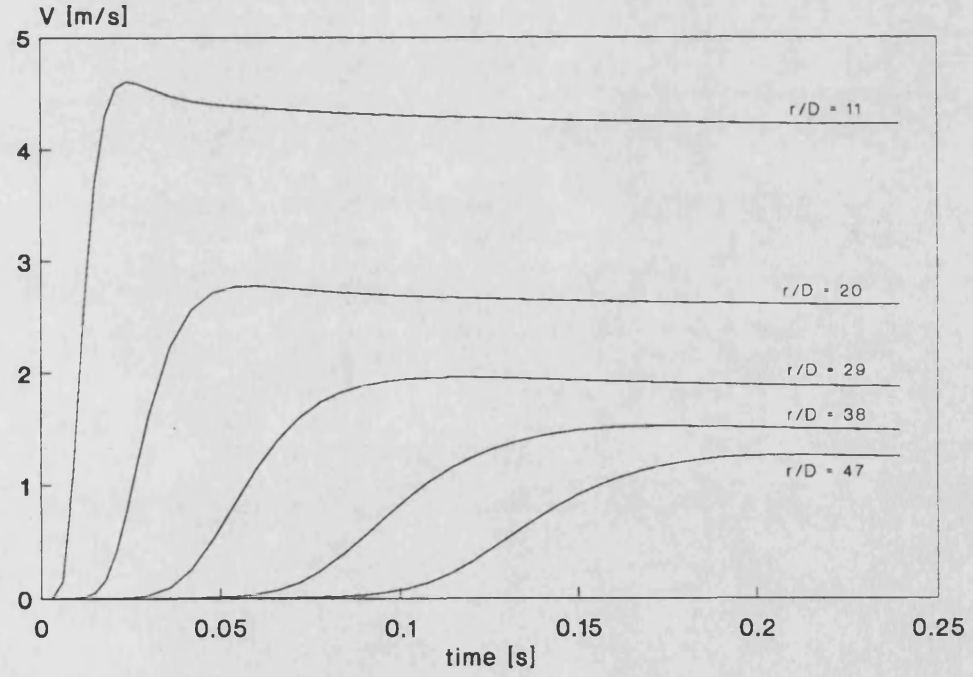

Fig. 7.40: velocity versus time profiles

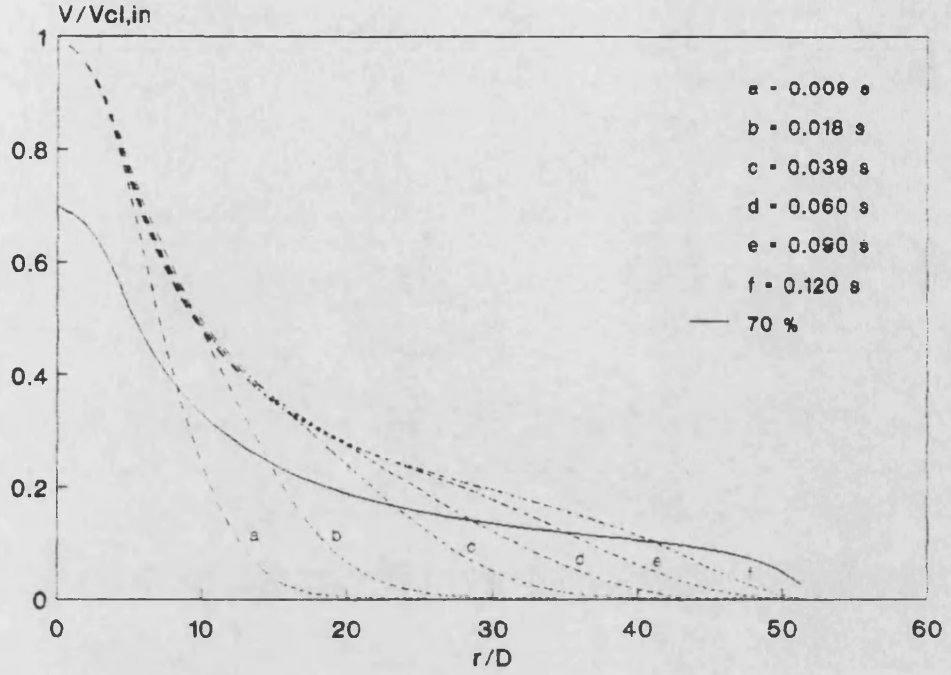

Fig. 7.41: def. of jet arrival time

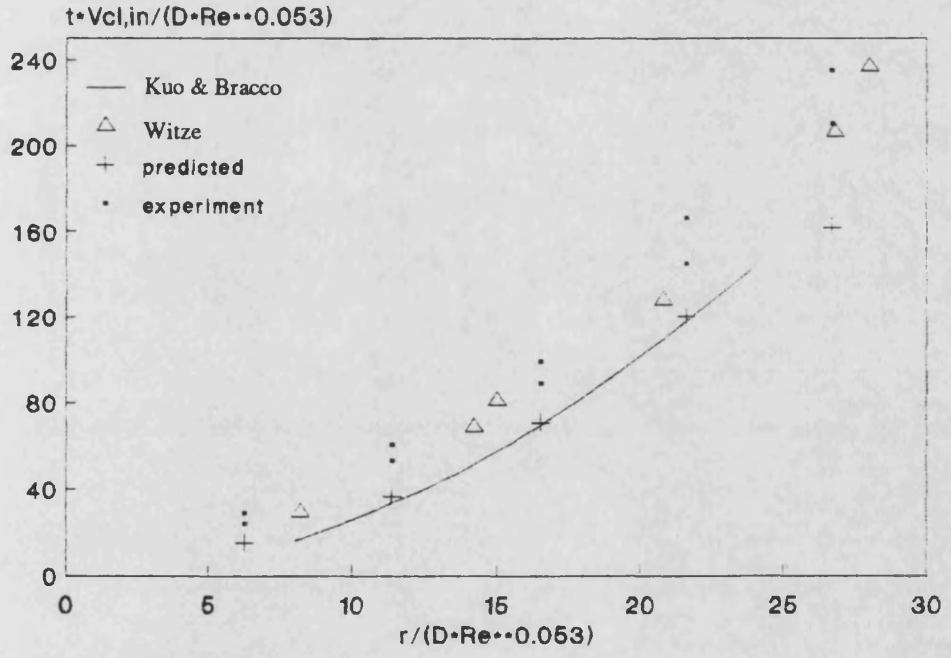

Fig. 7.42: nondimensional 70 % jet penetration

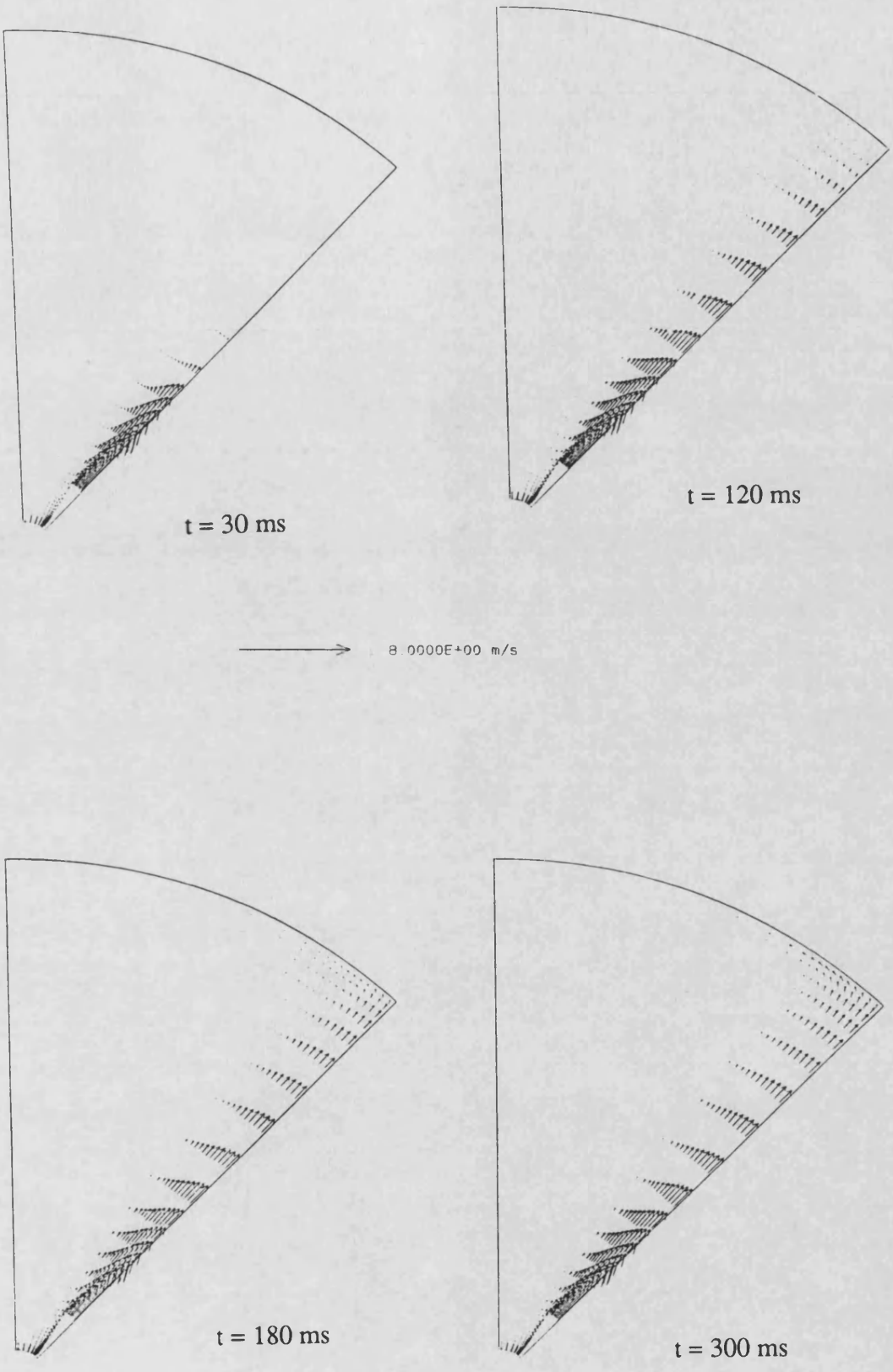

Fig. 7.43: temporal development of velocity vectors in r - θ plane (jet symmetry plane)

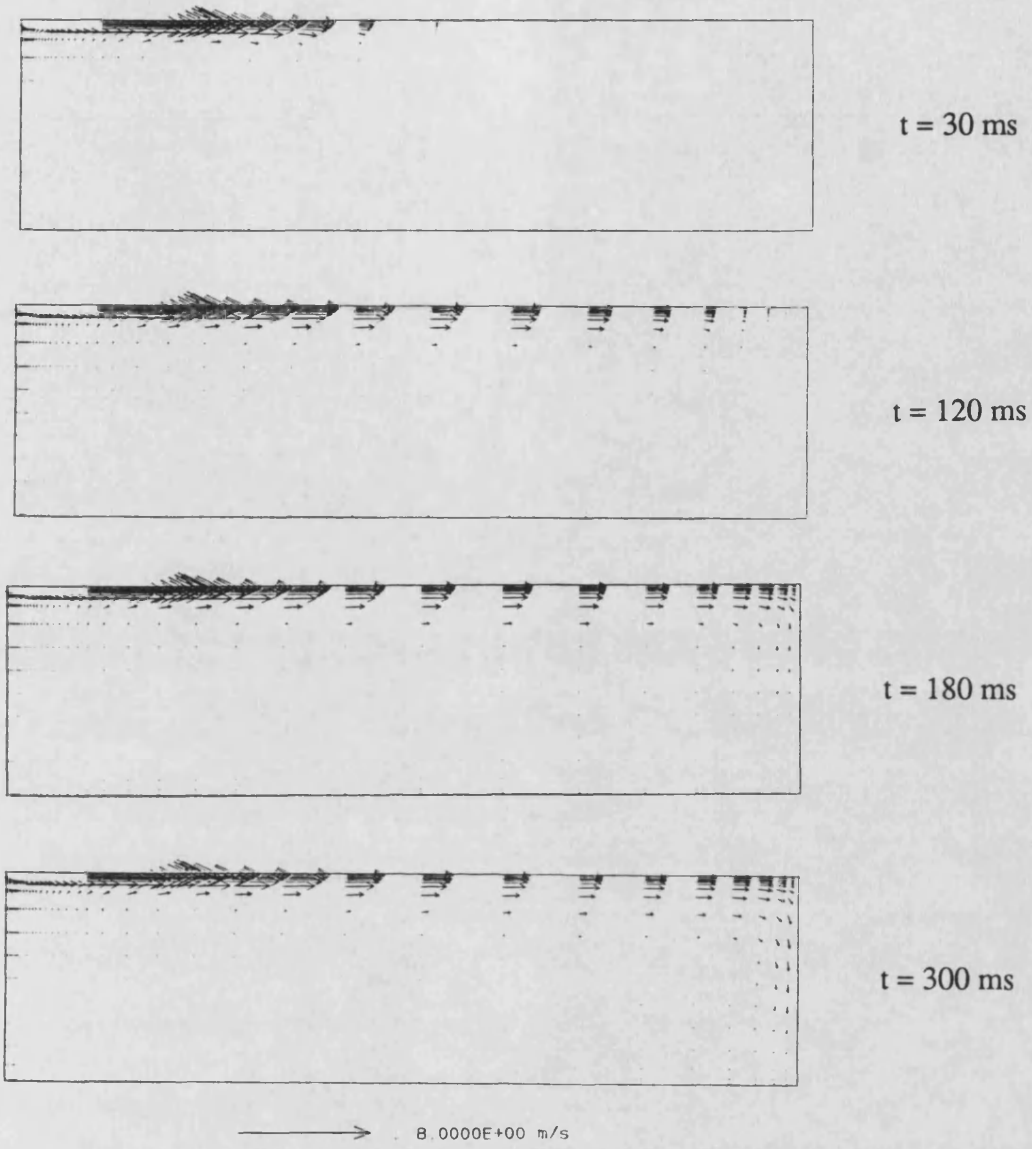

Fig. 7.44: temporal development of velocity vectors in r - z plane (jet symmetry plane)

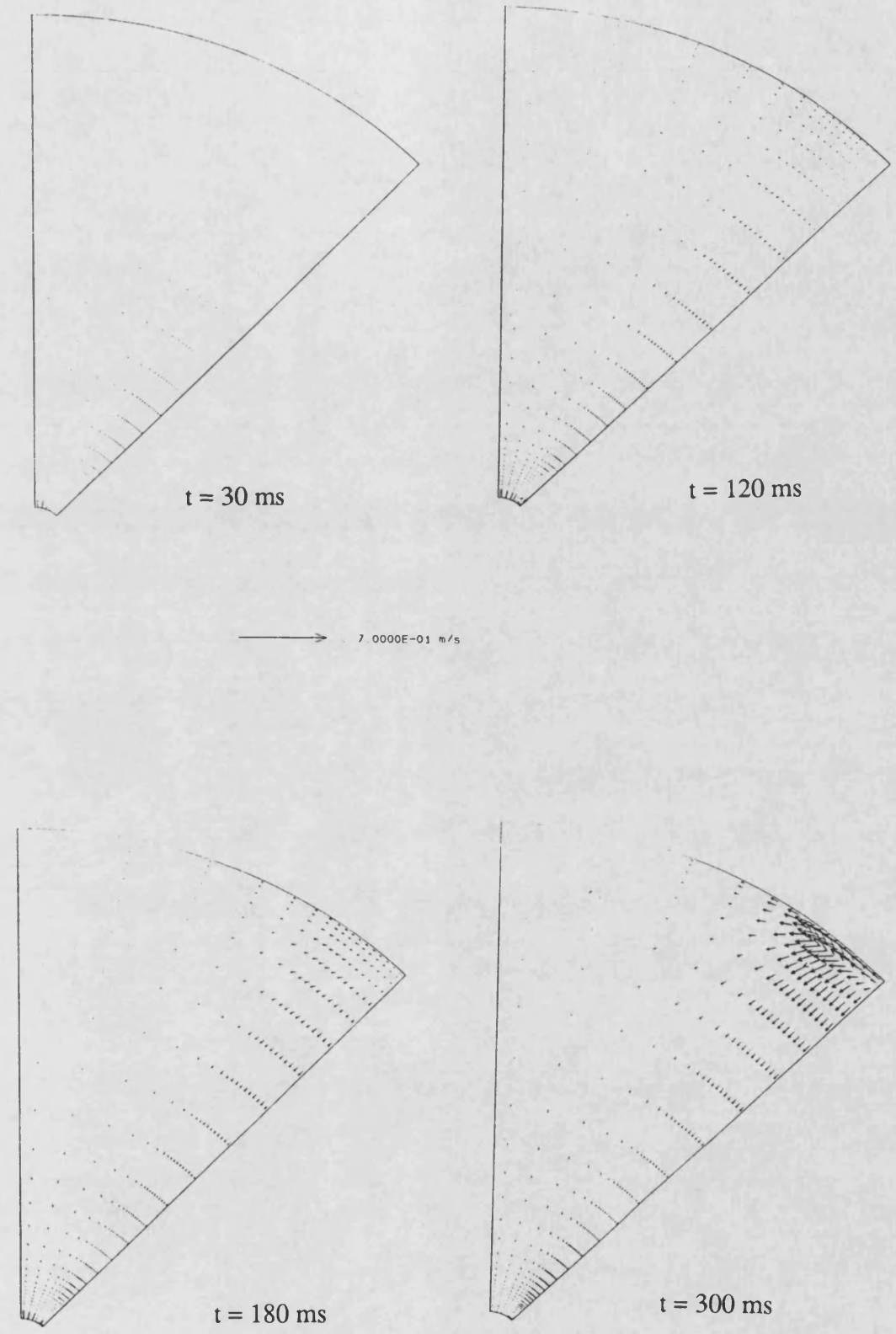

Fig. 7.45: temporal development of velocity vectors in r - θ plane, z = 27 mm

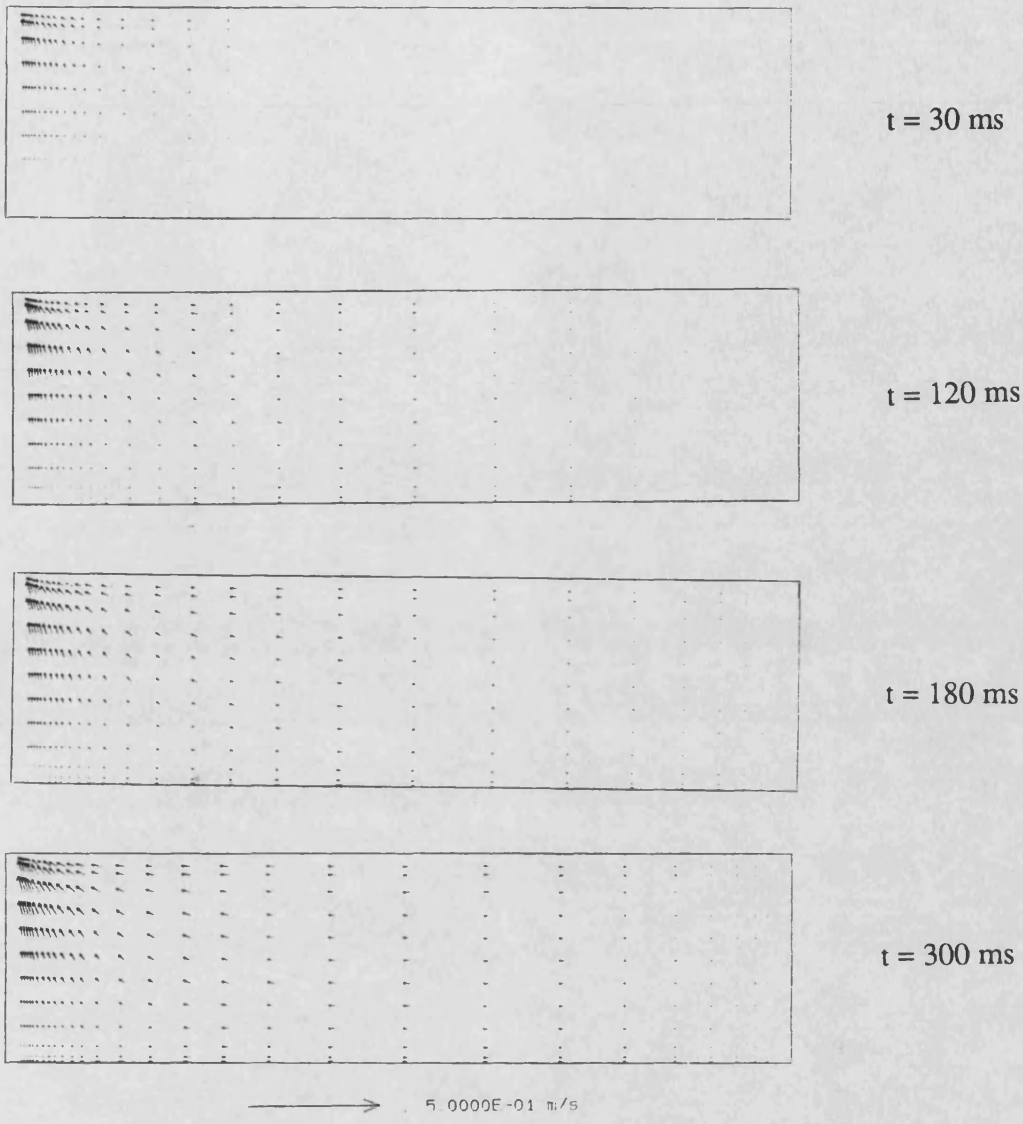

Fig. 7.46: temporal development of velocity vectors in r - z plane, θ = 33 degrees

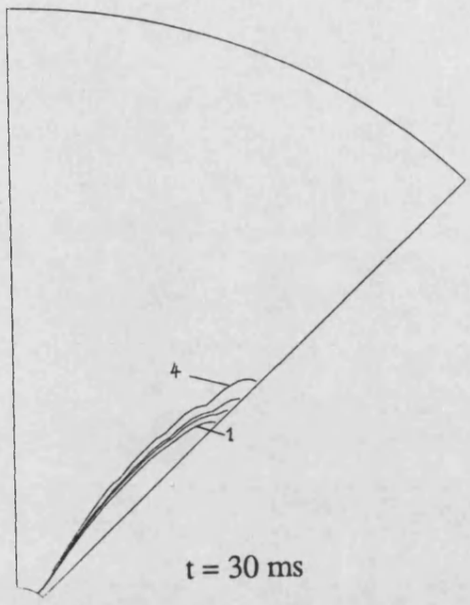

t = 30 ms

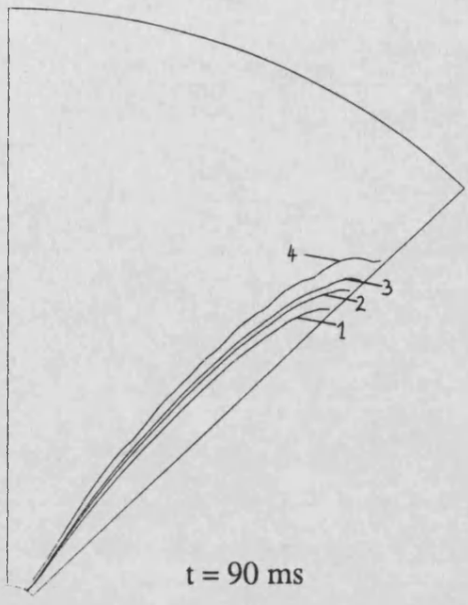

t = 90 ms

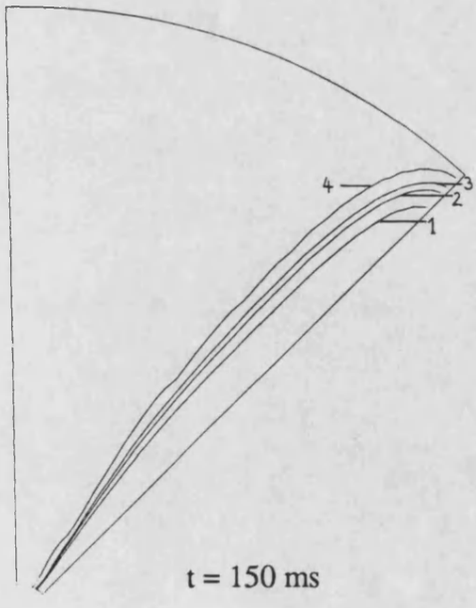

t = 150 ms

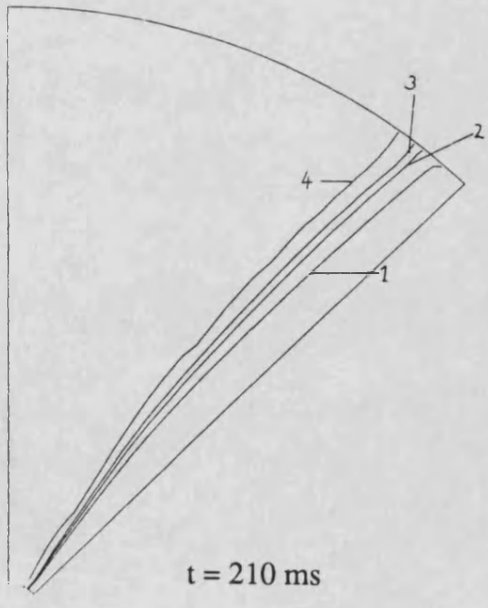

t = 210 ms

cont.

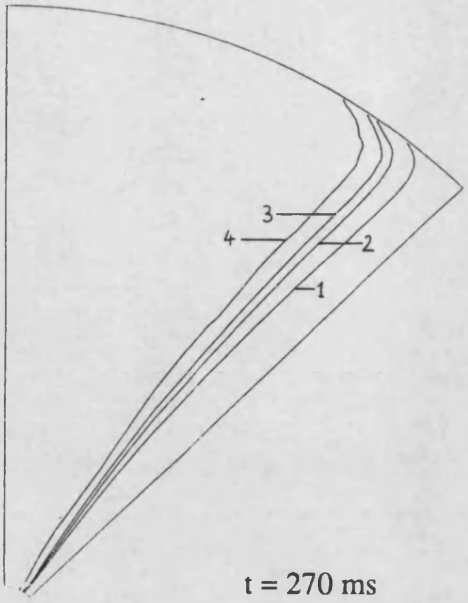

t = 270 ms

Fig. 7.47: temporal development of air - fuel ratio contours in r - θ plane (jet symmetry plane)

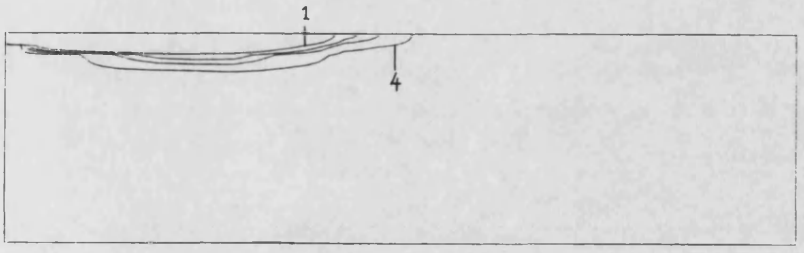

t = 30 ms

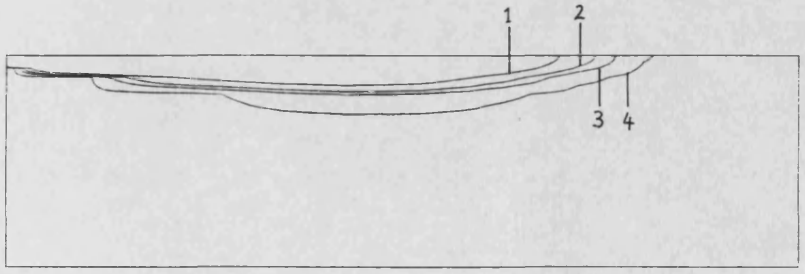

t = 90 ms

cont.

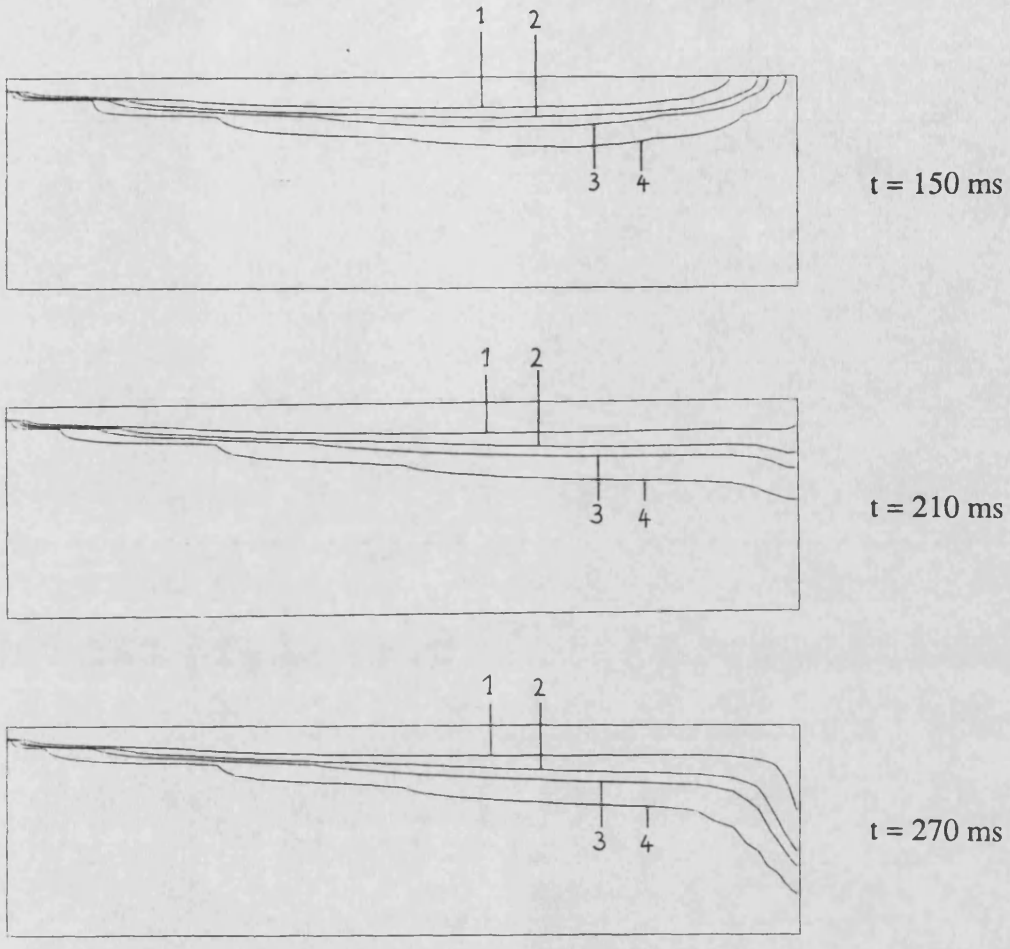

Fig. 7.48: temporal development of air - fuel ratio contours in r - z plane (jet symmetry plane)

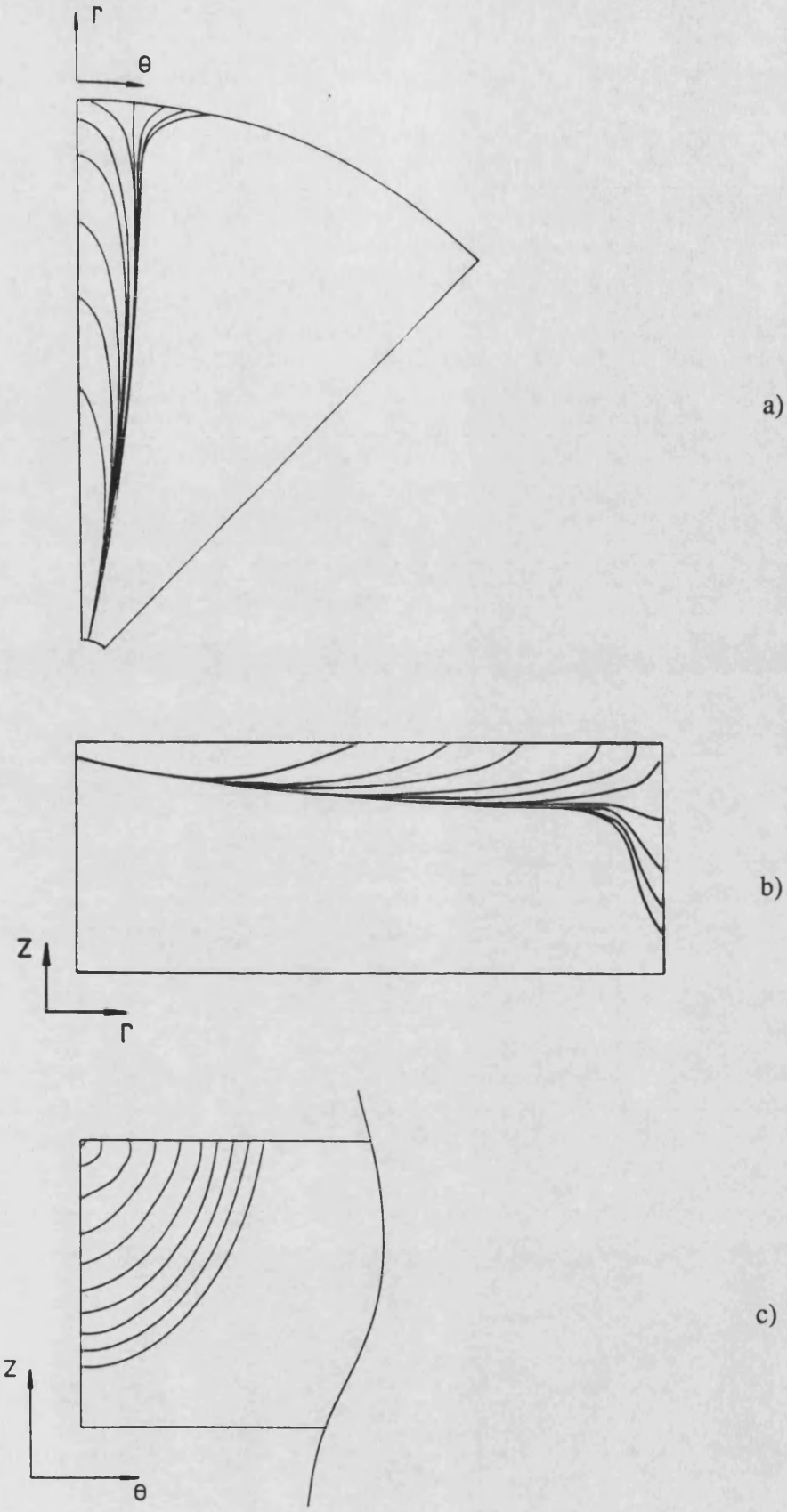

Fig. 7.49: temporal development of 25 : 1 air - fuel ratio contours in a) r - θ plane, b) r - z plane and c) z - θ plane

CHAPTER 8

8. INJECTION INTO SWIRLING FIELD: COMPUTATIONAL STUDY

The numerical model described in the previous chapter has been extended to predict steady state and impulsive injections into a swirling flow field. In the present chapter computational results are presented and compared with experimental data reported in chapter six. The chapter is structured as follows: in section 8.1 the problem is defined with reference to the data input file 'Q1' and subroutine 'Ground'. The swirling flow field generated prior to injection is discussed in section 8.2. The discussion is followed in section 8.3 by a detailed analysis of the flow field obtained during steady state injections for three different swirl rates: 30, 40 and 50 rpm. Results are presented as profiles of radial velocity and turbulence intensity at five radial locations. Furthermore, vector plots are presented together with contour plots of angular velocity and kinetic energy for the r - θ plane bisecting the nozzle exit. These plots are complemented by contour plots of kinetic energy and streamwise vorticity in four r - z planes downstream of the point of injection. Transient results are discussed in section 8.4 for a swirl rate of 50 rpm. Results are shown as velocity profile plots, contour plots and vector plots at different time steps to capture the temporal development of the flow in both the r - θ plane bisecting the nozzle and a selection of r - z planes downstream of the injector. The concluding remarks in section 8.5 summarize the chapter.

8.1 Problem Definition

The flow under investigation is defined in the data input file 'Q1' which is organized similar to the input file for the undeflected jet discussed in chapter seven. It is thus not proposed to give a detailed account of the various groups appearing in the 'Q1' file but rather to focus on new input statements specific to the modified flow configuration. The problem specification is divided into two parts relating to (i) the generation of a swirling

field and (ii) the injection process. An annotated listing of the input file is reproduced in appendix C1. A modification to a turbulence model constant and the computation and output of newly defined variables is implemented in subroutine 'Ground'. The relevant code sequences are listed in appendix C2.

8.1.1 Data Input in PHOENICS 'Q1' File

In the input file reproduced in appendix C1 use is made of the 'RUN' facility in the first program line to specify that two consecutive runs are to be performed. The first run generates the swirling field without injection in the framework of a group structure comprising 24 groups. The 'STOP' command separating the two runs after group 24 is followed by input commands pertaining to the injection. Commands from the first run may be overwritten, if no new statements are supplied the settings from run one still apply to the second run. Hence, for example no commands relating to the computational mesh are required in run two. Figure 7.3 illustrates how consecutive runs are implemented in the PHOENICS solution algorithm by an additional loop around the entire solution sequence. Each run is solved until convergence before the solution proceeds to the next run.

The computational mesh defined in groups 3 to 5 is illustrated in figure 8.1. In the simulation of a single jet injection the flow field far upstream of the nozzle is, unlike in the case of e.g. a four hole nozzle, distinctly different from the flow downstream of the injector. It is hence not possible to apply symmetry conditions in the r - θ plane. The jet centre at the point of injection is indicated in figure 8.1 ($\theta = 0$ deg.). In the immediate entrainment region the grid spacing is very fine and not symmetrical with respect to the nozzle centre. The mesh is considerably finer downstream of the point of injection to capture the mixing processes in the deflected jet. In large parts of the computational domain well removed from the point of injection the mesh is rather

coarse. These regions are characterized by very little hydrodynamic activity and are, since the jet development is the focus of attention, of no particular interest to the present study. Computer time and memory requirements for this flow configuration are high compared with the undeflected jet, it is hence important to economize where possible while simultaneously ensuring that no numerical inaccuracies are introduced by the relative coarseness of the mesh in certain regions of the flow domain. Numerical errors are known to occur for example where a coarse mesh coincides with skewed velocity vectors. In flow regions far removed from the point of injection the swirling flow field is expected to be closely aligned with the cylindrical polar mesh, thus fairly large cells are acceptable. The grid spacing in radial (y) and axial (z) direction remains unchanged from the undeflected jet simulation reported in chapter seven. The numerical grid thus comprises 56 x 43 x 18 cells in circumferential, radial and axial direction respectively. The variables solved for are the standard variables, i.e. pressure and the three velocity components. In addition, computer storage is provided in group 7 for four variables calculated in subroutine 'Ground', viz. angular velocity (OMEGA), streamwise mean vorticity (VORT), resultant velocity vector (VECT) and turbulence intensity (TINT). Two consecutive runs are performed to (i) generate the swirling flow field and (ii) simulate the injection process. To enhance convergence in the first run an initial velocity field corresponding to a solid body rotation of 50 rpm is specified in group 11. Boundary conditions are set in group 13 for the r - z plane at IX = 1 and IX = NX (cyclic boundary) and for the tank side wall and bottom. Both walls rotate at 50 rpm. Since no fluid enters or leaves the domain during swirl generation prior to injection it is not necessary to specify a pressure boundary condition for the first run, it is however important to stipulate some arbitrary value as a reference pressure for the iteration process. The reference pressure is a numerical requirement and has no effect on the flow field generated in the first run, however, it enhances convergence of the second run if a realistic value is chosen. Here, the pressure in one of the cell areas that form the outflow boundary in the second run is set to zero. Several under - relaxation factors in the range from 0.01 to 0.0001 were examined and the

solution of the first run was found to be fairly insensitive towards these settings, however during injection in the second run strong oscillations and divergence occurred for false time steps larger than 0.0001. This value was hence specified in group 17 for the three velocity components, kinetic energy and dissipation rate and maintained during the second run.

Run two was used to simulate the steady state and impulsive injection into a swirling flow field, accordingly for the latter case the steady state option is deactivated at the beginning of the second run and the number and size of time steps are set. The flow field is stored for post processing after user defined time intervals. Restart runs are performed for progressing time steps with a restart input file derived from the 'Q1' file shown in appendix C1. In the present study the flow field was stored and analyzed at 40, 80, 120, 160, 220 and 300 milliseconds after start of injection. As in the undeflected jet simulation, solution of the concentration C1 is activated to predict the temporal development of air - fuel ratios. In the experimental study the rotating cylindrical drum is stopped immediately before the start of injection to simulate stationary cylinder walls. In the numerical model the input commands pertaining to boundaries rotating at constant angular velocity do not allow zero velocity to be specified, a very small value (0.001 rad/s) is hence chosen for the cylinder wall and bottom. As in the case of the undeflected jet a parabolic inlet velocity profile is defined at the point of injection. Eighteen cells cover the nozzle in circumferential direction. For each cell the kinetic energy and rate of dissipation associated with the incoming flow are calculated using the inlet velocity in each cell and the constants selected for the undeflected jet (chapter seven). The concentration of the fluid entering the domain at the nozzle is set to unity while zero concentration is prescribed for the domain at the start of injection. The outflow is located opposite the nozzle as indicated by the shaded area in figure 8.1. The number of sweeps of the entire domain had to be increased compared with the undeflected jet simulation. This is attributed to the smaller under - relaxation factors and the increased number of cells, requiring more iterations for the

convective and diffusive transport terms to penetrate the entire field to obtain convergence.

8.1.2 Subroutine 'Ground'

In contrast to the input file 'Q1', subroutine 'Ground' allows the user to access arrays of the variables solved for during the iteration process. It has been demonstrated in the previous chapter how this facility can be used to generate output files with newly calculated variables like normalized velocities and jet half width. Similar use of 'Ground' has been made in the case of the deflected jet and it is the purpose of this section to describe the Fortran sequences inserted into 'Ground'.

Annotated sections from 'Ground' are reproduced in appendix C2. In group 1 computer storage is allocated for cell face and cell centre geometry data. In addition, memory is assigned to two auxiliary variables (EASP1 and EASP2) in which subsequently calculated velocity gradients are stored. The turbulence model constants (appendix A) are also specified in group 1 together with the van Kármán constant (AK) and the wall roughness parameter E (section 3.4). The turbulence model constants remain unaltered compared with the undeflected jet simulation. Although the injection into a nonuniform crossflow represents a distinctly different configuration where the interaction between jet and crossflow is expected to lead to a different shear stress distribution, no support for a modified set of constants could be found in the literature. The predictions of jets issuing into a uniform crossflow reported by Jones and McGuirk [27] and Patankar [24] both use the standard turbulence model constants. Sykes et al [96] chose the turbulence model constants for a jet emitted normal to a uniform free stream to give a good fit to the prediction for the undeflected jet. This practice is also adopted in the present study.

In group 19 non - standard variables are calculated and output files are written for subsequent plotting of profiles of velocity, turbulence intensity and kinetic energy at five radial locations. As a new variable the streamwise component of vorticity is solved for. The general form may be written in cylindrical polar co-ordinates as [97]:

$$\Omega = \text{rot}\ \vec{U} = \left(\frac{1}{r}\frac{\partial U_z}{\partial \theta} - \frac{\partial U_\theta}{\partial z}, \frac{\partial U_r}{\partial z} - \frac{\partial U_z}{\partial r}, \frac{1}{r}\frac{\partial (rU_\theta)}{\partial r} - \frac{1}{r}\frac{\partial U_r}{\partial \theta}\right) \tag{8.1}$$

where Ω is the vorticity and $\vec{U}$ the mean velocity vector. Since mainly the streamwise component is of interest, it is sufficient to calculate Ω_θ from the mean velocity gradients in constant r - z planes using service subroutines provided in the framework of subroutine 'Ground'. A non - dimensional form is chosen for velocities and cell face distances, the streamwise vorticity component is hence calculated from

$$\Omega_\theta = \frac{\partial (U_z / V_{in})}{\partial (r/D)} - \frac{\partial (U_r / V_{in})}{\partial (z/D)} \tag{8.2}$$

where V_{in} is the maximum jet velocity at the nozzle exit (10 m/s) and D the sidelength of the square nozzle hole.

At the penultimate sweep and last time step further variables are calculated for the r - θ plane bisecting the nozzle exit: angular velocity (GOM), velocity vector (VECT) and turbulence intensity (TINT). Subroutine SETYX writes the calculated values into arrays using identifiers assigned by the program (47, 48, 50). Computer storage has been allocated in 'Q1' with the STORE command. Radial velocity, turbulence intensity and kinetic energy are written to output files for 110 degrees segments at five radial locations. The data is subsequently used for profile plotting. These profiles are not symmetric with respect to the nozzle centre but comprise angles of 40 degrees upstream of the point of injection and 70 degrees downstream in order to capture the curvature of the jet.

8.2 Swirling Flow Field

The grid used for modelling the swirling flow field covers the entire domain in the horizontal r - θ plane (figure 8.1), whereas in vertical direction only the part from the tank bottom to the plane bisecting the nozzle exit is considered (figure 7.2). When modelling the injection into a quiescent medium in chapter seven, use of symmetry conditions led to savings in computer storage and run time. In the case of a swirling flow field established prior to injection the same symmetry conditions cannot be applied in the horizontal r - θ plane. The number of cells in circumferential direction was increased from 17 to 56, thus increasing computer memory requirements by a factor of 3.3. To capture the influence of frictional forces exerted from the stationary tank top the entire vertical extent of the domain would have to be modelled with a reasonably fine grid near the top boundary. This effort was computationally not acceptable and it was therefore decided to neglect the velocity gradients induced by the stationary tank lid and restrict the computational domain to the bottom part of the analogue model with a symmetry condition at the horizontal plane bisecting the nozzle exit. The effect of the stationary top boundary was examined by Gan [23] who modelled a 90 degree segment over the entire vertical extent for a swirl rate of 30 rpm using a k - ε turbulence model. His curve of mean tangential velocity against radius shows a marked deviation from the corresponding curve for a solid body rotation, but likewise deviates considerably from measured data at five radial locations. The predicted tangential velocities show a nonlinear behaviour with a sharp drop near the outer wall followed by a gradual decrease towards the centre. It is also interesting to note that Gan [23] measured rms values of turbulence fluctuation up to ten times larger than predicted. This suggests a deficiency in the turbulence model which appears not to predict the correct turbulence level for pure swirling flow. Launder [77] reports that the flow structure in swirling flows is strongly influenced by the action of Coriolis forces in the Reynolds - stress budget. Coriolis terms do not appear in the kinetic energy equation and the k - ε model is hence known to have no effect on the flow pattern.

Algebraic stress models or Reynolds stress models with second moment closure have been demonstrated to be more suitable to predict rotational flows [77]. It was not within the scope of the present study to implement a turbulence model of the second moment closure type in an attempt to correctly model the swirling field. In more complex modelling work where factors like inlet port geometry, more complicated combustion chamber geometries and the effect of piston movement are taken into account, this aspect gains significance and more refined turbulence models may be called for. It is however worth noting that due to the complexity of these models very recent studies (e.g. Ahmadi-Befrui et al [98]) still use the k - ε model to simulate in-cylinder air motion and undertake elaborate experimental work to validate predictions. In this study a correct representation of the swirling field would have been desirable from a validation point of view since detailed experimental data on steady state and transient deflected jets is available. However, in the light of the k - ε model's inherent weakness in predicting pure swirl (exemplified by Gan's [23] prediction of the swirling flow field) it was decided to restrict attention to a linearly varying crossflow which was generated by applying a symmetry boundary condition at the plane bisecting the nozzle exit. For practical purposes valuable insight into the mixing pattern at different swirl rates and under transient conditions can be obtained from this flow configuration. The velocity distribution in the injector plane for a swirl rate of 50 rpm is shown in figure 8.2, together with experimental data from figure 6.28.

Numerical results for steady state injections at three swirl rates (30, 40 and 50 rpm) are presented and discussed in the following section.

8.3 Steady State Injection into Swirling Flow Field

The experimental results reported in chapter six illustrate some of the essential features of the fully three - dimensional jet emitted normal to a nonuniform crossflow. They

show the development of the initially normal jet through a bending phase to a flow aligned with the swirling field. In the present section numerical solutions are presented for the same flow configuration. It is apparent from the experimental results that at a swirl rate of 50 rpm the jet does not penetrate to the cylinder wall. For this reason two lower swirl rates were also examined numerically (30 and 40 rpm) in order to approximately identify the angular velocity which yields the most favourable mixing pattern. The results give a detailed picture of the three - dimensional flow in various r - θ, r - z and z - θ planes. To the author's knowledge no prediction of a jet issuing normally into a linearly increasing crossflow have been previously published. Numerous numerical solutions for free and confined uniform crossflows are reported in the literature, e.g. references 24, 27 and 96. In most cases the computational mesh is fairly coarse with Sykes' [96] study using the finest grid allowing for a detailed examination of the flow field. In this context the work of Lin et al [99] is also of interest who examined the flow field resulting from radial injections into a combustor using a Reynolds stress model with second moment closure. For the present flow configuration Gan [23] obtained numerical solutions for a swirl rate of 30 rpm simulating steady state injections from a four hole nozzle. Due to computer memory limitations his mesh was restricted to 25 x 23 x 23 cells covering one quadrant of the analogue model. The aim of the present study is to provide a comprehensive picture of the flow field generated during injection for three different swirl rates (30, 40 and 50 rpm) using a single hole nozzle. Modelling a one hole nozzle arrangement eliminates interference between neighbouring jets as was observed experimentally by Gan [23] for high swirl rates and hence allows the mixing pattern produced by a single jet to be studied. During the numerical solution values for all variables solved for may be stored in computer memory for the entire computational domain. A careful selection of data is hence important so as to extract meaningful information for the flow field analysis. To give a fully three dimensional picture of the jet development numerical results are presented for a selection of z - θ, r - θ and r - z planes in the following form:

z - θ plane: - radial velocity profiles

- turbulence intensity profiles

r - θ plane: - velocity vector plots

- angular velocity contours

- kinetic energy contours

r - z plane: - kinetic energy contours

- mean streamwise vorticity contours

In the following discussion attention is drawn first to the 50 rpm swirl rate for which experimental data is available. Following this analysis consideration is given to the numerical solution for angular velocities of 30 and 40 rpm.

Swirl rate 50 rpm

One major difference between the experimental results and the numerical prediction has already been discussed in the previous section, viz. the tangential velocity distribution in the swirl field generated prior to injection (figure 8.2). The measured values vary nonlinearly in radial direction with their magnitude not exceeding 50 % of the predicted velocities. Figure 8.3 illustrates that the predicted linear increase results in a more rapid jet deflection than was observed experimentally. While at the inner three radii the peak velocities agree well, at r/D = 38 the maximum predicted velocity has decayed to 0.17 m/s compared with 0.45 m/s obtained during measurements. Computer predictions suggest that at r/D = 47 the jet is completely deflected with the radial velocity approaching zero. Along with the more rapid predicted velocity decay goes a slight shift in the angular location of measured and predicted maximum velocity. While at the inner two radii the predicted velocity peaks are upstream of the corresponding measured peaks, at r/D = 29 they nearly coincide and at r/D = 38 the predicted peak has drifted downstream of the measured maximum velocity. This behaviour suggests a

shorter zone of maximum deflection (figure 6.30) with a sharper bend in the jet axis predicted by the numerical model. At all radial locations the simulation can be seen to yield narrower velocity profiles. Near the nozzle exit the predicted velocity gradients at the outer jet boundary are steeper than the measured gradients. In the wake region downstream of the point of injection both the measured and the predicted profiles show a much reduced gradient. It appears that the former extends further downstream, however, as explained in chapter six, the experimental results at very low velocities may not be entirely reliable. More insight into the spread of the jet can be gained from the turbulence intensity profiles depicted in figure 8.4. For the inner three radii they give a good indication as to where the downstream jet boundary is located and confirm the observations from the velocity profiles, i.e. that the predicted jet is narrower with a smaller wake region. At r/D = 38 the predicted upstream boundary is no longer clearly defined as this is the region where the jet is strongly deflected. The maximum at approximately 20 deg. coincides with the radial velocity maximum (figure 8.3) at the same radius and may be taken as an indication that the outer jet boundary is located in the region of 15 to 20 deg. . No inner boundary is predicted, the jet is too far deflected and its body almost completely aligned with the swirling flow. Again, the predicted wake region is considerably smaller than the experimental results suggest. A few remarks are called for to explain the evident discrepancy in the predicted and measured turbulence intensity profiles at r/D = 11. It is recalled that the turbulence intensity is particularly sensitive towards variations in mean velocity when this is very small since the mean velocity vector appears in the denominator of the turbulence intensity expression. At jet boundaries where high levels of turbulence activity coincide with mean velocities approaching zero, high levels of turbulence intensity are therefore to be expected. Near the nozzle exit the jet cross section has not yet been strongly distorted by the action of shear and hence exhibits a stagnation point on its upstream side and a low velocity region on its downstream side as a consequence of the jet obstructing the crossflow. These two low velocity areas are predicted and result in marked turbulence intensity peaks on either side of the jet. The experimental method may have failed to

capture the very small mean velocities and consequently yields lower turbulence intensity values.

Apart from serving as an indicator for the jet boundaries, turbulence intensity profiles also help identify areas where numerical errors (e.g. false diffusion caused by the Hybrid scheme) affect the solution. These errors not only depend on the level of mean velocity, but also on the velocity gradients which in turn influence the level of kinetic energy via the production term in the k - equation (4.13). The turbulence intensity derived from k may hence be regarded as an indicator of numerical inaccuracies. The underpredicted extent of the wake region in figure 8.4 reflects a deficiency of the Hybrid scheme to accurately capture recirculating flows. Hoholis [28] found the Quick scheme to perform better in recirculating zones resulting from jet impingement on cylinder walls.

An alternative way of obtaining an insight into the mixing pattern lies in examining the flow field in the two remaining planes, i.e. the r - θ and the r - z plane. First, attention is drawn to figures 8.5 to 8.7 depicting velocity vectors together with contours of kinetic energy and angular velocity in two different r - θ planes. For reasons of clarity velocity vectors in the immediate vicinity of the nozzle are not shown. The figures illustrate the extent to which the jet penetrates the domain and the size of the recirculation zone downstream of the point of injection. The kinetic energy contours in figure 8.5 show the region where the numerical model predicts turbulence activity. The contour shapes follow very closely the velocity vector field, an observation that is consistent with a finding from the experimental study (chapter 6), i.e. the jet axis deduced from the velocity maxima agrees well with the jet axis constructed from the kinetic energy maxima. The bunching of contours on the jet's upstream side indicates strong mixing while downstream of the jet the contour gradient is much shallower, suggesting a smaller degree of turbulent mixing in the wake region. At the contour closest to the nozzle exit (no. 6) the action of shear along the edge of the jet is discernible from the two peaks at the outer and inner jet boundary. Further into the

domain the jet cross section is more distorted resulting in only one contour peak. After the zone of maximum deflection this peak is no longer clearly defined and at the outermost contour (no. 1) shear at the outer boundary of the deflected jet leads to a very round contour shape. An interesting feature in figure 8.5 is the absence of any sign of a wall jet. The velocity vectors near the wall are completely aligned with the swirling flow and the level of turbulence induced by the wall is considerably smaller than 0.001 m^2/s^2. Experimental results reported earlier (figure 6.33) show fluctuating velocities approaching zero at r/D = 47.

From the vector field it would appear that large parts of the domain remain unaffected by the injection, however, the angular velocity contours in figures 8.6 and 8.7 show that the mean velocity field in the entire analogue model is influenced. In figure 8.6 contour 1 (5.236 rad/s) corresponds to 50 rpm which prevailed in the entire domain before the injection. Compared with the state before injection, contour 1 may be regarded as a line where no circumferential momentum transfer occurs. Inside contour 1 the angular velocity is less than 5.236 rad/s as a consequence of the jet decelerating the cross flow. Circumferential momentum is transferred to the jet leading to its deflection. On the other hand, the jet imparts momentum to the surrounding fluid, initially in radial direction only, but as it passes through the bending phase, also in tangential direction. This tangential momentum transfer accelerates the swirling flow as illustrated by contours 2 and 3 in figure 8.6. Shown are contours of $\omega = U/r$ and, although the transferred tangential momentum will not be uniform in radial direction, the radius appearing in the denominator leads to larger values for ω at small radii. The influence of the tangential momentum transfer can also be seen from figure 8.7 depicting the flow field in a $r - \theta$ plane well removed from the nozzle, i.e. at z = 30 mm. The vector plot suggests pure swirling flow while the angular velocity contours show the momentum transfer in radial and tangential direction resulting from the injection. The swirling flow in the entire plane has been accelerated, no contour values of 50 rpm are predicted.

From the results presented in figures 8.3 to 8.6 the jet trajectory and envelope may be constructed and compared with experimental data as shown in figures 8.8 and 8.9. Here two different observations are relevant:

(i) The predicted jet trajectory shows a sharper bend with a shorter zone of maximum deflection (cf. figure 6.30). This is mainly attributed to the difference in the predicted and measured swirling field prior to injection (figure 8.2). In the vicinity of the nozzle exit the jet's radial momentum dominates and the higher predicted tangential velocities do not lead to a more rapid deflection. On the contrary, near the nozzle the radial momentum is sustained longer suggesting less mixing at the edge of the jet. As the jet penetrates further and decelerates, the higher predicted tangential velocities can be seen to lead to a more rapid jet deflection.

(ii) The measured jet envelope is wider with a more extensive wake region than predicted by the numerical model (figure 8.9). The outer boundaries follow a pattern similar to the trajectories. The smaller predicted wake region is an important feature from a mixing point of view and suggests a weakness of the numerical model (e.g. numerical diffusion) to predict the correct level of mixing on the lee side of the jet. In the context of the Diesel engine application this is a serious limitation when examining different swirl rates and injection characteristics.

The discussion of the 50 rpm case is concluded by examining contours of kinetic energy and streamwise vorticity in four different r - z planes. The planes are located 4.5, 8.5, 15.0 and 25.0 degrees downstream of the nozzle centre as indicated in figures 8.1 and 8.5 to 8.7. The kinetic energy contours from figure 8.10 complement those from figure 8.5 so as to provide a three dimensional picture of the turbulence activity induced by the injection process. With increasing downstream distance the contours are seen to propagate towards the cylinder wall, e.g. contours 2, 4 and 5. In the wake region the level of kinetic energy diminishes with increasing distance from the centreline and the contours are consistent with the flow field representation from figure 8.5. In z -

direction the injection can be seen to leave large areas of the domain unaffected, clearly indicating that a horizontal injection is not suitable for the intended Diesel engine application. It is also interesting to note that at θ = 15.0 and 25.0 degree the locus of maximum kinetic energy is not on the symmetry plane bisecting the nozzle exit but some distance below that plane. This is taken as an indication of a vortex forming due to the shear along the edge of the jet. Further evidence of this vortex is given in figure 8.11 depicting contours of the streamwise component of vorticity calculated from eqn. (8.2). Vortex development is discussed in some detail by Sykes et al [96] for a jet issuing into a uniform cross flow. By examining the production and diffusion terms in the vorticity equation he concludes that the main features of the flow are a result of the injection of a series of vortex rings and subsequent diffusion of these rings. As the rings become sufficiently diffused the effects of the *transverse* components of vorticity in the rings are largely cancelled by the interaction between neighbouring rings. This leads to the characteristic appearance of a *streamwise* pair of line vortices of which, for reasons of symmetry, one half is shown in figure 8.11 for four locations downstream of the injector. The cross - sectional shape of the vortex structure seems to be similar to that of the kinetic energy field (figure 8.10). The core of the vortex structure is seen to propagate towards the cylinder wall as it is convected downstream. Following the development of individual contours it is evident that the vortex strength diminishes with increasing downstream distance. In the immediate vicinity of the nozzle (i.e. at θ = 4.5 deg.) contours are still largely influenced by vorticity emitted from the jet source. Further into the domain the mechanism outlined above leads to the appearance of line vortices that characterize the distorted jet cross section in a cross flow.

Swirl rates 40 and 30 rpm

The plots relating to swirl rates of 40 and 30 rpm show similar features and are best discussed collectively. Figures relating to 40 and 30 rpm are respectively grouped as 8.12 - 8.17 and 8.18 - 8.23. In each group profiles of radial velocity and turbulence intensity are presented first, vector plots in the r - θ plane with superimposed kinetic

energy and angular velocity contours second, and contours of kinetic energy and streamwise vorticity in the r - z plane third. Since no experiments were undertaken for swirl rates of 40 and 30 rpm, it is not possible to make any categoric statements as to the validity of these predictions. It is however instructive to compare the numerical results with the 50 rpm case examined earlier (figures 8.3 - 8.11). A number of observations are relevant:

- The velocity profiles (figures 8.12 and 8.18) are narrow with a steep gradient on the upstream side and a shallower gradient on the lee side of the jet. As in the 50 rpm case no extensive wake region is predicted which is again attributed to numerical errors as outlined earlier in this section. At the inner two radii the negative velocities on the upstream side of the jet indicate fluid being entrained. The effect of the different swirl rates on the velocity decay can be seen midway into the domain: at r/D = 29 the maximum radial velocities for 30, 40 and 50 rpm are respectively 1.52, 1.20 and 0.88 m/s and at r/D = 38 the corresponding values are predicted as 0.70, 0.38 and 0.17 m/s.
- The turbulence intensity profiles for 40 rpm (figure 8.13) and 30 rpm (figure 8.19) give a good indication as to where the downstream boundary is located near the injector, however, at r/D = 38 and 47 this boundary is poorly defined. A similar observation was made for the 50 rpm case (figure 8.4) and is attributed to the numerical model which fails to capture the precise extent of the recirculation zone downstream of the jet. The outer jet boundary is readily identified at the inner three radii and, for 30 rpm, also at r/D = 38. Both the turbulence intensity and the radial velocity profiles near the cylinder wall show that for 30 rpm the jet penetrates further in radial direction.
- Plots illustrating the velocity vector field together with contours of kinetic energy and angular velocity are provided in figures 8.14 and 8.15 for 40 rpm and figures 8.20 and 8.21 for 30 rpm. Examining the kinetic energy contours in figures 8.14 and 8.20 together with those for 50 rpm (figure 8.5) clearly illustrates the

influence of different swirl rates on the degree of deflection and the size of the recirculation zone on the lee side of the jet. As in the 50 rpm case discussed earlier, it seems likely that the extent of the wake region is underpredicted as a result of numerical diffusion caused by the Hybrid scheme. The widening of contours 1 to 4 with growing swirl rate suggests an increased level of diffusion with stronger mixing activity as the swirl rate increases. The sectors enclosed by the 0.001 m^2/s^2 contour for 30, 40 and 50 rpm are respectively 40, 45 and 63 degrees.

The influence of the injection process on the swirling field can also be visualised with the aid of figures 8.15 and 8.21 depicting angular velocity contours. Contour 1 corresponds to the swirl rate prevailing in the entire domain prior to injection and may thus be regarded as a contour where no tangential momentum is transferred between the jet and its surroundings. The extent of this contour in circumferential direction can be seen to depend on the swirl rate. Comparing the corresponding figures for the three swirl rates, the upstream side of contour 1 can be seen to drift nearer to the centreline and the size of the sector (defined by tangents through the origin and both contour sides) is increasing from 51 and 55 to 58 degrees at 30, 40 and 50 rpm respectively.

- Contours of kinetic energy and streamwise vorticity in four r - z planes downstream of the point of injection are shown in figures 8.16 and 8.17 for 40 rpm and 8.22 and 8.23 for 30 rpm. It is important to realize that these figures represent a view of the r - z plane rather than a cross sectional view normal to the jet axis. This is particularly noticeable near the nozzle where the contours extend back to the injector, further downstream they bear closer resemblance to cross sections perpendicular to the jet axis. The kinetic energy contours supplement figures 8.14 and 8.20 so as to provide a three dimensional picture of the kinetic energy field. As already pointed out when discussing the 50 rpm injection, substantial parts of the domain appear to be largely unaffected by the injection process.

Similarities between kinetic energy contours and lines of streamwise vorticity are evident. The shapes of these contours are in broad agreement, both exhibit similar features as the jet bends with increasing distance from the injector. In particular, the locus of maximum kinetic energy and vorticity can be seen to propagate towards the cylinder wall and the shape of individual contours follows similar patterns. For example, the k - contour for 0.01 m^2/s^2 in figure 8.16 grows in radial direction as the jet progresses until θ = 15 deg.. At this point the inner boundary has advanced into the domain giving the contour an elliptical appearance. Further downstream at θ = 25 deg. it has decreased in size and the overall level of kinetic energy has diminished, indicating a weakening in turbulence activity. The extent of the 0.01 m^2/s^2 contour at θ = 15 deg. corresponds approximately to the proportions of the 0.001 m^2/s^2 contour at θ = 25 deg.. The vorticity contours in figure 8.17 exhibit very similar characteristics (e.g. contours 2 and 3), reaching their maximum width at θ = 15 deg.. Further downstream at θ = 25 deg. the vorticity can be seen to have lost intensity.

The similarity between kinetic energy and vorticity contours can be accounted for by the fact that the latter is derived from mean velocity gradients which also appear in the production term of the kinetic energy equation (4.13). The similarity may be taken as an indication that the production term plays a dominating role in eqn. (4.13).

A comparison of figures 8.10, 8.16 and 8.22 illustrates the effect of different swirl rates on the kinetic energy distribution resulting from the injection. Near the point of injection (θ = 4.5 and 8.5 deg.) there is good agreement between the contours representing large values of k. For the lowest swirl rate and hence the smallest degree of deflection the weak kinetic energy contours show the strongest penetration. This trend is gradually reversed with increasing angular distance from the nozzle. At θ = 15 deg. the extent of 30 rpm and 40 rpm contours for 0.01 and 0.05 m^2/s^2 is broadly in agreement (although for 30 rpm centred slightly further into the domain) while at θ = 25 deg. turbulence activity is diminishing

in the 30 rpm case. As a consequence of the strongest deflection at 50 rpm, contours of k = 0.001 and 0.01 m^2/s^2 are wider at θ = 25 deg. than predicted for the two other swirl rates.

For the streamwise vorticity in figures 8.11, 8.17 and 8.23 very similar observations can be made. Near the nozzle at θ = 4.5 and 8.5 deg. the deviation from a cross sectional view normal to the jet axis is most noticeable with the contours reaching back to the injector. The jet axis for a swirl rate of 50 rpm shows the strongest deflection, the contours at θ = 15 and 25 deg. in figure 8.11 may hence be regarded as the nearest representation of the vortex structure in the plane normal to the jet axis.

Comparison of injections for swirl rates of 30, 40 and 50 rpm

The preceding remarks were mainly of a qualitative nature. In the present section quantitative data inferred from the results described above is discussed with reference to figures 8.24 to 8.27.

The predicted trajectories for the three swirl rates in figure 8.24 are derived from radial velocity profiles and kinetic energy contours. The comparison with experimental results for 50 rpm (figure 8.8) discussed in chapter six inspires confidence in the validity of the predictions. It appears that hydrodynamic processes at the outer boundary are fairly accurately captured by the model and that variations between the measured and predicted jet axes are due to the different swirling fields prior to injection. In figure 8.24 the trajectories clearly illustrate the effect of different swirl velocities on the rate of deflection. At r/D = 47 all three jets have transferred most of their radial momentum to the surrounding fluid, although not to the same extent. At 30 rpm the radial velocity at r/D = 47 is still predicted to 0.11 m/s while for 40 rpm the jet has decelerated to 0.04 m/s. For 50 rpm the jet is completely aligned with the swirling flow. To determine the most favourable swirl rate from a mixing point of view the jet axes should be viewed together with the jet envelopes shown in figure 8.25. Judging from the

comparison with experimental data obtained for 50 rpm (figure 8.9) the outer boundaries appear to be well predicted. At the inner boundaries however, the location of the jet's edge is only defined at the inner three radii. The turbulence intensity peaks on the downstream side in figures 8.4, 8.13 and 8.19 are due to the very low mean velocities near the centre of the recirculation zone. Further into the domain, i.e. outside the wake region, turbulence intensity profiles are obscured by the deflected body of the jet. Here profiles normalized with the velocity vector no longer serve as an indicator for the downstream boundary since the circumferential velocity begins to dominate the mean velocity expression. The observations made when discussing figure 8.9, i.e. that the extent of the recirculation zone is underpredicted, seem also to apply to the downstream boundaries obtained at the inner three radii for 30 and 40 rpm. This is mainly attributed to numerical diffusion and to the k - ε turbulence model which is known to perform poorly in recirculating flows [77].

An interesting feature of the deflected jet is its growth viewed in cross sections perpendicular to the jet axis. Due to the ambiguity as to where the downstream boundary is located in figure 8.25 a different indicator for the spread of the jet is chosen, viz. the edge is defined as the point where the magnitude of the velocity vector reaches 1 % of the inlet velocity (0.1 m/s). It is recognized that rates of spread derived from this definition are also affected by the inaccurate prediction of the recirculation zone, however, an argument in favour of this definition is rooted in the fact that numerical diffusion mainly affects velocity gradients and is less likely to distort the mean velocity field. Figures 8.26 and 8.27 show the widening of the jet along its axis and velocity vector contours used to construct these curves. The co-ordinates chosen in figure 8.26 are the width, ζ, in the r - θ plane perpendicular to the jet axis and the axis itself, ξ, from figure 8.24. Both co-ordinates are non-dimensionalized with the side length of the nozzle hole, D. In figure 8.27 the contours depict cross sections in the symmetry plane of the jet and hence represent the narrowest part of the kidney shaped structure. The initial rate of spread, i.e. the gradient in figure 8.26, shows

reasonable agreement between the three swirl cases. Only in the vicinity of the cylinder wall near the tip of the 0.1 m/s contour is the spread decreasing. The narrower shape at low swirl velocities leads to a more rapid spread decay.

8.4 Impulsive Injection into Swirling Flow

From a Diesel engine point of view the most interesting of the four cases considered in the present study is the transient jet emitting into the combustion chamber model in which swirl has been generated prior to injection. Numerical results for this configuration show the developing form of the jet, the variation of fuel concentration within it, and the effect of swirl on this distribution. As in the previous section, results are presented and discussed with reference to velocity profiles at five radial locations, vector and contour plots in the horizontal r - θ plane, and cross sectional views in the r - z plane at four angular locations downstream of the point of injection.

Figures 8.28 to 8.32 compare the temporal jet development predicted at r/D = 11, 20, 29, 38 and 47 with experimental data presented in chapter six. The time steps considered are 40, 80, 160, 220 and 300 milliseconds after begin of injection. While the qualitative agreement is generally good, there are some discrepancies regarding the maximum radial velocity along the jet trajectory, the width of the jet and the degree of deflection.

At r/D = 11 the predicted jet profile can be seen to be fully developed after 40 ms and, with the exception of the recirculation region, not to change noticeably during the injection. Some variation between the predicted and measured profiles is apparent as the jet proceeds, particularly near the end of the injection process at 160, 220 and 300 ms. Here the measured outer edge and velocity peak can be seen to be located slightly further upstream than predicted by the numerical model. This tendency is most noticeable some distance into the domain at r/D = 29, 38 and 47. If one compares the

transient results with the steady state injection (which may be regarded as the limit of the transient case, figure 8.3), it is interesting to note that the agreement between the angular location of measured and predicted peak velocities is generally good. Moreover, the profiles predicted towards the end of the injection agree well with steady state predictions, indicating that there is little difference between the trajectory of the developing jet and the steady state jet axis. In contrast, the experimental results show a smaller rate of deflection in the early stages of jet development compared with steady state measurements, reflecting a gradual drifting of the jet axis towards the steady state limit. Gan [23] also measured an increasing rate of deflection midway into the domain as the jet progresses in time. An explanation for the discrepancy between the transient numerical and experimental results may lie in the influence exerted by the different swirl velocities (figure 8.2) towards which the developing jet is particularly sensitive. The effect of lower swirl velocities on the jet tip in the experimental study may lead to a smaller rate of deflection while the fully developed jet can be seen to be less sensitive towards the different swirl velocities.

Attention is now drawn to the spread of the jet and the developing recirculation region downstream of the nozzle. A comparison with steady state predictions (figure 8.3) shows that the numerical model for the impulsive jet predicts a fairly rapid approach to the steady state profile shape. At r/D = 11 the temporal resolution is not sufficiently high to observe the growth of the jet. After 40 ms the main part of the jet is already fully developed whereas the entrainment region can be seen to grow at a much slower rate. The negative velocities developing on the lee side of the jet serve as an indication of the growing influence the jet is exerting on its surroundings. The entrained mass leads to an increasing rate of spread as illustrated by the profiles at r/D = 20 and 29. As expected, the entrained fluid on the downstream side causes the inner jet boundary to widen. After approximately 160 ms it has nearly reached its steady state shape. At r/D = 38 the jet passes through its zone of maximum deflection (figure 8.24 and 8.25). As it bends the radial velocity decreases and reaches zero close to 35 degrees

when the jet is completely aligned with the swirling flow. In figure 8.31 the jet can be seen to reach its steady state profile shape between 160 and 220 ms after the start of injection. In the vicinity of the wall at r/D = 47 the jet is fully deflected and, as for the steady state injection, zero radial velocity is predicted.

The predicted steady state approach is considerably faster than recorded during measurements. Remarks on the rate of deflection as indicated by the angular location of the peak radial velocity have already been made. From a comparison of figures 8.28 to 8.32 and figure 8.3 it is also apparent that the recirculation region downstream of the jet is not yet fully established at the end of injection. While the predicted profiles can be seen to approach the steady state fairly rapidly, at t = 300 ms the downstream side of the measured profiles has not spread as far as observed during steady state injections. It appears that the recirculation zone formed as a result of shear induced entrainment takes longer to develop than the jet itself.

More insight into the mixing pattern resulting from the injection can be gained by examining figure 8.33 which illustrates the development of the velocity vector field in the r - θ plane bisecting the nozzle exit at t = 40, 80, 120, 160, 220 and 300 milliseconds after begin of injection. Also shown are passive scalar contours at these time intervals representing air - fuel ratios of 10:1, 17:1, 25:1 and 100:1. Following Way [22] the mixing pattern may be described in terms of two dimensionless parameters pertaining to the penetration of the jet in radial direction and the tangential movement. The radial penetration parameter, K_p, is obtained by calculating the penetration of a free undeflected jet with a constant cone angle from an origin at the apex of the cone.

$$K_P = \sqrt{\frac{h \; frac}{D_N}} \tag{8.3}$$

where h is the height of the analogue model, frac the fraction of tank volume injected and D_N the equivalent nozzle diameter. The dimensionless tangential parameter, K_S, is

taken as the angle swept by the swirl during the injection period considered (expressed in degrees):

$$K_S = \omega\, t_i = 6\, \omega_{rpm}\, t_i \ [deg] \qquad (8.4)$$

where the swirl speed is taken in revs per minute and t_i represents the time interval. A derivation of K_P and K_S is given in appendix D. The relative effect of swirl to penetration is expressed by $K_R = K_S/K_P$. The following table shows the dimensionless parameters corresponding to the time steps considered:

t_i[ms]	K_P	K_S	K_R
40	0.0792	12	152
80	0.1112	24	214
120	0.1371	36	263
160	0.1583	48	303
220	0.1856	66	355
300	0.2168	90	415

During injection the relative effect of swirl to penetration changes with time as illustrated by the variation of K_R in figure 8.34. In the early stages of jet development penetration is relatively strong resulting in small values of K_R and very little deflection. As the jet proceeds the influence of swirl, expressed by K_S, increases and the jet starts to bend. The contours on the downstream side of the trajectory can be seen to widen as a result of growing hydrodynamic mixing activity.

The air - fuel ratio contours in figure 8.33 clearly indicate that at the end of injection the mixture in large parts of the domain is weaker than required for a stoichiometric combustion (A/F ~ 17:1). In radial direction the 17:1 contour penetrates up to r/D = 37; in circumferential direction an angle of approximately 45° is covered by the stoichiometric mixture contour at r/D = 32, however, closer to the nozzle and near the cylinder wall this segment is significantly smaller. In the vicinity of the nozzle exit the relatively small swirl velocities result in strong radial penetration with very little jet deflection. Consequently, hardly any tangential passive scalar transport is predicted for small radii, leaving substantial parts of the domain with an in-combustible mixture. For

a qualitative comparison figure 8.35 shows photographic records obtained by Way [22] for 50 rpm and K_R = 460. From figures 8.33 and 8.35 suggestions for an improved mixing pattern may be inferred:

- The radial penetration for a swirl rate of 50 rpm is insufficient for both K_R = 415 (figure 8.33) and K_R = 460 (figure 8.35). A stronger penetration may be achieved by either increasing K_P or by reducing K_S, both measures would lead to a smaller value of K_R. A smaller swirl velocity would reduce the angular extent covered by the stoichiometric contour and might hence require more nozzle holes in the injector. It therefore appears that a stronger penetration resulting from a higher injection pressure at the end of injection is needed to penetrate closer to the wall.
- The largest circumferential extent of the 17:1 contour of 45° suggests that eight nozzle holes would be necessary to fill the entire combustion chamber with a combustible mixture. Alternatively, a higher swirl rate is needed together with an increased injection pressure at the end of injection to compensate for the larger rate of deflection. The analogue model is based on an engine with a constant injection pressure of 120 bar which is low by today's standard.
- In the centre of the combustion chamber mixing in circumferential direction is very poor. From the temporal jet development in figure 8.33 it is apparent that at small time steps the relative effect of swirl to penetration is too small. Given a constant angular velocity of 50 rpm, a larger value of K_R and hence a more favourable mixing pattern can be obtained by reducing the injection pressure at the begin of injection.

From these observations it follows that a more uniform value of K_R throughout the injection process would be desirable. For a constant swirl rate this can be achieved by starting the injection process with a relatively low pressure which is increased as the injection progresses. Numerical simulations which systematically change the penetration parameter K_P can help determine a pressure variation which leads to a more rapid formation of a combustible mixture in the chamber. In a real engine the fast

formation of a combustible mixture will reduce the ignition delay period and consequently reduce the rate of pressure increase and the maximum cylinder pressure. Experimental studies reported by Abthoff et al [1] and Mayer [2] use a 'split injection device' to control the initial rate of fuel discharge. By reducing the amount of fuel discharged during the ignition delay period (corresponding to a small value of K_p) they obtained a considerably reduced rise in cylinder pressure and a smaller first peak in the heat release diagram. Since combustion noise is mainly influenced by maximum cylinder pressure and the pressure gradient, 'split injection' leads to a marked reduction in noise level. The effect on NO_x emissions was also favourable; under test bed conditions a reduction by 25 % was measured. This is attributed to the improved combustion efficiency as a consequence of a better mixture preparation. Hydrocarbon emissions remained unchanged compared with a conventional injection system.

The discussion of the transient deflected jet is completed by focusing on the development of air - fuel ratio contours and lines of constant streamwise vorticity in four r - z planes downstream of the point of injection (θ = 4.5, 8.5, 15 and 25 degrees). First, reference is made to figures 8.36 to 8.39 depicting air - fuel ratio contours at the same time intervals as illustrated in figure 8.33. In the immediate vicinity of the nozzle exit (θ = 4.5 deg.) the fuel distribution does not change after 80 milliseconds, indicating that there is no transport in vertical direction during most of the injection process. Similar observations apply to the angular locations further downstream of the point of injection; at θ = 8.5 and 15 deg. the steady state is reached after 120 milliseconds when no further vertical transport is predicted. As in the case of the undeflected jet, mixing due to shear induced entrainment and diffusive transport is not seen to affect the spread of constant mixture ratio contours for the rest of the injection period. At θ = 15 and 25 deg. the arrival of the stoichiometric mixture contour can be observed and, together with figure 8.33, the developing contour envelope is readily visualised. At θ = 25 deg. air - fuel ratios at the first time interval are smaller than 300:1, and only after 120 milliseconds appear the first signs of the

stoichiometric contour. The gradual widening of contours with increasing distance from the point of injection reflects a shift from mainly convective transport near the nozzle to stronger diffusive activity as the jet progresses.

While mixture formation in the horizontal plane may be influenced by the swirl and penetration parameters, in vertical direction the angle of injection relative to the horizontal plane is the only control parameter. To enhance air - fuel mixing in the r - z plane vertical air motion would be necessary. In an actual engine this motion is generated by piston movement and the shape of the piston bowl.

The temporal development of the vortex structure at the tip of the jet is illustrated in figures 8.40 to 8.43. A comparison with steady state results discussed earlier (figure 8.11) shows that near the nozzle the steady state is reached after approximately 80 milliseconds while further downstream the contours at 120 milliseconds agree well with the corresponding steady state vortex shapes in figure 8.11. Qualitative similarities between the vortex structure and the air - fuel ratio contours are evident, suggesting that mean velocity gradients play a prominent part in the transport of passive scalar quantities.

8.5 Concluding Remarks

A numerical model for predictions of steady state and impulsive injections into a swirling flow field has been described and results were presented and discussed in two parts.

First, the steady state deflected jet was examined for three different swirl rates and computational results compared with experimental data reported in chapter six. Agreement was generally good and the main features of the flow were well predicted. For example, the location of the jet trajectory, the velocity decay along the trajectory and

the width of the outer jet boundary were in good agreement. Differences were observed with regard to the recirculation zone downstream of the point of injection where the numerical model predicted less hydrodynamic activity than was measured during experiments. This weakness can be attributed equally well to numerical or turbulence model errors and it is not possible to identify the precise source of disagreement between predictions and experimental results. While the Hybrid scheme used to model convective transport is known to cause numerical diffusion in flow regions where the mean velocity is skewed relative to the cell face areas, the k - ε turbulence model is another potential source of error. It is improbable that any turbulent scalar viscosity model can provide accurate calculation of the six components of the turbulent stress tensor, all of which are significant in three - dimensional flows with recirculation. For steady state injections the effect of different swirl rates (30, 40 and 50 rpm) on the jet trajectories and boundaries has been compared. In all three cases the radial momentum was not sufficient for a wall jet to form as a result of impingement on the cylinder wall.

The impulsive jet was modelled for injections into a swirling field of 50 rpm. Using dimensionless parameters for penetration and swirl, the relative effect of these parameters on the temporal development of air - fuel ratio boundaries was examined. It was concluded that for a uniform swirling field a constant injection pressure does not yield a favourable mixture distribution in the combustion chamber model. Mixture formation and hence engine performance in terms of pollutant emissions and noise can be improved by a variable injection pressure starting with a low pressure that is gradually increased during the injection. The optimum injection pressure characteristic can be determined from parametric studies examining the relative effect of swirl to penetration.

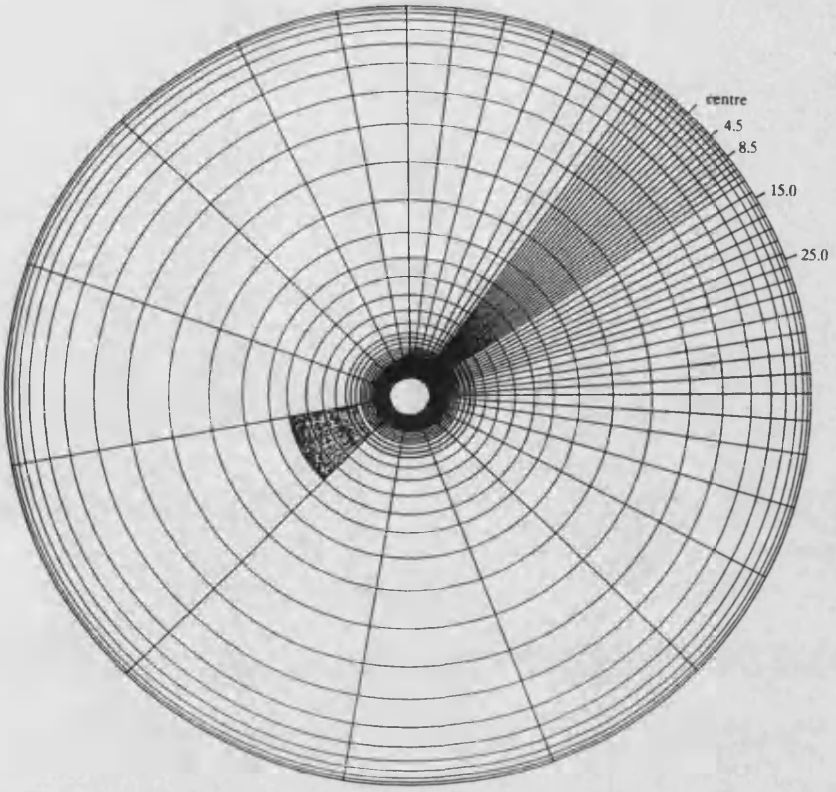

Fig. 8.1: Computational mesh for deflected jet

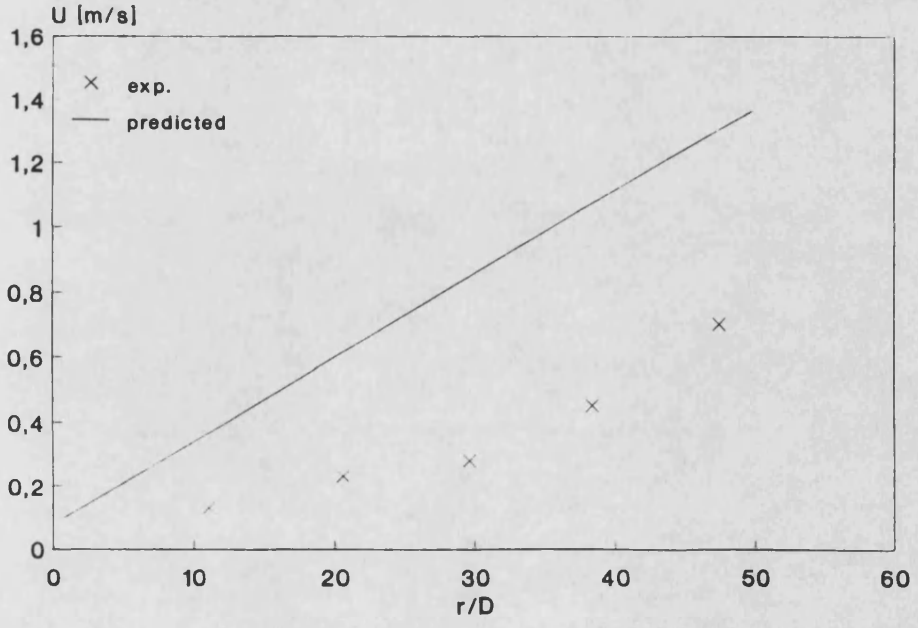

Fig. 8.2: Predicted and measured tangential swirl velocity distribution, 50 rpm

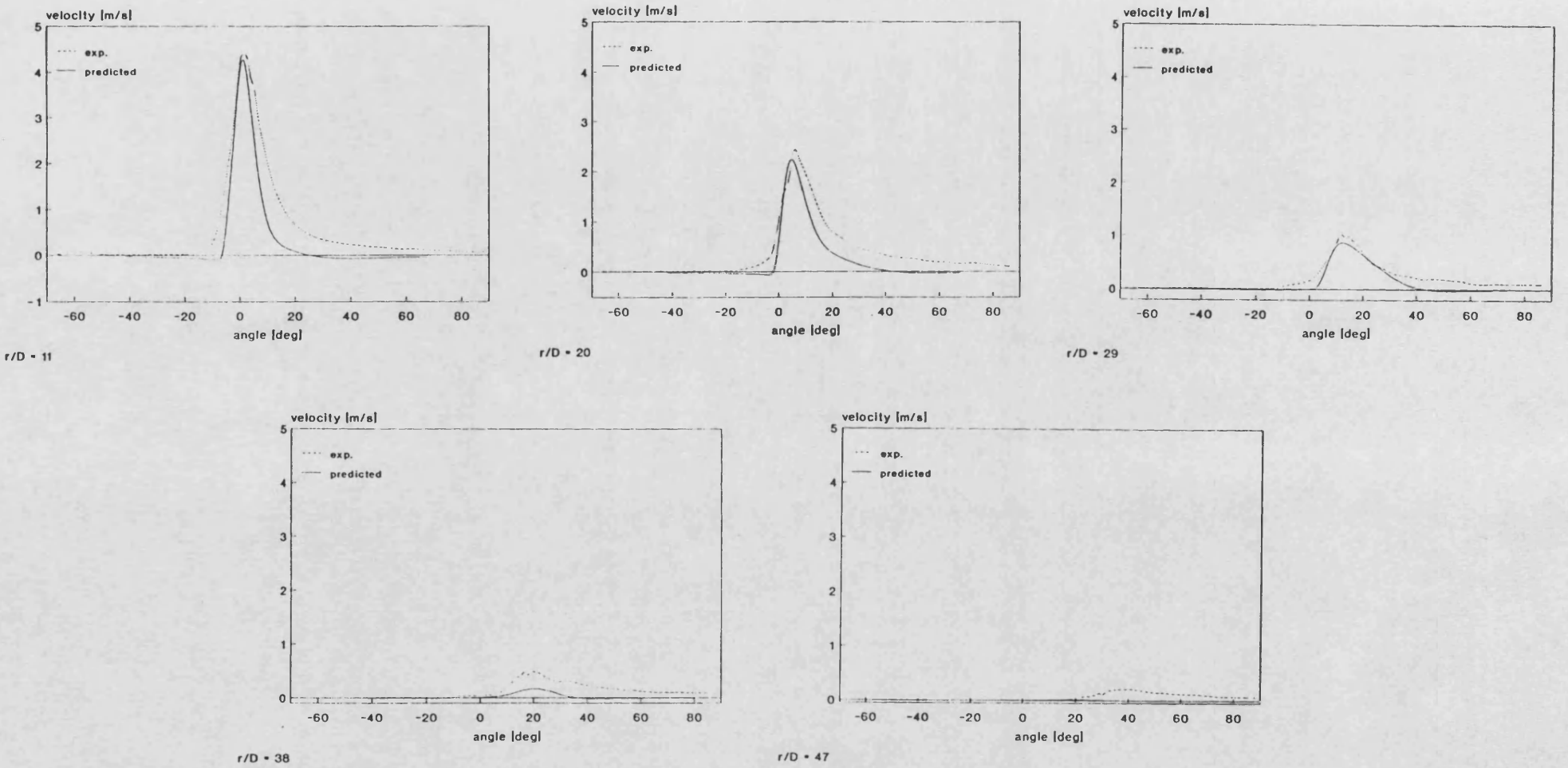

Fig. 8.3: Predicted and measured radial velocity profiles at r/D = 11, 20, 29, 38 and 47, 50 rpm

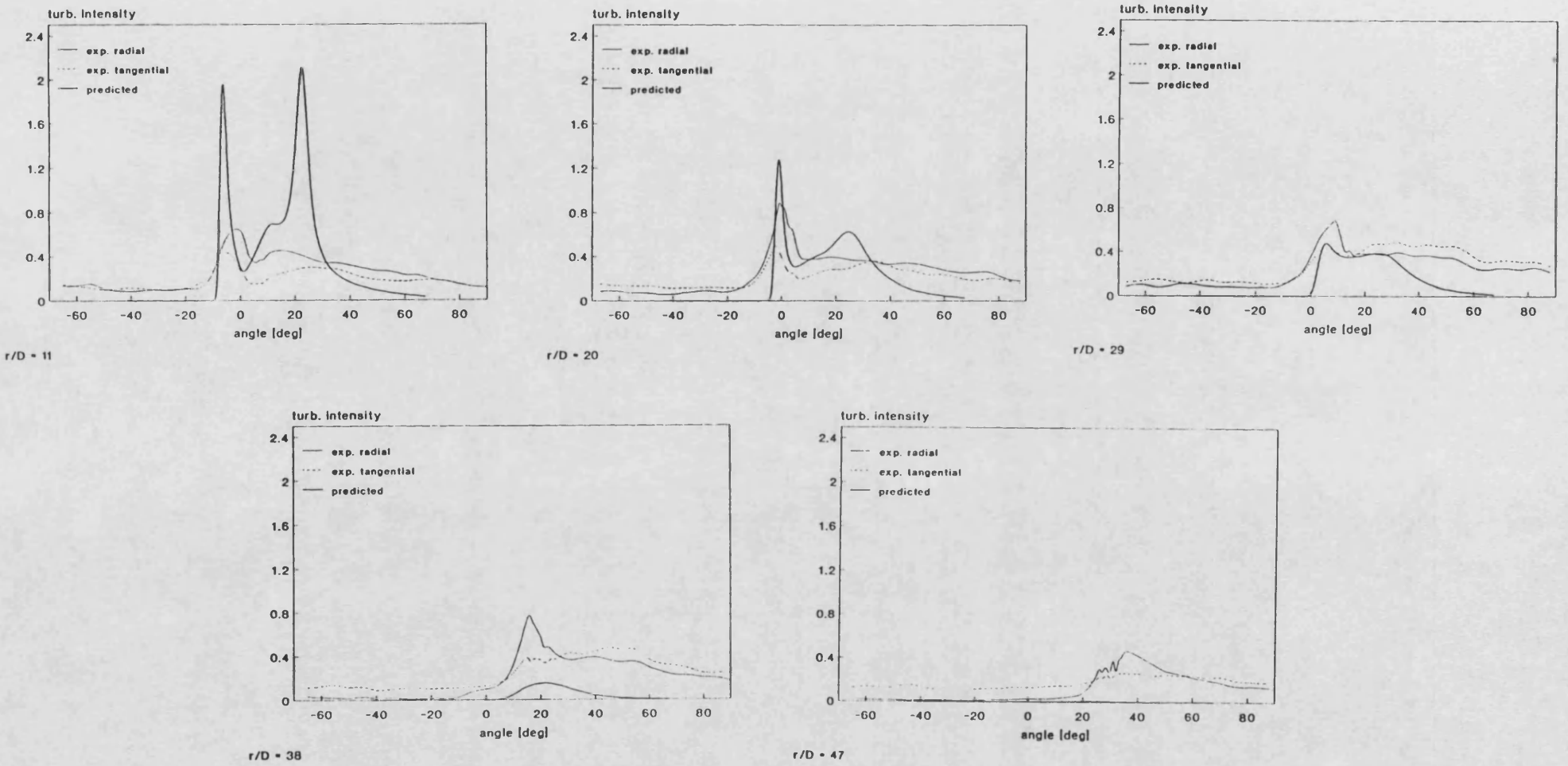

Fig. 8.4: Predicted and measured turbulence intensity profiles at

r/D = 11, 20, 29, 38 and 47, 50 rpm

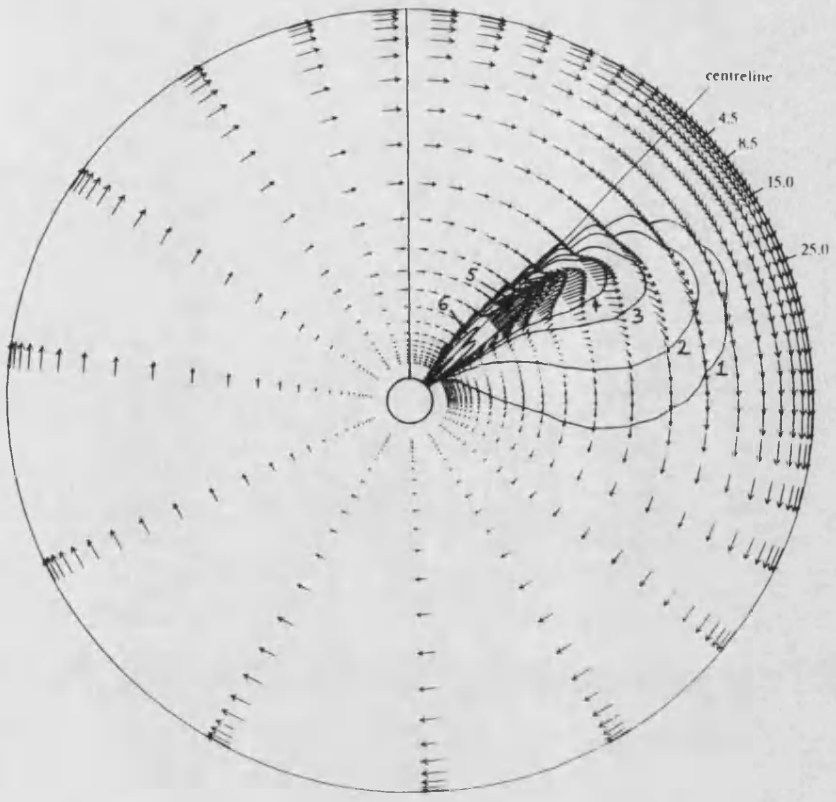

contour	KE [m^2/s^2]
1	0.001
2	0.01
3	0.05
4	0.1
5	0.5
6	1.5

Fig. 8.5: Vector plot with superimposed kinetic energy contours for the r - θ plane bisecting the nozzle, 50 rpm

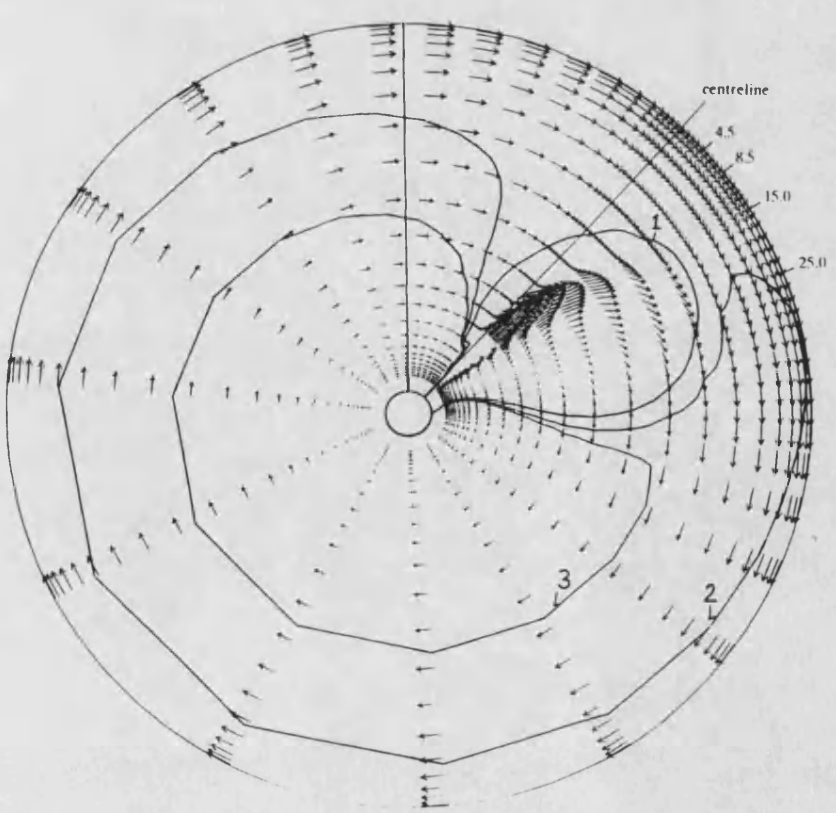

contour	ω [rad/s]
1	5.236
2	5.6
3	5.8

Fig. 8.6: Vector plot with superimposed angular velocity contours for the r - θ plane bisecting the nozzle, 50 rpm

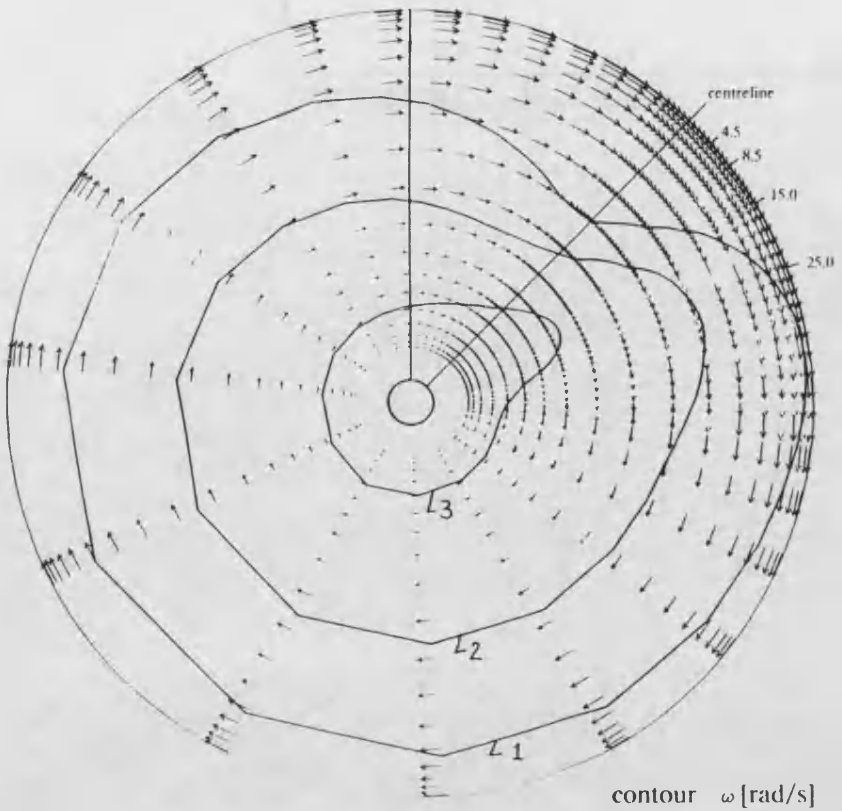

contour	ω [rad/s]
1	5.6
2	5.8
3	7.0

Fig. 8.7: Vector plot with superimposed angular velocity contours for the r - θ plane at z = 30 mm, 50 rpm

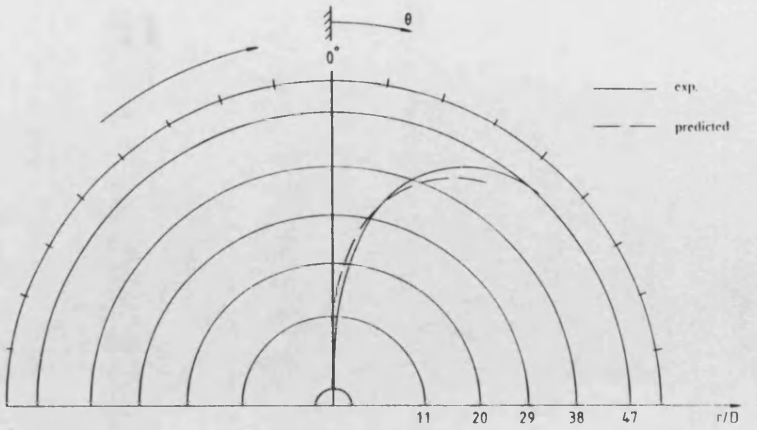

Fig. 8.8: Comparison of jet centrelines inferred from radial velocity profiles (Fig. 8.3), kinetic energy contours (Fig. 8.5) and experimental data (Fig. 6.35), 50 rpm

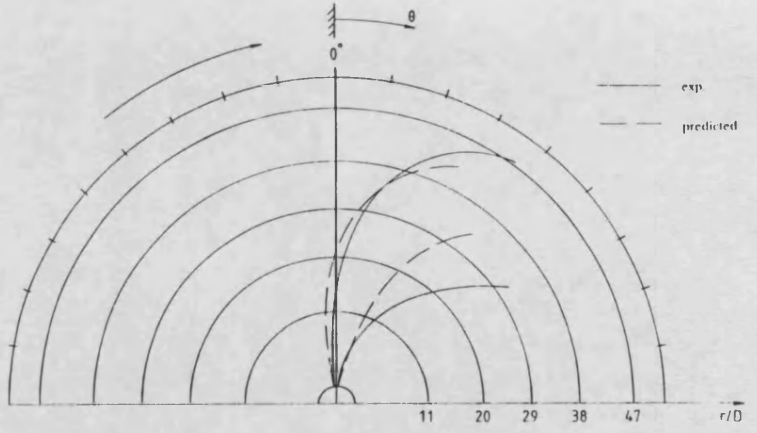

Fig. 8.9: Comparison of predicted and measured jet envelope, 50 rpm

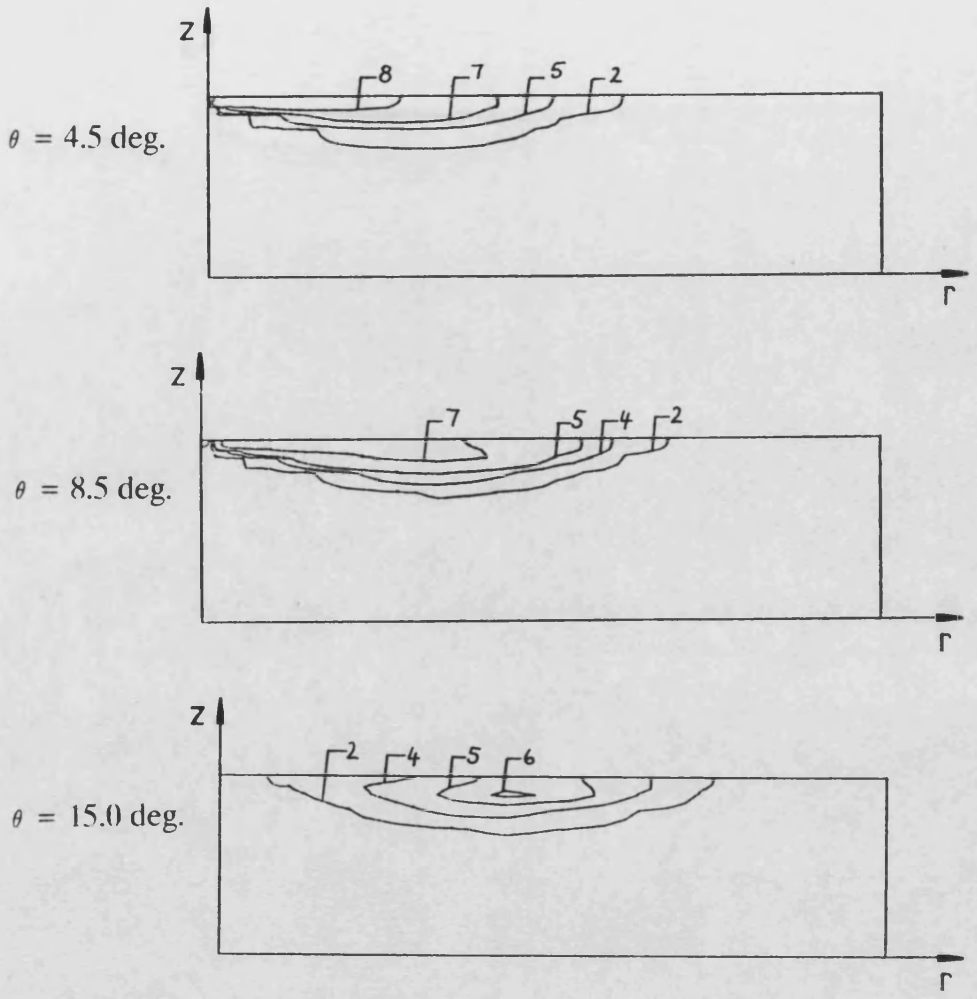

contour	KE [m²/s²]
1	0.001
2	0.01
3	0.03
4	0.05
5	0.1
6	0.14
7	0.3
8	0.7

Fig. 8.10: Kinetic energy contours in the r - z plane at θ = 4.5, 8.5, 15.0 and 25.0 deg., 50 rpm

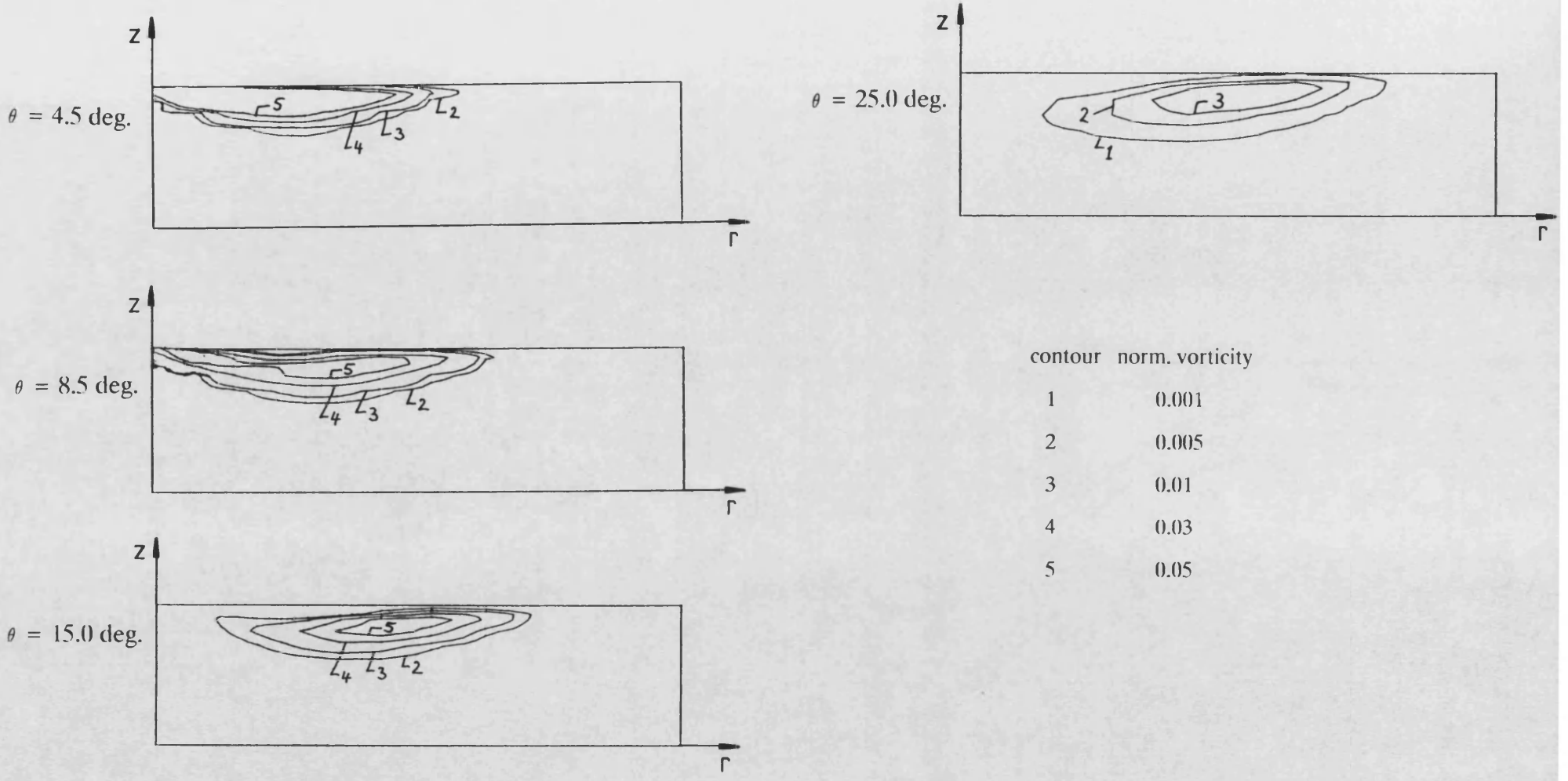

contour	norm. vorticity
1	0.001
2	0.005
3	0.01
4	0.03
5	0.05

Fig. 8.11: Mean streamwise vorticity contours in the r - z plane at θ = 4.5, 8.5, 15.0 and 25.0 deg., 50 rpm

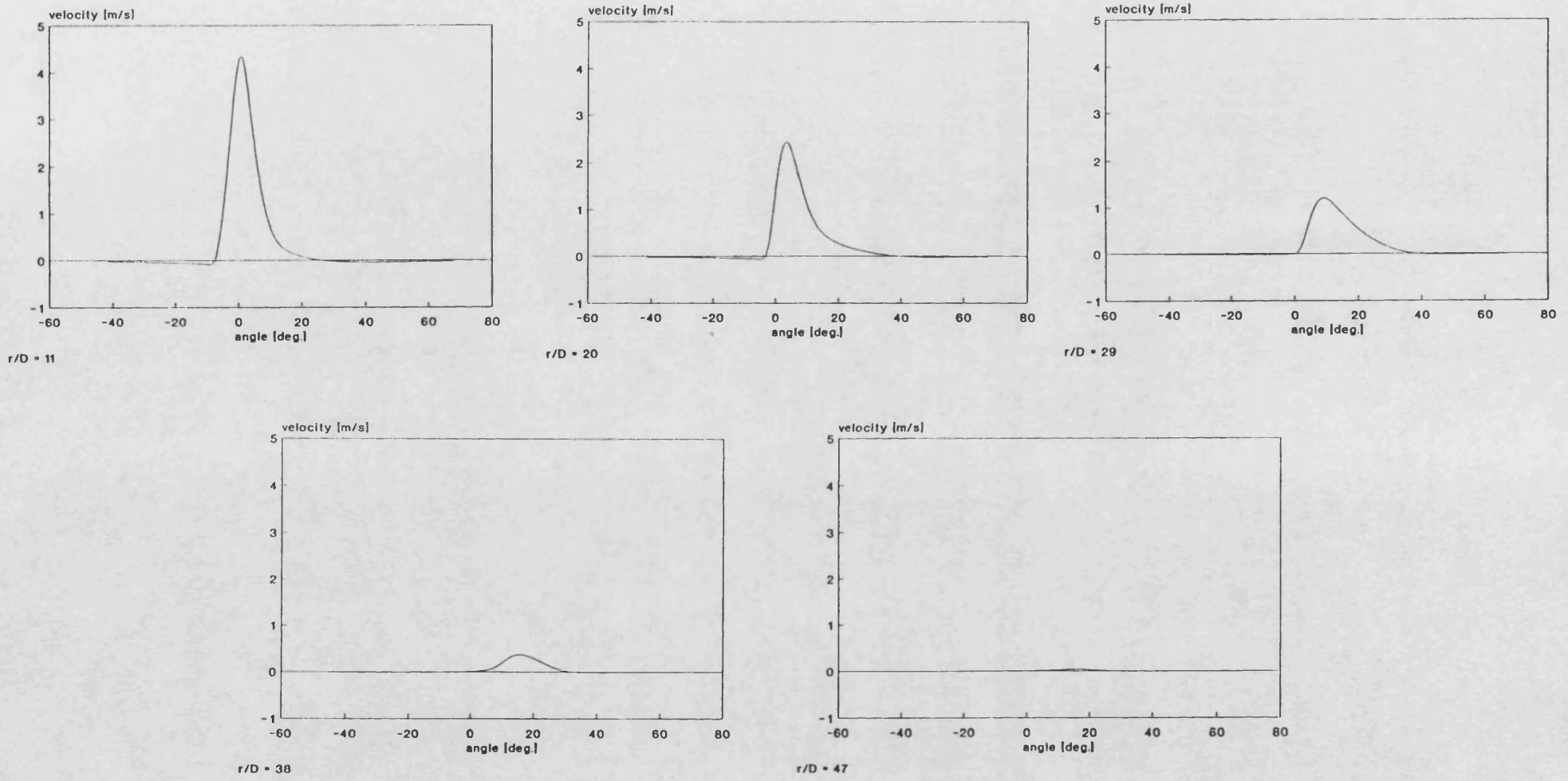

Fig. 8.12: Predicted radial velocity profiles at r/D = 11, 20, 29, 38 and 47, 40 rpm

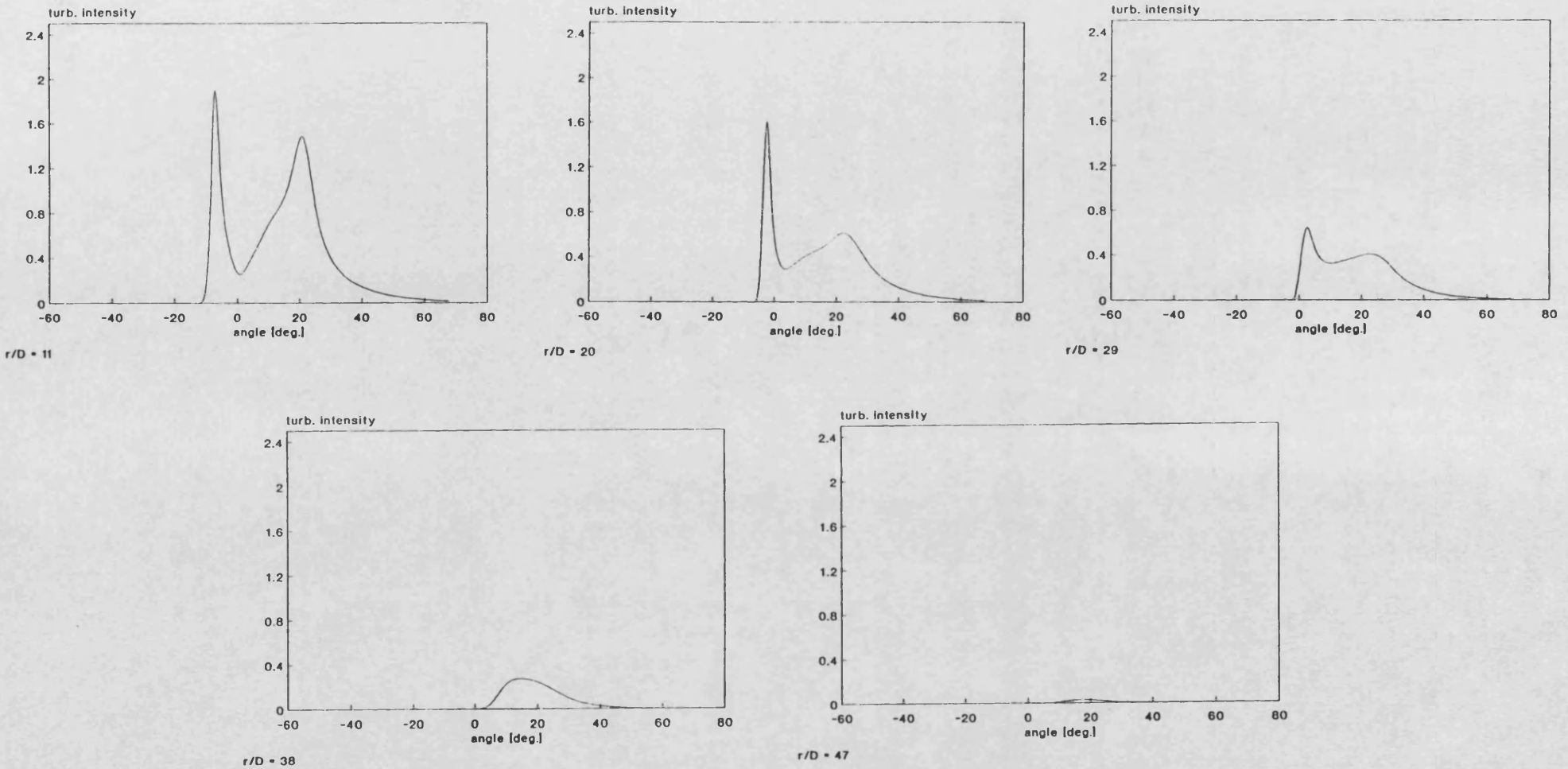

Fig. 8.13: Predicted turbulence intensity profiles at r/D = 11, 20, 29, 38 and 47, 40 rpm

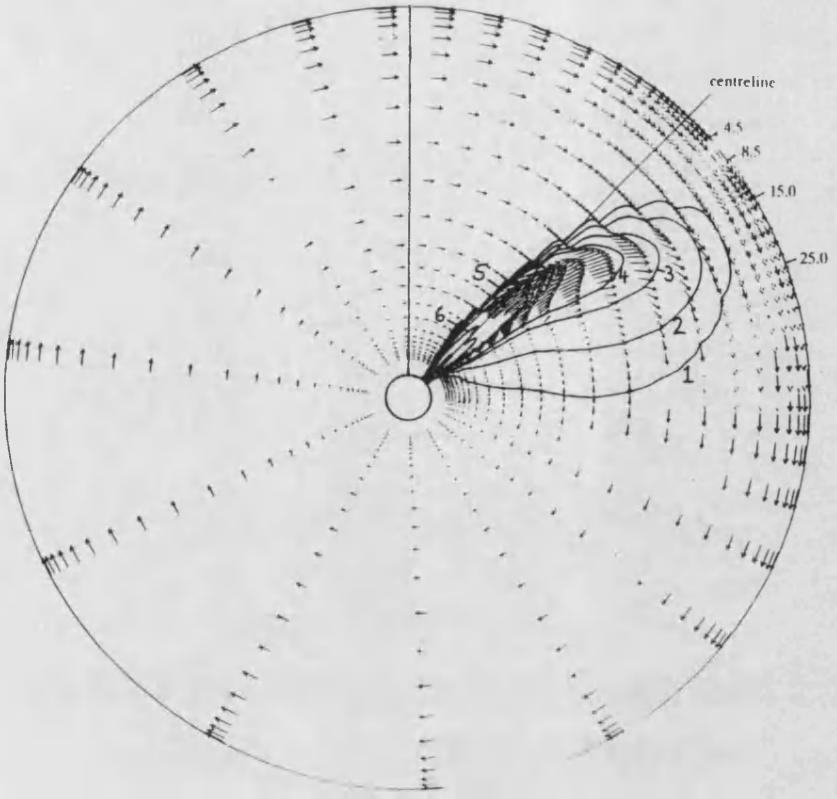

contour	KE [m^2/s^2]
1	0.001
2	0.01
3	0.05
4	0.1
5	0.5
6	1.5

Fig. 8.14: Vector plot with superimposed kinetic energy contours for the r - θ plane bisecting the nozzle, 40 rpm

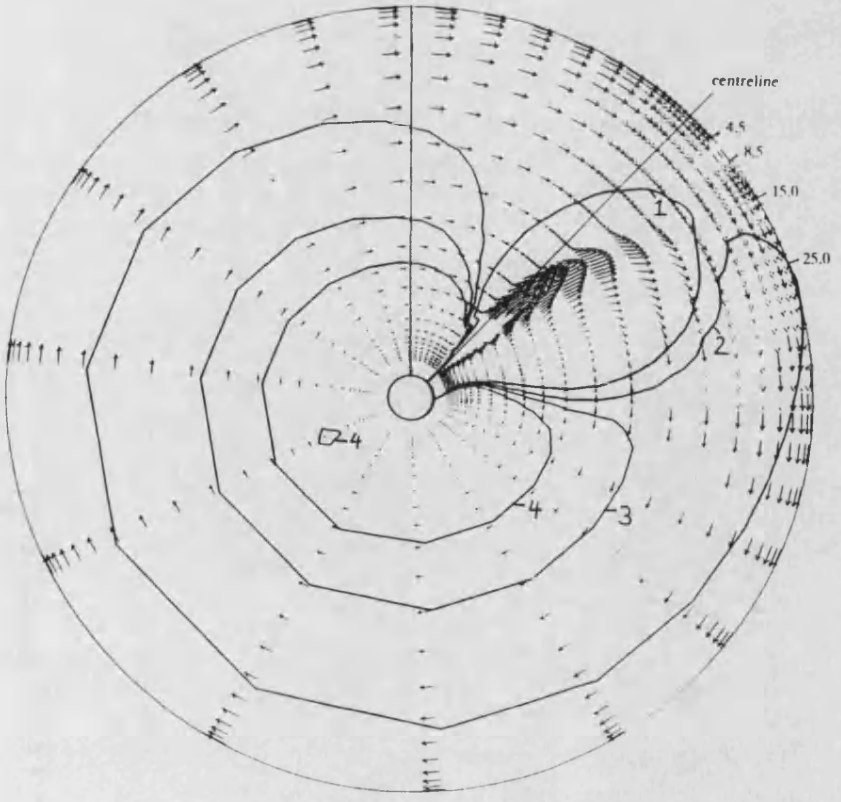

contour	ω [rad/s]
1	4.189
2	4.5
3	4.7
4	5.0

Fig. 8.15: Vector plot with superimposed angular velocity contours for the r - θ plane bisecting the nozzle, 40 rpm

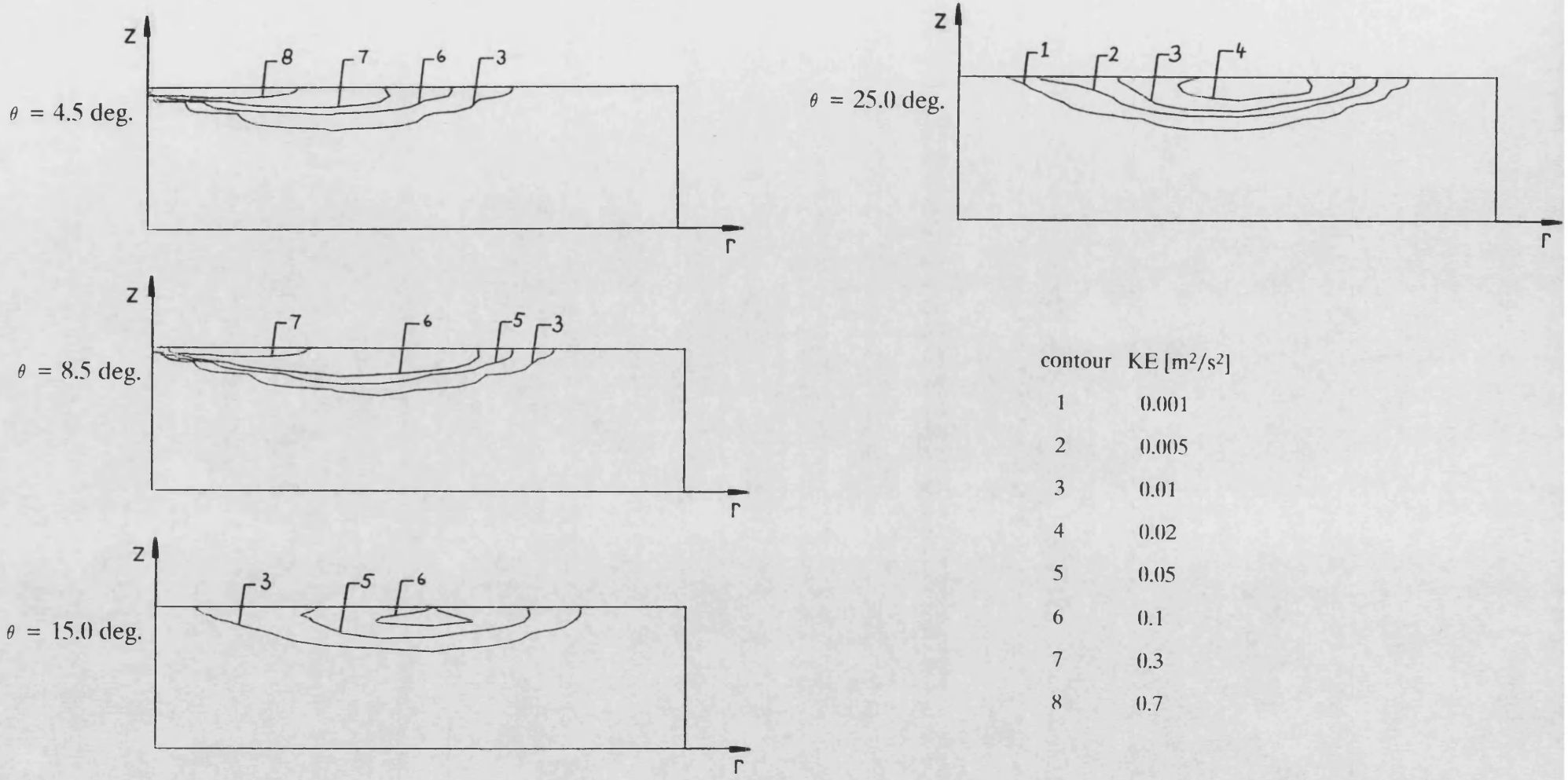

contour	KE [m^2/s^2]
1	0.001
2	0.005
3	0.01
4	0.02
5	0.05
6	0.1
7	0.3
8	0.7

Fig. 8.16: Kinetic energy contours in the r - z plane at θ = 4.5, 8.5, 15.0 and 25.0 deg., 40 rpm

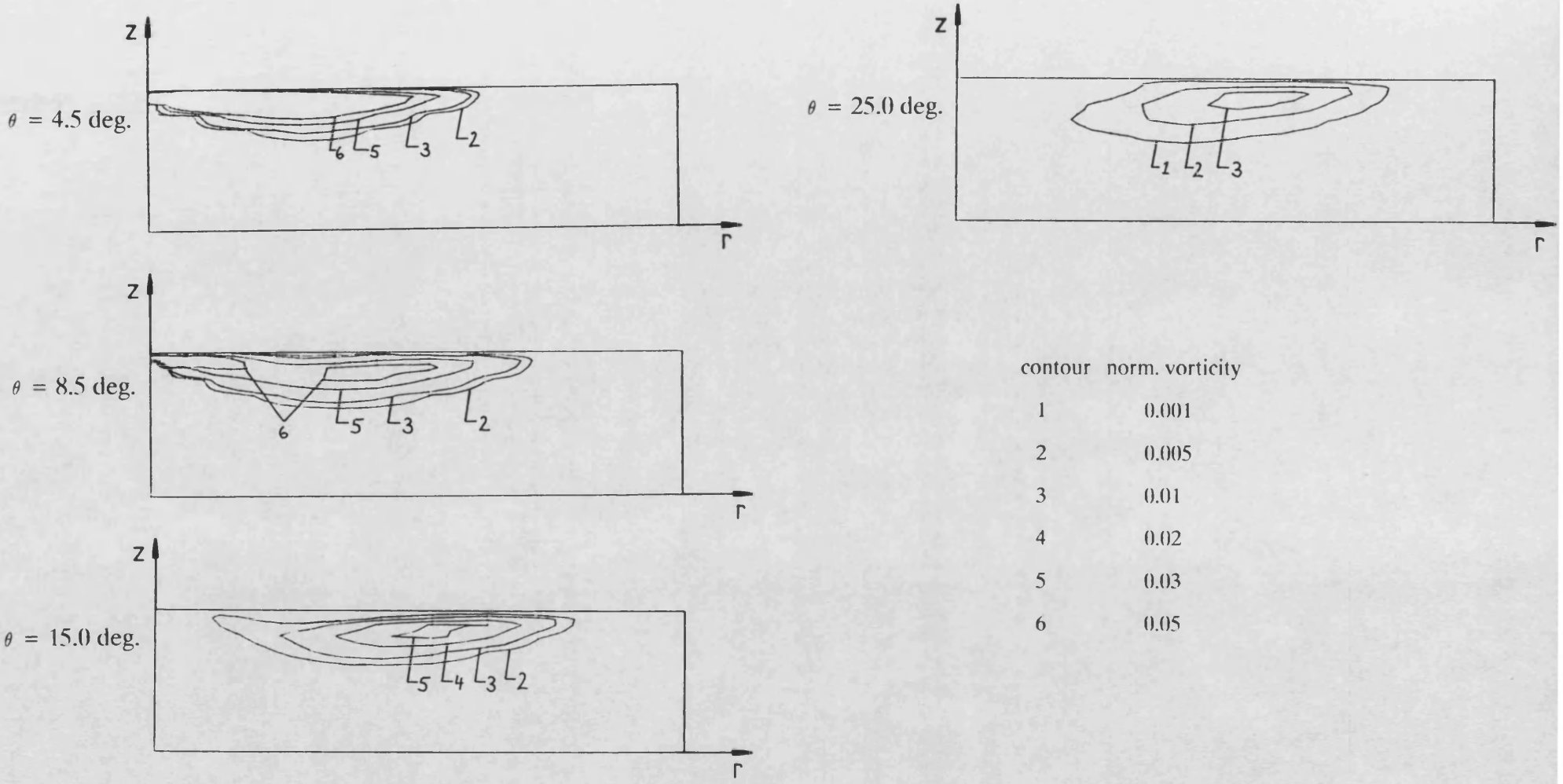

contour	norm. vorticity
1	0.001
2	0.005
3	0.01
4	0.02
5	0.03
6	0.05

Fig. 8.17: Mean streamwise vorticity contours in the r - z plane at θ = 4.5, 8.5, 15.0 and 25.0 deg., 40 rpm

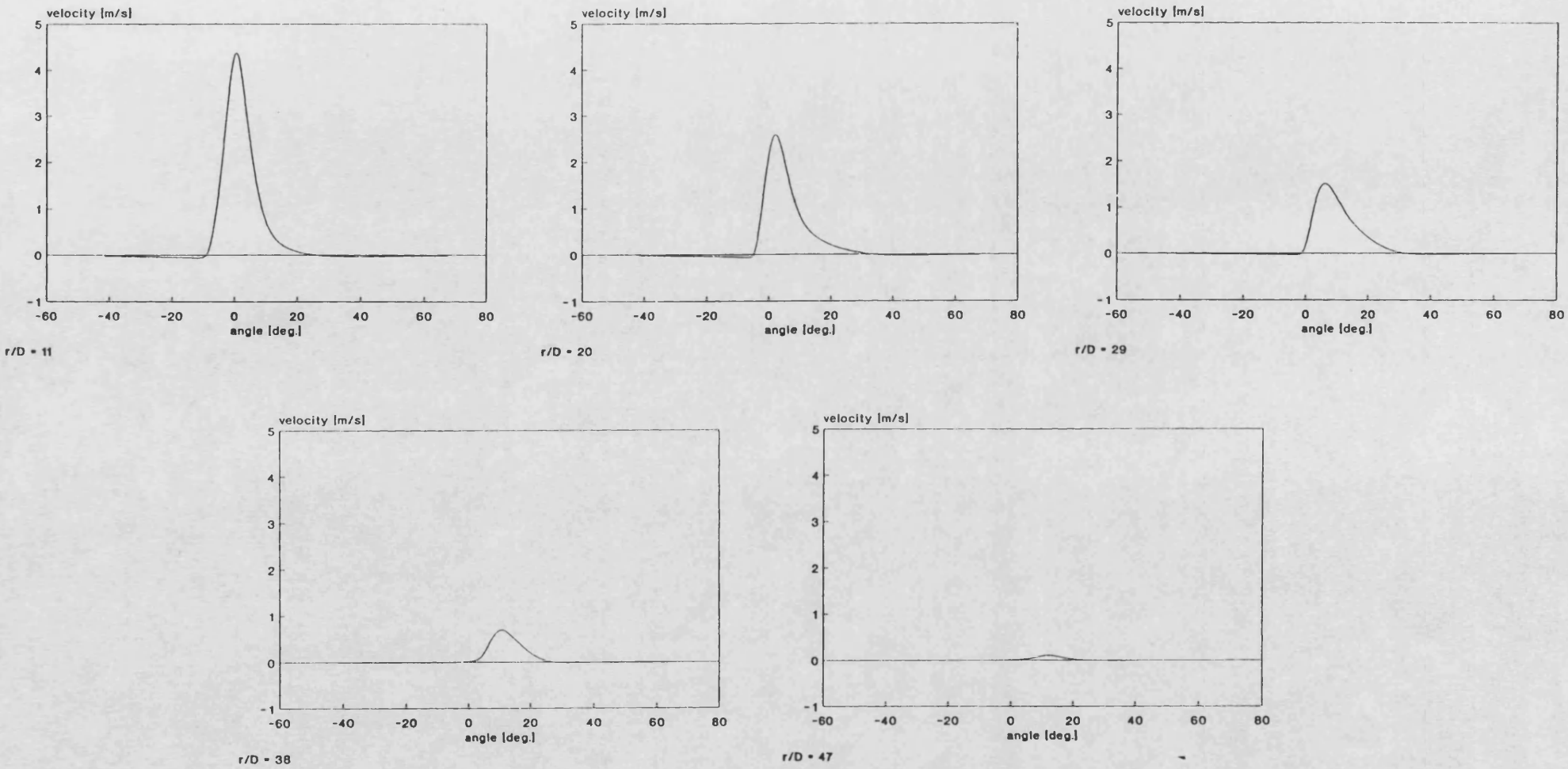

Fig. 8.18: Predicted radial velocity profiles at r/D = 11, 20, 29, 38 and 47, 30 rpm

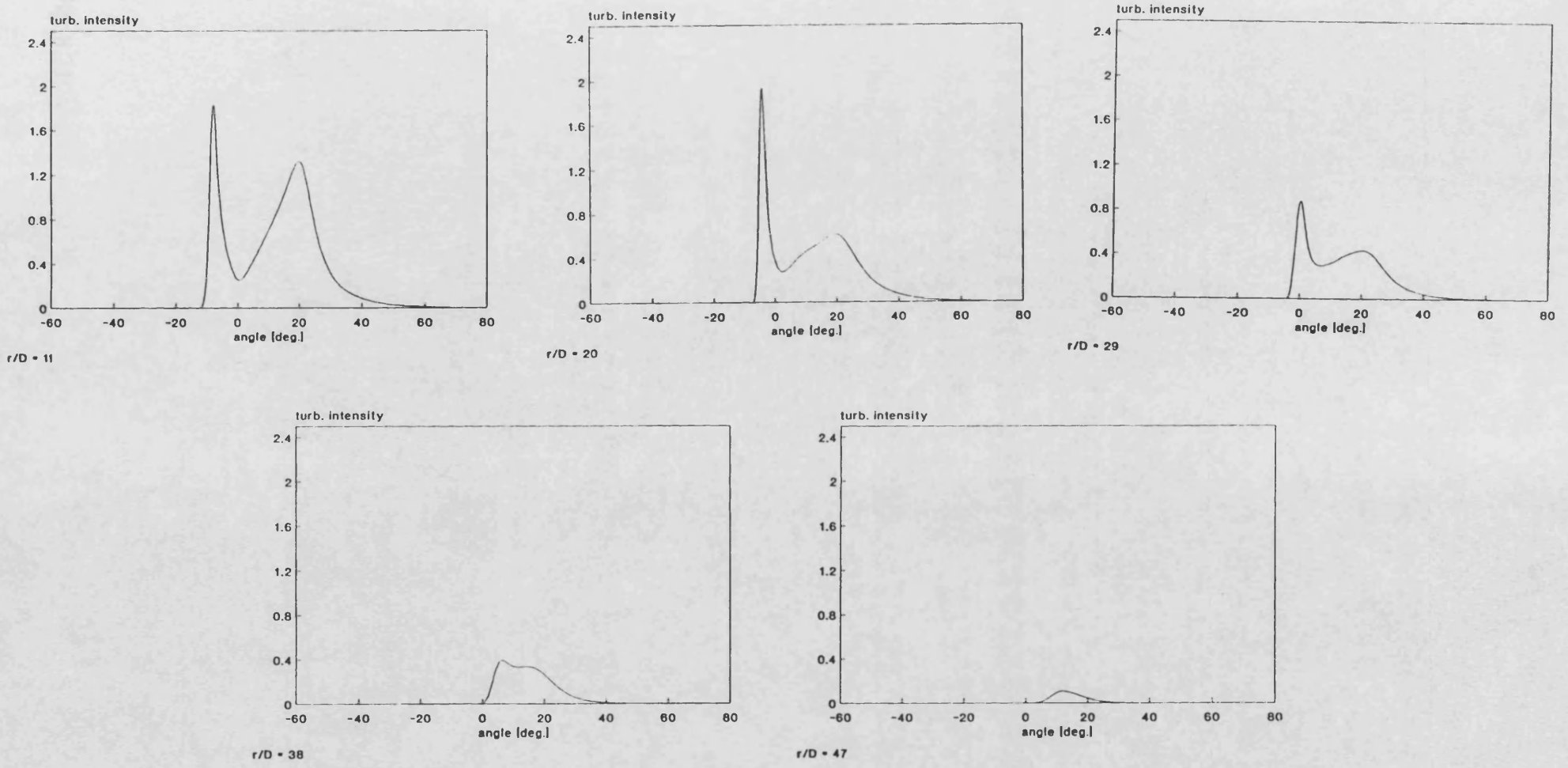

Fig. 8.19: Predicted turbulence intensity profiles at r/D = 11, 20, 29, 38 and 47, 30 rpm

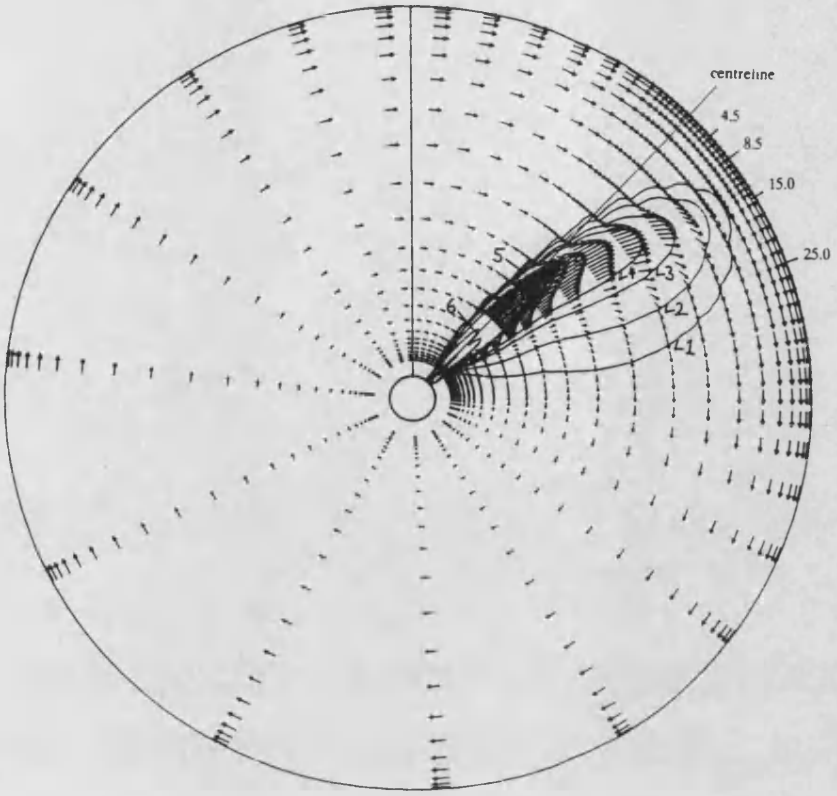

contour	KE [m^2/s^2]
1	0.001
2	0.01
3	0.05
4	0.1
5	0.5
6	1.5

Fig. 8.20: Vector plot with superimposed kinetic energy contours for the r - θ plane bisecting the nozzle, 30 rpm

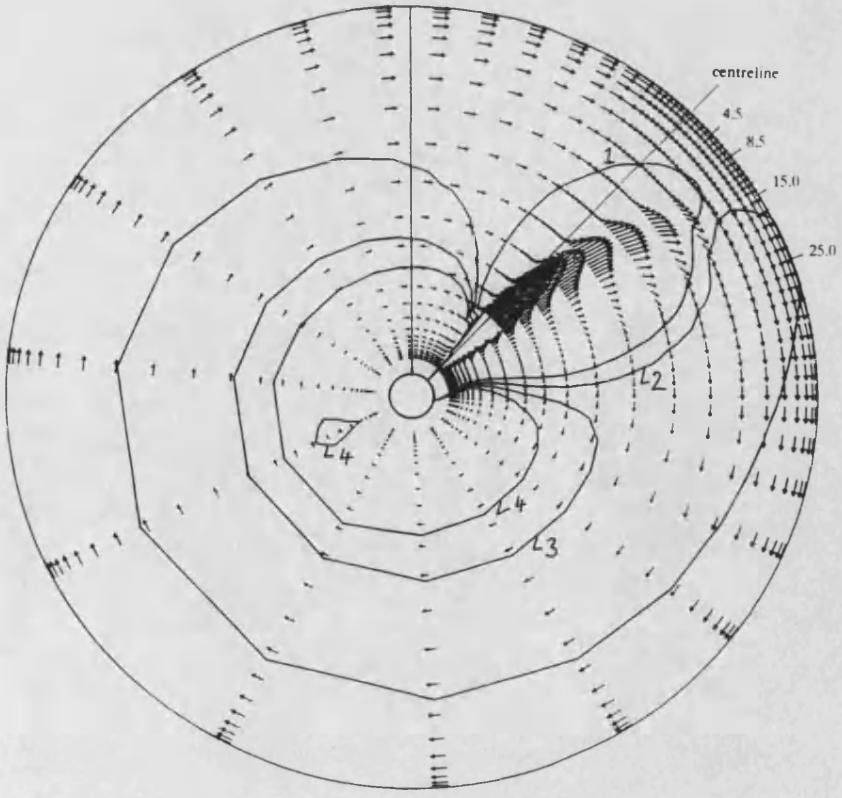

contour	ω [rad/s]
1	3.1416
2	3.4
3	3.6
4	3.8

Fig. 8.21: Vector plot with superimposed angular velocity contours for the r - θ plane bisecting the nozzle, 30 rpm

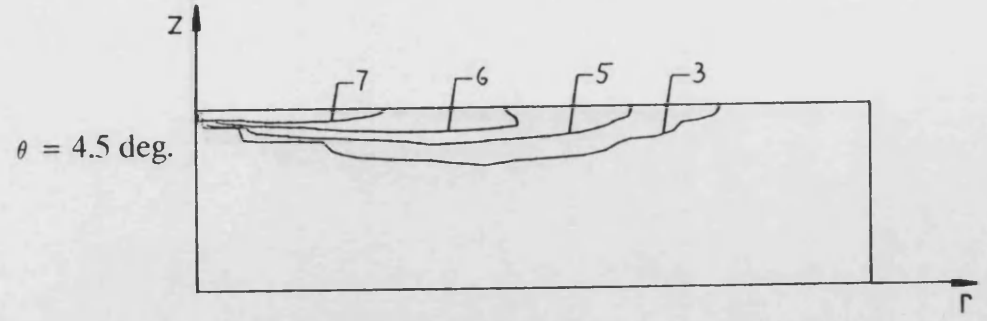

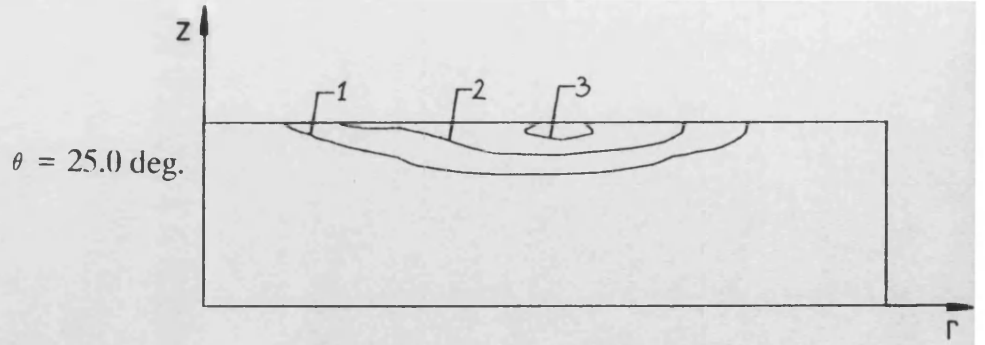

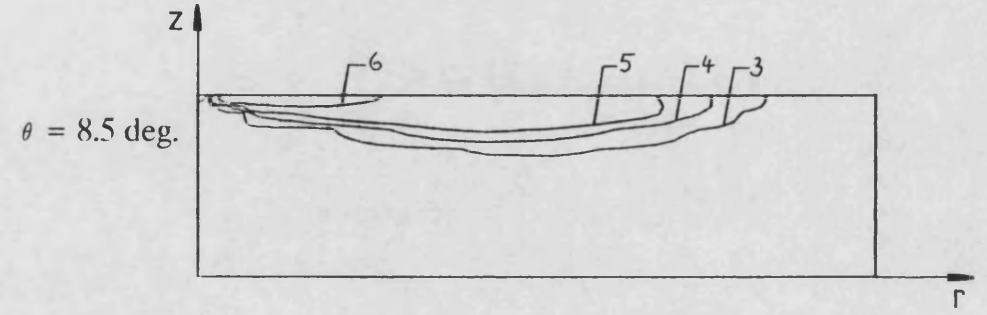

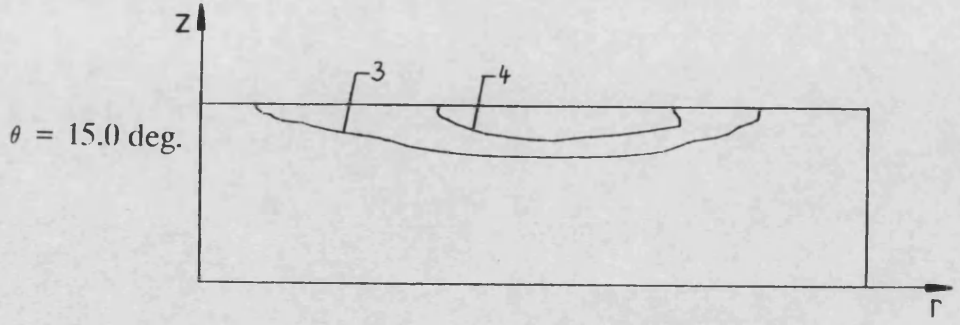

contour	KE [m^2/s^2]
1	0.001
2	0.005
3	0.01
4	0.05
5	0.1
6	0.3
7	0.7

Fig. 8.22: Kinetic energy contours in the r - z plane at θ = 4.5, 8.5, 15.0 and 25.0 deg., 30 rpm

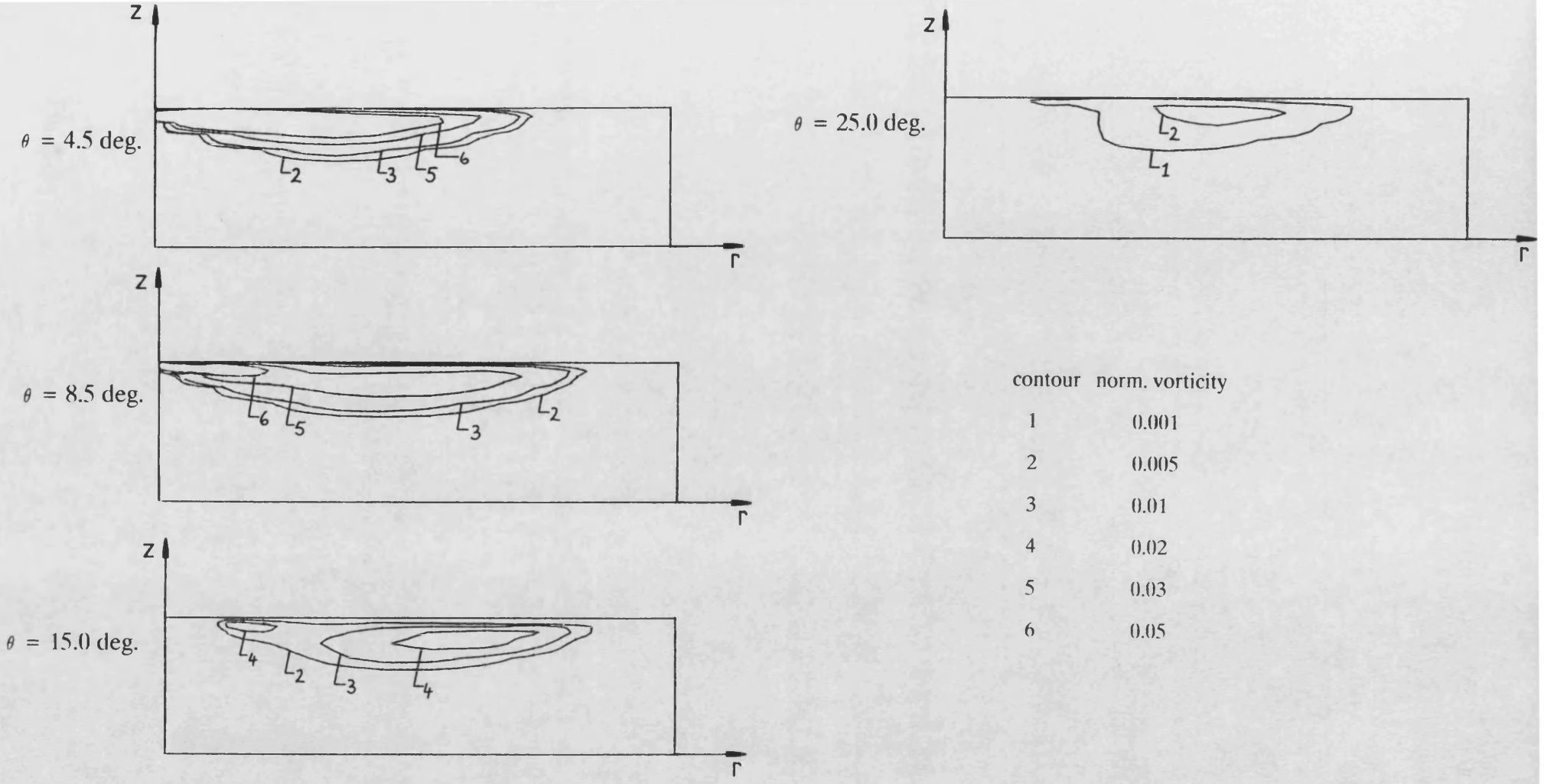

contour	norm. vorticity
1	0.001
2	0.005
3	0.01
4	0.02
5	0.03
6	0.05

Fig. 8.23: Mean streamwise vorticity contours in the r - z plane at θ = 4.5, 8.5, 15.0 and 25.0 deg., 30 rpm

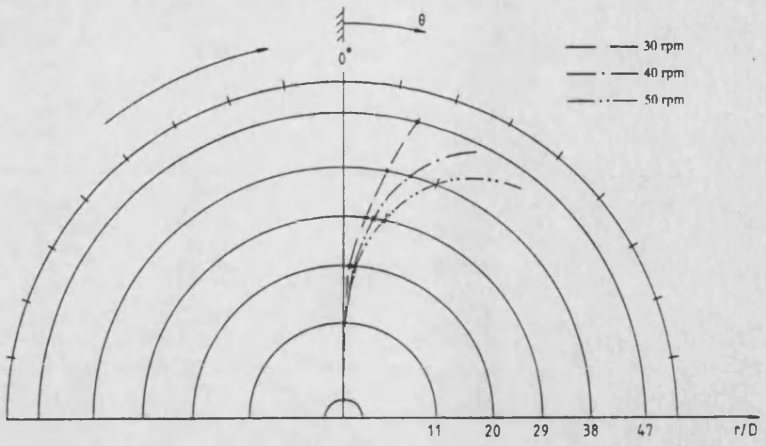

Fig. 8.24: Predicted jet trajectories for 30, 40 and 50 rpm

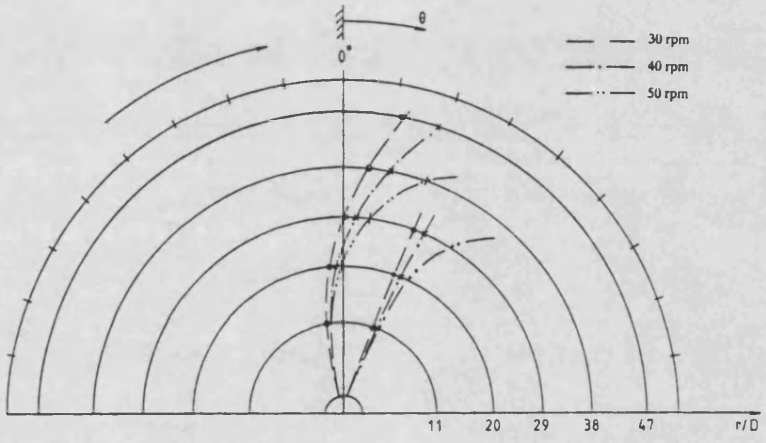

Fig. 8.25: Predicted jet envelopes for 30, 40 and 50 rpm

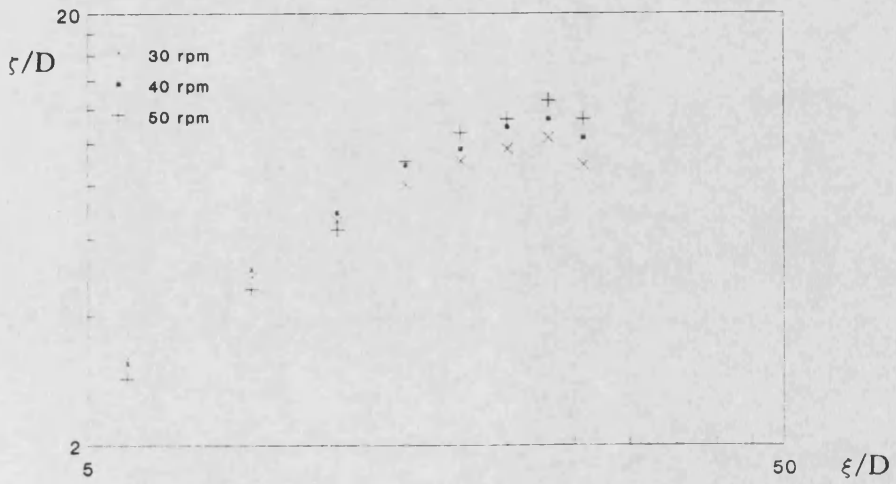

Fig. 8.26: Jet widening along the jet trajectory based on 1 % jet exit velocity

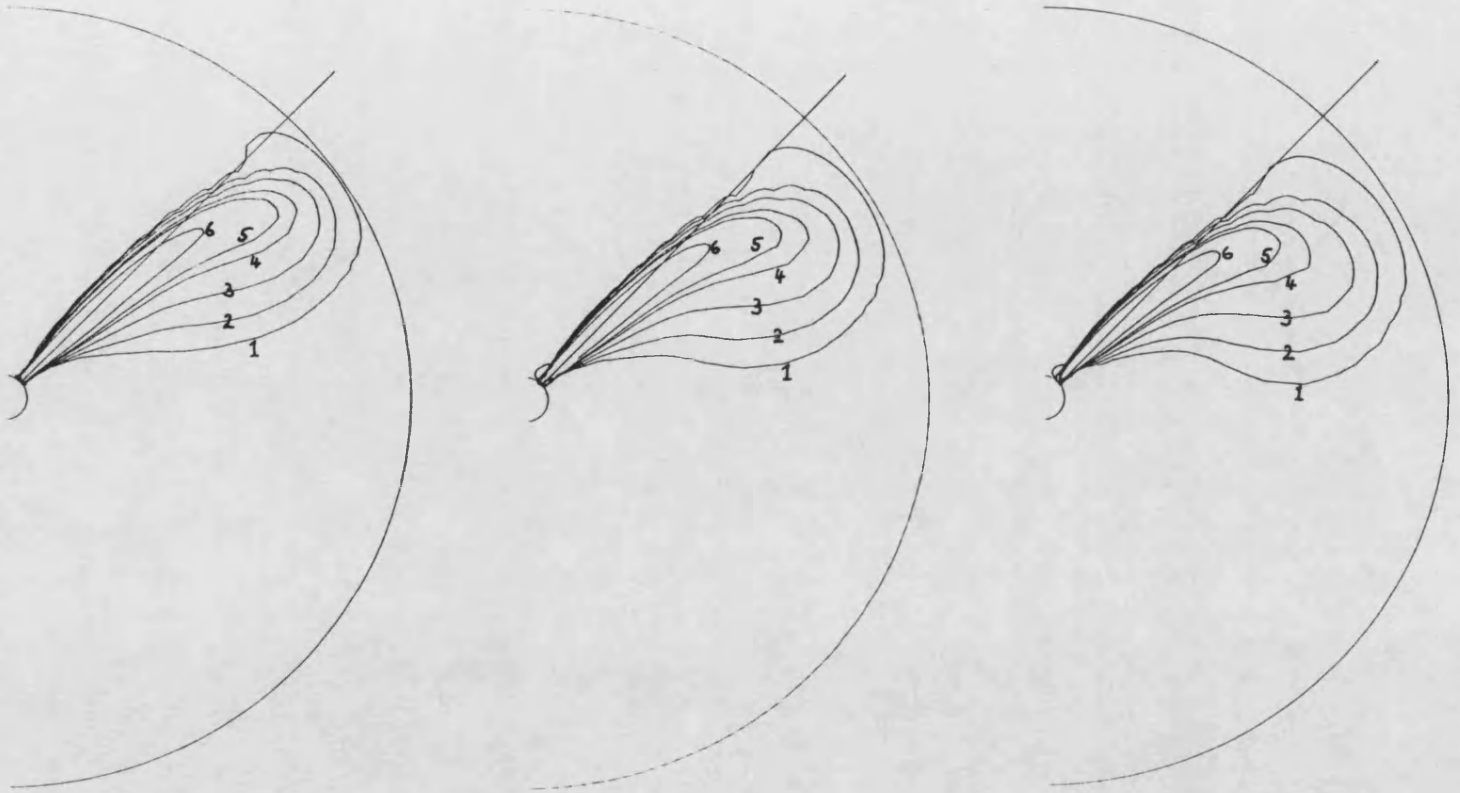

contour	velocity [m/s]
1	0.01
2	0.1
3	0.3
4	0.7
5	1.0
6	2.0

Fig. 8.27: Predicted velocity vector contours for a) 30, b) 40 and c) 50 rpm

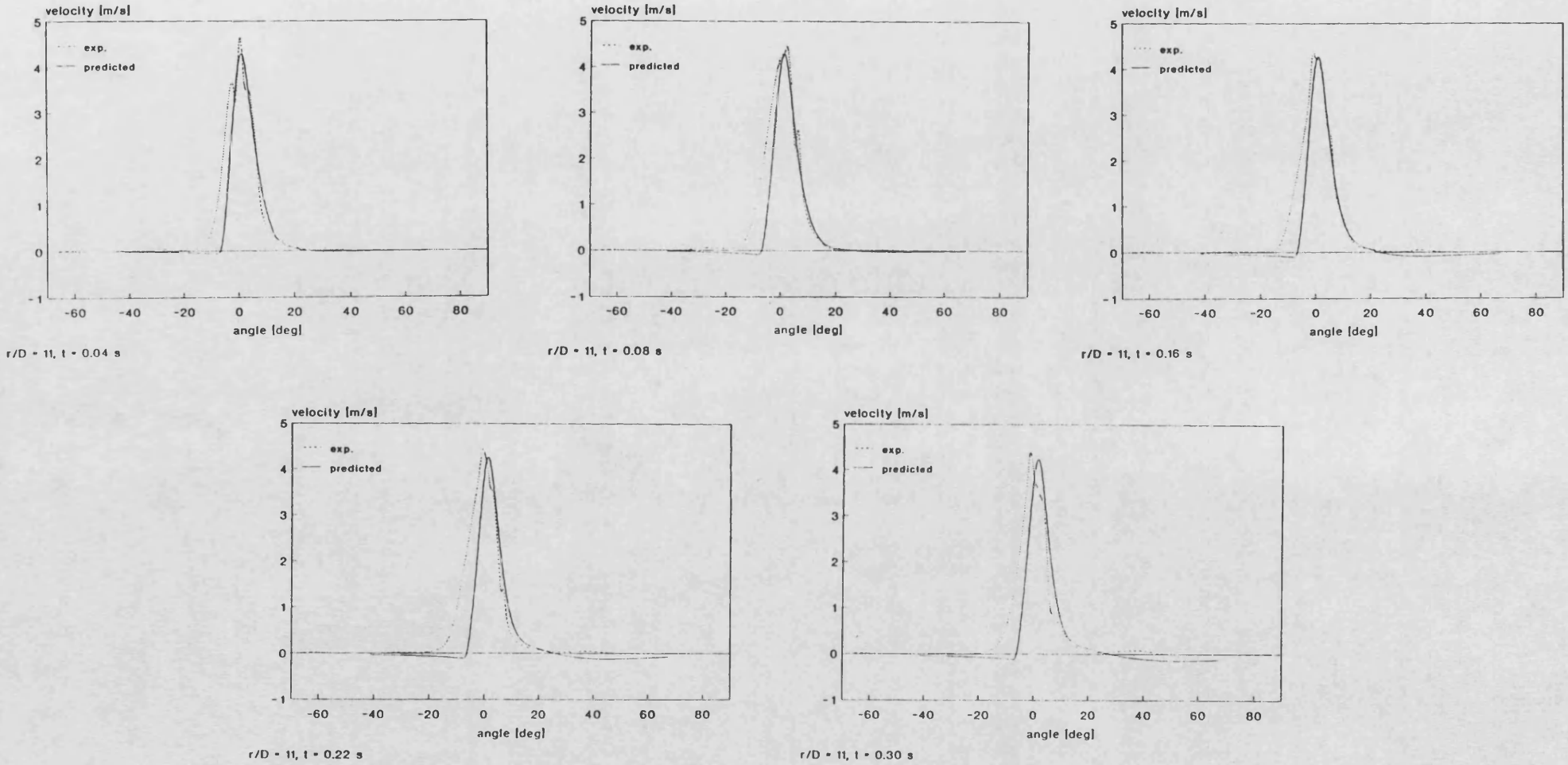

Fig. 8.28: Comparison of predicted and measured temporal development of radial velocities under swirling conditions, r/D = 11

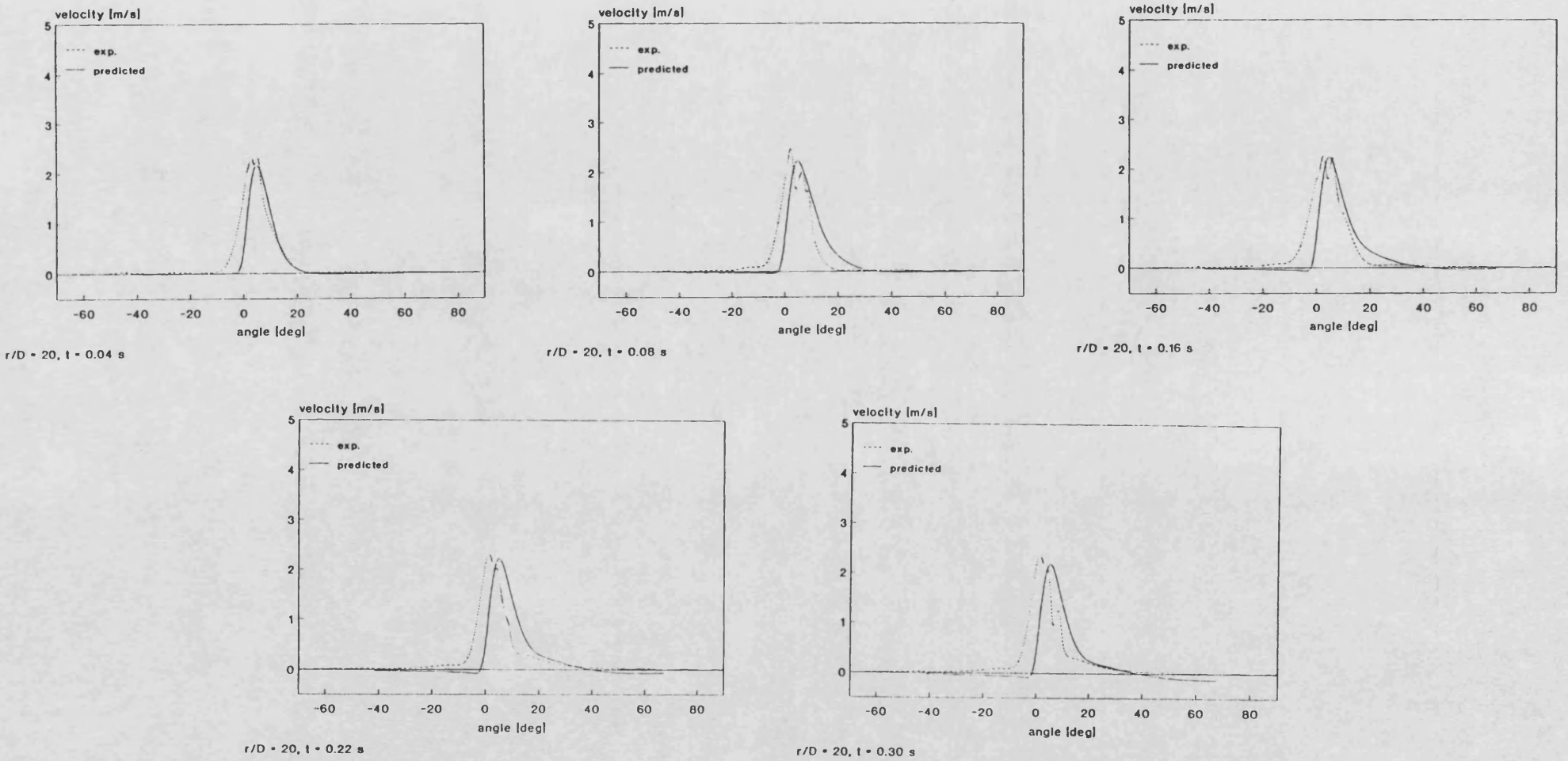

Fig. 8.29: Comparison of predicted and measured temporal development of radial velocities under swirling conditions, r/D = 20

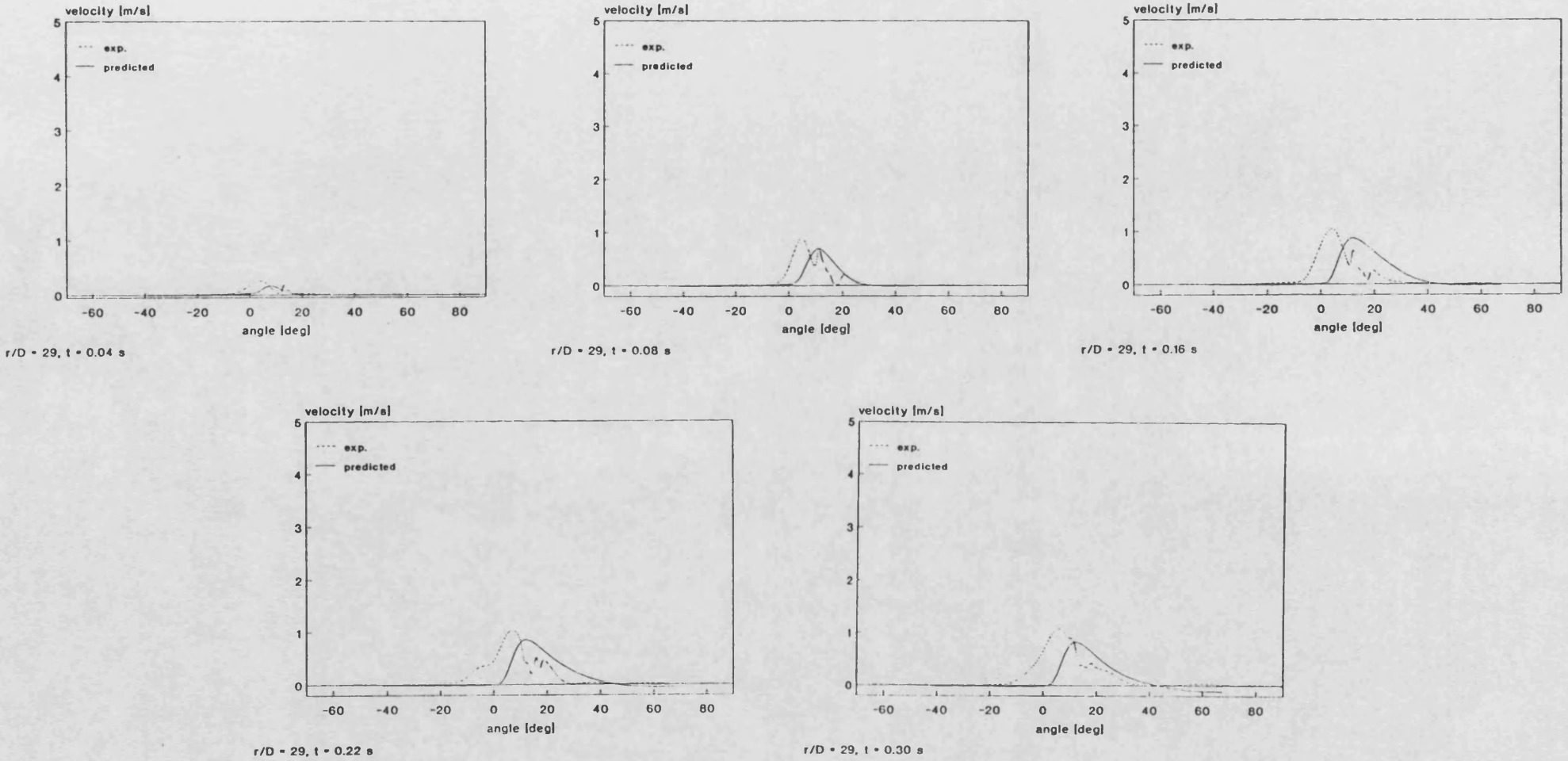

Fig. 8.30: Comparison of predicted and measured temporal development of radial velocities under swirling conditions, r/D = 29

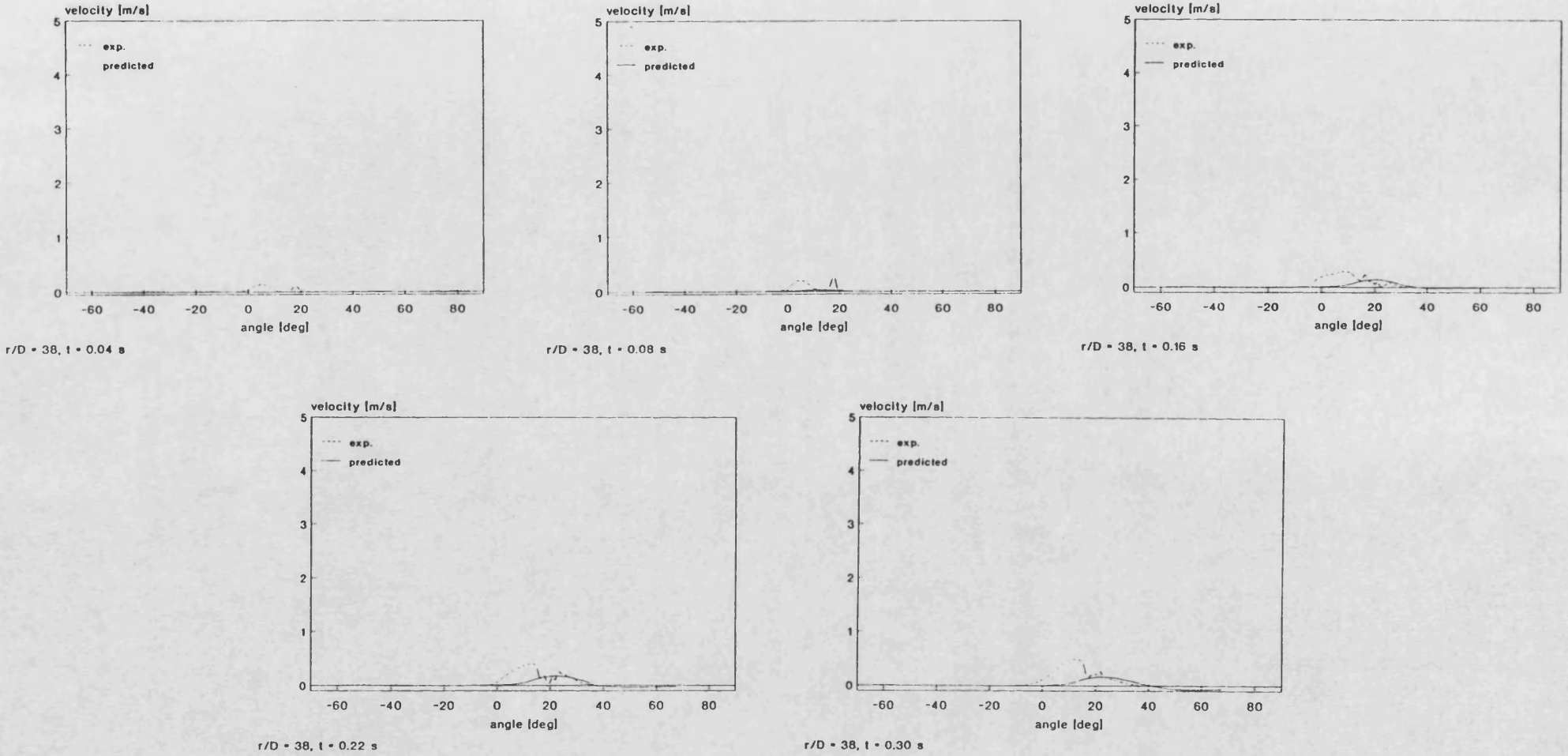

Fig. 8.31: Comparison of predicted and measured temporal development of radial velocities under swirling conditions, r/D = 38

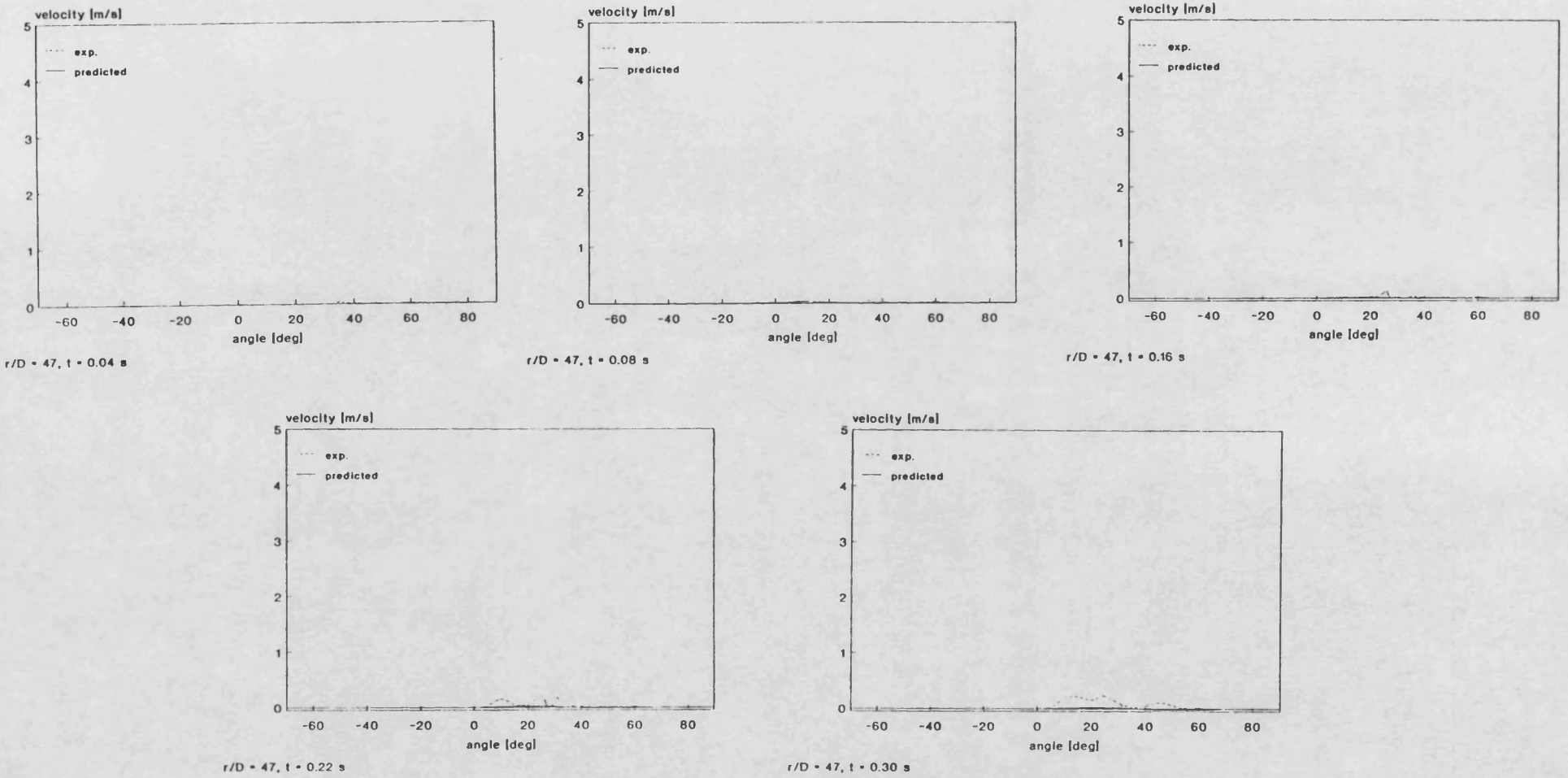

Fig. 8.32: Comparison of predicted and measured temporal development of radial velocities under swirling conditions, r/D = 47

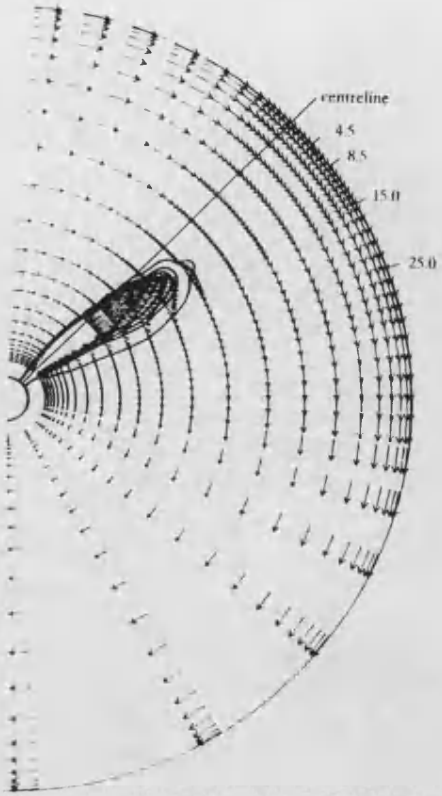

t_i = 40 ms
K_R = 152

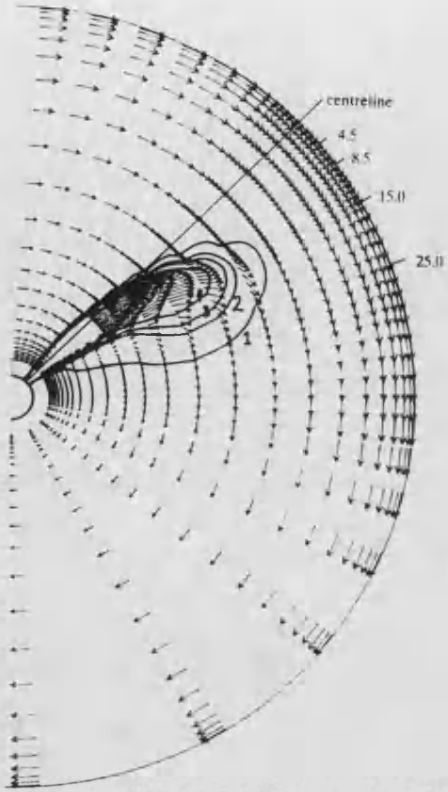

t_i = 80 ms
K_R = 214

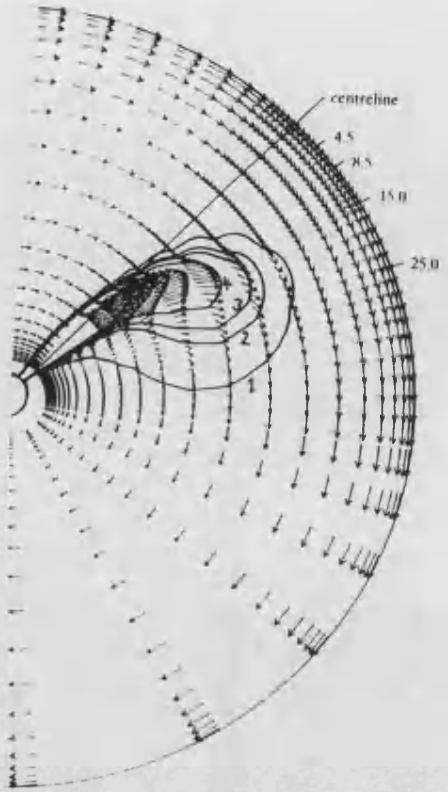

t_i = 120 ms
K_R = 263

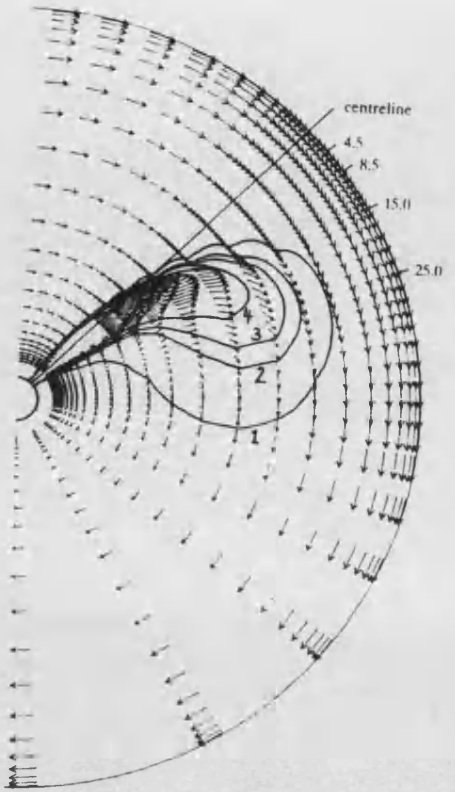

t_i = 160 ms
K_R = 303

contour	A/F ratio
1	100:1
2	25:1
3	17:1
4	10:1

cont.

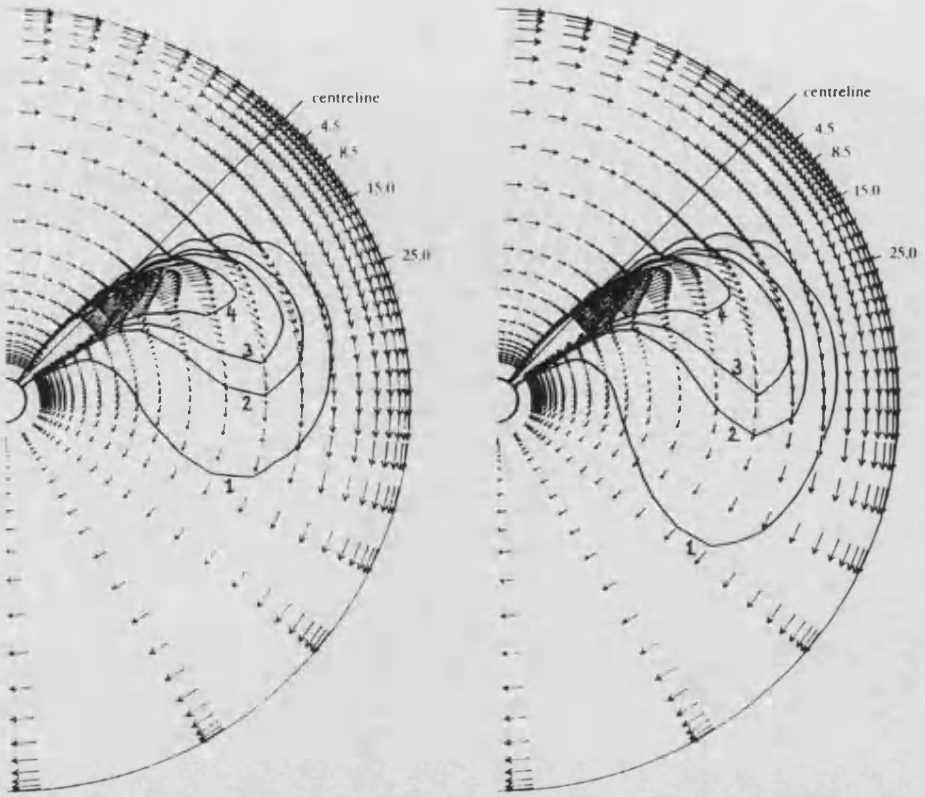

t_i = 220 ms
K_R = 355

t_i = 300 ms
K_R = 415

Fig. 8.33: Temporal development of mean velocity vector field with superimposed air/fuel ratio contours

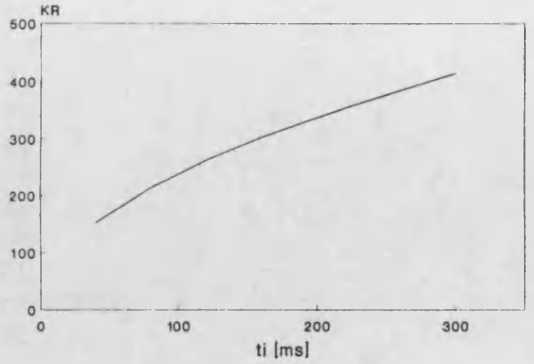

Fig. 8.34: Variation of the relative effect of swirl to penetration with time

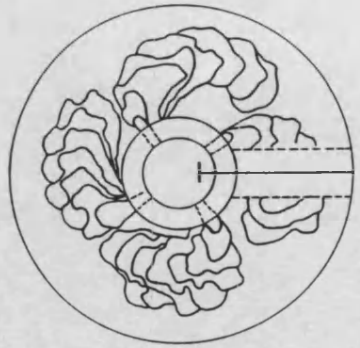

Fig. 8.35: Air/fuel ratio contours from photographic records for 50 rpm, Way

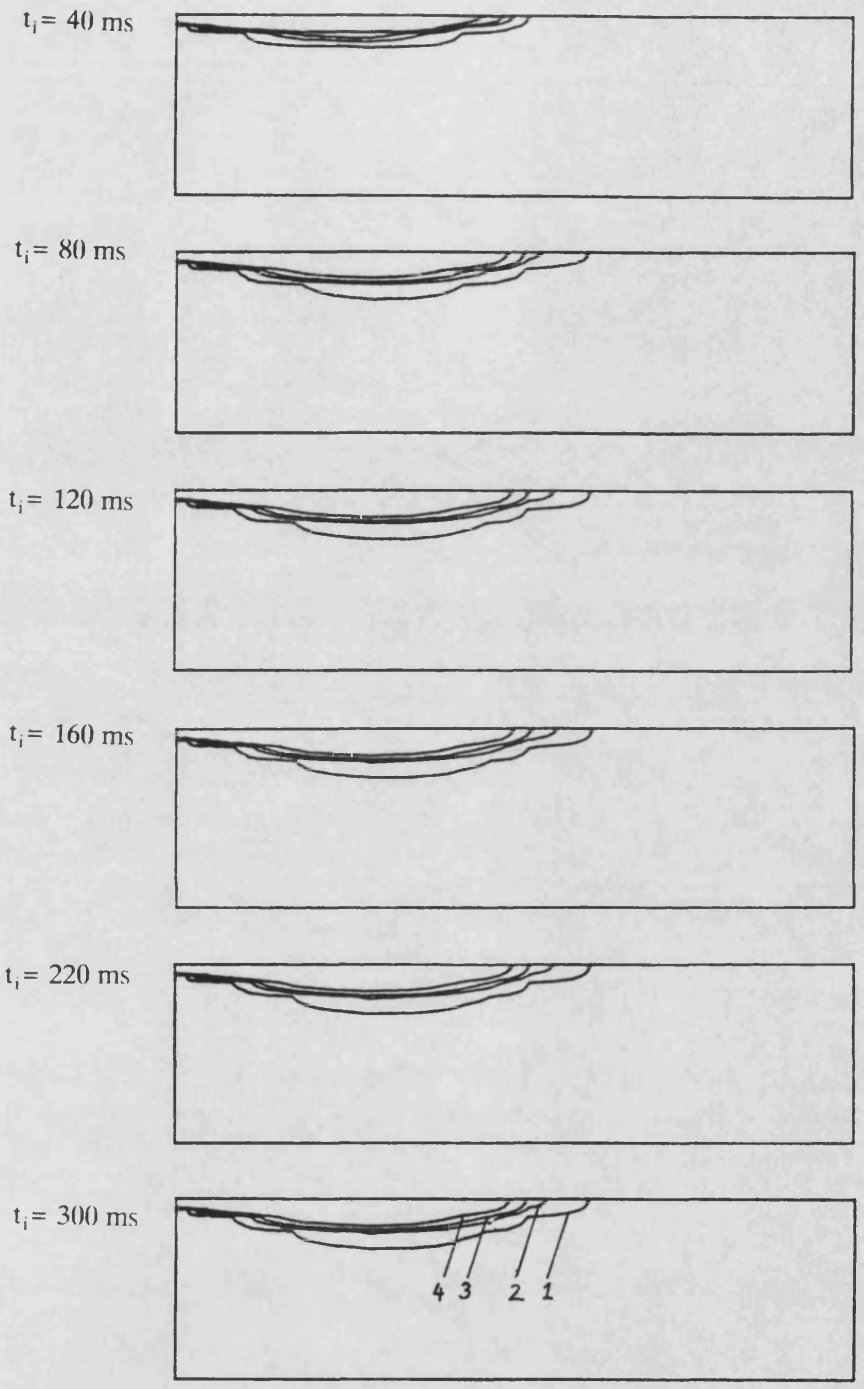

contour	A/F ratio
1	100:1
2	25:1
3	17:1
4	10:1

Fig. 8.36: Temporal development of air/fuel ratio contours in the r - z plane at θ = 4.5 deg.

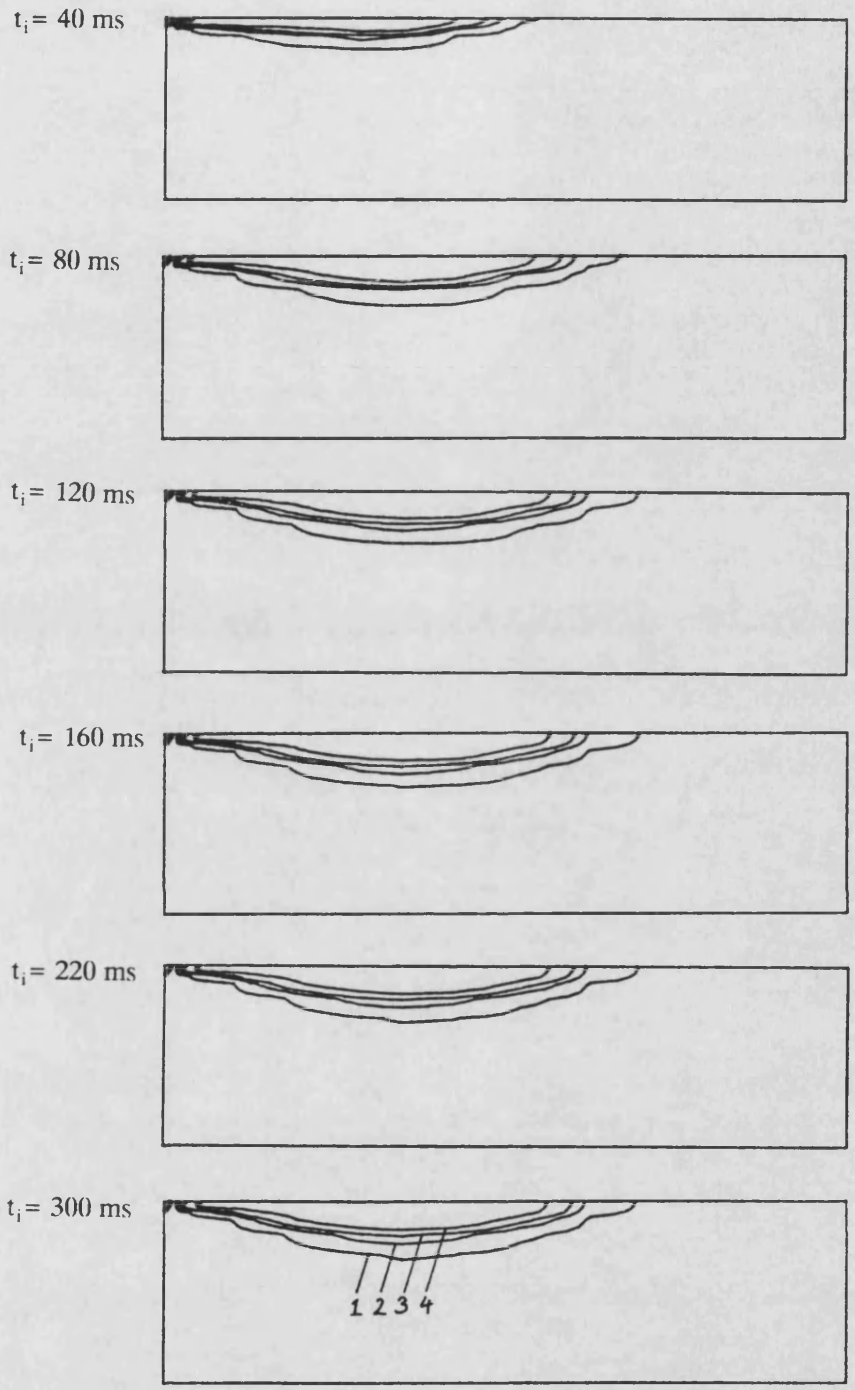

contour	A/F
1	100:1
2	25:1
3	17:1
4	10:1

Fig. 8.37: Temporal development of air/fuel ratio contours in the r - z plane at θ = 8.5 deg.

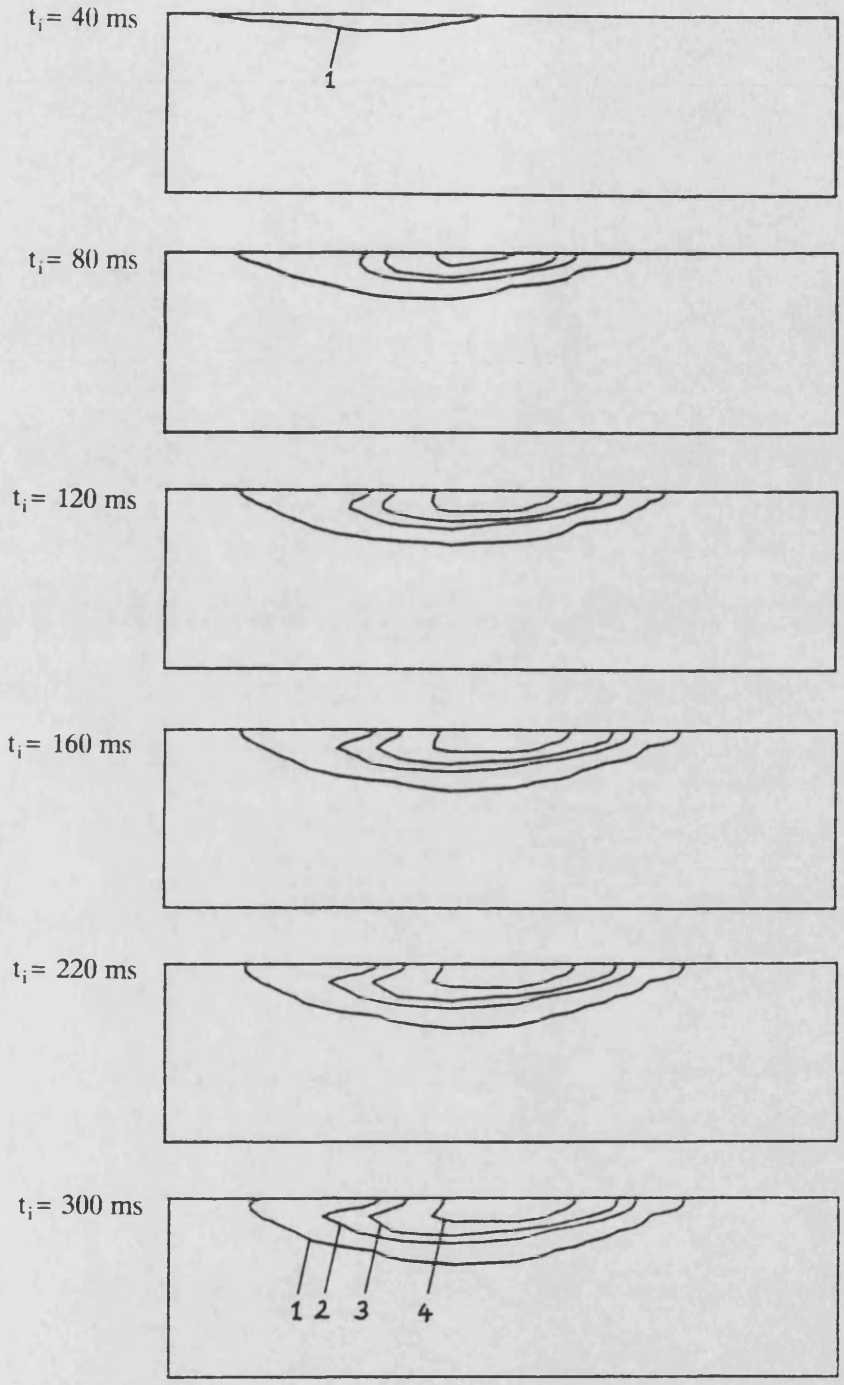

contour	A/F
1	100:1
2	25:1
3	17:1
4	10:1

Fig. 8.38: Temporal development of air/fuel ratio contours in the r - z plane at θ = 15.0 deg.

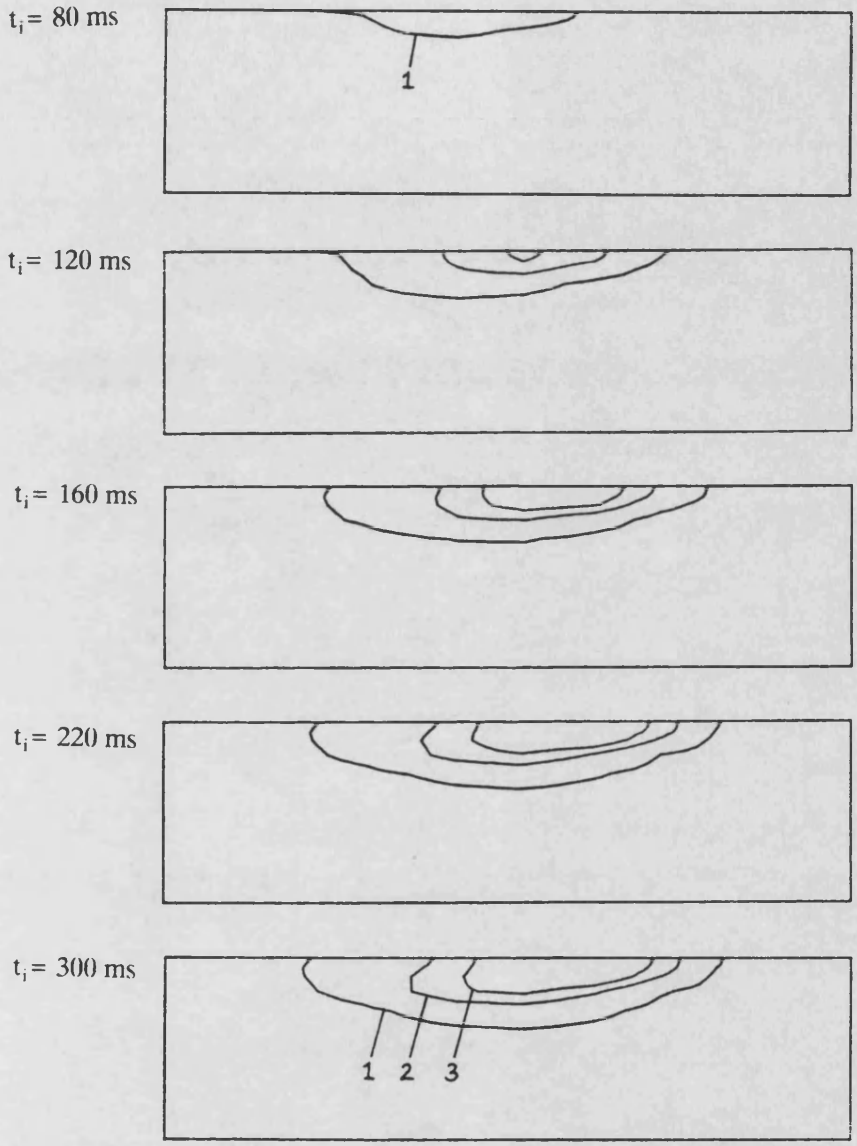

contour	A/F
1	100:1
2	25:1
3	17:1

Fig. 8.39: Temporal development of air/fuel ratio contours in the r - z plane at θ = 25.0 deg.

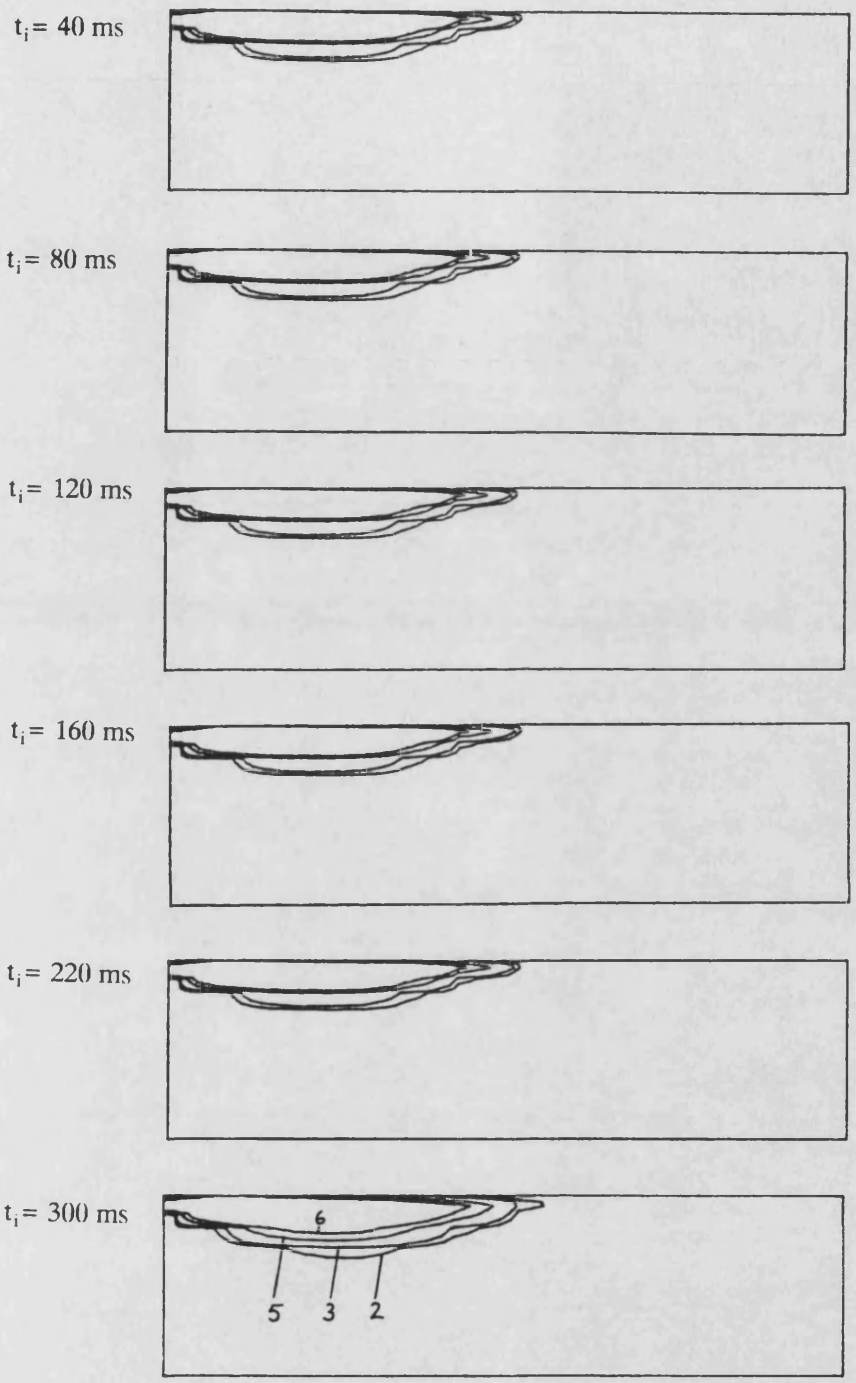

contour	norm. vorticity
1	0.001
2	0.005
3	0.01
4	0.02
5	0.03
6	0.05

Fig. 8.40: Temporal development of mean streamwise vorticity contours in the r - z plane at θ = 4.5 deg.

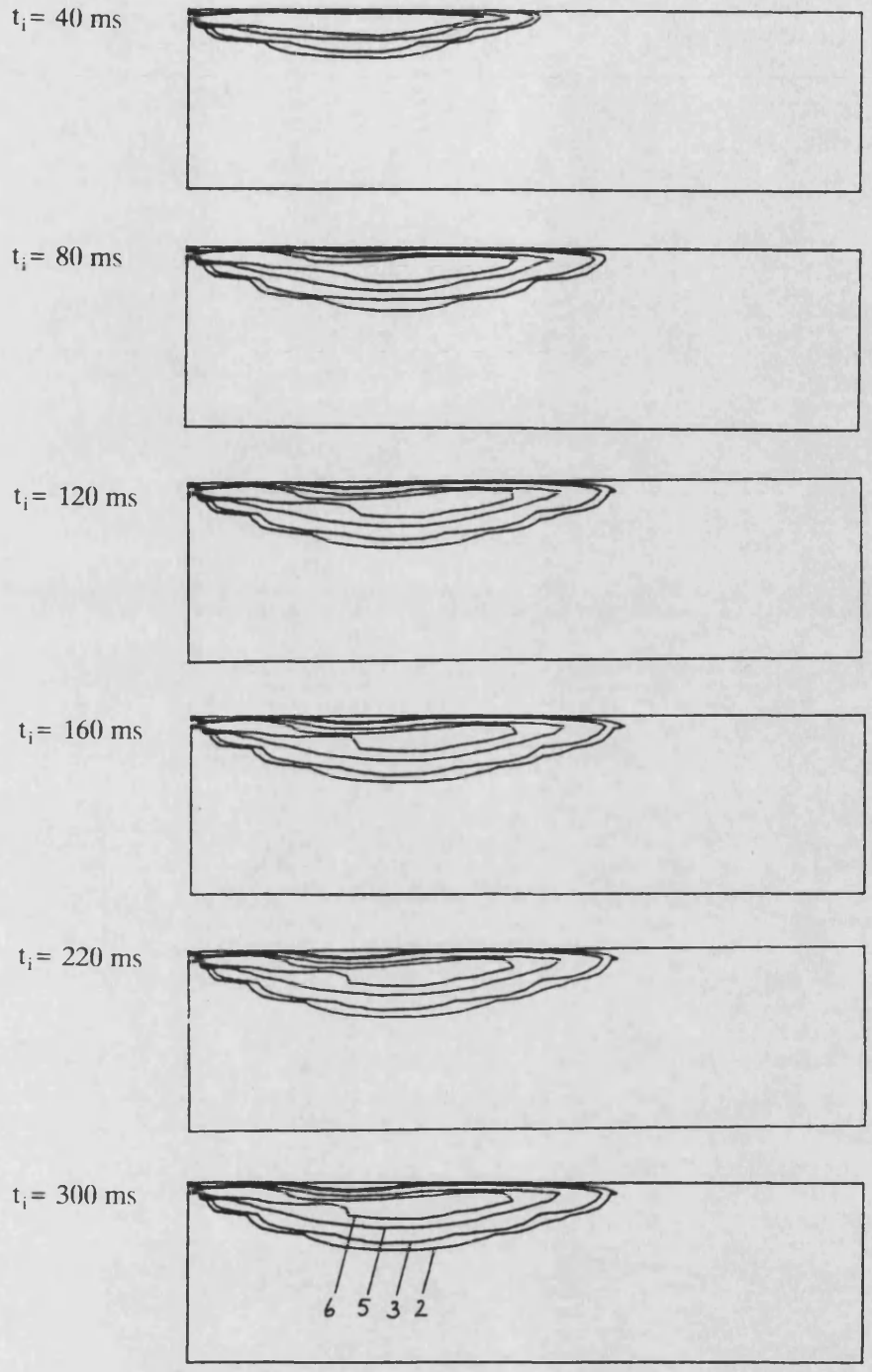

contour	norm. vorticity
1	0.001
2	0.005
3	0.01
4	0.02
5	0.03
6	0.05

Fig. 8.41: Temporal development of mean streamwise vorticity contours in the r - z plane at θ = 8.5 deg.

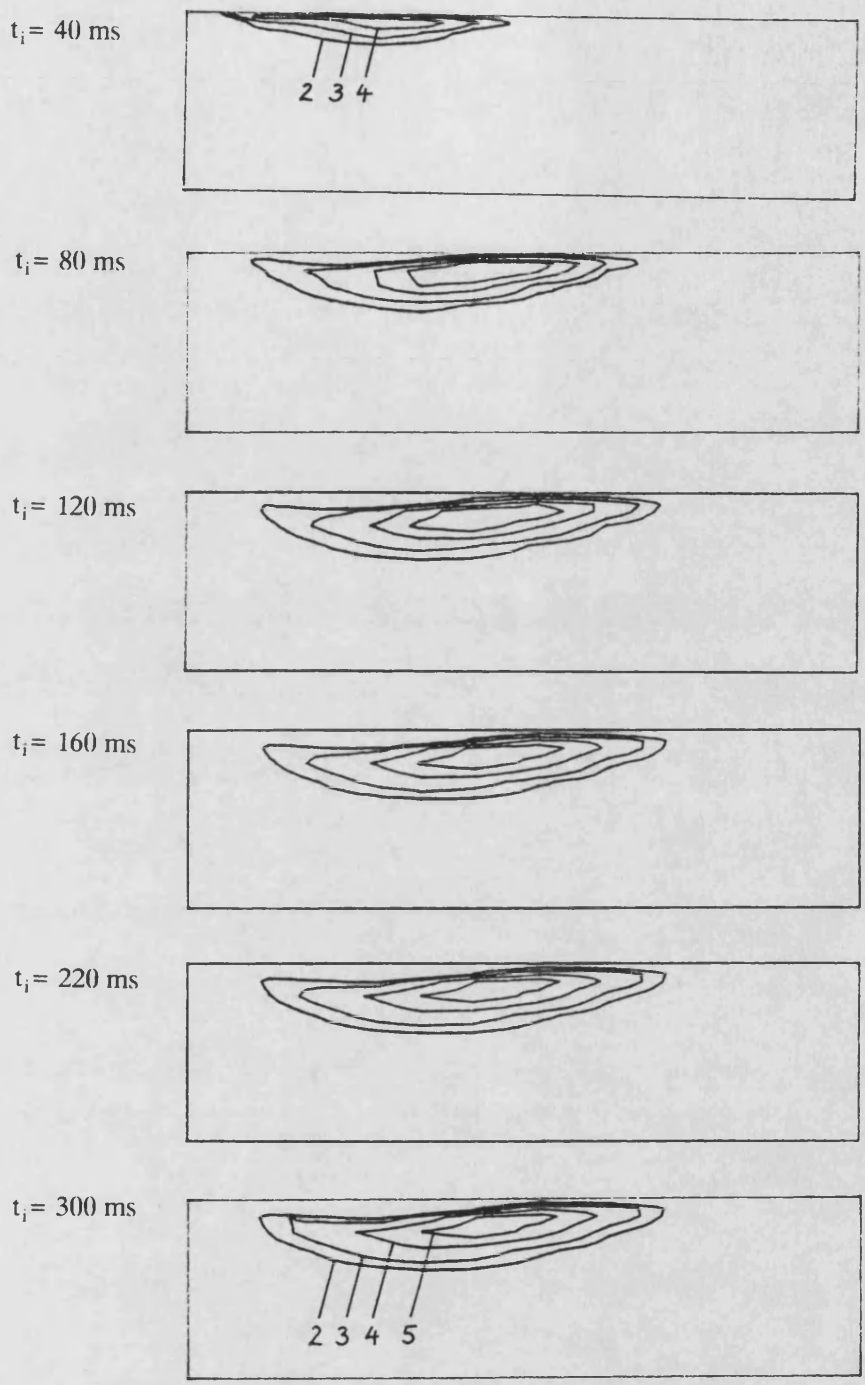

contour	norm. vorticity
1	0.001
2	0.005
3	0.01
4	0.02
5	0.03
6	0.05

Fig. 8.42: Temporal development of mean streamwise vorticity contours in the r - z plane at θ = 15.0 deg.

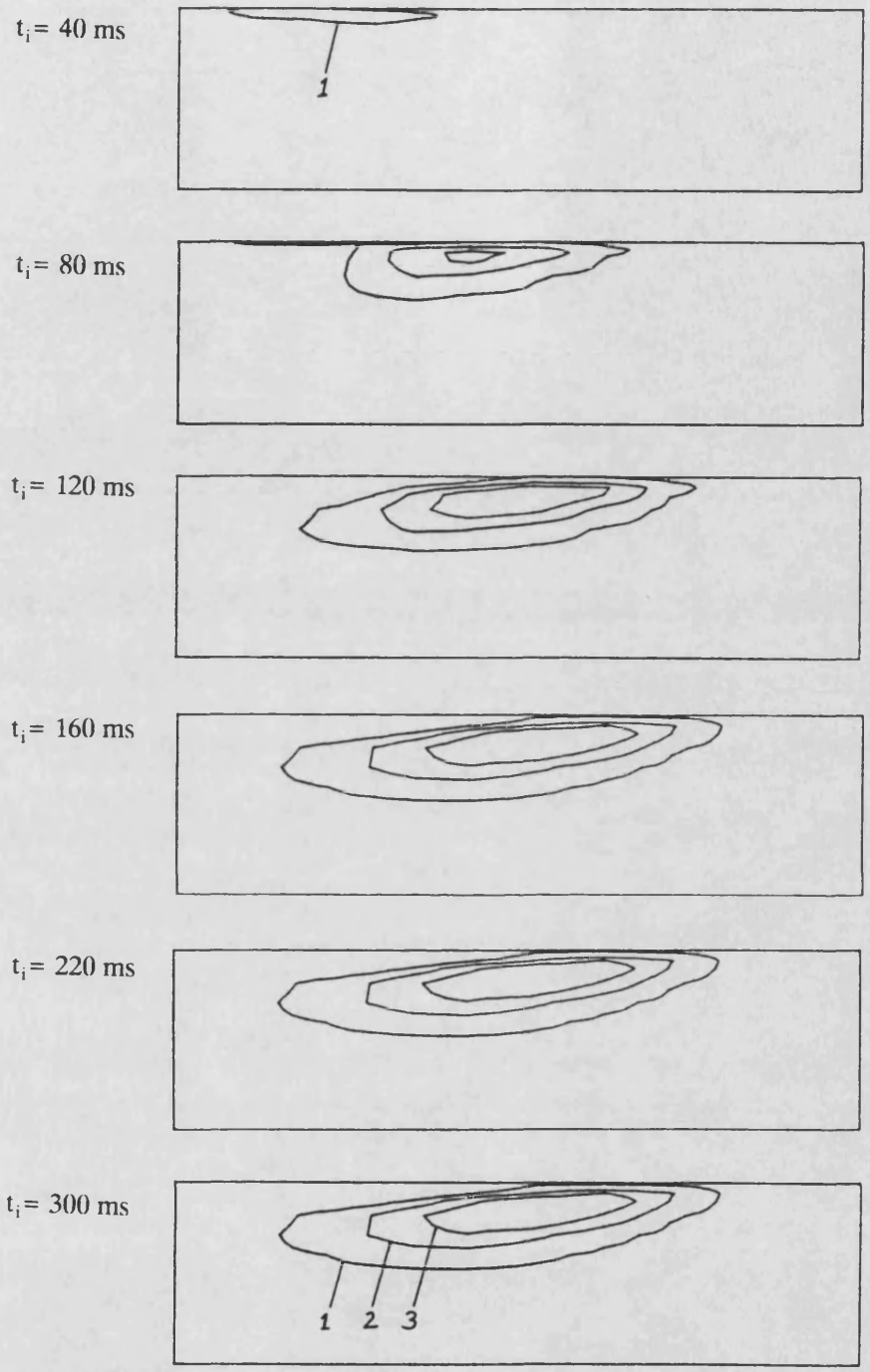

contour	norm. vorticity
1	0.001
2	0.005
3	0.01
4	0.02
5	0.03
6	0.05

Fig. 8.43: Temporal development of mean streamwise vorticity contours in the r - z plane at θ = 25.0 deg.

CHAPTER 9

9. CONCLUSIONS AND RECOMMENDATIONS FOR FUTURE WORK

A detailed computational and experimental study has been presented of turbulent jet injection into a Diesel engine combustion chamber model. In the absence of two phase phenomena, chemical reactions and piston movement, the flow field associated with steady state and impulsive injections has been analysed for quiescent and swirling conditions. A three dimensional numerical model has been developed to predict the mixing pattern resulting from the injection process for four flow configurations:

(i) steady state injections under quiescent conditions

(ii) impulsive injections under quiescent conditions

(iii) steady state injections under swirling conditions

(iv) impulsive injections under swirling conditions

A literature survey indicated a lack of detailed spatially resolved experimental data which could be used for validation purposes. Thus, an experimental programme was devised which yielded quantitative data of mean and fluctuating velocities in the flow configurations considered.

From the experimental data the jet's shear layer and centreline could be identified for the deflected and undeflected case. The jet tip penetration recorded during transient measurements showed that the impulsive jet is not as strongly deflected as the steady state jet. This observation casts some doubt on the validity of the quasi steady state assumption made in integral jet mixing models.

The computational study also explored the capabilities of a 'packaged' fluid dynamics code applied to jet mixing problems and to undertake sensitivity studies with a view to identifying weaknesses and improve predictions.

Specifically, for the undeflected jet parametric studies were carried out concerning the effect of grid density and orientation, boundary conditions, and turbulence model settings. Adjustments to a turbulence model constant were found to have a significant effect on the centreline velocity decay and a non - standard value was adopted to obtain agreement with experimental data. The location of the recirculation zone outside the jet boundary could not be predicted accurately, similarly, for the deflected jet the size of the recirculation zone downstream of the point of injection was underpredicted. This deficiency was attributed to the Hybrid scheme used for convective transport terms and the eddy viscosity turbulence model. It can to some extent be viewed as a trade off for the numerical stability of the code; in most cases convergence could be obtained within a reasonable number of iterations.

Under swirling conditions the turbulence model was found to be inadequate to correctly predict the swirling field generated prior to injection. It was argued that a second moment closure model would be fundamentally more accurate. By introducing non - dimensional parameters for jet penetration and swirl, the value of the model as a tool for optimising injection pressure characteristics and matching these characteristics to the swirling flow field was demonstrated. Parametric studies of the relative effect of swirl to penetration will yield injection pressure characteristics which lead to a more homogeneous air - fuel mixture distribution in the combustion chamber model. Such a mixture is likely to result in improved combustion efficiency and a reduced pressure gradient due to a shorter ignition delay period.

Results of parametric studies may be scaled to predict the mixing pattern in the real engine prior to combustion, thus allowing the time required for the formation of a combustable mixture to be estimated. The scale relationships are given in chapter six. In extrapolating numerical results from the analogue model, the limitations of the analogy outlined in chapter six must be taken into account.

Despite the limitations of the numerical model with regard to the approximation of

convective transport and the turbulence model, the ability to perform parametric studies, not only concerning the relative effect of swirl to penetration, but also with respect to the combustion chamber shape, nozzle design and injection angles at no experimental cost must be viewed as a distinct advantage. An optimised model from a hydrodynamic point of view may then form the basis for extensions to include multi - phase features and combustion.

It is recommended that future work concentrate on further improving the pure jet mixing model for the swirling case by introducing (i) a quadratic scheme for convective transport and (ii) a second moment closure model to account for turbulence. Recent research reported in the literature [32, 84] suggests that these two areas are the most promising for improving predictive capabilities of fluid dynamic codes. This is by no means a simple task and is at present beyond the capabilities of a code aimed at the industrial community rather than research institutions. It is however important that these aspects be addressed in an effort to accurately capture the hydrodynamic features of the flow before further progress can be made towards a comprehensive model for the combustion process in DI Diesel engines.

References

1. Abthoff J., Fortnagel M., Krämer M. (1988): 'Das direkteinspritzende Brennverfahren in seiner Eignung als Antrieb für Personenwagen', MTZ 49 pp 345

2. Mayer K.P. (1984): 'Fuel economy, emissions and noise of multi-spray light duty DI diesels - current status and development trends', SAE Paper 841288

3. Ikegami M., Komatsu G., Nishiwaki K. (1986): 'Numerical simulation of flow in an engine cylinder', Bulletin of JSME, Vol. 29, No. 248

4. Fischer H., Melcher T. (1989): 'Mehrdimensionale Verbrennungsrechnung - ein Werkzeug für die Brennraumentwicklung', MTZ 50 pp 173

5. Gosman A.D., Harvey P.S. (1982): 'Computer analysis of fuel - air mixing and combustion in an axisymmetric DI Diesel', SAE Paper 820036

6. Watkins A.P. (1988): 'Overview of computational modelling in IC engines', 3rd biennial colloquium on comutational fluid dynamics, UMIST 1988

7. Gosman A.D., Johns R.J.R. (1980): 'Computer analysis of fuel - air mixing in DI Diesel engines', SAE Paper 800091

8. Gosman A.D. (1986): 'Flow processes in cylinders' in 'Thermodynamics and gas dynamics of internal combustion engines' (Eds. Horlock J.H., Winterbone D.), Vol. 2

9. Gosman A.D., Johns, R.J.R., Watkins A.P. (1986): 'Development of prediction methods for in - cylinder processes in reciprocating engines' in 'Thermodynamics and gas dynamics of internal combustion engines' (Eds. Horlock J.H., Winterbone D.), Vol. 2

10. Gosman A.D., Tsui Y.Y., Yafidis C. (1985): 'Flow in model engine with a shrouded valve - a combined experimental and computational study', SAE Paper 850498

11. Ahmadi-Befrui B., Gosman A.D., Watkins A.P. (1984): 'Prediction of in - cylinder flow and turbulence with three versions of k - ε turbulence model and comparison with data' Proceedings of Symp. on flows in internal combustion engines II ASME FED 20 pp 27

12. Gosman A.D., Tsui Y.Y., Watkins A.P. (1984): 'Calculation of three dimensional air motion in model engines', SAE Paper 840229

13. Ahmadi-Befrui B., Arcoumanis C., Bicen A.F., Gosman A.D., Jahanbakhsh A., Whitelaw J.H. (1982): 'Calculations and measurements of the flow in a motored model engine and implications to open - chamber direct - injection engines', Proc. A.S.M.E. symposium on three - dimensional turbulent shear flows

14. Brandl F., Reverencic I., Cartellieri W., Dent J.C. (1979): 'Turbulent air flow in the bowl of a DI diesel engine and its effect on engine performance' SAE Paper 790040

15. Melton R.B. (1971): 'Diesel fuel injection viewed as a jet phenomenon', SAE Paper 710132

16. Newman J.A., Brzustowski T.A. (1971): 'Behavior of a liquid jet near the thermodynamic critical region', AIAA Journal, Vol 9, No. 8, pp 1595

17. Chiu W.S., Shahed S.M., Lyn W.T. (1976): 'A transient spray mixing model for diesel combustion', SAE Paper 760128

18. Abramovich G.N. (1963): 'The theory of turbulent jets', MIT Press Cambridge Mass. USA

19. Idoum A. (1984): 'Investigation of the effect of swirl and impingement on fuel air mixing in diesel engines using a water model', MSc Thesis, University of Bath

20. Horner (1981): 'Trajectories and evaporation rates of fuel droplets in a swirling air jet in a DI diesel engine', MSc Thesis, University of Bath

21. Idoum A., Wallace F.J., Packer J.P., Charlton S.J. (1985): 'An experimental and analytical study of jet impingement and wall jets in high swirl DI diesel engines using the hydraulic analogy', SAE Paper 850263

22. Way R.J.B. (1977): 'Investigation of interaction between swirl and jets in direct injection diesel engines using a water model', SAE Paper 770412

23. Gan X.P.: PhD Thesis 1990, University of Bath

24. Patankar S.V., Basu D.K., Alpay S.A. (1977): 'Prediction of the three - dimensional velocity field of a deflected turbulent jet', Transactions of the A.S.M.E., Dec. 1977, pp 758

25. Kuo T.W., Bracco F.V. (1982): 'On the scaling of transient laminar, turbulent and spray jets', SAE Paper 820038

26. Kuo T.W., Bracco F.V. (1982): 'On the scaling of impulsively started incompressible turbulent round jets', Journal of Fluids Engineering, Vol. 104, pp 191

27. Jones W.P., McGuirk J.J. (1979): 'Computation of a round turbulent jet discharging into a confined cross - flow', Turb. Shear Flows 2, pp 233

28. Hoholis E.G. (1985): 'Numerical simulation and experimental investigation of jet injection into a quiescent combustion chamber model', PhD Thesis, UMIST

29. Rodi W. (1982): 'Examples of turbulence models for incompressible flows', AIAA Journal, Vol. 20, No. 7, pp 872

30. Malin M.R. (1988): 'Prediction of radially spreading turbulent jets', AIAA Journal, Vol. 26, No. 6, pp 750

31. Pope S.B. (1978): 'An explanation of the turbulent round jet/plane - jet anomaly', AIAA Journal, Vol. 16, No. 3, pp 279

32. Lin C.A., Leschziner M.A. (1988): 'Towards modelling 3D jet injection in swirling flow with second - moment closure', 3rd biennial colloquium on computational fluid dynamics, UMIST 1988

33. Adler D., Lyn W.T. (1971): 'The steady evaporation and mixing of a spray in a gaseous swirl', Int. J. Heat Mass Transfer, Vol. 14, pp 793

34. Wilson M. (1986): 'Integral modelling of jets of variable composition in generalised crossflows', PhD Thesis, University of Bath

35. Khaleghi H., Watkins A.P. (1988): 'Spray modelling in 3D IC - engine cylinders', 3rd biennial colloquium on computational fluid dynamics, UMIST 1988

36. Brandstätter W., Killmann I. (1988): 'Computersimulation der Strömung, Gemischbildung und Verbrennung in Motoren', MTZ 49, pp 177

37. Arcoumanis C., Whitelaw J.H. (1987): 'Fluid mechanics of internal combustion engines - a review', Proc. Instn. Mech. Engrs., Vol 201, No. C1, pp 57

38. Bassoli C., Bodritti G., Cornetti G.M. (1985): 'Optimum air momentum and spray formation for DI diesel', SAE Paper 850501

39. Bracco F.V. (1985): 'Modeling of engine sprays', SAE Paper 850394

40. Tindal M.J., Williams T.J., Harcombe A.T. (1987): 'Fuel spray formation in an experimental swirl chamber', SAE Paper 870451

41. Packer J.P., Wallace F.J., Adler D., Karimi E.R. (1983): 'Diesel fuel jet mixing under high swirl conditions', IMechE C80/83, pp 9

42. Packer J.P., Wallace F.J., Wilson M., While C.L. (1984): 'An investigation of mixing and combustion under swirled DI diesel engine conditions', A.S.M.E. Winter meeting, New Orleans

43. White C.L., Wallace F.J. (1986): 'Heat release tests and high - speed photography using a high swirl bomb simulating the combustion process in the DI diesel engine', SAE Paper 861274

44. Adler D., Baron A. (1979): 'Prediction of a three - dimensional circular turbulent jet in crosslow', AIAA Journal, Vol. 17, No. 2, pp 168

45. Packer J.P. (1983): 'Diesel type combustion studies in high swirl chambers', PhD Thesis, University of Bath

46. Kamotani Y., Greber I. (1971): 'Experiments on a turbulent jet in a cross flow', Case Western Reserve University, NASA CR - 72893

47. Witze P.O. (1980): 'The impulsively started incompressible turbulent jet', Sandia Laboratories, SAND80 - 8617

48. Gigg H.C., Syed M.H. (1970): 'The problem of predicting rate of heat release in diesel engines', Symposium on diesel engine combustion, IMechE 1970

49. Meguerdichian M., Watson N. (1978): 'Prediction of mixture formation and heat release in diesel engines', SAE Paper 780225

50. Brandstätter W., Fischer H., Melcher T. (1988): 'Multidimensional engine combustion modelling - a challange for supercomputers', 2nd international symposium 'Use of supercomputers in the european automotive industry', Turin, April 1988

51. Brandstätter W., Johns R.J.R. (1986): 'Computer simulation of external and internal turbulent flows in the automotive industry', in 'Supercomputer applications in Automotive research and engineering development', Proc. Int. Conf. Supercomputer applications in the automotive industry, Ed. C. Marino

52. Spalding D.B. (1971): 13th International Symposium on Combustion pp 649, The Combustion Institute 1971

53. Magnussen B.F., Hjertager B.H. (1976): 'On mathematical modelling of turbulent combustion with special emphasis on soot formation and combustion', 16th international symposium on combustion, pp 719, The Combustion Institute 1976

54. Argueyrolles B., Souhaite P., Gauffie S., Borghi R. (1986): 'Apllication of a presumed p.d.f. model of turbulent combustion to reciprocating engines - part 2, in 'Supercomputer applications in Automotive research and engineering development', Proc. Int. Conf. Supercomputer applications in the automotive industry, Ed. C. Marino

55. Sforza P.M., Mons R.F. (1978): 'Mass, momentum, and energy transport in turbulent free jets', Int. J. Heat Mass Transfer, Vol. 21, pp 371

56. Prandtl L. (1942): 'Bemerkungen zur Theorie der freien Turbulenz', ZAMM, 22, pp 241

57. Packer J.P., Wallace F.J. (1981): 'Jet mixing studies for high swirl DI diesel combustion chambers', Combustion presentation: UMIST Sept. 1981

58: Bird R.B., Stewart W.E., Lightfoot E.N. (1960): 'Transport Phenomena', John Wiley & Sons, 1960

59. Hinze J.O. (1959): 'Turbulence', McGraw Hill Series in Mechanical Engineering

60. Launder B.E., Spalding D.B. (1974): 'The numerical computation of turbulent flows', Computer Methods in applied Mechanics and Engineering 3, pp 269

61. Rodi W. (1984): 'Turbulence models and their application in hydraulics - a state of the art review', Institut für Hydromechanik, Universität Karlsruhe

62. CHAM Ltd. (1988): 'The PHOENICS beginners guide', Technical Report TR 100

63. Bradshaw P., Cebeci T., Whitelaw J.H. (1981): 'Engineering calculation methods for turbulent flows'

64. Tennekes H., Lumley J.L. (1972): 'A first course in turbulence', 6th edition, MIT Press 1972

65. Reynolds W.C. (1980): 'Modeling of fluid motions in engines - an introductory overview', in 'Combustion modeling in reciprocating engines', ed. J.N. Mattavi

66. Gosman A.D. (1985): 'Multidimensional modeling of cold flows and turbulence in reciprocating engines', SAE Paper 850344

67. Spalding D.B. (1980): 'Numerical modeling of fluid mechanics, heat transfer and combustion processes: a lecture course', Imperial College CFDU report HTS/80/81

68. Gibson M.M., Jones W.P., McGuirk J.J., Whitelaw J.H. (1984): 'Turbulence models for computational fluid dynamics' , outline lecture notes, Imperial College, London 1984

69. Prandtl L. (1925): 'Über die ausgebildete Turbulenz', ZAMM, 5, pp 136

70. Morse A.P. (1977): 'Axisymmetric turbulent shear flows with and without swirl', PhD Thesis, London University, 1977

71. McGuirk J.J., Rodi W. (1977): 'The calculation of three - dimensional free jets', Symposium on turbulent shear flows, Pennsylvania State University, April 1977

72. Launder B.E., Morse A.P., Rodi W., Spalding D.B. (1973): 'The prediction of free shear flows - a comparison of the performance of six turbulence models', Proc. NASA Langley Free Turbulent Shear Flow Conf. Vol. 1, NASA SP 320

73. Schetz J.A. (1980): 'Injection and mixing in turbulent flow', Progress in Astronautics and Aeronautics, Vol. 68

74. Taulbee D.B., Hussein H., Capp S. (1987): 'The round jet: experiment and inferences on turbulence modeling', Proc. 6th Turb. Shear Flows Symp., Paper 10.5, Toulouse 1987

75. Malin M.R. (1986): PhD Thesis, Imperial College, London

76. McGuirk J.J., Rodi W. (1978): 'A depth - avaraged mathematical model for the near field of side discharges into open - channel flow', J. Fluid Mech., Vol. 86, part 4, pp 761

77. Launder B.E. (1989): 'Second - moment closure: present and future?', Int. J. Heat and Fluid Flow, Vol. 10, No. 4, pp 282

78. Launder B.E. (1988): 'Turbulence modelling - a preview', 3rd biennial colloquium on computational fluid dynamics, UMIST 1988

79. Launder B.E., Reece G.J., Rodi W. (1975): 'Progress in the development of a Reynolds - stress turbulence closure', J. Fluid Mech., Vol. 68, part 3, pp 537

80. Spalding D.B. (1989): 'The PHOENICS computer code', in 'Computer simulation for fluid flow, heat and mass transfer, and combustion in reciprocating engines', ed. N.C. Markatos, Hemisphere 1989

81. Patankar S.V. (1980): 'Numerical heat transfer and fluid flow', McGraw Hill, 1980

82. CHAM Ltd. (1988): 'PHOENICS Reference Manual' Technical report TR 200

83. Gosman A.D., Issa R.I. (1989): Post experience course in computational fluid dynamics, lecture notes, Imperial College, London, Sept. 1989

84. Leschziner M.A. (1989): 'Modeling turbulent recirculating flows by finite - volume methods - current status and future directions', Int. J. Heat and Fluid Flow, Vol. 10, No. 3, pp 186

85. CHAM Ltd. (1987): 'The PHOENICS equations', Technical report TR 99

86. Spalding D.B. (1983): lecture course on computational fluid dynamics, Imperial College, London

87. Markatos N.C. (1989): 'Introduction to computational fluid dynamics and applications to the automotive industry', in 'Computer simulation for fluid flow, heat and mass transfer, and combustion in reciprocating engines', ed. N.C. Markatos, Hemisphere 1989

88. Burt R., Troth K.A. (1970): 'Penetration and vaporization of diesel fuel sprays', IMechE Symp. on diesel engine combustion, paper no. 15, 1970

89. Perry, A.E. (1982): 'Hot - wire anemometry', Clarendon Press Oxford, 1982

90. Bruun H.H. (1987): 'Advanced hot - wire anemometry course', lecture 6, UMIST, 1987

91. White C.L. (1986): 'Interim report on hot - film anemometry work with the water rig', School of Mech. Eng., University of Bath

92. Wygnanski I., Fiedler H. (1969): 'Some measurements in the self - preserving jet', J. Fluid Mech., Vol. 38, part 3, pp 577

93. Gordier R.I. (1959): 'Studies on fluid jets discharging normally into moving liquid', University of Minnesota, St. Anthony Falls Hydraulic Laboratory, Technical Paper No. 28, Series B

94. Rajaratnam N. (1976): 'Turbulent jets', Developments in water science, Elsevier, 1976

95. Davis M. : Personal communication

96. Sykes R.I., Lewellen W.S., Parker S.F. (1986): 'On the vorticity dynamics of a turbulent jet in a crossflow', J. Fluid Mech., Vol. 168, pp 393

97. Bronstein I.N., Semendjajew K.A. (1981): 'Taschenbuch der Mathematik', BSB B.G. Teubner Verlagsgesellschaft, Leipzig

98. Ahmadi-Befrui B., Brandstätter W., Pitcher G., Troger C., Wigley G. (1990): 'Simulationsmodell zur Berechnung der Luftbewegung in Zylindern von Verbrennungsmotoren', MTZ 51, pp 440

99. Lin C.A., Leschziner M.A. (1989): 'Computation of three - dimensional injection into swirling combustor model flow with second - moment closure', Proc. 6th int. conference on numerical methods in laminar and turbulent flows, Swansea, 1989

100. van Basshuysen R, Stock D., Bauder R. (1990): 'Audi Turbodieselmotor mit Direkteinspritzung', MTZ 51, pp 4

101. Leschziner M.A. (1988): 'Computational modelling of complex turbulent flow - industrial expectations and reality', Computing methods in fluid - flow applications, BHRA, June 1988

Appendices

Appendix A

Governing equations:

	ϕ	Γ_ϕ	S_ϕ
continuity	1	0	0
circumferential momentum	u	μ_e	$\frac{1}{r}\frac{\partial}{\partial r}\left[r\mu_e\left(\frac{1}{r}\frac{\partial v}{\partial \theta} - \frac{u}{r}\right)\right] + \frac{1}{r}\mu_e\left[r\frac{\partial(\frac{u}{r})}{\partial r} + \frac{1}{r}\frac{\partial v}{\partial \theta}\right] + \frac{1}{r}\frac{\partial}{\partial \theta}\left[\mu_e\left(\frac{\partial u}{r\partial \theta} + \frac{2v}{r}\right)\right] + \frac{\partial}{\partial z}\left(\mu_e\frac{\partial w}{r\partial \theta}\right) - \frac{\rho v u}{r} - \frac{\partial p}{r\partial \theta}$
radial momentum	v	μ_e	$\frac{1}{r}\left(r\mu_e\frac{\partial v}{\partial r}\right) + \frac{1}{r}\frac{\partial}{\partial \theta}\left[\mu_e\frac{r\partial(\frac{u}{r})}{\partial r}\right] - 2\frac{\mu_e}{r}\left[\frac{\partial u}{r\partial \theta} + \frac{v}{r}\right] + \frac{\partial}{\partial z}\left(\mu_e\frac{\partial w}{\partial r}\right) + \frac{\rho u^2}{r} - \frac{\partial p}{\partial r}$
axial momentum	w	μ_e	$\frac{1}{r}\frac{\partial}{\partial r}\left(r\mu_e\frac{\partial v}{\partial z}\right) + \frac{1}{r}\frac{\partial}{\partial \theta}\left(\mu_e\frac{\partial u}{\partial z}\right) + \frac{\partial}{\partial z}\left(\mu_e\frac{\partial w}{\partial z}\right) - \frac{\partial p}{\partial z}$
turb. kinetic energy	k	$\frac{\mu_e}{\sigma_k}$	$G_k - \rho\varepsilon$
dissipation of kin. energy	ε	$\frac{\mu_e}{\sigma_\varepsilon}$	$(C_1\varepsilon G_k - C_2\rho\varepsilon^2)/k$
scalar quantity	C	$\frac{\mu_e}{\sigma_c}$	0

where

$$\mu_e = \mu_l + \mu_t$$

$$\mu_t = C_\mu \rho k^2/\varepsilon$$

$$G_k = \mu_t\left[2\left(\frac{\partial w}{\partial z}\right)^2 + 2\left(\frac{\partial v}{\partial r}\right)^2 + 2\left(\frac{\partial u}{r\partial \theta} + \frac{v}{r}\right)^2 + \left(\frac{\partial w}{\partial r} + \frac{\partial v}{\partial z}\right)^2 + \left(\frac{\partial u}{\partial z} + \frac{\partial w}{r\partial \theta}\right)^2 + \left(\frac{\partial v}{r\partial \theta} + \frac{\partial u}{\partial r} - \frac{u}{r}\right)^2\right]$$

Turbulence model constants:

C_μ	C_1	C_2	σ_k	σ_ε
0.09	1.47	1.92	1.0	1.30

Reynolds flux equation [[78], neglecting buoyancy effects:

$$\frac{D\,\overline{u_i\varphi}}{Dt} = \frac{\partial}{\partial x_k}\left(C_{s\varphi}\,\overline{u_k u_l}\,\frac{k}{\varepsilon}\,\frac{\partial \overline{u_i\varphi}}{\partial x_l}\right) + P_{i\varphi 1} + P_{i\varphi 2} + \phi_{i\varphi}$$

where $P_{i\varphi 1} = -\,\overline{u_k u_j}\,\frac{\partial \phi}{\partial x_k}$

$$P_{i\varphi 2} = -\,\overline{\varphi u_k}\,\frac{\partial U_i}{\partial x_k}$$

$$\phi_{i\varphi} = -\,C_{1\varphi}\,\frac{\varepsilon}{k}\,\overline{u_i\varphi} - C_{2\varphi}\,P_{i\varphi 2}$$

$$C_{s\varphi} = 0.15\,, \quad C_{1\varphi} = 3.0\,, \quad C_{2\varphi} = 0.5$$

Appendix B

B1: 'Q1' input file for transient undeflected jet

```
    GROUP 1. Run title and other preliminaries
    £
TEXT(CONSTANT DENSITY JET ISSUING INTO A TANK)
    £
    GROUP 2. Transience; time-step specification
    £
NOWIPE=T
    £
STEADY=F
    £
TFIRST=0.0
TLAST=1.0
LSTEP=5
    £
TFRAC(1)=-5;TFRAC(2)=0.003
    £
    GROUP 3. X-direction grid specification
    £
    £ POLAR GRID
    £
CARTES=F
    £
NX=17


REAL(ALPHA1,ALPNOZ)
INTEGER(NXALP1,NXNOZ,NXCLIN)
XULAST=3.14159/4
    £
    £ ALPNOZ is the nozzle exit angle corresponding to a
    £         nozzle width of 2.5 mm
    £ ALPHA1 is the angle to make up the quadrant
    £
ALPHA1=0.6283;ALPNOZ=0.1571
NXALP1=7;NXNOZ=10
    £
    £ define variable names for First and Last nozzle
    £ cells in x-direction
    £
INTEGER(NXNOZF,NXNOZL)
NXNOZF=NXALP1+1;NXNOZL=NXALP1+NXNOZ
NXCLIN=NXNOZL
    £
XFRAC(1)=-1;XFRAC(2)=0.1257/(-XFRAC(1)*XULAST)
XFRAC(3)=1;XFRAC(4)=0.1759/(XFRAC(3)*XULAST)
XFRAC(5)=1;XFRAC(6)=0.1257/(XFRAC(5)*XULAST)
XFRAC(7)=1;XFRAC(8)=0.0817/(XFRAC(7)*XULAST)
XFRAC(9)=1;XFRAC(10)=0.0565/(XFRAC(9)*XULAST)
XFRAC(11)=1;XFRAC(12)=0.0377/(XFRAC(11)*XULAST)
XFRAC(13)=1;XFRAC(14)=0.0251/(XFRAC(13)*XULAST)
XFRAC(15)=NXNOZ;XFRAC(16)=(XULAST-ALPHA1)/(XFRAC(15)*XULAST)
    £
    GROUP 4. Y-direction grid specification
    £
NY=43
INTEGER(NYINJ,NYNOZ)
REAL(YINCOL,YNOZ)
NYINJ=1;NYNOZ=1
YINCOL=15.9E-3;YNOZ=0.3333E-3
YVLAST=276.E-3-YINCOL+YNOZ
    £
RINNER=YINCOL-YNOZ
    £
YFRAC(1)=-1;YFRAC(2)=YNOZ/(-YFRAC(1)*YVLAST)
YFRAC(3)=12;YFRAC(4)=4.E-3/(YFRAC(3)*YVLAST)
YFRAC(5)=6;YFRAC(6)=6.E-3/(YFRAC(5)*YVLAST)
YFRAC(7)=4;YFRAC(8)=8.E-3/(YFRAC(7)*YVLAST)
YFRAC(9)=3;YFRAC(10)=10.E-3/(YFRAC(9)*YVLAST)
YFRAC(11)=1;YFRAC(12)=7.E-3/(YFRAC(11)*YVLAST)
YFRAC(13)=1;YFRAC(14)=9.E-3/(YFRAC(13)*YVLAST)
YFRAC(15)=1;YFRAC(16)=11.E-3/(YFRAC(15)*YVLAST)
```

```
YFRAC(17)=1;YFRAC(18)=13.E-3/(YFRAC(17)*YVLAST)
YFRAC(19)=1;YFRAC(20)=13.1E-3/(YFRAC(19)*YVLAST)
YFRAC(21)=1;YFRAC(22)=18.E-3/(YFRAC(21)*YVLAST)
YFRAC(23)=1;YFRAC(24)=23.E-3/(YFRAC(23)*YVLAST)
YFRAC(25)=2;YFRAC(26)=54.E-3/(YFRAC(25)*YVLAST)
YFRAC(27)=1;YFRAC(28)=23.E-3/(YFRAC(27)*YVLAST)
YFRAC(29)=1;YFRAC(30)=20.E-3/(YFRAC(29)*YVLAST)
YFRAC(31)=1;YFRAC(32)=14.E-3/(YFRAC(31)*YVLAST)
YFRAC(33)=1;YFRAC(34)=10.E-3/(YFRAC(33)*YVLAST)
YFRAC(35)=1;YFRAC(36)=7.E-3/(YFRAC(35)*YVLAST)
YFRAC(37)=1;YFRAC(38)=5.E-3/(YFRAC(37)*YVLAST)
YFRAC(39)=1;YFRAC(40)=3.E-3/(YFRAC(39)*YVLAST)
YFRAC(41)=1;YFRAC(42)=2.E-3/(YFRAC(41)*YVLAST)
    £
    GROUP 5. Z-direction grid specification
    £
    £ define first and last injection cell
    £
INTEGER(NOZF,NOZL)
NOZF=14
NOZL=18
    £
REAL(ZNDIAM)
ZNDIAM=2.5E-3
    £
NZ=18
ZWLAST=72.5E-3
    £
ZFRAC(1)=-1;ZFRAC(2)=1.E-3/(-ZFRAC(1)*ZWLAST)
ZFRAC(3)=1;ZFRAC(4)=2.E-3/(ZFRAC(3)*ZWLAST)
ZFRAC(5)=1;ZFRAC(6)=5.E-3/(ZFRAC(5)*ZWLAST)
ZFRAC(7)=7;ZFRAC(8)=55.E-3/(ZFRAC(7)*ZWLAST)
ZFRAC(9)=1;ZFRAC(10)=4.E-3/(ZFRAC(9)*ZWLAST)
ZFRAC(11)=1;ZFRAC(12)=2.E-3/(ZFRAC(11)*ZWLAST)
ZFRAC(13)=1;ZFRAC(14)=1.E-3/(ZFRAC(13)*ZWLAST)
ZFRAC(15)=5;ZFRAC(16)=ZNDIAM/(ZFRAC(15)*ZWLAST)
    £
    GROUP 6. Body-fitted coordinates or grid distortion
    GROUP 7. Variables stored, solved & named
    £
    £ whole field solution for pressure
    £
SOLUTN(P1,Y,Y,Y,N,N,N)
SOLUTN(U1,Y,Y,N,N,N,N)
SOLUTN(V1,Y,Y,N,N,N,N)
SOLUTN(W1,Y,Y,N,N,N,N)


SOLUTN(C1,Y,Y,N,N,N,N)
    £
    GROUP 8. Terms (in differential equations) & devices
    £
TERMS(P1,Y,Y,Y,Y,Y,N)
TERMS(U1,Y,Y,Y,Y,Y,N)
TERMS(V1,Y,Y,Y,Y,Y,N)
TERMS(W1,Y,Y,Y,Y,Y,N)
TERMS(C1,Y,Y,Y,Y,Y,N)
    £
    GROUP 9. Properties of the medium (or media)
    £
TURMOD(KEMODL)
    £
    £ constant water density
    £
RHO1=1000.0
    £
    £ laminar viscosity at 15 deg. celsius
    £
ENUL=1.2E-6
    £
    GROUP 10. Inter-phase-transfer processes and properties
    GROUP 11. Initialization of variable or porosity fields
    £
    RESTRT(ALL)
    £
```

```
    GROUP 12. Convection and diffusion adjustments
    GROUP 13. Boundary conditions and special sources
    £
    £ no cyclic boundary conditions
    £
XCYCLE=F
    £
    £   injector
    £   --------
    £
    £ define initial KE and EP settings
    £
REAL(V1AVER,TKEIN,EPSIN,FLUX)
FLUX=1.0E-5
V1AVER=6.0
TKEIN=0.0045*V1AVER**2.0
EPSIN=(0.1643*TKEIN**1.5)/(0.09*ZNDIAM)
    £
FIINIT(KE)=TKEIN


FIINIT(EP)=EPSIN
    £
    £ define kinetic energy and dissipation rate at each cell
    £ of inlet patch using the cell velocity as velocity scale
    £ and the nozzle diameter (ZNDIAM) as length scale
    £
REAL(TKIN8,TKIN9,TKIN10,TKIN11,TKIN12,TKIN13,TKIN14,TKIN15)
REAL(TKIN16,TKIN17)
REAL(EPIN8,EPIN9,EPIN10,EPIN11,EPIN12,EPIN13,EPIN14,EPIN15)
REAL(EPIN16,EPIN17)
    £
TKIN8=0.0045*0.9947**2.0
EPIN8=(0.1643*TKIN8**1.5)/(0.09*ZNDIAM)
    £
TKIN9=0.0045*2.8264**2.0
EPIN9=(0.1643*TKIN9**1.5)/(0.09*ZNDIAM)
    £
TKIN10=0.0045*4.4335**2.0
EPIN10=(0.1643*TKIN10**1.5)/(0.09*ZNDIAM)
    £
TKIN11=0.0045*5.7652**2.0
EPIN11=(0.1643*TKIN11**1.5)/(0.09*ZNDIAM)
    £
TKIN12=0.0045*6.9886**2.0
EPIN12=(0.1643*TKIN12**1.5)/(0.09*ZNDIAM)
    £
TKIN13=0.0045*8.004**2.0
EPIN13=(0.1643*TKIN13**1.5)/(0.09*ZNDIAM)
    £
TKIN14=0.0045*8.765**2.0
EPIN14=(0.1643*TKIN14**1.5)/(0.09*ZNDIAM)
    £
TKIN15=0.0045*9.3723**2.0
EPIN15=(0.1643*TKIN15**1.5)/(0.09*ZNDIAM)
    £
TKIN16=0.0045*9.779**2.0
EPIN16=(0.1643*TKIN16**1.5)/(0.09*ZNDIAM)
    £
TKIN17=0.0045*9.9783**2.0
EPIN17=(0.1643*TKIN17**1.5)/(0.09*ZNDIAM)
    £
    £ define flowrates in individual inlet cells
    £
REAL(FLRT8,FLRT9,FLRT10,FLRT11,FLRT12,FLRT13,FLRT14)
REAL(FLRT15,FLRT16,FLRT17)
    £


FLRT8=RHO1*0.9947
FLRT9=RHO1*2.8264
FLRT10=RHO1*4.4335
FLRT11=RHO1*5.7652
FLRT12=RHO1*6.9886
FLRT13=RHO1*8.004
FLRT14=RHO1*8.765
FLRT15=RHO1*9.3723
FLRT16=RHO1*9.779
FLRT17=RHO1*9.9783
    £
```

```
    £ define ten nozzle patches and decompose inlet velocity
    £ vector into radial (V1) and circumferential (U1) component
    £ in each cell, PATCH 8 corresponds to nozzle edge, PATCH 17
    £ to the centreline, parabolic velocity profile
    £
PATCH(NOZ8,SOUTH,8,8,1,1,NOZF,NOZL,1,LSTEP)
COVAL(NOZ8,P1,FLUX,FLRT8/FLUX)
COVAL(NOZ8,V1,ONLYMS,0.9836)
COVAL(NOZ8,U1,ONLYMS,0.1481)
COVAL(NOZ8,KE,ONLYMS,TKIN8)
COVAL(NOZ8,EP,ONLYMS,EPIN8)
COVAL(NOZ8,C1,ONLYMS,1.0)
    £
PATCH(NOZ9,SOUTH,9,9,1,1,NOZF,NOZL,1,LSTEP)
COVAL(NOZ9,P1,FLUX,FLRT9/FLUX)
COVAL(NOZ9,V1,ONLYMS,2.8013)
COVAL(NOZ9,U1,ONLYMS,0.3758)
COVAL(NOZ9,KE,ONLYMS,TKIN9)
COVAL(NOZ9,EP,ONLYMS,EPIN9)
COVAL(NOZ9,C1,ONLYMS,1.0)
    £
PATCH(NOZ10,SOUTH,10,10,1,1,NOZF,NOZL,1,LSTEP)
COVAL(NOZ10,P1,FLUX,FLRT10/FLUX)
COVAL(NOZ10,V1,ONLYMS,4.403)
COVAL(NOZ10,U1,ONLYMS,0.5196)
COVAL(NOZ10,KE,ONLYMS,TKIN10)
COVAL(NOZ10,EP,ONLYMS,EPIN10)
COVAL(NOZ10,C1,ONLYMS,1.0)
    £
PATCH(NOZ11,SOUTH,11,11,1,1,NOZF,NOZL,1,LSTEP)
COVAL(NOZ11,P1,FLUX,FLRT11/FLUX)
COVAL(NOZ11,V1,ONLYMS,5.735)
COVAL(NOZ11,U1,ONLYMS,0.5896)
COVAL(NOZ11,KE,ONLYMS,TKIN11)
COVAL(NOZ11,EP,ONLYMS,EPIN11)


COVAL(NOZ11,C1,ONLYMS,1.0)
    £
PATCH(NOZ12,SOUTH,12,12,1,1,NOZF,NOZL,1,LSTEP)
COVAL(NOZ12,P1,FLUX,FLRT12/FLUX)
COVAL(NOZ12,V1,ONLYMS,6.9626)
COVAL(NOZ12,U1,ONLYMS,0.603)
COVAL(NOZ12,KE,ONLYMS,TKIN12)
COVAL(NOZ12,EP,ONLYMS,EPIN12)
COVAL(NOZ12,C1,ONLYMS,1.0)
    £
PATCH(NOZ13,SOUTH,13,13,1,1,NOZF,NOZL,1,LSTEP)
COVAL(NOZ13,P1,FLUX,FLRT13/FLUX)
COVAL(NOZ13,V1,ONLYMS,7.9842)
COVAL(NOZ13,U1,ONLYMS,0.5625)
COVAL(NOZ13,KE,ONLYMS,TKIN13)
COVAL(NOZ13,EP,ONLYMS,EPIN13)
COVAL(NOZ13,C1,ONLYMS,1.0)
    £
PATCH(NOZ14,SOUTH,14,14,1,1,NOZF,NOZL,1,LSTEP)
COVAL(NOZ14,P1,FLUX,FLRT14/FLUX)
COVAL(NOZ14,V1,ONLYMS,8.7516)
COVAL(NOZ14,U1,ONLYMS,0.4847)
COVAL(NOZ14,KE,ONLYMS,TKIN14)
COVAL(NOZ14,EP,ONLYMS,EPIN14)
COVAL(NOZ14,C1,ONLYMS,1.0)
    £
PATCH(NOZ15,SOUTH,15,15,1,1,NOZF,NOZL,1,LSTEP)
COVAL(NOZ15,P1,FLUX,FLRT15/FLUX)
COVAL(NOZ15,V1,ONLYMS,9.365)
COVAL(NOZ15,U1,ONLYMS,0.3696)
COVAL(NOZ15,KE,ONLYMS,TKIN15)
COVAL(NOZ15,EP,ONLYMS,EPIN15)
COVAL(NOZ15,C1,ONLYMS,1.0)
    £
PATCH(NOZ16,SOUTH,16,16,1,1,NOZF,NOZL,1,LSTEP)
COVAL(NOZ16,P1,FLUX,FLRT16/FLUX)
COVAL(NOZ16,V1,ONLYMS,9.777)
COVAL(NOZ16,U1,ONLYMS,0.2287)
COVAL(NOZ16,KE,ONLYMS,TKIN16)
COVAL(NOZ16,EP,ONLYMS,EPIN16)
COVAL(NOZ16,C1,ONLYMS,1.0)
    £
```

```
PATCH(NOZ17,SOUTH,17,17,1,1,NOZF,NOZL,1,LSTEP)
COVAL(NOZ17,P1,FLUX,FLRT17/FLUX)
COVAL(NOZ17,V1,ONLYMS,9.9781)
COVAL(NOZ17,U1,ONLYMS,0.0731)


COVAL(NOZ17,KE,ONLYMS,TKIN17)
COVAL(NOZ17,EP,ONLYMS,EPIN17)
COVAL(NOZ17,C1,ONLYMS,1.0)
    £
    £    quadrantside at IX=1
    £    ---------------------
    £
PATCH(SIDEX1,WEST,1,1,1,NY,1,NZ,1,LSTEP)
COVAL(SIDEX1,P1,FIXP,0.0)
COVAL(SIDEX1,KE,ONLYMS,SAME)
COVAL(SIDEX1,EP,ONLYMS,SAME)
    £
    £    tank wall at IY = NY
    £    --------------------
    £
PATCH(TWALL,NWALL,1,NX,NY,NY,1,NZ,1,LSTEP)
COVAL(TWALL,U1,GRND2,0.0)
COVAL(TWALL,W1,GRND2,0.0)
COVAL(TWALL,KE,GRND2,GRND2)
COVAL(TWALL,EP,GRND2,GRND2)
    £
    £    tank floor at IY = 1
    £    --------------------
    £
PATCH(BWALL,LWALL,1,NX,1,NY,1,1,1,LSTEP)
COVAL(BWALL,U1,GRND2,0.0)
COVAL(BWALL,V1,GRND2,0.0)
COVAL(BWALL,KE,GRND2,GRND2)
COVAL(BWALL,EP,GRND2,GRND2)
    £
    GROUP 14. Downstream pressure for PARAB=.TRUE.
    GROUP 15. Termination of sweeps
    £
LSWEEP=250
    £
    GROUP 16. Termination of iterations
    GROUP 17. Under-relaxation devices
    £
RELAX(P1,LINRLX,0.5)
RELAX(U1,FALSDT,0.001)
RELAX(V1,FALSDT,0.001)
RELAX(W1,FALSDT,0.001)
RELAX(KE,FALSDT,0.001)
RELAX(EP,FALSDT,0.001)
RELAX(C1,FALSDT,0.001)
    £


    GROUP 18. Limits on variables or increments to them
    GROUP 19. Data communicated by satellite to GROUND
    £
IG(1)=NOZF;IG(2)=NOZL
RG(1)=ZNDIAM
    £
    GROUP 20. Preliminary print-out
    GROUP 21. Print-out of variables
    £
OUTPUT(P1,Y,N,N,Y,N,Y)
OUTPUT(U1,Y,N,N,Y,N,Y)
OUTPUT(V1,Y,N,N,Y,N,Y)
OUTPUT(C1,Y,N,N,N,N,N)
    £
    GROUP 22. Spot-value print-out
    GROUP 23. Field print-out and plot control
    £
IPROF=3
ISTPRF=1;ISTPRL=LSTEP;NTPRIN=1
NXPRIN=1;IXPRF=NX;IXPRL=NX
NYPRIN=1;IYPRF=1;IYPRL=NY
NZPRIN=1;IZPRF=NZ;IZPRL=NZ
ITABL=0
```

```
    £
    £ V1 vs time profile at r = 72 mm (IY=29)
    £
PATCH(V1PRO1,PROFIL,NX,NX,29,29,NZ,NZ,1,LSTEP)
PLOT(V1PRO1,V1,0.0,0.0)
PLOT(V1PRO1,C1,0.0,0.0)
    £
    £ V1 vs time profile at r = 117 mm (IY=32)
    £
PATCH(V1PRO2,PROFIL,NX,NX,32,32,NZ,NZ,1,LSTEP)
PLOT(V1PRO2,V1,0.0,0.0)
PLOT(V1PRO2,C1,0.0,0.0)
    £
    £ V1 vs time profile at r = 165 mm (IY=34)
    £
PATCH(V1PRO3,PROFIL,NX,NX,34,34,NZ,NZ,1,LSTEP)
PLOT(V1PRO3,V1,0.0,0.0)
PLOT(V1PRO3,C1,0.0,0.0)
    £
    £ V1 vs time profile at r = 215 mm (IY=36)
    £
PATCH(V1PRO4,PROFIL,NX,NX,36,36,NZ,NZ,1,LSTEP)
PLOT(V1PRO4,V1,0.0,0.0)
PLOT(V1PRO4,C1,0.0,0.0)
    £
    £ V1 vs time profile at r = 249 mm (IY=38)
    £
PATCH(V1PRO5,PROFIL,NX,NX,38,38,NZ,NZ,1,LSTEP)
PLOT(V1PRO5,V1,0.0,0.0)
PLOT(V1PRO5,C1,0.0,0.0)
    £
    GROUP 24. Dumps for restarts
STOP
```

B2: 'Ground' coding for transient undeflected jet

```
C---  GROUP 19. Special calls to GROUND from EARTH
C
   19 GO TO (191,192,193,194,195,196,197,198),ISC
  191 CONTINUE
C   * ------------------- SECTION 1 ---- START OF TIME STEP.
      RETURN
  192 CONTINUE
C   * ------------------- SECTION 2 ---- START OF SWEEP.
      RETURN
  193 CONTINUE
C   * ------------------- SECTION 3 ---- START OF IZ SLAB.
      RETURN
  194 CONTINUE
C   * ------------------- SECTION 4 ---- START OF ITERATION.
      RETURN
  195 CONTINUE
C   * ------------------- SECTION 5 ---- FINISH OF ITERATION.
      RETURN
  196 CONTINUE
C   * ------------------- SECTION 6 ---- FINISH OF IZ SLAB.
C
C-----NORMALISED JET PROPERTY PRINTOUT AT FINAL SWEEP
C     ------------------------------------------------


C
      IF(ISWEEP.NE.LSWEEP-1) RETURN
C
      NOZF=IG(1)
      NOZL=IG(2)
C
      IF(IZSTEP.NE.NOZL) RETURN
C
      IF(G19FST) THEN
         OPEN(25,FILE='JTPROF.RES',STATUS='UNKNOWN')
         G19FST=.FALSE.
      ENDIF
C
C-----CONSTANTS
C
      DJET=RG(1)*2.0
      VJET=10.0
      NXCLIN=17
C
C-----GET GEOMETRIC AND FLOW QUANTITIES
C     ---------------------------------
C
      CALL GETZ(ZWNZ,GZG,NZM)
      CALL GETYX(YV2D,GYN,NYM,NXM)
      CALL GETYX(YG2D,GYC,NYM,NXM)
      CALL GETYX(XG2D,GXG,NYM,NXM)
      CALL GETYX(V1,GV1,NYM,NXM)
      CALL GETYX(12,GKE,NYM,NXM)
      CALL GETYX(13,GEP,NYM,NXM)
C
      DO 1961 IY=1,NY
C
C-----DIMENSIONLESS JET QUANTITIES
C     ----------------------------
C
      YNORTH=(GYN(IY,NXCLIN))/DJET
      YCENTRE=(GYC(IY,NXCLIN))/DJET
      YCEN=GYC(IY,NXCLIN)
      VCLIN=GV1(IY,NXCLIN)
      VCLIN3=VCLIN*VCLIN*VCLIN
      VFREE=0.01*VCLIN
      VEDV=VCLIN/VJET
      TKECL=GKE(IY,NXCLIN)
```

```
C-----JET HALF WIDTH (WEST SIDE OF JET CENTRELINE)

C     ------------------------------------------
C
      VHLF=VFREE+0.5*(GV1(IY,NXCLIN)-VFREE)
C
      DO 1962 IX=1,NXCLIN-1
         VELPW=GV1(IY,IX)
         VELEW=GV1(IY,IX+1)
         XPW=GXG(IY,IX)
         XEW=GXG(IY,IX+1)
      IF(VHLF.GE.VELPW.AND.VHLF.LE.VELEW) GO TO 1963
         GO TO 1962
 1963 XRAT=(VHLF-VELPW)/(VELEW-VELPW+1.0E-10)
C
C     JET CENTRELINE AT PI/4 = 0.785398 RAD
C
      XWIDTH=0.785398-(XPW+XRAT*(XEW-XPW))
      XWEST=XWIDTH*GYN(IY,NXCLIN)/DJET
C
      GO TO 1964
 1962 CONTINUE
 1964 CONTINUE
C
C-----TABULAR PRINTOUT
C     ----------------
C
      IWRIT=IWRIT+1
      IF(IWRIT.EQ.1) WRITE(25,501)
      WRITE(25,502) IY,YNORTH,YCENTRE,VEDV,XWEST,TKECL
C
C-----FORMAT STATEMENTS
C
  501 FORMAT(/3X,'IY',4X,'Y/D(N)',6X,'Y/D(C)',6X,'VCL/V11N',5X,'0.5 X/D',
     &       5X,'KE')
C
  502 FORMAT(1X,I4,5(1X,1PE11.3))
C
C-----V1 VELOCITY PROFILES AT DISCRETE IY LOCATIONS
C     ---------------------------------------------
C
C-----FIRST PROFILE AT IY = 29 (R = 72 mm)
C
      IF(IY.NE.29) GO TO 2961
C
      IF(G19SCND) THEN
         OPEN(29,FILE='Y29',STATUS='UNKNOWN')
         G19SCND=.FALSE.


      ENDIF
C
      DO 1965 IX=NXCLIN,1,-1
         ANG29=0.785398-GXG(IY,IX)
         RAD29=ANG29*GYN(IY,NXCLIN)
         ETA29=RAD29/(XWEST*DJET)
         Y29V1=GV1(IY,IX)
         Y29KE=GKE(IY,IX)
         Y29EP=GEP(IY,IX)
         Y29EPN=Y29EP*YCEN/VCLIN3
C
C    --TABULAR PRINTOUT
C
      IWRIT2=IWRIT2+1
      IF(IWRIT2.EQ.1) WRITE(29,504)
      WRITE (29,505) IY,IX,Y29V1,Y29KE,ETA29,Y29EPN,ANG29
C
 1965 CONTINUE
C
 2961 CONTINUE
C
```

B3: Output in r - θ plane bisecting the nozzle exit

IY	Y/D(N)	Y/D(C)	VCL/V1IN	0.5 X/D	KE
1	6.666E-02	3.333E-02	9.945E-01	7.204E-03	3.848E+01
2	1.333E-01	9.999E-02	9.891E-01	1.420E-02	3.349E+01
3	2.000E-01	1.667E-01	9.826E-01	2.111E-02	2.948E+01
4	2.667E-01	2.333E-01	9.754E-01	2.799E-02	2.621E+01
5	3.333E-01	3.000E-01	9.680E-01	3.484E-02	2.349E+01
6	4.000E-01	3.667E-01	9.607E-01	4.169E-02	2.122E+01
7	4.667E-01	4.333E-01	9.534E-01	4.855E-02	1.929E+01
8	5.333E-01	5.000E-01	9.461E-01	5.541E-02	1.764E+01
9	6.000E-01	5.667E-01	9.390E-01	6.228E-02	1.621E+01
10	6.667E-01	6.333E-01	9.319E-01	6.916E-02	1.497E+01
11	7.333E-01	7.000E-01	9.248E-01	7.606E-02	1.389E+01
12	8.000E-01	7.667E-01	9.180E-01	8.297E-02	1.294E+01
13	8.667E-01	8.333E-01	9.113E-01	8.989E-02	1.209E+01
14	1.067E+00	9.667E-01	8.918E-01	1.105E-01	1.020E+01
15	1.267E+00	1.167E+00	8.738E-01	1.311E-01	8.760E+00
16	1.467E+00	1.367E+00	8.566E-01	1.516E-01	7.638E+00
17	1.667E+00	1.567E+00	8.398E-01	1.721E-01	6.746E+00
18	1.867E+00	1.767E+00	8.228E-01	1.928E-01	6.025E+00
19	2.067E+00	1.967E+00	8.055E-01	2.137E-01	5.434E+00
20	2.467E+00	2.267E+00	7.751E-01	2.550E-01	4.580E+00
21	2.867E+00	2.667E+00	7.470E-01	2.964E-01	3.945E+00
22	3.267E+00	3.067E+00	7.192E-01	3.385E-01	3.459E+00

21	2.867E+00	2.667E+00	7.470E-01	2.964E-01	3.945E+00
22	3.267E+00	3.067E+00	7.192E-01	3.385E-01	3.459E+00
23	3.667E+00	3.467E+00	6.892E-01	3.817E-01	3.080E+00
24	4.333E+00	4.000E+00	6.483E-01	4.534E-01	2.628E+00
25	5.000E+00	4.667E+00	6.091E-01	5.274E-01	2.288E+00
26	5.667E+00	5.333E+00	5.619E-01	6.066E-01	2.021E+00
27	7.067E+00	6.367E+00	4.957E-01	7.690E-01	1.621E+00
28	8.867E+00	7.967E+00	4.312E-01	9.817E-01	1.257E+00
29	1.107E+01	9.967E+00	3.718E-01	1.246E+00	9.499E-01
30	1.367E+01	1.237E+01	3.219E-01	1.562E+00	7.067E-01
31	1.629E+01	1.498E+01	2.779E-01	1.888E+00	5.369E-01
32	1.989E+01	1.809E+01	2.362E-01	2.322E+00	3.856E-01
33	2.449E+01	2.219E+01	2.003E-01	2.850E+00	2.680E-01
34	2.989E+01	2.719E+01	1.720E-01	3.431E+00	1.868E-01
35	3.529E+01	3.259E+01	1.516E-01	3.972E+00	1.373E-01
36	3.989E+01	3.759E+01	1.371E-01	4.406E+00	1.086E-01
37	4.389E+01	4.189E+01	1.248E-01	4.810E+00	8.988E-02
38	4.669E+01	4.529E+01	1.108E-01	5.176E+00	7.907E-02
39	4.869E+01	4.769E+01	9.155E-02	5.514E+00	7.381E-02
40	5.009E+01	4.939E+01	6.790E-02	5.792E+00	7.664E-02
41	5.109E+01	5.059E+01	4.166E-02	5.969E+00	9.696E-02
42	5.169E+01	5.139E+01	1.922E-02	5.993E+00	1.348E-01
43	5.209E+01	5.189E+01	0.000E+00	3.764E+01	5.293E-04

B4: Output at constant radius

IY	IX	V1	KE	ETA	EP-NORM	R/Y
29	17	3.718E+00	9.499E-01	6.976E-02	1.543E-01	7.855E-03
29	16	3.597E+00	9.531E-01	2.093E-01	1.542E-01	2.356E-02
29	15	3.375E+00	9.587E-01	3.488E-01	1.542E-01	3.927E-02
29	14	3.084E+00	9.480E-01	4.883E-01	1.493E-01	5.498E-02
29	13	2.757E+00	9.110E-01	6.278E-01	1.377E-01	7.069E-02
29	12	2.418E+00	8.475E-01	7.673E-01	1.203E-01	8.640E-02
29	11	2.087E+00	7.637E-01	9.068E-01	9.998E-02	1.021E-01
29	10	1.773E+00	6.682E-01	1.046E+00	7.936E-02	1.178E-01
29	9	1.485E+00	5.690E-01	1.186E+00	6.046E-02	1.335E-01
29	8	1.224E+00	4.725E-01	1.325E+00	4.435E-02	1.492E-01
29	7	9.255E-01	3.576E-01	1.507E+00	2.786E-02	1.696E-01
29	6	5.605E-01	2.168E-01	1.785E+00	1.211E-02	2.010E-01
29	5	2.127E-01	9.352E-02	2.204E+00	2.842E-03	2.481E-01
29	4	2.247E-02	4.267E-02	2.817E+00	5.366E-04	3.172E-01
29	3	-3.515E-02	6.077E-02	3.738E+00	8.980E-04	4.209E-01
29	2	-4.651E-02	2.324E-01	5.077E+00	5.751E-03	5.717E-01
29	1	-4.966E-02	9.407E-01	6.417E+00	4.000E-02	7.225E-01

Appendix C

C1: 'Q1' input file for two consecutive runs: (i) generation of swirling flow field and (ii) transient injection

```
 TALK=T;RUN( 1, 2);VDU=DUM-TERM
    GROUP 1. Run title and other preliminaries
    £
TEXT(CONSTANT DENSITY JET ISSUING INTO A TANK)
    £
    GROUP 2. Transience; time-step specification
    £
NOWIPE=T
    £
    GROUP 3. X-direction grid specification
    £
    £ POLAR GRID  ( 360 deg.)
    £
CARTES=F
    £
NX=56
REAL(ALPNOZ)
INTEGER(NXNOZ,NXCLIN)
    £
    £ ALPNOZ is the nozzle exit angle corresponding to a
    £         nozzle width of 5 mm
    £
ALPNOZ=0.31415


NXNOZ=18
    £
XULAST=3.14159*2.0
    £
    £ define variable names for First and Last nozzle
    £ cells in x-direction
    £
INTEGER(NXNOZF,NXNOZL)
    £
NXNOZF=8;NXNOZL=25
NXCLIN=16
    £
XFRAC(1)=-3;XFRAC(2)=0.3666/(-XFRAC(1)*XULAST)
XFRAC(3)=1;XFRAC(4)=0.10472/(XFRAC(3)*XULAST)
XFRAC(5)=1;XFRAC(6)=0.06981/(XFRAC(5)*XULAST)
XFRAC(7)=1;XFRAC(8)=0.05236/(XFRAC(7)*XULAST)
XFRAC(9)=1;XFRAC(10)=0.03491/(XFRAC(9)*XULAST)
XFRAC(11)=NXNOZ;XFRAC(12)=ALPNOZ/(XFRAC(11)*XULAST)
XFRAC(13)=3;XFRAC(14)=0.052359/(XFRAC(13)*XULAST)
XFRAC(15)=9;XFRAC(16)=0.31419/(XFRAC(15)*XULAST)
XFRAC(17)=5;XFRAC(18)=0.2618/(XFRAC(17)*XULAST)
XFRAC(19)=1;XFRAC(20)=0.06981/(XFRAC(19)*XULAST)
XFRAC(21)=1;XFRAC(22)=0.087266/(XFRAC(21)*XULAST)
XFRAC(23)=1;XFRAC(24)=0.13963/(XFRAC(23)*XULAST)
XFRAC(25)=1;XFRAC(26)=0.19199/(XFRAC(25)*XULAST)
XFRAC(27)=1;XFRAC(28)=0.29671/(XFRAC(27)*XULAST)
XFRAC(29)=1;XFRAC(30)=0.43633/(XFRAC(29)*XULAST)
XFRAC(31)=1;XFRAC(32)=0.5236/(XFRAC(31)*XULAST)
XFRAC(33)=2;XFRAC(34)=1.22174/(XFRAC(33)*XULAST)
XFRAC(35)=1;XFRAC(36)=0.5236/(XFRAC(35)*XULAST)
XFRAC(37)=1;XFRAC(38)=0.43633/(XFRAC(37)*XULAST)
XFRAC(39)=1;XFRAC(40)=0.34907/(XFRAC(39)*XULAST)
XFRAC(41)=1;XFRAC(42)=0.2618/(XFRAC(41)*XULAST)
XFRAC(43)=1;XFRAC(44)=0.17453/(XFRAC(43)*XULAST)
    £
    GROUP 4. Y-direction grid specification
    £
NY=43
INTEGER(NYINJ,NYNOZ)
REAL(YINCOL,YNOZ)
NYINJ=1;NYNOZ=1
YINCOL=15.9E-3;YNOZ=0.3333E-3
YVLAST=276.E-3
```

```
RINNER=YINCOL-YNOZ
    £


YFRAC(1)=-1;YFRAC(2)=YNOZ/(-YFRAC(1)*YVLAST)
YFRAC(3)=12;YFRAC(4)=4.E-3/(YFRAC(3)*YVLAST)
YFRAC(5)=6;YFRAC(6)=6.E-3/(YFRAC(5)*YVLAST)
YFRAC(7)=4;YFRAC(8)=8.E-3/(YFRAC(7)*YVLAST)
YFRAC(9)=3;YFRAC(10)=10.E-3/(YFRAC(9)*YVLAST)
YFRAC(11)=1;YFRAC(12)=7.E-3/(YFRAC(11)*YVLAST)
YFRAC(13)=1;YFRAC(14)=9.E-3/(YFRAC(13)*YVLAST)
YFRAC(15)=1;YFRAC(16)=11.E-3/(YFRAC(15)*YVLAST)
YFRAC(17)=1;YFRAC(18)=13.E-3/(YFRAC(17)*YVLAST)
YFRAC(19)=1;YFRAC(20)=13.1E-3/(YFRAC(19)*YVLAST)
YFRAC(21)=1;YFRAC(22)=18.E-3/(YFRAC(21)*YVLAST)
YFRAC(23)=1;YFRAC(24)=23.E-3/(YFRAC(23)*YVLAST)
YFRAC(25)=2;YFRAC(26)=54.E-3/(YFRAC(25)*YVLAST)
YFRAC(27)=1;YFRAC(28)=23.E-3/(YFRAC(27)*YVLAST)
YFRAC(29)=1;YFRAC(30)=20.E-3/(YFRAC(29)*YVLAST)
YFRAC(31)=1;YFRAC(32)=14.E-3/(YFRAC(31)*YVLAST)
YFRAC(33)=1;YFRAC(34)=10.E-3/(YFRAC(33)*YVLAST)
YFRAC(35)=1;YFRAC(36)=7.E-3/(YFRAC(35)*YVLAST)
YFRAC(37)=1;YFRAC(38)=5.E-3/(YFRAC(37)*YVLAST)
YFRAC(39)=1;YFRAC(40)=3.E-3/(YFRAC(39)*YVLAST)
YFRAC(41)=1;YFRAC(42)=2.E-3/(YFRAC(41)*YVLAST)

    GROUP 5. Z-direction grid specification
INTEGER(NOZF,NOZL)
NOZF=14
NOZL=18
    £
REAL(ZNDIAM)
ZNDIAM=2.5E-3
    £
NZ=18
ZWLAST=72.5E-3
    £
ZFRAC(1)=-1;ZFRAC(2)=1.E-3/(-ZFRAC(1)*ZWLAST)
ZFRAC(3)=1;ZFRAC(4)=2.E-3/(ZFRAC(3)*ZWLAST)
ZFRAC(5)=1;ZFRAC(6)=5.E-3/(ZFRAC(5)*ZWLAST)
ZFRAC(7)=7;ZFRAC(8)=55.E-3/(ZFRAC(7)*ZWLAST)
ZFRAC(9)=1;ZFRAC(10)=4.E-3/(ZFRAC(9)*ZWLAST)
ZFRAC(11)=1;ZFRAC(12)=2.E-3/(ZFRAC(11)*ZWLAST)
ZFRAC(13)=1;ZFRAC(14)=1.E-3/(ZFRAC(13)*ZWLAST)
ZFRAC(15)=5;ZFRAC(16)=ZNDIAM/(ZFRAC(15)*ZWLAST)
    £
    GROUP 6. Body-fitted coordinates or grid distortion
    GROUP 7. Variables stored, solved & named
    £
    £ whole field solution for pressure


SOLUTN(P1,Y,Y,Y,N,N,N)
SOLUTN(U1,Y,Y,N,N,N,N)
SOLUTN(V1,Y,Y,N,N,N,N)
SOLUTN(W1,Y,Y,N,N,N,N)
    £
STORE(OMEGA)
STORE(VORT)
STORE(VECT)
STORE(TINT)
    £
    GROUP 8. Terms (in differential equations) & devices
    £
TERMS(P1,Y,Y,Y,N,Y,N)
TERMS(U1,Y,Y,Y,N,Y,N)
TERMS(V1,Y,Y,Y,N,Y,N)
TERMS(W1,Y,Y,Y,N,Y,N)
    £
    GROUP 9. Properties of the medium (or media)
    £
TURMOD(KEMODL)
    £
    £ constant water density
    £
```

```
RHO1=1000.0
    £
    £ laminar viscosity at 15 deg. celsius
    £
ENUL=1.2E-6
    £
    GROUP 10. Inter-phase-transfer processes and properties
    GROUP 11. Initialization of variable or porosity fields
    £
    £ initialize solid body rotation
    £
FIINIT(U1)=5.236
IURINI=-1
    £
    GROUP 12. Convection and diffusion adjustments
    GROUP 13. Boundary conditions and special sources
    £
    £ cyclic boundary conditions
    £
XCYCLE=T
    £
    £  moving walls to generate swirling field
    £


PATCH(ROTATUDR,NORTH,1,NX,NY,NY,1,NZ,1,1)
COVAL(ROTATUDR,U1,ONLYMS,5.236)
    £
PATCH(BOTTOUDR,LOW,1,NX,1,NY,1,1,1,1)
COVAL(BOTTOUDR,U1,ONLYMS,5.236)
    £
    £ pressure - relief condition
    £
PATCH(PRELIEF,HIGH,51,51,30,30,NZ,NZ,1,1)
COVAL(PRELIEF,P1,FIXP,0.0)
    £
    GROUP 14. Downstream pressure for PARAB=.TRUE.
    GROUP 15. Termination of sweeps
    £
LSWEEP=100
    £
    GROUP 16. Termination of iterations
    GROUP 17. Under-relaxation devices
    £
RELAX(P1,LINRLX,0.5)
RELAX(U1,FALSDT,0.0001)
RELAX(V1,FALSDT,0.0001)
RELAX(W1,FALSDT,0.0001)
RELAX(KE,FALSDT,0.0001)
RELAX(EP,FALSDT,0.0001)
    £
    GROUP 18. Limits on variables or increments to them
    GROUP 19. Data communicated by satellite to GROUND
    GROUP 20. Preliminary print-out
    GROUP 21. Print-out of variables
    £
IURPRN=-1
    £
OUTPUT(P1,Y,N,N,Y,N,Y)
OUTPUT(U1,Y,N,N,Y,N,Y)
    £
    GROUP 22. Spot-value print-out
    £
    GROUP 23. Field print-out and plot control
    £
NXPRIN=1;IXPRF=16;IXPRL=16
NYPRIN=1;IYPRF=1;IYPRL=NY
NZPRIN=1;IZPRF=NZ;IZPRL=NZ
IPLTF=1;IPLTL=LSWEEP;NPLT=1
ITABL=3
    £


    GROUP 24. Dumps for restarts
    £
STOP
```

```
TEXT(INJECTION INTO SWIRLING FIELD)
    £
STEADY=F
    £
TFIRST=0.0
TLAST=1.0
LSTEP=3
    £
TFRAC(1)=-3;TFRAC(2)=0.004
    £
SOLUTN(C1,Y,Y,N,N,N,N)
    £
TERMS(C1,Y,Y,Y,Y,Y,N)
TERMS(U1,Y,Y,Y,Y,Y,N)
TERMS(V1,Y,Y,Y,Y,Y,N)
TERMS(W1,Y,Y,Y,Y,Y,N)
TERMS(P1,Y,Y,Y,Y,Y,N)
    £
RELAX(C1,FALSDT,0.001)
OUTPUT(C1,Y,N,N,Y,N,Y)
    £
    £ stop moving walls
    £
PATCH(ROTATUDR,NORTH,1,NX,NY,NY,1,NZ,1,1)
COVAL(ROTATUDR,U1,ONLYMS,0.001)
    £
PATCH(BOTTOUDR,LOW,1,NX,1,NY,1,1,1,1)
COVAL(BOTTOUDR,U1,ONLYMS,0.001)
    £
REAL(FLUX)
FLUX=1.0E-5
    £
    £ define flowrates and turbulence of incoming flow
    £ for each individual cell assuming parabolic vel. profile
    £
REAL(TKE8,TKE9,TKE10,TKE11,TKE12,TKE13,TKE14,TKE15,TKE16)
REAL(TKE17,TKE18,TKE19,TKE20,TKE21,TKE22,TKE23,TKE24,TKE25)
    £
REAL(EPS8,EPS9,EPS10,EPS11,EPS12,EPS13,EPS14,EPS15,EPS16)
REAL(EPS17,EPS18,EPS19,EPS20,EPS21,EPS22,EPS23,EPS24,EPS25)
    £
TKE8=0.0045*1.1205**2.0


TKE10=0.0045*4.8075**2.0
TKE11=0.0045*6.2823**2.0
TKE12=0.0045*7.5113**2.0
TKE13=0.0045*8.4945**2.0
TKE14=0.0045*9.2319**2.0
TKE15=0.0045*9.723**2.0
TKE16=0.0045*9.969**2.0
TKE17=TKE16;TKE18=TKE15;TKE19=TKE14;TKE20=TKE13;TKE21=TKE12
TKE22=TKE11;TKE23=TKE10;TKE24=TKE9;TKE25=TKE8
    £
EPS8=(0.1642*TKE8**1.5)/(0.09*ZNDIAM)
EPS9=(0.1642*TKE9**1.5)/(0.09*ZNDIAM)
EPS10=(0.1642*TKE10**1.5)/(0.09*ZNDIAM)
EPS11=(0.1642*TKE11**1.5)/(0.09*ZNDIAM)
EPS12=(0.1642*TKE12**1.5)/(0.09*ZNDIAM)
EPS13=(0.1642*TKE13**1.5)/(0.09*ZNDIAM)
EPS14=(0.1642*TKE14**1.5)/(0.09*ZNDIAM)
EPS15=(0.1642*TKE15**1.5)/(0.09*ZNDIAM)
EPS16=(0.1642*TKE16**1.5)/(0.09*ZNDIAM)
EPS17=EPS16;EPS18=EPS15;EPS19=EPS14;EPS20=EPS13;EPS21=EPS12
EPS22=EPS11;EPS23=EPS10;EPS24=EPS9;EPS25=EPS8
    £
    £ injector
PATCH(NOZ8,SOUTH,8,8,1,1,NOZF,NOZL,1,LSTEP)
COVAL(NOZ8,P1,FLUX,RHO1*1.1205/FLUX)
COVAL(NOZ8,V1,ONLYMS,1.1082)
COVAL(NOZ8,U1,ONLYMS,0.16562)
COVAL(NOZ8,KE,ONLYMS,TKE8)
COVAL(NOZ8,EP,ONLYMS,EPS8)
COVAL(NOZ8,C1,ONLYMS,1.0)
    £
```

```
PATCH(NOZ9,SOUTH,9,9,1,1,NOZF,NOZL,1,LSTEP)
COVAL(NOZ9,P1,FLUX,RHO1*3.0869/FLUX)
COVAL(NOZ9,V1,ONLYMS,3.0605)
COVAL(NOZ9,U1,ONLYMS,0.40292)
COVAL(NOZ9,KE,ONLYMS,TKE9)
COVAL(NOZ9,EP,ONLYMS,EPS9)
COVAL(NOZ9,C1,ONLYMS,1.0)
    £
PATCH(NOZ10,SOUTH,10,10,1,1,NOZF,NOZL,1,LSTEP)
COVAL(NOZ10,P1,FLUX,RHO1*4.8075/FLUX)
COVAL(NOZ10,V1,ONLYMS,4.8075)
COVAL(NOZ10,U1,ONLYMS,0.5442)
COVAL(NOZ10,KE,ONLYMS,TKE10)
COVAL(NOZ10,EP,ONLYMS,EPS10)
COVAL(NOZ10,C1,ONLYMS,1.0)


PATCH(NOZ11,SOUTH,11,11,1,1,NOZF,NOZL,1,LSTEP)
COVAL(NOZ11,P1,FLUX,RHO1*6.2823/FLUX)
COVAL(NOZ11,V1,ONLYMS,6.2534)
COVAL(NOZ11,U1,ONLYMS,0.6021)
COVAL(NOZ11,KE,ONLYMS,TKE11)
COVAL(NOZ11,EP,ONLYMS,EPS11)
COVAL(NOZ11,C1,ONLYMS,1.0)
    £
PATCH(NOZ12,SOUTH,12,12,1,1,NOZF,NOZL,1,LSTEP)
COVAL(NOZ12,P1,FLUX,RHO1*7.5113/FLUX)
COVAL(NOZ12,V1,ONLYMS,7.5113)
COVAL(NOZ12,U1,ONLYMS,0.5893)
COVAL(NOZ12,KE,ONLYMS,TKE12)
COVAL(NOZ12,EP,ONLYMS,EPS12)
COVAL(NOZ12,C1,ONLYMS,1.0)
    £
PATCH(NOZ13,SOUTH,13,13,1,1,NOZF,NOZL,1,LSTEP)
COVAL(NOZ13,P1,FLUX,RHO1*8.4945/FLUX)
COVAL(NOZ13,V1,ONLYMS,8.4786)
COVAL(NOZ13,U1,ONLYMS,0.5186)
COVAL(NOZ13,KE,ONLYMS,TKE13)
COVAL(NOZ13,EP,ONLYMS,EPS13)
COVAL(NOZ13,C1,ONLYMS,1.0)
PATCH(NOZ14,SOUTH,14,14,1,1,NOZF,NOZL,1,LSTEP)
COVAL(NOZ14,P1,FLUX,RHO1*9.2319/FLUX)
COVAL(NOZ14,V1,ONLYMS,9.2231)
COVAL(NOZ14,U1,ONLYMS,0.4027)
COVAL(NOZ14,KE,ONLYMS,TKE14)
COVAL(NOZ14,EP,ONLYMS,EPS14)
COVAL(NOZ14,C1,ONLYMS,1.0)
    £
PATCH(NOZ15,SOUTH,15,15,1,1,NOZF,NOZL,1,LSTEP)
COVAL(NOZ15,P1,FLUX,RHO1*9.723/FLUX)
COVAL(NOZ15,V1,ONLYMS,9.72)
COVAL(NOZ15,U1,ONLYMS,0.2545)
COVAL(NOZ15,KE,ONLYMS,TKE15)
COVAL(NOZ15,EP,ONLYMS,EPS15)
COVAL(NOZ15,C1,ONLYMS,1.0)
    £
PATCH(NOZ16,SOUTH,16,16,1,1,NOZF,NOZL,1,LSTEP)
COVAL(NOZ16,P1,FLUX,RHO1*9.969/FLUX)
COVAL(NOZ16,V1,ONLYMS,9.9686)
COVAL(NOZ16,U1,ONLYMS,0.087)
COVAL(NOZ16,KE,ONLYMS,TKE16)
COVAL(NOZ16,EP,ONLYMS,EPS16)
COVAL(NOZ16,C1,ONLYMS,1.0)


PATCH(NOZ17,SOUTH,17,17,1,1,NOZF,NOZL,1,LSTEP)
COVAL(NOZ17,P1,FLUX,RHO1*9.969/FLUX)
COVAL(NOZ17,V1,ONLYMS,9.9686)
COVAL(NOZ17,U1,ONLYMS,-0.087)
COVAL(NOZ17,KE,ONLYMS,TKE17)
COVAL(NOZ17,EP,ONLYMS,EPS17)
COVAL(NOZ17,C1,ONLYMS,1.0)
    £
PATCH(NOZ18,SOUTH,18,18,1,1,NOZF,NOZL,1,LSTEP)
COVAL(NOZ18,P1,FLUX,RHO1*9.723/FLUX)
COVAL(NOZ18,V1,ONLYMS,9.72)
COVAL(NOZ18,U1,ONLYMS,-0.2545)
COVAL(NOZ18,KE,ONLYMS,TKE18)
COVAL(NOZ18,EP,ONLYMS,EPS18)
COVAL(NOZ18,C1,ONLYMS,1.0)
```

```
PATCH(NOZ19,SOUTH,19,19,1,1,NOZF,NOZL,1,LSTEP)
COVAL(NOZ19,P1,FLUX,RHO1*9.2319/FLUX)
COVAL(NOZ19,V1,ONLYMS,9.2231)
COVAL(NOZ19,U1,ONLYMS,-0.4027)
COVAL(NOZ19,KE,ONLYMS,TKE19)
COVAL(NOZ19,EP,ONLYMS,EPS19)
COVAL(NOZ19,C1,ONLYMS,1.0)

PATCH(NOZ20,SOUTH,20,20,1,1,NOZF,NOZL,1,LSTEP)
COVAL(NOZ20,P1,FLUX,RHO1*8.4945/FLUX)
COVAL(NOZ20,V1,ONLYMS,8.4786)
COVAL(NOZ20,U1,ONLYMS,-0.5186)
COVAL(NOZ20,KE,ONLYMS,TKE20)
COVAL(NOZ20,EP,ONLYMS,EPS20)
COVAL(NOZ20,C1,ONLYMS,1.0)
    £
PATCH(NOZ21,SOUTH,21,21,1,1,NOZF,NOZL,1,LSTEP)
COVAL(NOZ21,P1,FLUX,RHO1*7.5113/FLUX)
COVAL(NOZ21,V1,ONLYMS,7.4881)
COVAL(NOZ21,U1,ONLYMS,-0.5893)
COVAL(NOZ21,KE,ONLYMS,TKE21)
COVAL(NOZ21,EP,ONLYMS,EPS21)
COVAL(NOZ21,C1,ONLYMS,1.0)
    £
PATCH(NOZ22,SOUTH,22,22,1,1,NOZF,NOZL,1,LSTEP)
COVAL(NOZ22,P1,FLUX,RHO1*6.2823/FLUX)
COVAL(NOZ22,V1,ONLYMS,6.2534)
COVAL(NOZ22,U1,ONLYMS,-0.6021)
COVAL(NOZ22,KE,ONLYMS,TKE22)
COVAL(NOZ22,EP,ONLYMS,EPS22)
COVAL(NOZ22,C1,ONLYMS,1.0)


PATCH(NOZ23,SOUTH,23,23,1,1,NOZF,NOZL,1,LSTEP)
COVAL(NOZ23,P1,FLUX,RHO1*4.8075/FLUX)
COVAL(NOZ23,V1,ONLYMS,4.7766)
COVAL(NOZ23,U1,ONLYMS,-0.5442)
COVAL(NOZ23,KE,ONLYMS,TKE23)
COVAL(NOZ23,EP,ONLYMS,EPS23)
COVAL(NOZ23,C1,ONLYMS,1.0)
    £
PATCH(NOZ24,SOUTH,24,24,1,1,NOZF,NOZL,1,LSTEP)
COVAL(NOZ24,P1,FLUX,RHO1*3.0869/FLUX)
COVAL(NOZ24,V1,ONLYMS,3.0605)
COVAL(NOZ24,U1,ONLYMS,-0.40292)
COVAL(NOZ24,KE,ONLYMS,TKE24)
COVAL(NOZ24,EP,ONLYMS,EPS24)
COVAL(NOZ24,C1,ONLYMS,1.0)
    £
PATCH(NOZ25,SOUTH,25,25,1,1,NOZF,NOZL,1,LSTEP)
COVAL(NOZ25,P1,FLUX,RHO1*1.1205/FLUX)
COVAL(NOZ25,V1,ONLYMS,1.1082)
COVAL(NOZ25,U1,ONLYMS,-0.16562)
COVAL(NOZ25,KE,ONLYMS,TKE25)
COVAL(NOZ25,EP,ONLYMS,EPS25)
COVAL(NOZ25,C1,ONLYMS,1.0)
    £ outflow
    £
PATCH(OUTFL,HIGH,51,51,20,30,NZ,NZ,1,LSTEP)
COVAL(OUTFL,P1,FIXP,0.0)
    £
LSWEEP=500
    £
IURPRN=0
    £
OUTPUT(P1,Y,N,N,N,N,Y)
OUTPUT(U1,Y,N,N,N,N,Y)
OUTPUT(V1,Y,N,N,N,N,Y)
    £
    GROUP 22. Spot-value print-out
    £
    GROUP 23. Field print-out and plot control
    £
NXPRIN=1;IXPRF=1;IXPRL=45
NYPRIN=1;IYPRF=1;IYPRL=NY
NZPRIN=1;IZPRF=NZ;IZPRL=NZ
IPLTF=FSWEEP;IPLTL=LSWEEP;NPLT=10
ITABL=3
    £
STOP
```

C2: 'Ground' coding for transient undeflected jet

```
C--- GROUP 1. Run title and other preliminaries
C
    1 GO TO (1001,1002),ISC
 1001 CONTINUE
C
      CALL MAKE(XG2D)
      CALL MAKE(YV2D)
      CALL MAKE(YG2D)
      CALL MAKE(ZWNZ)
      CALL MAKE(EASP1)
      CALL MAKE(EASP2)
C
      RETURN
 1002 CONTINUE
      CALL SUB4R(CMU,0.5478,CD,0.1643,CMUCD,0.09,C1E,1.47)
      CALL SUB3R(C2E,1.92,AK,0.435,EWAL,9.0)
      RETURN
C*********************************************************************
C
```

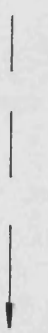

```
C--- GROUP 19. Special calls to GROUND from EARTH
C
   19 GO TO (191,192,193,194,195,196,197,198),ISC
  191 CONTINUE
C   * -------------------- SECTION 1 ---- START OF TIME STEP.
      RETURN
  192 CONTINUE
C   * -------------------- SECTION 2 --- START OF SWEEP.
      RETURN
  193 CONTINUE
C   * -------------------- SECTION 3 ---- START OF IZ SLAB.
      RETURN
  194 CONTINUE
C   * -------------------- SECTION 4 ---- START OF ITERATION.
C
      CALL FNDWDY(EASP1,W1)
      CALL FNDVDZ(EASP2,V1)
C
      CALL FN10(49,EASP1,EASP2,0,-0.0005,0.0005)
C
      RETURN
  195 CONTINUE
C   * -------------------- SECTION 5 ---- FINISH OF ITERATION.
```

```
      RETURN
  196 CONTINUE
C    * ------------------- SECTION 6 ---- FINISH OF IZ SLAB.
C
C-----NORMALISED PRINTOUT AT FINAL SWEEP
C     ------------------------------------
C
      IF(ISTEP.NE.LSTEP) RETURN
C
      IF(ISWEEP.NE.LSWEEP-1) RETURN
C
C
C-----GET GEOMETRIC AND FLOW QUANTITIES
C     -------------------- ------------
C
      CALL GETYX(YG2D,GYC,NYM,NXM)
      CALL GETYX(XG2D,GXG,NYM,NXM)
      CALL GETYX(U1,GU1,NYM,NXM)
      CALL GETYX(V1,GV1,NYM,NXM)
      CALL GETYX(W1,GW1,NYM,NXM)
      CALL GETYX(12,GKE,NYM,NXM)
C
      DO 1961 IY=1,NY


      DO 1962 IX=1,NX
C
      GOM(IY,IX)=GU1(IY,IX)/GYC(IY,IX)
      VECT(IY,IX)=SQRT(GU1(IY,IX)**2+GV1(IY,IX)**2+GW1(IY,IX)**2)
      TINT(IY,IX)=SQRT(GKE(IY,IX))/VECT(IY,IX)
C
 1962 CONTINUE
C
 1961 CONTINUE
C
      CALL SETYX(50,GOM,NYM,NXM)
      CALL SETYX(48,GVE,NYM,NXM)
      CALL SETYX(47,GTI,NYM,NXM)
C

      IF(IZ.NE.NZ) RETURN
C
      DO 3961 IY=1,NY
C
C-----V1 VELOCITY PROFILES AT DISCRETE IY LOCATIONS
C     ---------------------------------------- ------
C
C-----FIRST PROFILE AT IY = 29

      IF(IY.NE.29) GO TO 2961
C
      IF(G19SCND) THEN
         OPEN(29,FILE='Y29',STATUS='UNKNOWN')
         G19SCND=.FALSE.
      ENDIF
C
      DO 1965 IX=1,46
         ANG29=GXG(IY,IX)
         WINK29=ANG29*180.0/3.14159-45.0
         Y29V1=GV1(IY,IX)
         Y29TI=TINT(IY,IX)
         Y29KE=GKE(IY,IX)
C
C-----TABULAR PRINTOUT
C
      IWRIT2=IWRIT2+1
      IF(IWRIT2.EQ.1) WRITE(29,504)
      WRITE (29,505) IY,IX,Y29V1,Y29TI,Y29KE,WINK29
C
 1965 CONTINUE
C
 2961 CONTINUE
```

Appendix D

Derivation of dimensionless parameters for jet penetration, K_P, and swirl, Ks

K_P:

A constant momentum flux may be expressed by

$$\pi\ y^2\ (\tan^2\gamma)\ V^2\ \rho = \frac{\pi}{4}\ D_N^2\ V_{in}^2\ \rho$$

with

	γ	cone angle
	y	radial distance
	V	radial mean velocity
	V_{in}	injection velocity
	D_N	equivalent nozzle diameter

$$y\ (\tan\gamma)\ V = \frac{1}{2}\ D_N\ V_{in}$$

writing dy/dt for V

$$y\ \frac{dy}{dt} = \frac{D_N\ V_{in}}{2\ \tan\gamma}$$

and integrating

$$\int y\ dy = \int \frac{\gamma_N\ V_{in}}{2\ \tan\gamma}\ dt$$

gives

$$y^2 = \frac{D_N\ V_{in}}{\tan\gamma}\ t$$

The injection period t_i is expressed by the mass of the fluid in the analogue model, the injected mass fraction, and the mass flow at the nozzle:

$$t = (\frac{\pi}{4}\ D_T^2\ h\ \rho\ frac)/(\frac{\pi}{4}\ D_N^2\ V_{in}\ \rho)$$

with

	D_T	tank diameter
	h	tank height
	frac	mass fraction injected

$$t = (D_T^2\ h\ frac)/(D_N^2\ V_{in})$$

substituting:

$$y = \sqrt{\frac{D_N \; V_{in} \; D_T^2 \; h \; frac}{(\tan \gamma) \; D_N^2 \; V_{in}}}$$

$$\frac{y}{D_T} = \sqrt{\frac{h \; frac}{(\tan \gamma) \; D_N}}$$

Assuming the cone angle γ to be constant the dimensionless radial distance is taken as penetration parameter:

$$K_P = \sqrt{\frac{h \; frac}{D_N}}$$

K_S:

The dimensionless swirl parameter used is the angle swept during the injection period considered:

$$K_S = \omega \; t_i = 6 \; \omega_{rpm} \; t_i \; [deg]$$

K_R:

The relative effect of swirl to penetration is expressed by K_R:

$$K_R = \frac{K_S}{K_P}$$